Structure and Bonding 170
Series Editor: D.M.P. Mingos

D. Michael P. Mingos *Editor*

The Chemical Bond II

100 Years Old and Getting Stronger

Springer

170
Structure and Bonding

Aims and Scope

The series *Structure and Bonding* publishes critical reviews on topics of research concerned with chemical structure and bonding. The scope of the series spans the entire Periodic Table and addresses structure and bonding issues associated with all of the elements. It also focuses attention on new and developing areas of modern structural and theoretical chemistry such as nanostructures, molecular electronics, designed molecular solids, surfaces, metal clusters and supramolecular structures. Physical and spectroscopic techniques used to determine, examine and model structures fall within the purview of *Structure and Bonding* to the extent that the focus is on the scientific results obtained and not on specialist information concerning the techniques themselves. Issues associatedwith the development of bonding models and generalizations that illuminate the reactivity pathways and rates of chemical processes are also relevant.

The individual volumes in the series are thematic. The goal of each volume is to give the reader, whether at a university or in industry, a comprehensive overviewof an area where new insights are emerging that are of interest to a larger scientific audience. Thus each review within the volume critically surveys one aspect of that topic and places it within the context of the volume as a whole. The most significant developments of the last 5 to 10 years should be presented using selected examples to illustrate the principles discussed. A description of the physical basis of the experimental techniques that have been used to provide the primary data may also be appropriate, if it has not been covered in detail elsewhere. The coverage need not be exhaustive in data, but should rather be conceptual, concentrating on the new principles being developed that will allow the reader, who is not a specialist in the area covered, to understand the data presented. Discussion of possible future research directions in the area is welcomed.

Review articles for the individual volumes are invited by the volume editors.

In references *Structure and Bonding* is abbreviated *Struct Bond* and is cited as a journal.

More information about this series at http://www.springer.com/series/430

D. Michael P. Mingos
Editor

The Chemical Bond II

100 Years Old and Getting Stronger

With contributions by

S. Alvarez · B. Braida · D. Danovich · A. Falceto ·
A. Haaland · P.C. Hiberty · M. Kohout · P.L.A. Popelier ·
S. Shaik · B. Silvi · M. Tilset · W. Wu

Springer

Editor
D. Michael P. Mingos
University of Oxford
Oxford, United Kingdom

ISSN 0081-5993 ISSN 1616-8550 (electronic)
Structure and Bonding
ISBN 978-3-319-33520-9 ISBN 978-3-319-33522-3 (eBook)
DOI 10.1007/978-3-319-33522-3

Library of Congress Control Number: 2016940193

Printed on acid-free paper

This Springer imprint is published by Springer Nature
The registered company is Springer International Publishing AG Switzerland

Preface

These three volumes of *Structure and Bonding* celebrate the 100th anniversary of the seminal papers by Lewis and Kossel. These papers, which formed the basis of the current view of the chemical bond, were published independently in 1916 and have greatly influenced the development of theoretical chemistry during the last century. Their essential ideas, which were initially formulated within classical Newtonian framework, have withstood many experimental tests and proved to be sufficiently flexible to incorporate the newer quantum mechanical ideas, which emerged in the 1920s and 1930s. Most importantly, Lewis' description of the covalent bond provided a graphical notation and a language for experimental chemists, which enabled generations of chemists to constructively discuss and predict the structures of molecules and graphically represent the course of chemical reactions. The Lewis and Kossel descriptions of chemical bonding are cornerstones of the undergraduate curriculum. They have achieved this pre-eminent distinction by evolving and incorporating a flexible view of chemical bonding, based on the symmetry characteristics and radial distribution functions of atomic orbitals. The development of a universally accepted notation for representing the bonds in inorganic and organic molecules has been particularly significant. Spectroscopic and structural results, which emerged as chemistry incorporated quantum mechanical concepts, provided detailed information concerning the structures of molecules not only in the solid state but also in the liquid and gas phases. These have provided increasingly rigorous tests of the bonding models, which emerged from the quantum mechanical description of the chemical bond.

The idea to celebrate this important anniversary in chemical evolution struck a chord with leading figures in the area of theoretical chemistry and resulted in the submission of 18 chapters, and it became necessary to produce three separate volumes of *Structure and Bonding* to satisfactorily account for the enormous influence Lewis and Kossel's seminal ideas had on modern chemistry. Following a historical introduction by myself, Volume 1 contains chapters by Dietar Stalke, Zhenyang Lin, Gernot Frenking, Jean-Francois Halet, Jen-Yves Saillard, José M. Goicoechea, John McGrady and Michael Hall covering a variety of

experimental and theoretical studies of topical chemical bonding issues. Examples include the implications of experimentally determined electron densities on Lewis bond structures, the Lewis description of lone pairs in transition metal complexes, dative Lewis bonds, the bonding patterns in large metal clusters and the role of carbonyl ligands in stabilising such clusters and the electronic properties of endohedral metal clusters.

Volume 2 starts with a detailed account of Lewis and Kossel's legacy in defining the bonding in ionic and covalent compounds of main group elements and addresses the thermochemical and bond length implications of the Lewis and Kossel models. The subsequent chapters by Paul Poppelier, Miroslav Kohout, Sason Shaik, Philippe Hiberty and Bernard Silvi use highly accurate theoretical calculations to address and explore the fundamental nature of the covalent bond. Discussions of quantum chemical topology, the definition of electron pairs in positional space, provide a deeper insight into the nature of the chemical bond and the relevance of the ELF topological approach to the Lewis bond model and the evolution of electron pair bonding in covalent, ionic and charge shift bonds. The Lewis description of the chemical bond was limited to single, double and triple bonds, but in recent years compounds with bond orders greater than three have become commonplace, and the final chapter by Santiago Alvarez compares the electronic characteristics of Cr–Cr quadruple and quintuple bonds.

In Volume 3, the implications of the Lewis bonding ideas for modern inorganic, organic and organometallic chemistry are discussed by Douglas Stephen, Philip Miller, Robert Crabtree, Malcolm Green, Ged Parkin, Didier Bourissou and Ghenwa Bouhadir. These fascinating articles demonstrate how non-conventional Lewis acids and bases have been used to develop new chemistry based on frustrated Lewis pairs and describe the modern coordination chemistry of triphosphine ligands and its catalytic implications. Lewis developed the concept that bases function by donating non-bonding electron pairs, but Crabtree recounts how this view has had to be modified by the discovery of complexes where π-bonds and σ-bonds act as donors. Green and Parkin extend the basic Lewis concepts to organometallic complexes with three-centre two-electron bonds. Bourissou and Bouhadir describe compounds where the lone pairs on transition metals are able to function as Lewis bases – a field which has grown enormously in recent years.

This brief summary provides an indication of how the basic ideas introduced by Lewis and Kossel have blossomed over the last century as a result of the nourishment provided by quantum theory and the love and attention bestowed on them by successive generations of chemists. We hope that the quality and depth of the many contributions in these three volumes will convince the reader that the sentiment expressed in the title of this series "The Chemical Bond 100 Years Old and Getting Stronger" is appropriate.

Oxford, UK D. Michael P. Mingos
April 2016

Contents

Struct Bond (2016) 170: 1–70
DOI: 10.1007/430_2015_192

Published online: 14 February 2016

Lewis and Kossel's Legacy: Structure and Bonding in Main-Group Compounds

Arne Haaland and Mats Tilset

Abstract In this article the authors provide a brief review of the main developments in our understanding of chemical bonding in representative compounds of the main group elements from Lewis' and Kossel's shell-setting articles in 1916 and until the present.

Keywords Bond energies · Coordination compounds · Coordination geometries · Covalent bonds · Covalent radii · Dative bonds · Electronegativity · Hypervalent compounds · Ionic bonds · Ionic radii · Subvalent compounds · The VSEPR model

Contents

A. Haaland (✉) and M. Tilset
Department of Chemistry, University of Oslo, PO Box 1033 Blindern, 0315 Oslo, Norway
e-mail: arne.haaland@kjemi.uio.no; mats.tilset@kjemi.uio.no

1 Introduction: The Contributions of G. N. Lewis, W. Kossel, and I. Langmuir from 1916 to 1923

The developments in the fields of atomic physics and chemistry that led up to the publications by G. N. Lewis and W. Kossel in 1916 have been described by Mingos [1]. We shall give a brief summary of their contributions to our understanding of chemical bonding before proceeding to an account of how their ideas have been developed and modified during the following decades.

Both Lewis [2] and Kossel [3] argued on the basis of a shell structure of the atoms. The first shell may contain one or two electrons and the second and third from one to eight. The chemical inertness of noble gas atoms, like Ne and Ar, suggested that atoms with eight electrons in the outmost shell are particularly stable. Kossel noted that the elements in the group preceding the noble gases, like F and Cl, have a strong tendency to form singly charged anions and that the atoms in the group preceding the halogens, like O and S, have a tendency to form doubly charged anions. On the other hand, the elements in the group following the noble

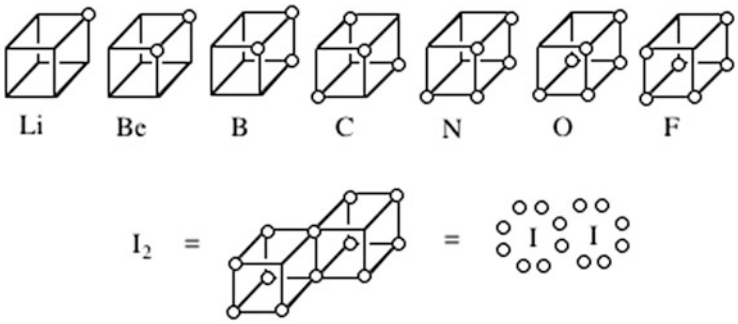

Fig. 1 *Above*: The electronic structures of the second-period elements from Li to F according to Lewis [2]. *Below*: The electronic structure of the iodine molecule

gases, like Na and K, tend to form singly charged cations, while Mg and Ca tend to form doubly charged cations. Thus the atoms or ions in the two series

$$\begin{array}{ccccc} O^{-2} & F^{-1} & Ne & Na^{+1} & Mg^{+2} \\ S^{-2} & Cl^{-2} & Ar & K^{+1} & Ca^{+2} \end{array},$$

all contain eight electrons in the outermost shell and are therefore particularly stable. Kossel concluded that formation of ionic compounds like the alkali metal halides is accompanied by transfer of one electron from the metal atom to the halogen to form an ion pair which is subsequently stabilized by Coulomb attraction.

Lewis initially based his theory of chemical bonding on his model of "cubical atoms" [2]. The atoms in the second period from Li to Ne consist of a "kernel" formed by the nucleus and the two electrons in the first (He) shell, while the number of electrons in the outmost shell increases from one in Li to eight in Ne. These electrons occupy positions at the corners of a cube (Fig. 1). After Ne the process repeats itself across the third period: The kernels now consist of ten electrons, two in the first and eight in the second shell. Like Li, Na and all the other alkali metal atoms have *one* electron in their outer shell; Mg and the other the alkaline earth metal atoms have *two*. Al and Sc have *three*; Si has *four* electrons in the outer shell. P and all the other elements in Group 15 have *five* electrons; S and all the other Group 16 elements have *six*. All the halogen atoms have *seven* electrons in the outer shell, and the noble gas atoms have *eight*. "The remaining elements [in Groups 13 and 14] form a class in which the atomic kernel is probably neither uniquely determined nor invariable during chemical change." We shall return to discuss these elements in Sect. 7.

Lewis based his bonding model on two general observations. Firstly, that the total number of valence electrons in a stable molecule is almost always an *even* number: "Among the tens of thousands of known compounds of the elements under consideration only a few exceptions [to this rule] are known," namely, NO, NO_2, ClO_2, and $(C_6H_5)_3C$ and other triaryl methyls. This observation suggests that bond formation is in some way accompanied by formation of electron pairs.

His second observation concerns the polarity of chemical compounds. Diatomic molecules like F_2 or Cl_2 are completely nonpolar. The highest polarity is found in ionic compounds like NaF or KCl, but in between there appears to be a large number of molecules of intermediate polarity. This observation suggests that the formation of bonds is frequently accompanied by a partial transfer of electrons between the bonded atoms. A good model for the chemical bond should therefore be flexible enough to allow a gradual transition from nonpolar to ionic bonding.

Lewis postulated that:

1. The atomic "kernels remain unaltered in all ordinary chemical changes."
2. "An atom [in a molecule] tends to hold an even number of electrons in the [valence] shell."
3. "The atomic shells are mutually interpenetrable." This means that an electron may occupy a position that represents a corner of each of the two cubical atoms and thus contributes to the number of electrons in the valence shell of both atoms.

After having constructed his model of the atom, Lewis went on to describe the formation of chemical bonds between two cubical atoms as due to sharing of edges or square faces: All halogen atoms are represented by a cube with one electron at each of seven corners and all dihalogen molecules by two cubes sharing an edge (Fig. 1). The three-dimensional figure of the two cubes might also be represented by a formula in which the atomic kernels are represented by the atomic symbol in boldface, all valence electrons are indicated by dots, and the two electrons on the shared edge are placed between the two kernels. Both kernels are thus surrounded by eight valence electrons. This presumably corresponds to a particularly stable arrangement. Lewis also represented the iodine molecule by a simple formula which indicates only the two shared electrons; I:I. He stresses that the two bonding electrons in a polar molecule like HCl will be closer to the negative end of the dipole and suggests that this may be indicated by introducing a space between the H atom and the electron pair, H :Cl.

In a doubly bonded molecule like O_2 or ethene, *two* electron pairs are shared between the two atoms, O::O or $H_2C::CH_2$. In a triply bonded molecule, three electron pairs are shared, N:::N or HC:::CH.

Lewis noted that the cubical model offered no simple representation of the triply bonded molecules. "Perhaps the chief reason for assuming the cubical structure was that this is the most symmetrical arrangement of eight electrons [. . .]. When we consider only known chemical phenomena, and their best interpretation in terms of atomic structure, we are led to assume a somewhat different arrangement of the group of eight electrons [. . .]. The group of eight electrons in which the [four] *pairs* are symmetrically placed about the center gives identically the model of the tetrahedral carbon atom which has been of signal utility throughout the whole of organic chemistry" [2].

Lewis' model suggests that the elements in Group 1 may form only one single bond, the elements in Group 2 may form two single bonds, and B and Al may form three. The number of bonds that these atoms may form is thus limited by the number of electrons available for bond formation. C and Si have four electrons in their

valence shells. After four single bonds have been formed, the atomic kernels are surrounded by a total of eight electrons. The elements in Group 15 may form three single bonds before reaching the octet, the elements in Group 16 two bonds, and the halogens one bond before reaching the octet. In the following we shall denote atoms that conform to these expectations as *Lewis-valent*. The H atom represents a special case, in so far as it only has one vacant position in its valence shell and therefore can only form one bond.

Lewis' model of the chemical bond was enthusiastically endorsed by Langmuir in a long and comprehensive article published 3 years later [4]. Langmuir coined the term "covalent" to denote a shared-electron-pair bond and showed how the concept could be used to correlate or predict the structures of a variety of molecules. In his history of chemistry, W. H. Brock writes that "Langmuir was to act as publicist for the shared pair immediately after the First World War. Lewis was a great teacher, but lacked the dash and charisma of Langmuir" [5].

Among the molecules that Langmuir discussed were also molecules that today would be described as "hypervalent," i.e., where the central atoms form more bonds than expected from the Lewis model. He was obviously reluctant to allow the central atoms to have more than eight electrons in their valence shell and resorted to ionic models; he described PCl_5 as a P^{+5} cation surrounded by five chloride anions. SF_6 was described as an S^{+6} cation surrounded by six fluoride anions at the corners of an octahedron. Langmuir showed that such an arrangement is stable with respect to dissociation to the separated ions, but failed to consider the energy required to transfer six electrons from the S to the F atoms.

Langmuir also mentioned a typical coordination compound, $(CH_3)_3B{:}NH_3$. "According to the octet theory this is a typical primary valence compound in no way different from organic compounds." The discussion about how the bonding in hypervalent molecules should be best described and about the distinction between normal covalent bonds on one side and "coordination links" on the other would, however, continue for several decades.

Seven years after his first article, Lewis wrote the classical monograph *Valence and the Structure of Atoms and Molecules* where he modified his model to bring it into better agreement with the relevant results obtained by physicists and chemists during the preceding decade: "To attempt to keep pace with the rapid developments in so many ramifications of science" is "an impossible task." "Nevertheless it is the same atom and the same molecule that is being studied by the organic chemist, the inorganic chemist and the physicist" [6].

In his revised model, Lewis abandoned the idea of an atom with more or less stationary electrons occupying positions at the corners of a cube, but retained his suggestion that a "chemical bond" corresponds to two electrons "lying between two atomic centers and held jointly in the shells of two atoms." At the same time he emphasized that "the rule eight," by which each atom in a molecule will always contain four electron pairs in the outmost shell, is *not* absolute and devoted a brief chapter to a discussion of the exceptions. The largest group of molecules that defy the rule of eight contain B or Al atoms or atoms from Group 1 or 2. Thus the boron atoms in tris-alkyl boranes and boron trihalides all contain three electron pairs in the valence shell. Like Langmuir, Lewis pointed to the existence of coordination

compounds like $(CH_3)_3B{:}NH_3$, but made no statement as to whether the coordinate link is different from a normal covalent B–N bond where B and N contribute one electron each.

Lewis noted that fused beryllium dichloride has a very low electrical conductivity and suggested that the Be–Cl bonds are covalent rather than ionic. This implies that the Be atom has only two electron pairs in the valence shell.

In 1923 nothing was known about the properties of gaseous monomeric alkali metal halides and Lewis wrote: "In my earliest speculations on this subject I thought of the molecule of sodium chloride as produced by the complete transfer of an electron from the sodium atom to the chlorine atom. But would this be found to be the case if we should study more carefully the properties of sodium chloride in the gas phase?" [6]. We shall consider bonding in the Group 1 and 2 metal halides in Sects. 2 and 3, respectively.

Lewis then turned his attention to hypervalent molecules. He rejected the suggestions that the SF_6 molecule should consist of a S^{+6} cation surrounded by six F^- anions, or that PCl_5 should consist of one P^{5+} cation surrounded by five Cl^- anions, or alternatively of a $[PCl_4]^+$ cation combined with one Cl^- anion. He concluded that the Cl atoms in PCl_5 are "directly attached to the phosphorus atom by a bonding pair of electrons" and that the latter "is surrounded by a group of ten electrons." Similarly the sulfur atom in SF_6 forms six bonds and is therefore surrounded by twelve electrons. He assumed that the SF_6 molecule has high symmetry, perhaps an octahedral structure [6]. This suggestion was commonly accepted and was confirmed 10 years later.

Even though Lewis accepted that the S atom in the hexafluoride could accommodate twelve electrons in the valence shell, he preferred to describe the bonding in sulfur trioxide in terms of three single electron-pair S–O bonds. After three nonbonding pairs had been assigned to each O atom, the S atom was left with only six electrons in its valence shell. For the sulfuric acid molecule, he suggested an electron structure where each of the four O atoms was surrounded by one bonding and three nonbonding electron pairs. This arrangement left the S atom with eight electrons in its valence shell. His proposed electron structure for SO_3 was later challenged by others, and models with one, two, or three SO double bonds were put forward. Such models would leave the central S atom with four, five, or six electron pairs in the valence shell. We shall discuss the properties of hypervalent compounds in Sect. 8.

2 Structure and Bonding in Crystalline Alkali Metal Halides

The first chemical compound to have its crystal structure determined by X-ray diffraction was NaCl (rock salt). The author of the study, which was published in 1913, was a young man of 23 years, William L. Bragg [7]. Two years later, he and his father, W. H. Bragg, shared the Nobel Prize in physics.

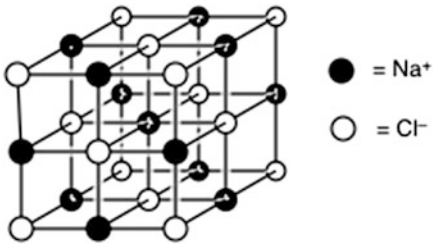

Fig. 2 The rock salt structure

The crystal structure of NaCl is face-centered cubic. Each ion, Na^+ or Cl^-, is surrounded by six ions of opposite charge at the corners of an octahedron (Fig. 2). The Na–Cl distance was found to be 280 pm, which is about 2 pm shorter than the presently accepted value.

It has since been established that of the 20 alkali metal halides, MX, seventeen have face-centered cubic structures. The exceptions, CsCl, CsBr, and CsI, all have body-centered cubic structures where each ion is surrounded by eight counterions at the corners of a cube.

The lattice energy ΔU_L of a crystalline alkali metal halide may be defined as the energy difference between the separated M^+ and X^- ions and the crystal in its equilibrium structure at zero K. The lattice energy cannot be measured directly, but may be computed from standard enthalpies of formation at zero K:

$$\Delta U_L = \Delta H_f^0(M^+(g)) + \Delta H_f^0(X^-(g)) - \Delta H_f^0(MX(s)).$$

During the 6-year period for 1918 to 1924, Born, Landé, Madelung, and others developed methods for quantitative calculation of the lattice energy of an ionic crystal from atomic properties. The basic assumption underlying their approach was that the energy of an ionic crystal is determined by two terms. The first term consists of the sum of all interionic Coulomb interaction energies. The second term consists of the sum of all repulsion energies between ions that are brought into close contact.

If the Coulomb interaction energy of a single ion pair $M^+ X^-$ is defined as zero for the ions at infinite distance from each other, the Coulomb energy of the pair at a finite distance R is given by

$$U_{Coul}(R) = -e^2/(4\pi\varepsilon_0 R),$$

where ε_0 is the vacuum permittivity. As the interatomic distance is decreased and the atoms are brought into closer contact, the Coulomb attraction is opposed by a rapidly increasing interatomic repulsion. Born and Landé suggested the repulsion energy of an given ion pair in close contact might be given by the simple relationship

$$U_{\mathrm{Born}}(R) = b_{\mathrm{MX}}/R^{\mathrm{n}},$$

where the magnitude of the Born constant b_{MX} depends on the nature of the interacting ions and n is a positive integer in the range from 8 to 12 [8, 9].

According to Born and Landé, the energy of one mole of a crystalline alkali metal halide MX with a shortest M–X distance of R is then given by

$$U_{\mathrm{BL}}(R) = -N_{\mathrm{A}}Me^2/(4\pi\varepsilon_0 R) + N_{\mathrm{A}}C_{\mathrm{N}}b_{\mathrm{MX}}/R^{\mathrm{n}} - E_0,$$

where N_{A} is the Avogadro number. The Madelung constant M is determined by summation of all interionic Coulomb interaction energies in the crystal: For face-centered structures $M = 1.748$ and for body-centered structures $M = 1.763$ [10]. C_{N} denotes the coordination number of the ions: six for face-centered and eight for body-centered structures. The last term, the zero point vibrational energy E_0, is insignificant and is usually neglected.

The Born constant may be eliminated by using the fact that the derivative of $U_{\mathrm{BL}}(R)$ with respect to R must be zero at the equilibrium bond distance R_{e}:

$$(\mathrm{d}U_{\mathrm{BL}}(R)/\mathrm{d}R)_{\mathrm{Re}} = N_{\mathrm{A}}Me^2/\left(4\pi\varepsilon_0 R_e^2\right) - nN_{\mathrm{A}}C_{\mathrm{N}}b_{\mathrm{MX}}/{R_{\mathrm{e}}}^{\mathrm{n}+1} = 0,$$

or

$$N_{\mathrm{A}}C_{\mathrm{N}}b_{\mathrm{MX}}/R_{\mathrm{e}}^{\mathrm{n}} = (1/n)N_{\mathrm{A}}Me^2/(4\pi\varepsilon_0 R_{\mathrm{e}}).$$

The lattice energy may therefore be written as

$$\Delta U_{\mathrm{L}} = U_{\mathrm{BL}}(R_{\mathrm{e}}) = -\left[N_{\mathrm{A}}Me^2/(4\pi\varepsilon_0 R_{\mathrm{e}})\right](1 - 1/n).$$

The energy of atomization of the crystal is

$$\Delta U_{\mathrm{atom}} = \left[N_{\mathrm{A}}Me^2/(4\pi\varepsilon_0 R_{\mathrm{e}})\right](1 - 1/n) - IE(\mathrm{M}) + EA(\mathrm{X}),$$

where IE(M) and EA(X) are the ionization energy of the metal atom and the electron affinity of the halogen atom, respectively.

In 1930 Sherman published the results of such lattice energy calculations for all the 20 alkali metal halides [11]. When the magnitude of the Born exponential n was varied with the size of the two ions from 6.0 in LiF to 12.0 in CsI to reflect the variation of the compressibility of the crystals, the lattice energies agreed with those computed from thermochemical data to within 2.5%. Decades would pass before chemists were able to calculate the atomization energies of nonionic compounds with such accuracy!

2.1 Structure and Bonding in Gaseous, Monomeric Alkali Metal Halides

In the years following World War II, spectroscopic studies yielded accurate equilibrium bond distances, R_e, dissociation energies D_o, vibrational frequencies ω, and electronic dipole moments μ_{el} for all the gaseous, monomeric alkali metal halides [12]. The M–X bonds in these monomers are not only exceptionally polar; they are also remarkably short and strong: Thus the bond distance in gaseous NaCl is 236 pm, 17 pm shorter than the arithmetic average of the bond distances in gaseous Na_2 and Cl_2 and 46 pm shorter than in the crystalline phase. The dissociation energy of gaseous NaCl is 408 kJ mol^{-1}, i.e., higher than the *sum* of the dissociation energies in gaseous Na_2 and Cl_2, 155 and 130 kJ mol^{-1}, respectively. Before discussing how the Born–Landé model may be used to estimate the dissociation energies, we pause to consider the shapes of the two ions.

The observed electric dipole moments of the gaseous alkali metal halides range from 6.28 Debye in LiF to 11.7 Debye in CsI. If the molecules are assumed to consist of two spherically symmetrical, singly charged ions, the dipole moments can be calculated from

$$\mu_{el}^{0} = e\ R_e.$$

All these calculated dipole moments are substantially *higher* than the experimental values. On the average calculated dipole moments are about 25% larger than the experimental, so it is clear that the charge distribution in alkali metal halide molecules deviates significantly from that predicted from the spherical ion model.

The assumption that the ions remain spherical when they are brought into close contact is in fact physically unreasonable: Each of the two ions will be polarized by the electric field created by the other. Thus the net positive charge on the cation will attract the electrons on the anion and pull them back into the region between the atomic kernels. To a first, linear approximation, the dipole moment thus induced on the anion is given by the product of the polarizability of the anion (α_a) and the strength of the electric field at the center of the anion created by the positive charge of the cation:

$$\mu_a^* = \alpha_a e/\left(4\pi\varepsilon_0 R_e^2\right).$$

Similarly the net charge on the anion induces an atomic dipole μ_c* on the cation. The directions of the induced dipole moments are such as to reduce the overall dipole moment of the molecule:

$$\mu_{el} = e\ R_e - \mu_a^* - \mu_c^*.$$

Calculations on a polarizable-ion model [13, 14] reproduce the experimental dipole moments with an average deviation of only 5% as compared to the 32% deviation obtained with spherical ion model.

We now return to the spherical ion model. According to the Born–Landé model, the energy for one mole of a pair of spherical ions M^+ and X^- at a distance of R is given by

$$U_g(R) = -N_A e^2/(4\pi\varepsilon_0 R) + N_A b_{MX}/R^n.$$

Using the fact that the derivative of $U_g(R)$ with respect to the bond distance is equal to zero at the equilibrium bond distance, one obtains

$$U_g(R) = -\left[N_A e^2/(4\pi\varepsilon_0 R_e)\right](1 - 1/n).$$

The dissociation energy of the gaseous monomers is then given by

$$\Delta U_{atom} = D_0 = \left[N_A e^2/(4\pi\varepsilon_0 R_e)\right](1 - 1/n) - IE(M) + EA(X) - E_0.$$

The dissociation energies calculated with the exponent $n = 10$ have been listed in reference [15]. The calculated dissociation energy of LiF is higher than the experimental value; all other calculated dissociation energies are too low. The largest deviations, about 15%, are found for the two iodides LiI and CsI. The average deviation for the 20 alkali metal halides is 8%, as compared to the 2.5% reported for the crystalline phase.

One possible reason for the large discrepancy between calculated and experimental dissociation energies of the gaseous molecules is that polarization effects have been neglected. The effect of the polarization is to stabilize the ion pair, i.e., to increase the dissociation energy. Since the anions are more polarizable than the cations, and since their polarizabilities increase as Group 17 is descended, the energy gain would increase from M^+F^- to M^+I^-. Indeed, calculations of the dissociation energies that include polarization effects reduce the discrepancies between calculated and experimental dissociation energies from 8 to 5%.

Because of the high symmetry of the crystal lattice, the electric fields created by the nearest neighbors of each ion will to a large extent cancel one another, and in any case the shape of each ion will reflect the symmetry of its surroundings. The excellent agreement between the energies of atomization calculated from spherical-ion model and those computed from thermochemical data provides a solid basis for a description of the crystalline alkali halides as completely ionic. It is possible that the fit between experimental and calculated dipole moments and dissociation energies of the gaseous monomers could be improved by inclusion of higher order polarizabilities, but in our view the agreement is already close enough to justify a description of the gaseous molecules as pairs of polarized ions formed by complete transfer of one electron from the metal to the halogen atom.

3 The Dihalides of the Group 2 and Group 12 Metals: From Ionic to Polar Covalent Bonding

3.1 Structures and Bonding in the Solid State

While the 20 Group 1 metal halides all adopt either a face-centered or a body-centered crystal structure, crystals of the 32 dihalides of the Group 2 and 12 metals form a bewildering array of at least 15 different structure types. Both the crystal and the gas-phase structures have recently been described and correlated in comprehensive reviews by Hoffman and coworkers [16, 17]. In this section we shall be particularly concerned with the crystal structures of the eight metal difluorides and the four mercury dihalides.

One year after he had published the crystal structure of NaCl and other alkali metal halides, L. W. Bragg proposed a crystal structure for the naturally occurring mineral fluorite (CaF_2) based on *three* X-ray reflections [18]. The structure consisted of a cubic unit cell with one metal ion at the center of the cube, eight ions at the corners, and six at the centers of the square faces, but *no* ions at the edges (Fig. 3). This unit cell may be divided into eight smaller cubes where every second corner in each is occupied by a metal ion. The eight fluoride ions were placed at the centers of these cubes. Each metal cation is thus surrounded by eight anions at the corners of a cube and each fluoride anion by four cations at the corners of a tetrahedron. Bragg's structure has subsequently been confirmed by others. The Ca–F contact distance is 236 pm.

The difluorides of strontium, barium, cadmium and mercury all adopt the fluorite crystal structure. The difluorides of magnesium and zinc adopt a "rutile"-type structure where each metal cation is surrounded by six F anions at the corners of an octahedron, and each anion is surrounded by three metal cations in a planar trigonal arrangement [19].

BeF_2 is tetramorphic: Crystal structures similar to those of α- and β- quartz and α- and β- cristobalite have all been characterized. Only very recently has one

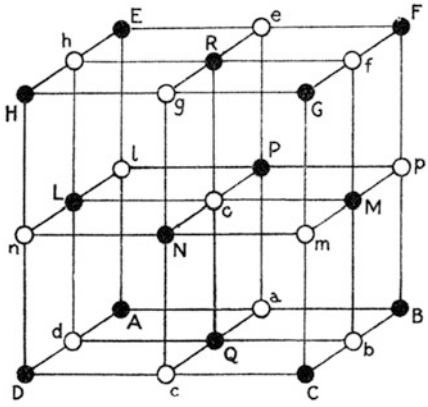

Fig. 3 The crystal structure of fluorite (CaF_2). Reproduced from Proceedings of the Royal Society A (1914)

modification been fully characterized by single crystal X-ray diffraction. Each Be ion is surrounded by four fluoride ions at the corners of a slightly distorted tetrahedron. The Be–F contact distance is 154 pm [20].

An indication of the charge distribution in these crystals may be obtained by comparing the energies of atomization calculated from the Born–Landé spherical-ion model with those obtained from experimental thermochemical data. Lattice energies calculated for the Ca, Sr, and Ba difluorides yield atomization energies that reproduce the experimental atomization energies to within 1%; calculations on MgF_2 reproduce the experimental atomization energy with a deviation of less than 3%. It is clear that these crystal difluorides are best described as perfectly ionic.

Even though ZnF_2 is isomorphic with MgF_2, and CdF_2 and HgF_2 are isomorphic with CaF_2, the lattice energy calculations yield atomization energies in poorer agreement with the experimental values: The calculated atomization energy of ZnF_2 is 9% lower than the experimental value, CdF_2 15% lower, and HgF_2 20% lower [21]. No lattice energy calculations have been reported for BeF_2. It is clear that the tendency to form ionic bonds decreases in the order

$$\text{Ba} \approx \text{Sr} \approx \text{Ca} > \text{Mg} > \text{Zn} > \text{Cd} > \text{Hg}.$$

Crystals of MgI_2, CaI_2, and CdI_2 are isomorphic. Lattice energy calculations yield atomization energies that are 17% below the experimental for Ca, 43% lower for Mg, and 80% lower for Cd [21]. It is clear that the tendency for fluorine to form ionic bonds is stronger than that of iodine.

The coordination number of the metal atom in crystalline dichlorides, dibromides, or diiodides is four if M=Be and six or higher if M=Mg, Ca, Sr, or Ba. The coordination numbers of Zn in the dichloride, dibromide, or diiodide are 4 or 6 and those of Cd 6 or 8. The coordination numbers of mercury dichloride, dibromide, and diiodide break the pattern: Crystalline $HgCl_2$ and $HgBr_2$ consist of linear HgX_2 molecules and crystalline HgI_2 of chains of edge-sharing HgI_4 tetrahedra. A second modification of HgI_2 with linear molecules is stable at higher temperature. The low coordination numbers of $HgCl_2$, $HgBr_2$, and HgI_2 are sufficient to show that the crystals are *not* held together by nondirectional Coulomb forces: The molecular units must be covalently bonded.

3.2 The Electrical Conductivities of Molten Dichlorides

It is well known that the molten alkali metal halides like NaCl are good electric conductors, and this is commonly taken as proof that the melt consists of ions rather than neutral molecules. As early as in 1926, Biltz and Klemm published a survey of the specific electrical conductivities of 45 metal halides at temperatures just above their melting points [22]. The resulting conductivities were found to vary over six orders of magnitude.

Table 1 The specific electrical conductivities, σ (in S cm^{-1}), of the Group 2 and 12 metal dichlorides just above their melting points (listed in parentheses) [22–25]

$BeCl_2$	$MgCl_2$	$CaCl_2$	$SrCl_2$	$BaCl_2$
1.56×10^{-7} (393°C)	1.01 (714°C)	2.01 (775°C)	2.00 (874°C)	2.03 (961°C)
		$ZnCl_2$	$CdCl_2$	$HgCl_2$
		0.0015 (290 °C)	1.87 (568°C)	3.4×10^{-5} (277)°C

No information is available about the conductivities of the Group 2 and 12 metal difluorides, presumably because of their high melting points and corrosive properties. The conductivities of the dichlorides are listed in Table 1. Like the conductivities of the alkali metal chlorides, the conductivities of the Mg, Ca, Sr, Ba, and Cd dichlorides lie in the range from 1.0 to 10 S cm^{-1}. These compounds are good conductors and the melts presumably contain high concentrations of ions.

The specific conductivity of $HgCl_2$ at its melting point is five orders of magnitude lower, $\sigma = 3.4 \times 10^{-5}$ S cm^{-1}. It increases slowly with increasing temperature; conductivity measurements under high pressures show that σ reaches a maximum value of 9.3×10^{-5} S cm^{-1} at 500°C. The concentration of ionic species in the melt is obviously very low at any temperature. Since the crystals contain covalently bonded $HgCl_2$ molecules, it is not surprising that these should be retained in the liquid phase.

The conductivity of $ZnCl_2$ at the melting point is hundred times higher than that of the Hg analogue, but a thousand times lower than that of $CdCl_2$. The conductivity increases rapidly with rising temperatures; at 863°C (130°C above its normal boiling point), it has increased to 0.94 S cm^{-1}, comparable to that of $CdCl_2$. The crystal structure of $ZnCl_2$ consists of chains of edge-sharing $ZnCl_4$ tetrahedra. A neutron diffraction study of the melt 40°C above the melting point has shown that the dominant structural motif is that of corner-sharing tetrahedra [26].

The conductivity of $BeCl_2$ is very low at the melting point (1.56×10^{-7} S cm^{-1}) but increases to 3.77×10^{-3} S cm^{-1} at the normal boiling point (482°C). Crystalline $BeCl_2$ is dimorphic, but the metal atoms are four-coordinate in both forms. The structure of the melt is probably similar to that of molten $ZnCl_2$. It is clear that the molten Zn or Be dichlorides contain oligomeric, presumably covalently bonded, species that are gradually broken down at higher temperatures. At the same time the concentration of ionic species increases.

3.3 Structure and Bonding in the Gaseous Monomers

It was long taken for granted that all monomeric dihalides of the Group 2 and 12 metals have linear equilibrium structures in the gas phase, similar to the structures of $HgCl_2$ and $HgBr_2$ in the solid phase. The first evidence that this might not be so was provided by the molecular beam studies published by Klemperer and coworkers in 1963 and 1964 [27, 28]. Some of the Group 2 dihalides,

CaF_2, SrF_2, and all the Ba dihalides, were deflected by inhomogeneous electric fields. These observations suggested that the molecules have permanent electric dipole moments, i.e., that their molecular structures are angular.

The determination of the molecular structures of monomeric metal halides by gas-phase electron diffraction began in the 1930s, but did not gain momentum until the 1960s. Since then the molecular structures of 27 out of the 32 Group 2 and 12 metal dihalides have been determined by this method (Table 2). These experimental investigations have been supplemented with an increasing number of computational studies. There is today general agreement that CaF_2, SrF_2, $SrCl_2$, and each of the four Ba dihalides have angular equilibrium structures with XMX angles varying from about 120° to about 150°. The reported calculated barriers to linearity vary from about 1 kJ mol^{-1} in $SrCl_2$ to 33 kJ mol^{-1} in BaF_2. The stabilization of the angular structures has been interpreted in terms of polarization of the metal cation, *sd*-hybridization, or a combination of both [16]. The dihalides of the Group 12 metals are all linear [17].

The experimentally determined MX bond distances of 27 dihalides of the Group 2 and 12 metals are listed in Table 2. In most cases they are accurate to better than ±2 pm. As in the case of the alkali metal monohalides, the bond distances of the Group 2 metal dihalides increase monotonically with increasing atomic numbers of the metal or halogen atoms. The bond distances in the Group 12 metal dihalides increase with the atomic number of the halogen, but the variation with the atomic number of the metal breaks the pattern: Hg forms shorter bonds than Cd. The shortening is probably due to a combination of relativistic effects and the lanthanide contraction [17].

For each metal atom, the bond energies decrease with increasing atomic number of the halogen atom. The M–X bond energies of the Group 12 metals decrease as the group is descended from Zn to Hg, but the variation of the Group 2 metal M–X bond energies is more irregular: For each halogen atom, there is a significant *decrease* of the bond energy between Be and Mg, followed by slower and more irregular *increase* from Mg to Ba.

Somewhat to our surprise, we have been unable to find reference to any published attempt to calculate these bond energies of the gaseous dihalides on the basis of the Born–Landé lattice energy model. We have therefore carried out such calculations at a level that reproduced the bond energies of the alkali metal halide monomers with an average deviation from the experimental values of 8%. All calculations were carried out on linear XMX structures. The ratio between these calculated values and their experimental counterparts are listed in the last column of Table 2.

For BeI_2 and seven dihalides of Zn, Cd, or Hg, the Born–Landé calculations on the monomers yield *negative* bond energies: The Coulomb interaction energies are not large enough to compensate for the energies required to remove two electrons from the metal atom. These molecules must therefore be described as completely covalent. Before going on, we pause to note that five of these eight covalent dihalides, namely, $ZnBr_2$, ZnI_2, $HgCl_2$, $HgBr_2$, and HgI_2, are known to be poor electric conductors in the molten state.

Table 2 Gaseous, monomeric dihalides of the Group 2 and 12 metals, MCl_2(g)

	R_{exp} (pm)	R_{calc} (pm)	$\angle_{exp}$ (°)	$\angle_{calc}$ (°)	q_M (au)	MBE_{exp} (kJ mol^{-1})	MBE_{calc}/ MBE_{exp}
BeF_2	139	138	Lin	Lin	1.29	635	91%
$BeCl_2$	180	180	Lin	Lin	1.03	461	51%
$BeBr_2$	194	196	Lin	Lin	0.93	386	32%
BeI_2	216	217	Lin	Lin	0.82	299	<0
MgF_2	177	175	Lin	Lin	1.46	513	91%
$MgCl_2$	218	218	Lin	Lin	1.24	390	66%
$MgBr_2$	233	233	Lin	Lin	1.15	334	51%
MgI_2	–	254	Lin	Lin	1.03	259	24%
CaF_2	–	201	~142	147	1.81	557	99%
$CaCl_2$	248	247	Lin	Lin	1.66	445	82%
$CaBr_2$	262	263	Lin	Lin	1.57	392	75%
CaI_2	284	284	Ln	Lin	1.46	323	61%
SrF_2	–	214	~108	131	1.80	541	100%
$SrCl_2$	263	266	~142	146	1.65	438	85%
$SrBr_2$	278	279	~180	154	1.63	396	79%
SrI_2	301	301	Lin	166	1.56	325	66%
BaF_2	–	226	~100	121	1.83	568	99%
$BaCl_2$	277[b]	277	~110	128	1.70	459	88%
$BaBr_2$	291	293	~138	131	1.65	413	82%
BaI_2	315	316	138	133	1.56	347	74%
ZnF_2	174	174	Lin	Lin	1.22	390	63%
$ZnCl_2$	207	210	Lin	Lin	0.99	318	27%
$ZnBr_2$	220	224	Lin	Lin	0.91	269	<0
ZnI_2	240	244	Lin	Lin	0.81	203	<0
CdF_2	–	194	Lin	Lin	1.26	329	63%
$CdCl_2$	228	229	Lin	Lin	1.03	273	21%
$CdBr_2$	239	243	Lin	Lin	0.95	232	<0
CdI_2	258	262	Lin	Lin	0.84	192	<0
HgF_2	194	194	Lin	Lin	1.12	254	35%
$HgCl_2$	225	229	Lin	Lin	0.90	224	<0
$HgBr_2$	238	243	Lin	Lin	0.82	184	<0
HgI_2	257	263	Lin	Lin	0.72	145	<0

Experimental and calculated bond distances (R) and valence angles ($\angle$); calculated APT net atomic charges on the metal atoms (q_M); mean bond energies at 0 K calculated from thermodynamic data, MBE_{exp}; and the ratio between mean bond energies calculated from ionic models, MBE_{calc}, and the experimental values. Experimental data from [29–32]. The experimental bond distances are in most cases accurate to better than ±2 pm. The experimental *MBE*s are probably accurate to about ±10 kJ mol^{-1}. For information about calculated parameters, see text

The calculations on CaF_2, SrF_2, and BaF_2 yield *MBE*s that differ from their experimental counterparts by 1% or less. There can be no doubt that the ionic bonding mode in the crystals is conserved in the gaseous monomers. The

calculations on BeF_2 and MgF_2 reproduce the experimental bond energies with a deviation of 9%, while calculations on $CaCl_2$, $SrCl_2$, $BaCl_2$, and $BaBr_2$ reproduce the experimental bond energies with deviations less than 20%. We note that that these three dichlorides are known to be good conductors of electricity in the molten state. We conclude that the bonding in the gaseous monomers of BeF_2, MgF_2, $CaCl_2$, $SrCl_2$, $BaCl_2$, and $BaBr_2$ is best described as close to the ionic limit. Born–Landé calculations on the fifteen dihalides that have not been mentioned in the two preceding paragraphs yield bond energies ranging from 21% to 79% of the experimental.

Very recently Foroutan-Nejad has carried out high-level quantum chemical calculation on the molecular structures and atomic charges in all the monomeric dihalides of the Group 2 and 12 metals.[1] The calculations reproduced the experimental bond distances with deviations of 2 pm or less. They also reproduced the angular structures obtained by experiment and previous calculations and added another possible member (SrI_2) to the list. The calculated barriers to linearity varied from 0.03 kJ mol^{-1} in SrI_2 to 22 kJ mol^{-1} in BaF_2 (see Table 2).

The calculated atomic polar tensor (ATP) charges on the metal atoms in the eight molecules that we have described as covalent range from +0.72 au in HgI_2 to +0.95 au in CdI_2. The bonds are covalent but polar. The atomic charges on the metal atom in the eight dihalides that we described as ionic or "close to the ionic limit" range from +1.29 in BeF_2 to +1.83 au in BaF_2. The atomic charges on the metal atoms in the remaining fifteen gaseous dihalides range from +0.99 au in $ZnCl_2$ to +1.63 au in $SrBr_2$.

The variation of the properties of the Group 2 and 12 metal dihalides thus provides an excellent illustration of Lewis' proposition that "the distinction between the most extreme polar and nonpolar types is only one of degree."

4 Ionic Radii

4.1 Atomic Radii from Unit Cell Dimensions

By 1920 the unit cell dimensions of 15 of the 17 alkali metal halides with the face-centered rock salt structures had been determined. The first attempt to utilize such data to estimate the size of individual ions appears to have been made by Alfred Landé [35]. He assumed that the alkali metal cations and halide anions could be regarded as spherical and concluded that the unit cell dimension *a* could be written

[1] C. Foroutan-Nejad, to be published. The structures of all molecules were optimized under $D_{\infty h}$ and C_{2v} symmetry at the B3LYP/def2–TZVPPD level using the Gaussian 09 rev D suite of programs [33]. Atomic polar tensor (APT) atomic charges were computed as one third of the sum of the first derivatives of the molecular electric dipole moment with respect to the three coordinates of each nucleus [34].

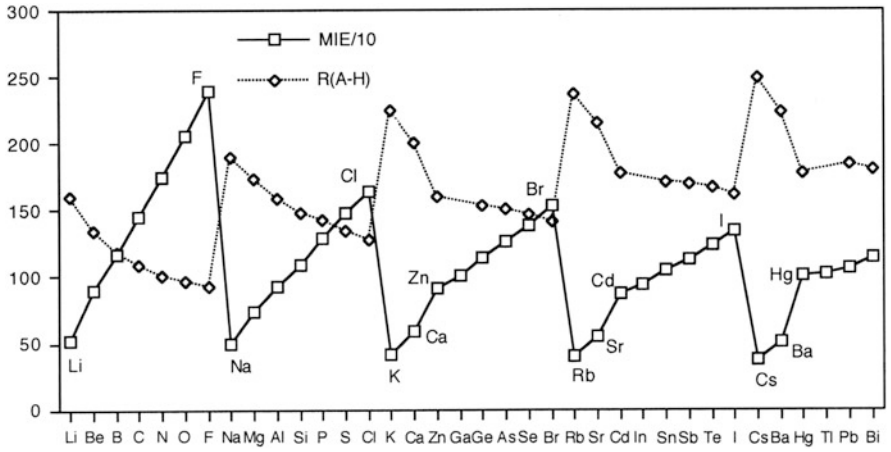

Fig. 4 Mean valence shell ionization energies, *MIE*, and A–H bond distances in hydrogen compounds of main-group elements (Group 18 elements excluded). The numbers on the perpendicular axis refer to *MIE*s in kJ mol^{-1} multiplied by 10^{-1} and to bond distances *R*(A–H) in pm. The experimental bond distances have been taken from the gaseous, monomeric compounds AH, ·AH, ·AH, $·AH_2$, AH_4, AH_3, AH_2, and HA of the elements in Groups 1, 2, 12, 13, 14, 15, 16, and 17, respectively. Note that bond distances for $·GaH_2$, $·InH_2$, and $·TlH_2$ are missing. Reproduced from [15]

as $a = 2r_+ + 2r_-$ where r_+ and r_- were the radii of the cation and anion, respectively (Fig. 4). Once the radius of *one* ion has been determined or estimated, the radii of all the others could be calculated from the unit cell dimension, but where to find the first radius? Further progress was only possible through additional assumptions or introduction of information from other sources. Landé solved the problem by assuming that the smallest cation, Li^+, is so much smaller than the anions that it can fit into the holes between them. This means that the diagonal of the cubic faces is equal to $\sqrt{2}r_-$ or $r_- = (1/\sqrt{2})\,a$. Once the radii of the four halide anions had been estimated from the unit cell dimensions of their lithium salts, the ionic radii of the three alkali metal cations, Na^+, K^+, and Rb^+, could be obtained from the cell dimensions of their salts. The radius of Li^+ ion was left unknown [35].

Three years later, Wasastjerna was able to present a table with more accurate radii for 16 ions, including O^{-2}, F^-, Na^+, and Mg^{+2} (Table 3) [36]. Wasastjerna fixed the ratio between the radius of an alkali metal cation and the radius of the isoelectronic halide anion (for instance, the ratio between the radii of Na^+ and F^-) using polarizability data from aqueous solutions. The polarizabilities of the halide anions were first determined under the assumption that the hydrogen ions do not contribute significantly to the molar polarizabilities of dissolved hydrogen halides. The polarizabilities of the cations could then be obtained from measurements on the salts. Molar polarizabilities are roughly proportional to the ionic volumes, and Wasastjerna fixed the radius ratio r_+/r_- as the fourth root of the polarizability ratio of the two ions (Table 3).

Table 3 The ionic radii (in pm) of singly and doubly charged ions of main-group elements according to Wasastjerna [36], Pauling [37] and Shannon [40]

	Wasastjerna	Pauling	Shannon		Wasastjerna	Pauling	Shannon
Li^+	–	76	90	Be^{+2}	–	45	59
Na^+	101	95	102	Mg^{+2}	75	65	72
K^+	130	133	138	Ca^{+2}	102	106	100
Rb^+	150	148	152	Sr^{+2}	120	113	118
Cs^+	175	169	167	Ba^{+2}	140	135	135
F^-	133	136	133	O^{-2}	132	140	140
Cl^-	172	181	181	S^{-2}	169	184	184
Br^-	192	195	196	Se^{-2}	177	198	198
I^-	219	216	220	Te^{-2}	191	221	221

The radii of ions are known to increase with increasing coordination numbers. The radii in the table refer to coordination numbers equal to six

In the 1939 edition of his classic book *The Nature of the Chemical Bond*, Pauling listed an extensive table of ionic radii of main-group elements obtained by fixing the radius ratios between the four isoelectronic ion pairs F^- and Na^+, Cl^- and K^+, Br^- and Rb^+, and I^- and Cs^+ as the inverse ratio between the effective nuclear charges $r_+/r_- = Z^-_{\text{eff}-}/Z^+_{\text{eff}}$ [37]. The effective nuclear charge of an atom or ion is defined as the difference between the true nuclear charge and the "screening constant" S reflecting the shielding of the nucleus by the other electrons: $Z_{\text{eff}} = Z - S$. Pauling had earlier estimated the shielding constants of the noble gas atoms by a combination of information about the shapes of the electron distribution in ground and excited states of one-electron atoms according to Schrödinger's quantum mechanics and experimental information about the atomic polarizabilities [38]. The exact procedure was not described, but his values for screening constants were not significantly different from those published by J. C. Slater 3 years later [39]. Assuming that the screening constants of the 10-electron ions F^- and Na^+ are equal to the screening constant of Ne, Pauling obtained the effective nuclear charges $Z_{\text{eff}} = 6.48$ for Na^+ and $Z_{\text{eff}} = 4.48$ for Li^-. Similarly the shielding constants of the 18-electron ions S^{-2}, Cl^-, K^+, and Ca^{+2} were assumed to equal that of Ar, those of the 36-electron ions to equal that of Kr, and those of the 54-electron ions to equal that of Xe. Pauling's ionic radii, which differed from Wasastjerna with up to 30 pm in the case of Te_{-2}, became widely used during in the following decades.

Finally, in 1976, R. D. Shannon published a table of "effective ionic radii" of ions formed from all elements except the noble gases based on observations of nearly 2,000 crystal structures [40]. The ionic radii of the di-negative ions of O, S, Se, and Te were, however, fixed at their Pauling values. The agreement between the ionic radii listed by Pauling and Shannon is generally good, but Shannon's ionic radii for Na^+ and Mg^{+2} are 7 pm larger than those of Pauling, presumably because the former was drawing on a larger amount of information.

How good are these values? Shannon's radii reproduce the observed interionic distances in the 17 alkali metal halides with the rock salt structures with an average

deviation of 3 pm and a maximum deviation of 5 pm. The ionic radii have been determined under the assumption that the size of an ion varies with the coordination number but is independent of the nature of the counterion. The deviations between observed and calculated distances presumably reflect the "natural variation" of the radius of an ion from one counterion to the other.

4.2 *Topological Analyses of Charge Densities in Ionic Crystals and "Crystal Radii"*

The first experimental determination of the charge density in a crystalline alkali metal halide appears to be the X-ray study of NaCl reported by Witte and Wölfel in 1955 [41]. The point of minimum charge density along the straight line between nearest neighbor cations and anions, the so-called bond critical point (*bcp*), was found at a distance of 117 pm from the cation and 165 pm from the anion. These distances were confirmed by an independent study published by Schoknecht 2 years later [42]. The bond critical point has often been regarded as marking the boundary between the two bonded atoms, yet the cation–*bcp* distance in NaCl was about 20 pm longer than Pauling's value for the ionic radius of Na^+ and the anion–*bcp* distance correspondingly shorter than the ionic radius of Cl^-. In the following years similar results were obtained in charge density studies of crystalline LiF, KBr, and RbCl.

When publishing his tables of effective ionic radii, Shannon referred to the results of the charge density studies and included a second table of "crystal radii" where the radius of each cation had been increased by addition of 14 pm and the radius of each anion reduced by the same amount. It should be clear that addition of the "crystal" radii of the cation and anion will produce the same interatomic distance as addition of the traditional "effective" ionic radii, but Shannon "felt that crystal radii correspond more closely to the physical size of the ions in a solid."

We believe that the introduction of the new set of "crystal radii" may have been premature. When the charge distribution in a molecule or crystal is analyzed through the atoms in molecules (AIM) approach, space is subdivided by drawing so-called zero-flux surfaces between the atoms [43]. These surfaces intersect the bond paths between the atoms at the bond critical points. Each atom is regarded as contained in a basin limited by the zero-flux surfaces. The electronic charge of each atom is then determined by integration over the atomic basin. Perrin has shown that AIM analysis of the charge created by two overlapping spherically symmetrical atomic charge densities, one more compact than the other, can lead to calculated AIM atomic charges different from those of the isolated charge densities [44]. He stressed that these charges are not due to deformation of the atomic charge densities but to the difference between the atomic radii and the criteria used to draw the zero-flux surfaces. It seems to us that if the term "physical size of the ions" in the crystal is to have any meaning within the context of AIM, it must refer to an atomic basin

Table 4 Dissociation energies of diatomic molecules in electron volts (eV)

	H:H	F:F	Cl:Cl	Br:Br	I:I
Bond dissociation energy, D(A–A)	4.44	2.80	2.468	1.962	1.535
		H:F	H:Cl	H:Br	H:I
Bond dissociation energy, D(A–B)		6.39	4.38	3.74	3.07
½ (D(A–A) + D(B–B)		3.62	3.45	3.20	2.99
Difference, Δ_{AB}		2.77	0.93	0.54	0.08
		Cl:F	Br:Cl	I:Br	I:Cl
Bond dissociation energy, D(A–B)		3.82	2.231	1.801	2.142
½ (D(A–A) + D(B–B)		2.63	2.215	1.748	2.001
Difference, Δ_{AB}		1.19	0.016	0.053	0.142

which must contain a total charge equal to that of the isolated ion. Yet we are not aware of any study to show that this condition is fulfilled.

More recently Tsirilson and coworkers have reported the results of highly accurate AIM charge density studies of NaF and the isomorphic MgO [45]. The cation–*bcp* and anion–*bcp* distances in NaF are 106 and 126 pm, respectively, whereas in MgO they are 92 and 119 pm, respectively. If these anion–*bcp* distances are taken to represent the radii of the ions, the radius of the O^{2-} ion is 7 pm *smaller* than the radius of the F^- ion!

5 Electronegativity and Electronegativity Coefficients

The concept of "electronegativity" has been used in chemistry for more than a 100 years. In his book of 1920, Lewis writes that "oxygen and fluorine are the most electronegative elements. By this we mean that they are the elements which show the strongest tendency to complete their octets and obtain as nearly as possible the exclusive possession of the eight electrons" [46].

The first attempt to quantify the property and thus enable a more straightforward comparison of the electronegativities of all elements appears to have been published by Linus Pauling in 1932 [47]. Table 4 has been borrowed from this article. By this time the dissociation energies of the thirteen diatomic molecules listed in the table had been determined by spectroscopic methods. Pauling quoted the dissociation energies in eV, and for reasons that will be apparent later, we have chosen to adhere to this unit.

As noted by Pauling, the dissociation energies of the heteroatomic molecules, AB, all exceeded the arithmetic mean of the dissociation energies of the two corresponding homoatomic molecules AA and BB:

$$\Delta_{AB} = D(AB) - \tfrac{1}{2}(D(AA) + D(BB)) > 0.$$

Pauling suggested that the dissociation energy of a perfectly covalent, nonpolar molecule should be given by the arithmetic mean and that the excess bond energies, Δ_{AB}, observed for the heteroatomic molecules in the table were due to the "ionic character" of the bonds, that is, to their polarity. The magnitude of the excess energy should therefore depend on the difference between the electronegativities of the two bonded atoms.

The known enthalpies of formation or combustion of polyatomic molecules allowed the calculation of the mean C–H bond energy in CH_4, the C–C bond energy in ethane, the mean O–H bond energy in H_2O, and the O–O bond energy in hydrogen peroxide. All together Pauling collected a sample of eight homoatomic bond energies D(A–A) (where A=H, C, N, O, F, Cl, Br, and I) and 21 heteroatomic bond energies between the same eight elements. In every case, with the possible exception of C–I, the heteroatomic bond energy was larger than the arithmetic mean of the two corresponding homoatomic bond energies.

Pauling assigned an "electronegativity coordinate" χ to each atom and searched for a relationship between Δ and the difference between the two electronegativity coordinates, $\chi_A - \chi_B$. This search led to a set of such coordinates that *approximately* satisfied the quadratic relationship with Δ:

$$\Delta_{AB}(\text{in eV}) = (\chi_A - \chi_B)^2.$$

The H atom was assigned a value of $\chi_H = 0.00$. The coordinates of the other seven elements ranged from 0.40 to 2.00 [47]:

H = 0.00	I = 0.40	C = 0.55	Br = 0.75	Cl = 0.94	N = 0.94	O = 1.40	F = 2.00

The agreement between the experimental values of Δ and those calculated from these electronegativity coordinates was not perfect: The value of $\chi_F = 2.00$ had been adjusted to give the optimal values for the excess energies of C–F, N–F, O–F, Cl–F, Br–F, and I–F bonds. The experimental values of Δ for these six bonds were reproduced with an average deviation of 0.15 eV. But the same optimal value of χ_F yielded an estimated excess energy of 4.00 eV in HF, as compared to the experimental value of 2.77 eV.

In the first edition of his book *The Nature of the Chemical Bond* that was published in 1939, Pauling defined electronegativity as "the power of an atom *in a molecule* to attract electrons to itself" and continued his efforts to quantify the property [37]. At the same time he changed his energy unit from eV to kcal/mol. That meant that the relationship between excess bond energy and χ was given by

$$\Delta_{AB}(\text{in kcal/mol}) = 23.06(\chi_A - \chi_B)^2. \quad (1)$$

Secondly he shifted his electronegativity scale by addition of a constant so that χ_H was increased from 0 to 2.1. Drawing on a larger body of thermochemical data [48], he was able to present a table of "electronegativity constants" for H and 13 other elements, those listed on the previous page plus Si, Ge, P, As, S, and Se. The

magnitude of the new electronegativity constants ranged from 1.8 for Si and Ge to 4.0 for F. The "values are given only to one decimal place on the scale; it is my opinion that this is the limit of their reliability."

Since the dissociation energies of many metal atom dimers M_2 were unknown, Pauling adopted a less rigorous approach in order to determine the electronegativity constants of metals. Consider the energy of formation of a gaseous metal halide MI from the gaseous reactants:

$$\tfrac{1}{2}\ M_2(g) + \tfrac{1}{2}\ I_2(g) = MI(g) \quad \Delta U_f^*(g)\,. \tag{2}$$

The energy of atomization of the reagents must be equal to the energy of the reaction plus the energy of atomization of the product:

$$\tfrac{1}{2}D(M-M) + \tfrac{1}{2}D(I-I) = \Delta U_f^*(g) + D(M-I).$$

Rearrangement yields

$$\Delta_{MI} = D(M-I) - [\tfrac{1}{2}D(M-M) + \tfrac{1}{2}D(I-I)] = -\Delta U_f^*(g).$$

The standard energy of formation of a crystalline alkali metal iodide, $\Delta U_f^\circ(MI(s))$, is defined as the energy of the reaction

$$M(s) + \tfrac{1}{2}I_2(s) = MI(s) \quad \Delta U_f^\circ(MI(s))\,. \tag{3}$$

Now, the two reaction enthalpies $\Delta U_f^*(g)$ (2) and $\Delta U_f^\circ(MI(s))$ (3) are equal if the energy required to vaporize solid I_2 plus the energy required to sublime the metal to form ½ mole of the gaseous dimer is equal to the energy required to sublime solid MI. Pauling argued that the three phase transition energies were determined mainly by van der Waals forces between the atoms and that these would tend to cancel one another and concluded that $\Delta_{MI} = -\Delta U_f^*(g) - \Delta U_f^\circ(MI(s))$. Generalization to other halogens and other metals forming di-, tri-, or tetrahalides, MX_n, yielded

$$\Delta_{MX} = -(1/n)\Delta U_f^\circ(MX_n(s)). \tag{4}$$

Pauling proceeded to use this simplified procedure to determine the electronegativities of twelve metallic elements in Groups 1, 2, and 13. The reader may not be completely convinced by his arguments, but the procedure did supply electronegativity coefficients in good agreement with those determined later by other approaches (see Table 5 below).

In 1961 A. L. Allred updated Pauling's electronegativity coefficients using the same approach, but basing his calculations on newer and more extensive thermochemical data [49]. These Allred–Pauling electronegativities have since been widely used in the literature.

Table 5 Electronegativity coefficients χ of main-group elements according to Allen (top), Allred and Rochow (middle), and Allred and Pauling (bottom)

Group 1		Group 2		Group 12		Group 13		Group 14		Group 15		Group 16		Group 17	
H	2.30														
	2.20														
	2.20														
Li	0.91	Be	1.58			B	2.05	C	2.54	N	3.07	O	3.61	F	4.19
	0.97		1.47				2.01		2.50		3.07		3.50		4.10
	0.98		1.57				2.04		2.55		3.04		3.44		3.98
Na	0.87	Mg	1.29			Al	1.61	Si	1.92	P	2.25	S	2.59	Cl	2.87
	1.01		1.23				1.47		1.74		2.06		2.44		2.83
	0.93		1.31				1.61		1.90		2.19		2.58		3.16
K	0.73	Ca	1.03	Zn	1.59	Ga	1.76	Ge	1.99	As	2.21	Se	2.43	Br	2.69
	0.91		1.04		1.66		1.82		2.02		2.20		2.48		2.74
	0.82		1.00		1.65		1.81		2.01		2.18		2.55		2.96
Rb	0.71	Sr	0.96	Cd	1.52	In	1.66	Sn	1.82	Sb	1.98	Te	2.16	I	2.36
	0.89		0.99		1.46		1.49		1.72		1.82		2.01		2.21
	0.82		0.95		1.69		1.78		1.96		2.05		2.10		2.66
Cs	0.66	Ba	0.88	Hg	1.76	Tl	1.79	Pb	1.85	Bi	2.01				
	–		–		–		–		–		–				
	0.79		0.89		2.00		1.62		1.87		2.02				

Over the years, the idea of a common quantitative electronegativity scale for all elements and the development of electronegativity coefficients have proven themselves as extremely useful tools for the ordering and prediction of chemical properties of molecules. They are undoubtedly among the most original and may prove to be the most enduring of Pauling's contributions to valence theory.

Even though χ is used to predict the properties of an atom *in a molecule*, it would be an advantage to define it in terms of properties of the isolated atom. The most successful of the early attempts was that of A. L. Allred and E. J. Rochow, whose operational definition of χ was based on the magnitude of the Coulomb attraction between the neutral atom and an additional electron at a distance equal to the covalent radius of the atom:

$$\chi_{A\&P} = 0.359 Z_{eff}/r^2{}_{cov} + 0.744. \quad (5)$$

Effective nuclear charges Z_{eff} were estimated using Slater's rules [39], and the covalent radii r_{cov} (in Å units) were taken from a compilation by Pauling [50]. The constant terms, 0.359 and 0.744, were introduced to transfer the new values of χ to the "Pauling scale" [51].

Finally, in 1989, L. C. Allen suggested a simple, precise definition of χ based on observable properties of the isolated atoms [52]. He began by defining the energies of the valence shell *s*- and *p*-electrons of a main-group element atom in terms of ionization energies. Consider the oxygen atom, which in the ground state has an s^2p^4 valence shell electron configuration. This configuration gives rise to fifteen different atomic states: the ninefold degenerate ^3P ground level, a fivefold degenerate ^1D level, and a singly degenerate ^1S level at higher energies. The configuration-averaged energy of the s^2p^4 ground state of the O atom is obtained as the average energy of these fifteen atomic states.

Removal of an *s*-electron gives an O^+ cation with the electron configuration s^1p^4. This electron configuration gives rise to 20 atomic states: a fourfold degenerate ^4S level, a tenfold degenerate ^2D level, and a sixfold degenerate ^2P level. The configuration-averaged energy of an O^+ cation with s^1p^4 configuration is calculated as the average energy of the 20 individual states. Finally Allen defined the *valence shell s-electron* (*ionization*) *energy*, ε_s, as the difference between the configuration-averaged energies of the s^1p^4 O^+ cation and the s^2p^4 neutral atom.

Removal of a *p*-electron from the O atom yields an O^+ cation with an s^2p^3 electron configuration which gives rise to a total of thirty separate states, and the *valence shell p-electron* (*ionization*) *energy*, ε_p, is calculated as the difference between the average energy of these thirty states of the ion and the configuration-averaged energy of the s^2p^4 neutral atom.

Finally Allen defined the electronegativity of the O atom as "the average one-electron energy of the valence shell electrons"

$$\left(n\varepsilon_s + m\varepsilon_p\right)/(n+m), \tag{6}$$

where n and m are the number of s- and p-electrons, respectively. The same quantity has also been referred to as the mean valence shell ionization energy *MIE*. The data necessary to calculate these energies for most atoms were available in the literature.

Division of the average one-electron energies by one Rydberg energy unit and multiplication by a scale factor SF = 2.300 yielded dimensionless electronegativity coefficients on the Pauling scale:

$$\chi_{\text{spec}} = \text{SF}\left(n\varepsilon_\text{s} + m\varepsilon_\text{p}\right)/(n+m). \tag{7}$$

In Table 5 we compare the electronegativity coefficients estimated by Allen (χ_A), Allred and Rochow (χ_AR), and Allred and Pauling (χ_P). The first set has been estimated from atomic energy level data, the second from the estimated Coulomb attraction between the neutral atom and a free electron, and the third from thermochemical bond energies. Considering the different approaches, the agreement between the three sets is remarkable and a powerful indication that the electronegativity concept reflects real and essential attributes of each atom.

As already mentioned, the concepts of electronegativity and electronegativity coefficients have brought order and deeper insight to many areas of chemistry, not least the structure and bonding in main-group element compounds. As an example of this, the reader may consult the calculated atomic charges in monomeric metal dihalides listed in Sect. 3. The electronegativity coefficients for the Group 2 metals decrease slowly but monotonically from 1.58 for Be to 0.88 for Ba. The electronegativity of Zn is very close to that of Be, χ_Cd is a little lower, and χ_Hg a little higher than χ_Be. The electronegativity of the halogens decrease sharply as the group is descended from $\chi_\text{F} = 4.19$ to $\chi_\text{I} = 2.36$. Consultation of Table 2 shows that for every metal in Groups 2 and 12, the calculated net charge on the metal atom decreases monotonically in the order $\text{MF}_2 > \text{MCl}_2 > \text{MBr}_2 > \text{MI}_2$. For every halogen atom, the charge on the Group 12 metal increases in the order $\text{BeX}_2 < \text{MgX}_2 < \text{CaX}_2 < \text{SrX}_2 < \text{BaX}_2$ while the charges on the Group 12 metal atoms vary in the order $\text{ZnX}_2 < \text{CdX}_2 > \text{HgX}_2$. These patterns are in complete agreement with the variation of the electronegativity coefficients.

According to the Born–Landé model, the dominant terms favoring the formation of strong ionic bonds in gaseous, monomeric alkali metal halides or alkaline earth metal dihalides are the large negative Coulomb interaction energies. The magnitude of these terms is determined by the ionic charges and the interatomic bond distances: The smaller the atoms or ions, the shorter the distance, and the stronger the bond. The major term opposing the formation of a strong bond is the energy required to ionize the metal atom. It appears reasonable then that the low Allen electronegativities of the metal atoms are associated with low ionization energies. It might appear logical to define the electronegativities of F, O, and the heavier elements in Groups 17 and 16 in terms of their electron affinities, but this would yield higher electronegativity coefficients for Cl and S than for F and O, a result at

variance with chemical experience. It is clear that the electron affinity of the isolated atom does not properly reflect "the power of an atom *in a molecule* to attract electrons to itself." As noted above, strong ionic bonds are favored by small atoms or ions. The success of the definition of electronegativities of the Group 16 and 17 atoms in terms of their ionization energies is probably due to a strong negative correlation between the mean ionization energies of an atom and its bonding radius (Fig. 4). The *MIE*s increase when a period is traversed from left to right, while the A–H bond distances decrease. The *MIE*s decrease as a group is descended, whereas the A–H bond distances increase. A high ionization energy indicates a small atomic radius, which in turn means a larger stabilizing Coulomb energy.

6 Covalent Compounds: Bond Distances and Coordination Geometries

6.1 The Crystal Structures of the Group 14 Elements

The crystal structure of diamond was first reported by W. H. and W. L. Bragg in 1913: Each carbon atom was found to be surrounded by four others at the corners on a perfect tetrahedron [53]. This result served as a final confirmation of the model of the "tetrahedral carbon atom" based on the work of Pasteur, Kekulé, Butlerov, and van't Hoff [54]. During the following decade, other X-ray studies showed that solid silicon, germanium, and gray tin have similar crystal structures. The covalent bonding radii of C, Si, Ge, and Sn could then be estimated as half the observed bond distances. An X-ray study of SiC (carborundum) yielded a structure based on the diamond lattice with half the C atoms replaced by Si atoms in such a way that each C atom was surrounded by four Si atoms, and vice versa. The Si–C bond distance was found to be 4 or 5 pm shorter than half the sum the covalent radii of the two atoms. This observation serves as a warning that atomic bonding radii are not strictly constant from one molecule or crystal to another.

6.2 Standard Tetrahedral Bond Radii

In 1926 M. H. Huggins published a set of bonding radii for twelve main-group elements "having four electron pairs in the valence shell" based on seventeen crystal structures including those of the four Group 14 elements referred to above [55].

Zinc sulfide is found in two crystalline forms, sphalerite (zinc blende) and wurtzite. The structure of the former is analogous to that of SiC. The second, wurtzite, is also constructed from perfectly tetrahedral ZnS_4 (or SZn_4) units, but

Table 6 Standard tetrahedral radii of main-group elements (in pm) [56]

Be: 107	B: 89	C: 77	N: 70	O: 66	F: 64
Mg: 140	Al: 126	Si: 117	P: 110	S: 104	Cl: 99
Zn: 131	Ga: 126	Ge: 122	As: 118	Se: 114	Br: 111
Cd: 148	In: 144	Sn: 140	Sb: 136	Te: 132	I: 128
Hg: 148	Tl: 147	Pb: 146	Bi: 146		

the arrangement of these units in space is different from that of sphalerite. All the Group 12 metal sulfides, selenides, and tellurides form crystals of one or both types, and the bond distances had been established. Huggins assumed that the radius of the S atom was 102 pm. This was 2.5 pm smaller than the half the observed S–S distance in FeS_2 where each S atom is surrounded by three Fe atoms and one S atom at the corner of a distorted tetrahedron. The radii of Zn, Cd, Hg, Se, and Te were then adjusted to yield the best overall fit with the nine observed bond distances. The wurtzite structures of the two oxides BeO and ZnO provided the information needed to determine the radii of beryllium and oxygen.

Eight years later Pauling and Huggins were able to publish standard tetrahedral bond radii of thirteen more elements [56]. The radii of the three Group 13 metals Al, Ga, and In and the four Group 15 elements from N to Sb were based on crystal data of eight binary Group 13–15 element compounds AB with sphalerite or wurtzite structures. The radius of the Mg atom was obtained from the observed bond distance in MgTe. Since no data were available for a suitable boron compound, the radius of B was predicted by interpolation alone, and the radii of the four halogen atoms were estimated by extrapolation (Table 6).

The "standard tetrahedral radii" obtained by Pauling and Huggins have sometimes been referred to as "tetrahedral covalent radii," but we prefer the original notation since we wish to reserve the term "covalent" for bonds to which each atom provides one electron. We shall return to this point in Sect. 9. Since these radii can only be used to predict bond distances between atoms that are both tetrahedrally coordinated, they are of limited utility. They were nevertheless of great interest at the time since they were the first radii that provided a quantitative illustration of the decrease of atomic bonding radii across the short periods of the periodic table and their increase as a group is descended.

6.3 Covalent Radii

The bond distances in crystals with rock salt, fluorite, diamond, sphalerite, or wurtzite structures could be determined with great accuracy because they could be calculated directly from the unit cell dimensions. The determination of bond distances in molecular compounds in general requires the determination of the coordinates of the individual atoms within the unit cell. In the early 1930s, such studies were time consuming and difficult, and the resulting bond distances were

usually accurate only to about 5 pm. Low-temperature techniques had not been developed, so compounds with melting points near or above room temperature could not be studied by X-ray crystallography.

Gas-phase electron diffraction as a technique for the determination of molecular structures was first developed by H. Mark and R. Wierl in 1930, but the usefulness of the method was demonstrated by studies of only a handful of molecules before the project was abandoned 3 years later [57]. After a visit to Mark's laboratory, L. Pauling and his graduate student L. Brockway built up an extremely productive electron diffraction group at California Institute of Technology. In 1936 they were able to publish a review article with structural information on nearly 150 different molecules determined with error limits ranging from 1 to 3 pm.

By 1939 Pauling was able to present a table of covalent radii for the hydrogen atom and the sixteen elements in the square defined by the positions of C, Sn, F, and I in the periodic table [37]. These radii were based on the bond distances in the crystalline elements of the Group 14 metals; the Group 15 elements P, As, and Sb; and the Group 16 elements S, Se, and Te, all determined by X-ray diffraction; the bond distances in H_2 and the dihalogen molecules determined by spectroscopic methods; and finally by the bond distances in the gaseous methyl derivatives of all the seventeen elements except Sb, Se, and Te determined by gas electron diffraction.

Two years later, V. Schomaker and D. P. Stevenson noted that bond distances between two very electronegative elements as in F_2, hydrogen peroxide, or hydrazine were significantly larger than suggested by addition of Pauling's covalent radii. An upward adjustment of these radii would, however, lead to overestimates of bond distances in molecules where F, O, or N is bonded to more electropositive elements. They suggested, therefore, that the radius of the F atom should be increased from 64 to 72 pm, the radius of O from 66 to 74 pm and the radius to N from 70 to 74 pm, and that bond distances in general should be calculated from the sum of bond radii reduced by an amount increasing with the electronegativity difference:

$$R_{AB} = r_A + r_B - \beta\left|\chi_A - \chi_B\right|,$$

where $\beta = 9$ pm [58]. Since it was known that bonds become stronger with increasing electronegativity difference, it did indeed seem reasonable that they should also become shorter.

As an increasing number of molecules with bonds between F, O, or N atoms and very electropositive elements like Si were studied in the following years, it became clear that the correction for electronegativity differences suggested by Schomaker and Stevenson was too small. Thus the experimentally determined Si–F bond distance in $FSiH_3$ was 13 pm shorter than estimated, the Si–O bond distance in $O(SiH_3)_2$ was 16 pm shorter, and the Si–N distance in $N(SiH_3)_3$ was 9 pm shorter than estimated.

Table 7 Covalent bonding radii (in pm) for calculations of single bond distances in Lewis-valent compounds with the modified Schomaker–Stevenson rule (Eq. 8)

H: 32.3				
B: 82*	C: 78.4	N: 71.9	O: 73.0	F: 77.2
Al: 125*	Si: 114.1	P: 109.5	S: 102.8	Cl: 100.5
Ga: 124*	Ge: 121.1	As: 121.2	Se: 116.3	Br: 113.9
In: 145*	Sn: 140.3	Sb: 140.6	Te: 135.6	I: 133.1
Tl: 148*	Pb: 150*	Bi: 151*		

Carbon-based radii are indicated by asterisks

The fit between estimated and experimentally determined bond distances could, however, be significantly improved by using a modified form of the Schomaker–Stevenson rule:

$$R_{AB} = r_A + r_B - \gamma\left|\chi_A - \chi_B\right|^{1.5}, \tag{8}$$

with $\gamma = 8.3$ pm and the use of Allen electronegativities [15]. The covalent single bond radii of H and the sixteen elements in the square defined by the four atoms C, Sn, F, and I were refined to fit reference bond distances for 100 of the 153 possible distinct atom pair combinations obtained by studies of 100 simple gas-phase molecules. The best radii, listed in Table 7, reproduce the experimental bond distances with an average error of 2.0 pm and a maximum error of 5.6 pm in O$(SiH_3)_2$. The seventeen bond distances involving methyl group carbon atoms were reproduced with average and maximum deviations of 1.2 and 2.2 pm, respectively.

Structural information on the gas-phase structures of simple derivatives of the five Group 13 elements or of the sixth period elements Pb and Bi is still scarce. The radii listed in Table 7 as "Carbon-based" have been obtained from the experimental bond distances in the gaseous molecules $Pb(CH_3)_4$, $Bi(CH_3)_3$, and $M(CH_3)_3$ (M=B, Al, Ga, In, and Tl).

6.4 *Coordination Geometries and* sp *Hybrid Atomic Orbitals*

In their landmark paper published in 1927, Heitler and London showed that a reasonably accurate value for the bond distance of the hydrogen molecule could be calculated from the wavefunction

$$\Psi(1,2) = \phi_A(1)\phi_B(2) + \phi_A(2)\phi_B(1),$$

where ϕ_A and ϕ_B denote a 1*s* atomic orbital on the two atoms A and B, respectively [59].

Their results provided quantum-mechanical backing for the Lewis shared-electron-pair model for the chemical bond. As noted in two more landmark articles published by Pauling [60] and Slater [61] in 1931, the calculations of Heitler and London also suggested that the chemical bond will be strongest if the two atomic

orbitals are directed in such a manner as to place a maximum electron density between the two nuclei. This in turn has implications for the coordination geometries of the two atoms. Se and Te atoms have two unpaired electrons in valence shell *p*-orbitals. The use of these electrons for bond formation would lead to valence angles of about 90°, perhaps somewhat larger due to repulsion between the geminal atoms. In fact crystalline Se and Te contain zigzag chains with valence angles of 105° and 102°, respectively.

Group 15 atoms have three unpaired electrons in the valence shell *p*-orbitals and the use of these electrons for bond formation would be again be expected to yield valence angles of about 90°. And indeed, crystalline As, Sb, or Bi was known to consist of buckled sheets of trigonal pyramidal atoms with valence angles ranging from 97° to 94°.

Both Pauling and Slater assumed that the valence shell electron configuration of a carbon atom had to be changed from s^2p^2 to s^1p^3 before four bonds could be formed and showed that the four *s*- and *p*-orbitals could be combined to form four orthogonal atomic orbitals directed toward the corners of a tetrahedron. The first step in the process was to form four normalized (but not orthogonal) *p*-orbitals:

$$\begin{array}{ll} p_1 = 1/\sqrt{3}(p_x + p_y + p_z) & p_2 = 1/\sqrt{3}(p_x - p_y - p_z) \\ p_3 = 1/\sqrt{3}\,(-p_x + p_y - p_z) & p_4 = 1/\sqrt{3}(-p_x - p_y + p_z) \end{array}.$$

The four new *p*-orbitals have the same shape as the original *p*-orbitals but are directed toward the corners of a tetrahedron. In the second step, each of the four *p*-orbitals was combined with the valence shell *s*-orbital:

$$\phi_i = (s + a\ p_i)/\sqrt{(1 + a^2)}.$$

The four "hybrid" orbitals thus obtained are orthogonal if the constant $a = \sqrt{3}$. Each hybrid orbital is pointed toward one corner of the tetrahedron and leads to a greater concentration of charge in this direction than pure *s*- or *p*-orbitals. These tetrahedral *sp* hybrid atomic orbitals thus provided a quantum-mechanical justification of the chemist's tetrahedral carbon atom as present in diamond and the alkanes.

The concept of an *sp* hybrid atomic orbital may be generalized to apply to any linear combination of an *s*- and a *p*-orbital:

$$sp^{\lambda} = (s + a\ p)/\sqrt{(1 + a^2)},$$

where the superscript denotes the *p*:*s* mixing ratio, $\lambda = a^2$. The *s*-character of a hybrid orbital is defined as $1/(1 + \lambda)$ and the *p*-character as $\lambda/(1 + \lambda)$. Two orthogonal *sp* hybrid orbitals with the same mixing ratio will have the same shape and are therefore described as "equivalent." The only way to obtain four equivalent hybrids is the formation of the tetrahedral sp^3 hybrids as described above. Combination of an *s*-orbital with two *p*-orbitals yields the three well-known trigonal planar sp^2

Table 8 Experimental ∠HAH and ∠CAC valence angles in gaseous hydrogen and methyl derivatives of the Group 15 and 16 elements

NH_3	107°	PH_3	93°	AsH_3	92°	SbH_3	92°	BiH_3	90°
$N(CH_3)_3$	111°	$P(CH_3)_3$	99°	$As(CH_3)_3$	96°	$Sb(CH_3)_3$	94°	$Bi(CH_3)_3$	97°
OH_2	104°	SH_2	92°	SeH_2	91°	TeH_2	90°		
$O(CH_3)_2$	112°	$S(CH_3)_2$	99°	$Se(CH_3)_2$	96°	$E(CH_3)_2$	93°		

hybrids, while combination of one *s*-orbital with one *p*-orbital yields the equally well-known linear sp^1 hybrids [60].

It is, however, also possible to form orthogonal hybrid *sp*-orbitals with non-integer mixing ratios. The angle spanned by two equivalent and orthogonal atomic orbitals increases smoothly with increasing *s*-character from 90° for two pure *p*-orbitals to 180° for two for sp^1 hybrid orbitals.

In Table 8 we compare the valence angles of simple hydrogen and methyl derivatives of the Group 15 and 16 elements. Since the valence shell electron configurations of the former are s^2p^3 for the Group 15 elements and s^2p^4 for the Group 16 elements, one might expect valence angles in the vicinity of 90° in all these compounds. And indeed the valence angles in BiH_3 and TeH_2 are both 90°. As Group 15 is ascended, the valence angles increase to 93° in PH_3 and 107° in NH_3, perhaps because the distances between H atoms decrease with decreasing size of the central atom. As Group 16 is ascended, the valence angles increase with decreasing size of the central atom to 104° in H_2O.

Valence angles in the methyl derivatives are consistently larger than in the hydrogen derivatives, presumably due to increased repulsion between the methyl groups, and reach their maxima in trimethylamine and dimethyl ether. The N and O atoms in $N(CH_3)_3$ and $O(CH_3)_2$ are probably best described as sp^3 hybridized. The influence of the size of the ligands is further illustrated by comparison with the valence angles in $N(SiH_3)_3$, 120° (corresponding to a planar coordination geometry at the N atom) and $O(SiH_3)_2$, 144°. In $O(SiMe_3)_3$ the SiOSi valence angle is 148° and in crystalline $O(SiPh_3)_2$ it is 180°.

6.5 Coordination Geometries and Electron Counts

In their classical paper published in 1940, Sidgwick and Powell began by pointing out the importance of the molecular structure of a compound for the understanding of both its bonding and reactivity [62]. They appreciated that physicists were able "to relate the stereochemistry of the molecule to the number of shared or unshared electrons in the polyvalent atom, and the electronic subgroups which these occupy," but added that "the chemist, who cannot always tell whether the bonds in a given molecule are *s*, *p*, or *d* even when this is clear to the physicist, would be glad to be able to infer the stereochemical type from some property of the molecule with which he is more familiar."

In their article they surveyed the structures of about three hundred compounds in an effort to investigate the relationship between the number of electrons in the valence shell of an atom and its coordination geometry. We shall limit our discussion to the structures of the two hundred compounds containing *singly* bonded main-group elements only. The structures surveyed included the three-dimensional network structures described above; puckered layer structures like those of the crystalline Group 15 elements As, Sb, and Bi; and strings like those found in crystalline Se or Te. They also included a large number of molecular compounds, mostly in the gas phase, and polyatomic ions found in crystals.

In the following, we shall denote the number of electron pairs in the valence shell of the central atom by a digit in italics behind the formula. The mercury dihalides HgX_2 (*2*) (X=Cl, Br or I) and the Hg–Hg-bonded dimeric monohalides Hg_2X_2 (*2*) all have two bonding electrons pairs (and no nonbonding electrons) in the valence shell of the mercury atoms and all adopt linear structures. The structure of the ion $[Tl(CH_3)_2]^+$ (*2*) is also linear.

The boron atoms in the four trihalides BX_3 (X=F, Cl, Br, or I) all have three bonding electron pairs in their valence shell and the coordination geometries are all trigonal planar. $SnCl_2$ (*3*) and $PbBr_2$ (*3*) are monomeric in the gas phase and had been reported to adopt angular structures with valence angles "closer to 120° than 180°." These angular structures suggest a trigonal planar arrangement of the three electron pairs in the valence shell of the metal atoms.

Sidgwick and Powell then turned their attention to molecules where the central atoms have four electron pairs in their valence shell. These molecules fell into three groups: molecules where the central atom is surrounded by four bond pairs, molecules where the central atom is surrounded by three bonding pairs and one nonbonding pair, and molecules where it is surrounded by two bonding and two nonbonding pairs. The first group included the carbon tetrahalides, SiF_4, $SiCl_4$, and $Si(CH_3)_4$, the cations $[N(CH_3)_4]^+$ and $[Cd(NH_3)_4]^{+2}$, and the $[BF_4]^-$ anion. All molecules or ions in this group adopt tetrahedral coordination geometries. The second group included $N(CH_3)_3$, $P(CH_3)_3$, and the trihalides of heavier Group 15 elements. These compounds all adopt trigonal pyramidal structures. Finally the third group included the dimethyl derivatives $E(CH_3)_2$ (E=O, S, and Se). All these compounds adopt angular structures.

Sidgwick and Powell also described a handful of molecules with five bonding electron pairs in the valence shell of the central atom: PF_5, PCl_5, PCl_3F_2, and $(CH_3)_2SbF_3$. All of them adopt trigonal bipyramidal structures. Their survey had turned up only one simple molecule with four bond pairs and one nonbonding electron pair in the valence shell, namely, $TeCl_4$. In a footnote added in proof, the coordination polyhedron of the Te atom was described as a trigonal bipyramid with one equatorial ligand missing. The linear structure of the $[I_3]^-$ anion (*5*) could be described as derived from a trigonal bipyramid with three equatorial ligands removed.

The number of molecules with *six* bonding electron pairs in the valence shell was relatively large and included the neutral molecules SF_6, SeF_6, and TeF_6 and the anions $[PCl_6]^-$, $[SbF_6]^-$, $[SiF_6]^{-2}$ $[GeF_6]^{-2}$, $[SnCl_6]^{-2}$, and $[PbCl_6]^{-2}$. All these

species had octahedral structures. The planar, quadratic structure of the $[ICl_4]^-$ (*6*) anion could be described as derived from an octahedron by removal of two ligands from opposite corners.

Sidgwick and Powell concluded that the coordination geometries of all the main-group element compounds surveyed were simply related to the number of electron pairs in the valence shell by assuming that the mean positions of these pairs were linear for two electron pairs, trigonal planar for three, tetrahedral for four, trigonal bipyramidal for five, and octahedral for six. It should be noted that these spatial arrangements are those that maximize the shortest distances between electron pairs. The electrons act as if they repel each other, and the Sidgwick–Powell model is now commonly referred to as the valence shell electron pair repulsion (VSEPR) model.

Eighteen years later (in 1957), the VSEPR model was further developed and its predictive power enhanced by R. J. Gillespie and R. S. Nyholm [63]. They interpreted the less-than-tetrahedral valence angles listed in Table 8 as evidence that the repulsion between a lone pair and a bond pair is greater than the repulsion between two bond pairs. Since a bond pair is extended further into space than a lone pair, it is reasonable to assume that it requires less space in the valence shell of the central atom. The larger than tetrahedral valence angles in trimethylamine and dimethyl ether are presumably determined by steric repulsion between the methyl groups.

When Powell and Sidgwick wrote their review, there was only one known structure of a neutral molecule where a hypervalent central atom had an electron lone pair in the valence shell, namely, $TeCl_4$ (*5*), and one such ion, I_3^- (*5*). Eighteen years later there were two more such molecules and one more ion. Gillespie and Nyholm pointed out that on the basis of the trigonal bipyramidal structure of a molecule with five electron pairs on the central atom, two structures were possible for $TeCl_4$. A structure with an axial lone pair would be destabilized by *three* bond pair–lone pair repulsions over a 90° valence angle, whereas a structure with an equatorial lone pair would be destabilized by only *two* such interactions. Since the repulsion between a lone pair and a bond pair is greater than the repulsion between two bond pairs, the molecule adopts the latter structure.

The central atom in ClF_3 (*5*) is surrounded by three bond pairs and two lone pairs. If the repulsion between two lone pairs is greater than the repulsion between a lone pair and a bond pair, then both lone pairs should occupy equatorial positions, and this is again what is observed. The repulsion between two electron pairs thus appears to decrease in the order

$$\text{Lone pair} - \text{lone pair} > \text{lone pair} - \text{bond pair} > \text{bond pair} - \text{bond pair}.$$

The same conclusion is reached by considering the square planar structure of the $[ICl_4]^-$ ion (*6*).

The XPX valence angles in the compounds F_3PO, Cl_3PO, F_3PS, and Cl_3PS had all been found to fall in the narrow range from 100° to 104°. Gillespie and Nyholm suggested, therefore, that the four electrons in the PO and PS double bonds should

Table 9 Equilibrium bond distances and valence angles in fluorinated methanes, $CH_{4-n}F_n$, $n = 0$ to 4

	R(C–H) (pm)	R(C–F) (pm)	∠HCH (°)	∠HCF (°)	∠FCF (°)
CH_4	108.7(1)		109.47		
CH_3F	108.6(2)	138.3(1)	110.2(3)	108.8(3)	
CH_2F_2	108.4(3)	135.1(1)	112.8(3)	108.6	108.5(1)
CHF_3	109.1(14)	132.8(3)		110.3(3)	108.6(3)
CF_4		131.5(2)			109.47

Estimated standard deviations are listed in parentheses in units of the last digit

be regarded as forming a single unit, though the four electrons would of course demand more space than a single bond pair.

Finally Gillespie and Nyholm compared the valence angles in NH_3 (107)°, NF_3 (102°), OH_2 (104°), and OF_2 (102°) and suggested that the more electronegative fluorine atoms would pull the bonding electron pairs further away from the N or O atom and thus reduce the space occupied by the two bonding electrons in the valence shell of the latter. This suggestion has since been confirmed by numerous structure determinations of heteroleptic compounds. Thus the three different valence angles in $Si(CH_3)_2F_2$ are ∠CSiC = 113°, ∠CSiF = 109°, and ∠FSiF = 105°, respectively. The smallest valence angles are those spanned by the more electronegative substituent. In the terminology of Gillespie and Hargittai, bonding domains in the valence shell of the central atom decrease in size with increasing electronegativity of the ligand [64].

6.6 *Inductive Effects on Bond Distances and Bond Energies*

The molecular structures of the fluorinated methanes have been accurately determined by rotational spectroscopy (Table 9). The C–H bond distances all fall in the narrow range from 108.4 to 109.1 pm. The C–F bond distance in CH_3F is indistinguishable from the value predicted by the modified Schomaker–Stevenson rule, 138.2 pm, but decreases monotonically with increasing number of F atoms to 131.5 pm in CF_4.

Comparison of the C–H bond dissociation energies of CH_4 and CHF_3, 438 and 443 kJ mol^{-1} respectively, indicates that the C–H bond strength, like the C–H bond length, remains approximately constant over the series. On the other hand, comparison of the C–F bond dissociation energies of CH_3F and CF_4, 459 and 540 kJ mol^{-1}, respectively, indicates that the C–F bonds become both shorter and stronger as the number of fluorine atoms bonded to C increases. In Table 11 we list the mean bond energies of CH_4 and CF_4 as well as the thermochemical C–F bond energies of the mixed compounds calculated by combining of their atomization energies with the mean C–H bond energy in CH_4. The introduction of a second F atom in CH_3F increases the energy of the original C–F bond by 30 kJ mol^{-1}, introduction of a

Table 10 Fluorinated methanes; mean bond energies (*MBE*) of CH_4 and CF_4 and C–F thermochemical bond energies (*TBE*) of $CH_{4-n}F_n$, $n = 1$ to 3; and net atomic charges obtained by natural atomic orbital analysis (NAO) of calculated electron densities [65]

	MBE (kJ mol^{-1})	C–F *TBE* (kJ mol^{-1})	*q*(H) (au)	*q*(F) (au)	*q*(C) (au)
CH_4	414		+0.18		–0.71
CH_3F		432	+0.13	–0.43	+0.03
CH_2F_2		462	+0.11	–0.42	+0.62
CHF_3		482	+0.10	–0.40	+1.09
CF_4	489			–0.37	+1.50

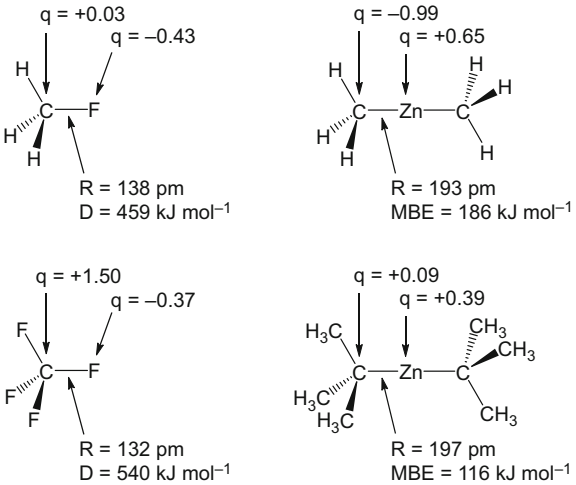

Fig. 5 C–F bond distances and bond dissociation energies and the net atomic charges on the C and F atoms in H_3CF and CF_4. Zn–C bond distances and mean Zn–C bond dissociation energies and the net atomic charges on the α-C and Zn atoms of Me_2Zn and *t*-Bu_2Zn

Table 11 Zn–C bond distances in dimethylzinc, diethylzinc, di-*iso*-propylzinc, and di-*tert*-butylzinc determined by gas electron diffraction and quantum chemical DFT calculations; mean Zn–C bond dissociation energies derived from experimental thermochemical data and from calculated energies of isodesmic reactions combined with the experimental bond dissociation energy of Me_2Zn; and net atomic charges of Zn and α–C atoms obtained by Mulliken population analysis

	R(Zn–C) (pm)		*MBE*(Zn–C) (kJ mol^{-1})			
	R_a exp	R_e calc	Exp	Calc	*q*(Zn) (au)	*q*(α-C) (au)
Me_2Zn	193.0	194.5	186 ± 2	–	+0.65	–0.99
Et_2Zn	195.0	196.0	157 ± 4	156 ± 8	+0.52	–0.62
i-Pr_2Zn	196.1	197.5	–	132 ± 8	+0.42	–0.07
t-Bu_2Zn	197.4	198.8	–	116 ± 8	+0.39	+0.09

third F atom increases the *MBE* of the two original C–F bonds by 20 kJ mol^{-1}, while introduction of a fourth F atom to leads to an *MBE* increase of about 10 kJ mol^{-1}.

According to the modified Schomaker–Stevenson rule, the C–F bond distance in CH_3F is shortened by about 17 pm due to the polarity of the bond. Is there any reason to believe that the introduction of another F atom increases the bond polarity? The net atomic charges obtained by natural bond analysis (NBA) of the calculated charge densities indicate that the charge on the hydrogen atoms remains nearly constant at 0.14 ± 0.04 au and the charge of the F atoms nearly constant at -0.40 ± 0.03 au. We note that both the sign and the magnitudes of the charges on the terminal H or F atoms are in accord with their electronegativities; while the electronegativity coefficient of F is 1.43 units higher than C, that of H is 0.35 units lower. Since the charges on the substituent atoms remain relatively constant over the series, the positive charge on the central carbon atoms increases stepwise from +0.03 in H_3CF to +1.50 in CF_4. The negative charge on the F atom is relatively unchanged from CH_3CH to CF_4, but the positive charge on the C atom is increased by nearly one atomic unit. The magnitude of calculated atomic charges may depend on their operational definition, but there can be little doubt that the C–F bonds become more polar as the number of F substituent increases (Table 10 and Fig. 5).

There is today sufficient evidence to conclude that when a more electronegative substituent is introduced at the most electropositive of two bonded atoms in a polyatomic molecule, this generally leads a shortening of the bond. To the extent that information of bond strength is available, the bond also becomes stronger.

Since introduction of a more electronegative substituent at the most electropositive of two bonded atoms generally leads to a stronger and shorter bond, one might expect that introduction of a more electronegative substituent at the most *electronegative* of the bonded two atoms generally would lead to a weaker and longer one. There is some evidence that this may be the case. The results of a comprehensive study of four dialkyl zinc compounds are presented in Table 11 and Fig. 5 [66].

The electronegativity coefficient of zinc is about one unit smaller than that of C, and this is clearly reflected in their atomic charges in dimethyl zinc, $q(\mathrm{Zn}) = +0.65$ and $q(\mathrm{C}_\alpha) = -0.99$, respectively. The net charge on the six H atoms is +0.22. Replacement of the electropositive H atoms at the α-C atoms by more electronegative methyl groups leads to a stepwise decrease of the negative charge on the α-C atoms; in di-*tert*-butylzinc they have become positively charged. The decreasing negative charge on the two α-C atoms is accompanied by a stepwise, but much smaller decrease of the positive charge on the Zn atom. If the magnitude of the product $-q(\mathrm{Zn})q(\alpha\text{–C})$ is used as a criterion, the Zn–C bonds become less polar when a H atom at the α–C is replaced by a methyl group. The mean Zn–C bond dissociation energy decreases from 186 ± 2 kJ mol^{-1} in Me_2Zn to 116 ± 8 kJ mol^{-1} in t-Bu_2Zn. At the same time the Zn–C bond distance increases from 193.0 to 197.4 pm. There is, however, not yet sufficient data available to allow us to conclude that the introduction of a more electronegative substituent at the most *electronegative* of two bonded atoms generally will have this effect.

7 Coordination Compounds and Electron Donor–Acceptor Bonds

7.1 Werner's Model for the Structures of Complex Salts of Transition Metals

Complex salts formed from transition metal cations, simple counterions like halide, sulfate, or nitrite anions, and a number of ammonia and/or water molecules have been known for several 100 years. The archetypical complex $Co(III)Cl_3(NH_3)_6$ was probably first prepared in France at the end of the eighteenth century. From the middle of the nineteenth century, complex salts became the focus of efforts to synthesize and isolate new compounds and studies to elucidate their chemical structures. By the time Alfred Werner started his research of the field in the early 1890s, the Scandinavian chemists Blomstrand and Jørgensen had developed a widely accepted structural model for complex salts where the transition metal cation was connected to each anion through one or more ammonia or water molecules. According to this model, the cation in $Co(III)Cl_3(NH_3)_6$ was connected to two of the chloride ions through a single bridging NH_3 molecule, while the third chloride was connected by a string of four NH_3 units. This $M(NH_3)_4Cl$ unit was assumed to be particularly stable (Fig. 6). In solution all chloride ions were immediately precipitated by addition of silver nitrate.

Heating of the hexamine complex leads to elimination of one ammonia molecule:

$$Co(III)Cl_3(NH_3)_6 = Co(III)Cl_3(NH_3)_5 + NH_3.$$

Addition of silver nitrate to this "pentamine" led to precipitation of only *two* equivalents of silver chloride. This observation was rationalized within the framework of the traditional Blomstrand–Jørgensen model by assuming that elimination of one ammonia molecule from the hexamine left one Cl^- ion directly linked to the metal cation and therefore unreactive (Fig. 6). Electric conductivity measurements of aqueous solutions of the pentamine would later show that the solutions contained

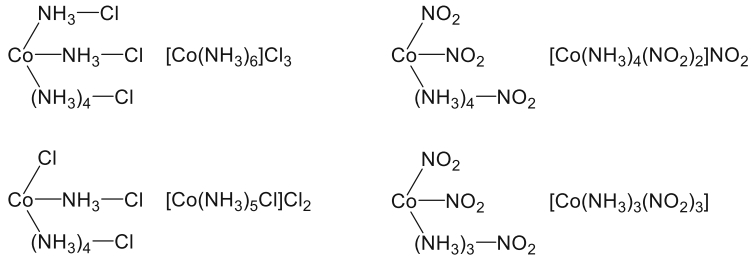

Fig. 6 *Left*: The structures of complex salts according to the Blomstrand–Jørgensen model. *Right*: The structures suggested by Werner

three ions rather than four: The chloride ion that did not form a precipitate with silver nitrate clearly remained firmly bonded to the Co(III) ion.

Werner found that mixing solutions of $Co(III)Cl_3(NH_3)_6$ and $K_2(PtCl_6)$ led to the simple reaction

$$2\ \ Co(III)Cl_3(NH_3)_6 + 3\ \ K_2(PtCl_6) = 6\ \ KCl + \left(Co(III)(NH_3)_6\right)_2(PtCl_6)_3.$$

The pentamine, however, reacted according to

$$Co(III)Cl_3(NH_3)_5 + K_2(PtCl_6) = 2\ \ KCl + \left(Co(III)(NH_3)_5Cl\right)(PtCl_6).$$

He found these results so "contradictory" that they led him to reject the traditional Blomstrand–Jørgensen structure model. Instead of forming chains between cations and anions, he assumed that all the six amine ligands in the hexamine were bonded directly to the metal cation and wrote the chemical formula as $[Co(NH_3)_6]Cl_3$ to underline this point. He described the bonding in terms of three "primary valences," that is, the three ionic bonds between Co(III) cation and the Cl^- anions, and six "secondary" bonds between the Co(III) cation and the six amine ligands. The cation was able to form six such secondary bonds, and the six amine ligands occupied positions at the corners of an octahedron with its center at the Co(III) cation. The anions were placed at a larger distance outside the octahedron. When one amine ligand was eliminated from the hexamine, the vacant position was taken over by a chloride ion (Fig. 6). This chloride ion was then bonded to the metal cation through both a primary and a secondary bond and was therefore unreactive.

Years of contentious discussion followed Werner's publication of his new model in 1893. Werner went on to prepare two nitrite complexes, the tetraamine $[Co(NO_2)_2(NH_3)_4](NO_2)$ and the trisamine $[Co(NO_2)_3(NH_3)_3]$, and measure their electrical conductivities in aqueous solution. Both the Blomstrand–Jørgensen and the Werner model suggest that two of the three nitrite ions in $[Co(NO_2)_2(NH_3)_4](NO_2)$ should be bonded directly to the metal atom. This means that an aqueous solution should contain just two ions, a $[Co(NO_2)_2(NH_3)_4]^+$ cation and a nitrite anion, and this was indeed found to be the case.

The Blomstrand–Jørgensen model suggested that the trisamine also should give two ions in aqueous solution, while the Werner model suggested that both the three amines and the three nitrite ions should be strongly bonded to the metal. This implied that the complex forms one molecular unit. And indeed, the electrical conductivity of the aqueous solution was found to be negligible. Werner's model was clearly the better!

Finally Werner succeeded in synthesizing and characterizing the *cis* and *trans* isomers of the octahedral cation in $[Co(III)Cl_2(NH_3)_4]Cl$. In 1913 he was awarded the Nobel Prize in chemistry [5].

7.2 Coordinate Links and Electron Donor–Acceptor Bonds

In his book on the electronic theory of valence that he first published in 1927 [67], N. V. Sidgwick began by classifying chemical bonds into three groups:

1. The polar or ionizable linkages between the oppositely charged ions in a salt
2. Nonpolar, non-ionizable linkages, especially prevalent in organic compounds
3. The coordinate links of Werner, capable of uniting apparently saturated molecules

Such "coordinate links" are formed "between two atoms, one of which gives the other a share of its own (previously unshared) electrons." He referred to the atom providing the electron pair as the electron donor and the bonding partner as the electron acceptor. A necessary condition for formation of a coordinate link was clearly that the electron donor, NH_3, OH_2, Cl^-, or NO_2^-, should possess an electron lone pair [67].

The coordinate link is therefore unlike a normal covalent bond where the two atoms each contribute one electron to the bonding pair. Sidgwick recognized that the coordinate link was covalent insofar as it was not ionic. He was also aware that coordinate links often were weak compared to normal covalent bonds and that coordination complexes like those formed from $BeBr_2$ or $AlCl_3$ with diethyl ether were very polar. He felt, therefore, that coordinate links were sufficiently different from normal covalent bonds to warrant a separate name.

Sidgwick's distinction between covalent bonds and coordinate links was widely accepted, and the terms "coordinate bonds," "electron donor–acceptor," and "dative" bonds were commonly used. But not all workers in the field believed that the distinction between a coordinate link and a normal covalent bond was real or significant. In the 1939 edition of *The Nature of the Chemical Bond*, Pauling listed three types of chemical bonds: electrostatic, covalent, and metallic [37]. He described the NO bond in $(CH_3)_3NO$ in terms of a Lewis structure wherein the N atom supplied the two electrons needed for a single covalent bond to the O atom which in addition carried three nonbonding electron pairs. He noted that bonds of this type had been described as a "coordinate links" and that an arrow had been used to indicate the transfer of electric charge from one atom to another, but dismissed the distinction as unnecessary: "We shall not find it convenient to make use of these names or these symbols." The statement was repeated verbatim in the 1960 edition [68].

In his book on the history of coordination chemistry, published in 1981, Kaufmann went one step further [69]. In his view the term "coordinate bond" does not carry any information on the properties of the bond or the complex; it only describes the reaction by which it had been formed: "The difference between a coordinate bond and an ordinary covalent bond consists solely in its mode of formation [...]. Once the bond is formed, the two types are identical." With hindsight it is easy to see that this sweeping claim was made on a too narrow basis of evidence. In his monograph, Kaufmann was nearly exclusively focused on

transition metal complexes. Only three complexes of main-group metals, $(NH_4)_2(SnCl_6)$, $(NH_4)_2(SiF_6)$, and alizarin (an aluminum calcium complex of hydroxyanthraquinone) were briefly mentioned in the text. Secondly, Kaufmann was only concerned with complexes where the transition element ion carried two, three, or four elementary charges. As we shall see below, a normal covalent bond and a coordinate link are easily distinguished if the acceptor atom is neutral or carries one positive charge, but the distinction becomes blurred if the acceptor atom carries two, three, or four elementary charges.

The best way to confirm, or falsify, Kaufmann's claim would probably be to prepare a complex where an amine or ether molecule is coordinated to a suitable acceptor atom (A) in a neutral, covalently bonded molecule and compare the length and strength of the coordinate linkage with the normal covalent A–N or A–O bonds in an amide or alkoxy derivative of the same element.

Before discussing the results of such studies, we pause to compare the observable properties of the simplest coordination compound, H_3NBH_3, with those of the isoelectronic, covalently bonded ethane molecule.

7.3 The Difference Between Coordinate and Normal Covalent Bonds: Amine Borane and Ethane

Formally the covalently bonded ethane molecule may be transformed into amine borane by transferring one proton from one of the C nuclei to the other. How does this affect molecular properties?

Minimum-energy rupture of the C–C bond in ethane yields two methyl radicals:

$$C_2H_6(g) = 2\ CH_3(g) \quad \Delta E = 373 \pm 2\ \text{kJ mol}^{-1}\,.$$

The C–C bond dissociation energy is comparable to the mean C–C bond energy in diamond calculated from the energy of atomization that is 359 kJ mol^{-1}.

Minimum-energy rupture of the N–B bond in H_3NBH_3, on the other hand, yields two electrically neutral closed-shell molecules:

$$H_3NBH_3(g) = H_3N(g) + BH_3(g) \quad \Delta E = 128 \pm 4\ \text{kJ mol}^{-1}\,.$$

The strength of the N–B bond in the complex is thus only 1/3 of the strength of the covalent C–C bond in ethane.

Two modifications of crystalline boron nitride are known. In the cubic modification, each B atom is surrounded by four N atoms at the corners of a tetrahedron and vice versa. The mean bond energy calculated from the energy of atomization is 321 kJ mol^{-1} and about 2.5 times larger than the N–B bond dissociation energy of the amine borane complex.

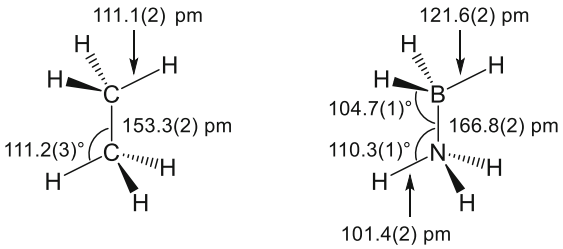

Fig. 7 The gas-phase structures of ethane and amine borane

The C–C bond distance in ethane is 153 pm, that is, about one pm shorter than in diamond (Fig. 7). The N–B bond distance in the complex is 167 pm, 11 pm longer than the bond distance in the cubic crystal modification. Addition of the N–C bond distance in $N(CH_3)_3$ and the B–C bond distance in $B(CH_3)_3$ and subtraction of the C–C bond distance in ethane suggest a N–B bond distance of 150 pm. We conclude that the N–B bond in amine borane is unusually long and weak.

The electric dipole moment of ethane is zero by symmetry. The gas-phase electric dipole moment of amine borane is 5.22 Debye. The negative pole is at the boron atom. If we assume that the two N–B bonding electrons are equally shared between the two atoms, the charge on the B atom would be $-e$ and that on the N atom $+e$. Multiplication with the experimental bond distance yields an estimated dipole moment of 8.0 Debye. The bonding electron pair is obviously *not* equally shared, but remains closer to the N atom. We shall nevertheless indicate the direction of negative charge transfer by an arrow pointing from the donor to the acceptor atom: N→B.

Ethane is a gas at room temperature. The melting point of the solid is –183°C. Amine borane, on the other hand, is a solid at room temperature; the melting point is +123°C. The 300°C difference in melting point is undoubtedly due to strong electrostatic interactions between neighboring molecules in the crystalline complex. Such interactions would presumably favor larger electron transfer from donor to acceptor. This may in turn be the reason for the observed shortening bond of the N–B bond: In the solid state the bond distance is actually 11 pm shorter than in the gas phase!

Since the N–B bond in amine borane is so weak, it is very sensitive to substitution effects as indicated by the following gas-phase dissociation energies:

$$\begin{array}{llll} H_3N-BH_3 & DE = 128\ kJ\,mol^{-1} & (CH_3)_3N-BH_3 & DE = 143\ kJ\,mol^{-1} \\ H_3N-B(CH_3)_3 & DE = 55\ kJ\,mol^{-1} & (CH_3)_3N-B(CH_3)_3 & DE = 55\ kJ\,mol^{-1} \end{array}.$$

One of us has suggested that a given single bond in a neutral molecule should be defined as normal covalent if minimum-energy bond rupture proceeds homolytically to yield electrically neutral radicals and as an electron donor–acceptor or dative bond if minimum-energy rupture proceeds heterolytically to yield neutral, closed-shell fragments [70]. The normal covalent or dative character of a given bond can then be determined by experiment or calculations.

Accumulated evidence over the past few decades has shown that dative bonds between two main-group element atoms are generally weaker, longer, more polar, and more sensitive to phase changes or substitution effects than normal covalent bonds between the same elements.

7.4 Aminoborane and Dative π-Bonding

The aminoborane molecule, H_2NBH_2, is isoelectronic with ethene. The molecular structure determined by microwave spectroscopy is ethene-like, planar, and with an N–B bond distance of 139 pm, 5 pm longer than in ethane (Fig. 8). The planar structure and the short N–B bond suggest the presence of π-bonding.

DFT calculations on H_2NBH_2 with large basis sets reproduce the experimentally determined N–B bond distance with a difference less than 1 pm [71]. The π-bond was then broken by rotation of the NH_2 fragment into an orthogonal orientation. Calculations on this orthogonal model of C_{2v} symmetry showed that the two π-electrons had returned to the N atom and that the N–B bond distance had increased. When the symmetry was reduced to C_s, the N atom became pyramidal (Fig. 8). The N–B bond distance was equal to the longest bond distance in the trisboryl amine. The calculated energy of the orthogonal structure was $\Delta E_\pi = 136$ kJ mol^{-1} higher than that of the planar equilibrium structure. Similar calculations on $(CH_3)_2NB(CH_3)_2$ yielded a rotational barrier of $E_\pi = 107$ kJ mol^{-1}. This value is in good agreement with the 110 kJ mol^{-1} barrier to internal rotation in $(CH_3)_2NB(CH_3)Ph$, Ph=phenyl, determined by variable temperature NMR spectroscopy.

The molecular structure of the trisboryl amine $N[B(SCH_2)_2]_3$ is shown in Fig. 8. The coordination geometries of the N and the three B atoms are all planar. The orientations of two ligand rings are such that the NBS_2 planes form angles of 10° with the plane defined by the central NB_3 fragment. The third ring is oriented in such a manner that the NBS_2 plane is nearly perpendicular to the NB_3 plane.

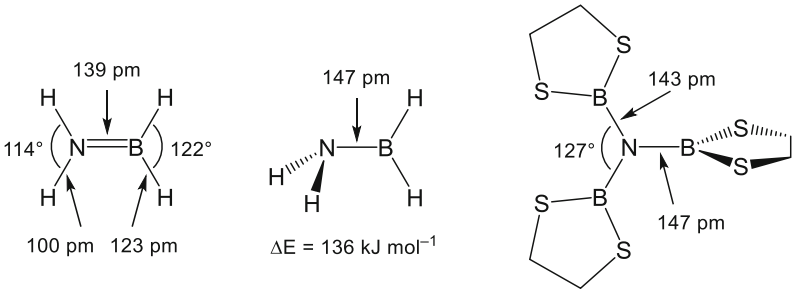

Fig. 8 *Left*: The gas-phase equilibrium molecular structure of the ethene analogue H_2NBH_2 and the structure and relative energy of the orthogonal form obtained by quantum chemical calculations. *Right*: The solid-state structure of $N[B(SCH_2)_2]_3$

The N–B bond distance to the perpendicular ring is equal to that calculated for the orthogonal form of H_2NBH_2, while the N–B bond distances to the two nearly coplanar rings are 4 pm shorter, presumably because of partial π- bonding.

7.5 Coordination Compounds of Aluminum

The simplest and best known coordination compound of aluminum is probably $(CH_3)_3NAl(CH_3)_3$. The gas-phase dissociation energy according to

$$(CH_3)_3NAl(CH_3)_3(g) = (CH_3)_3N(g) + Al(CH_3)_3(g),$$

is 126 kJ mol^{-1}, less than half the mean Al–N bond energy of crystalline aluminum nitride, 277 kJ mol^{-1}. The gas-phase dissociation energy of the analogous trimethylphosphine complex, 85 kJ mol^{-1}, is even lower. The molecular structures of the two complexes determined by gas electron diffraction are shown in Fig. 9.

The dative N→Al bond in $(CH_3)_3NAl(CH_3)_3$, 210 pm, is 20 pm longer than the Al–N bond in crystalline AlN and 28 pm longer than the normal covalent N–Al bond distance predicted by the modified Schomaker–Stevenson (MSS) rule; see Sect. 6. The dative P→Al bond in $(CH_3)_3PAl(CH_3)_3$ is about 23 pm longer than the covalent bond distance predicted by the MSS rule.

Comparison of the structures of the two complexes with that of the free acceptor shows that the Al–C bonds are elongated and pushed away from the electron donor as the complex is formed. These changes may be rationalized within the framework of the VSEPR model as the result of repulsion between incoming dative N→Al

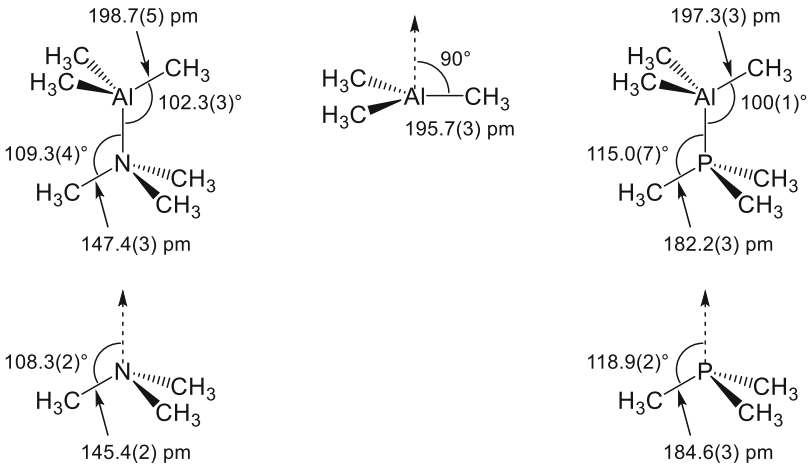

Fig. 9 The gas-phase molecular structures of the complexes $(CH_3)_3NAl(CH_3)_3$ and $(CH_3)_3PAl(CH_3)_3$, the free electron donors $(CH_3)_3N$ and $(CH_3)_3P$, and the free electron acceptor $Al(CH_3)_3$. Threefold symmetry axes are indicated by *stippled arrows*

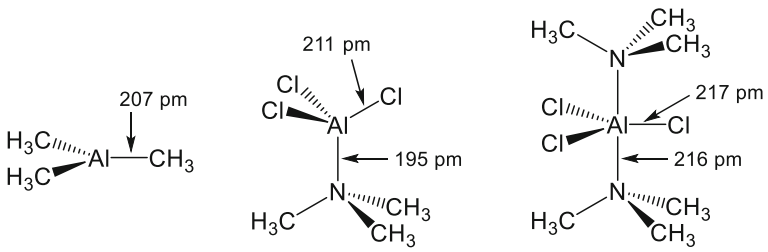

Fig. 10 The molecular structures of $AlCl_3$ in the gas phase and of the complexes $(CH_3)_3NAlCl_3$ and $[(CH_3)_3N]_2AlCl_3$ in the solid phase

bond electron pair and the three Al–C covalent bond electron pairs but may be augmented by steric repulsion between the entire donor molecule and the methyl groups bonded to the Al acceptor atom. It should be noted, however, that the three valence angles ∠DAlC (D=donor atom) are distinctly smaller than tetrahedral, thus indicating that the dative bond electron pair requires less space at the Al acceptor atom than the three covalent Al–C bond electron pairs.

While valence shell electron pair repulsion and the steric repulsion between the ligands act in a synergetic manner on the structure of the acceptor molecule, they are expected to act in opposite directions on the structure of the donor molecule. The VSEPR model predicts that partial removal of the lone pair on the donor atom (D) should lead to a widening of the ∠CDC valence angles and a shortening of the D–C bonds. Steric repulsion between the acceptor molecule and the methyl groups on the donor atom, on the other hand, should lead to a reduction of the ∠CDC valence angles and lengthening of the D–C bonds. The structures of the free $(CH_3)_3P$ donor molecule and the structural changes accompanying formation of the complex with $Al(CH_3)_3$ are both in complete agreement with the VSEPR model.

While the valence angles in the ammonia molecule, $\angle HNH = 107°$, are in agreement with the VSEPR model, the valence angle in free trimethylamine, $\angle CNC = 111°$, is larger than predicted, presumably due to steric repulsion between the methyl groups. While formation of the $(CH_3)_3NAl(CH_3)_3$ complex leads to the structural changes of the acceptor molecule predicted by both VSEPR and steric repulsions, the structural changes on the donor molecule are those predicted by steric repulsion alone.

The most strongly bonded amine alane complex is probably $(CH_3)_3NAlCl_3$ with a gas-phase dissociation energy of 198 ± 10 kJ mol^{-1} as compared to a dissociation energy of 126 kJ mol^{-1} in $(CH_3)_3NAl(CH_3)_3$. The crystal structure of the complex is shown in Fig. 10. The N→Al bond distance is 196 pm, 14 pm shorter than in gaseous $(CH_3)_3NAl(CH_3)_3$. The shortening is probably due to the inductive effect of the electronegative Cl atoms, but stabilizing dipole–dipole interactions in the crystalline phase may also contribute. The Al–Cl bond distance in the 1:1 complex is 4 pm longer than in the free $AlCl_3$ molecule.

The Al atom in the 2:1 complex is surrounded by five electron pairs in the valence shell, and the trigonal bipyramidal structure is in accordance with the

VSEPR model. The axial positions of the donor molecules are also in accordance with the VSEPR model, particularly if it is assumed that an accepted bond pair requires less space at the acceptor atom than a covalent bond pair. Addition of a second donor molecule increases the covalent Al–Cl distance by 6 pm and the dative N→Al bond distance by 21 pm.

7.6 *Aluminum Amides, Aluminum Imides, and Aluminum Nitride: Al–N Bonds with Partial Dative Character*

Dimethylaluminum dimethylamide, $(CH_3)_2AlN(CH_3)_2$, is dimeric in the solid and gas phases (Fig. 11). The rhombus formed by the two Al and the two bridging N atoms is nearly quadratic. The bridging Al–N distance is 14 pm shorter than the dative N→Al bond distance in $(CH_3)_3NAl(CH_3)_3$. The structure of the dimeric trisamide $[Al(N(CH_3)_2)_3]_2$ is very similar. The terminal Al–N bond distance is in agreement with the single covalent Al–N distance predicted by the MSS rule, 182 pm. In the following we shall use the latter as a reference value for a single covalent bond distance from N to a four-coordinate Al atom. Bonding in the central ring in the two molecules may be described in terms of two canonical forms, each with two covalent and two dative AlN bonds alternating around the ring. We therefore describe the bonds in the ring as 50% dative, and note that the observed bond distances are indistinguishable from the average of our reference value for a

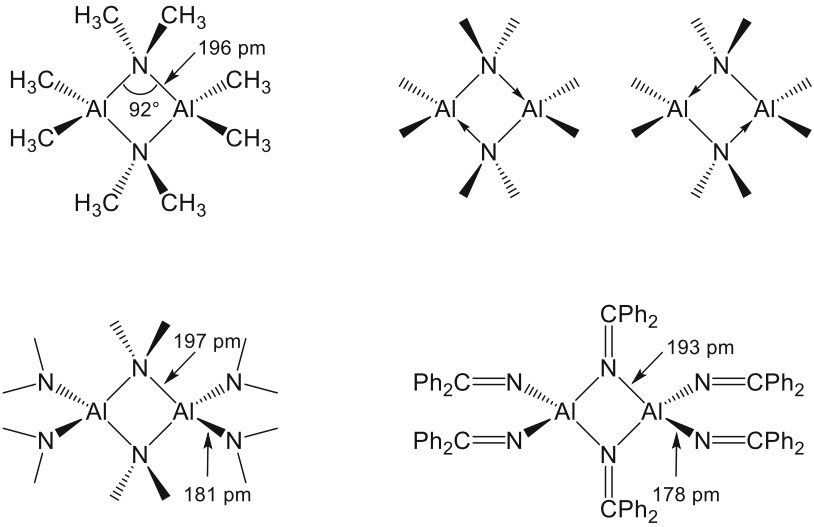

Fig. 11 The molecular structures of the dimeric aluminum amide $[(CH_3)_2AlN(CH_3)_2]_2$, the dimeric aluminum trisamide $[Al(N(CH_3)_2)_3]_2$, and the dimeric unsaturated aluminum trisamide $[Al(N{=}CPh_2)_3]_2$, Ph=phenyl

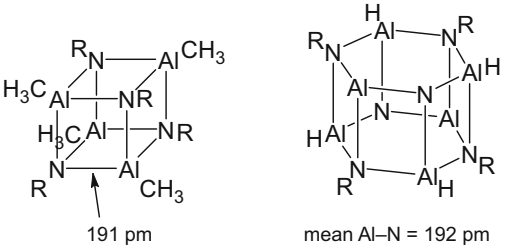

Fig. 12 The molecular structures of $(CH_3)_4Al_4$ (μ^3-NR)$_4$ and H_6Al_6 (μ^3-NR)$_6$, R=*iso*-propyl. Some of the H atoms and *iso*-propyl groups in the latter have been omitted for clarity

covalent single bond distance and the reference dative bond distance in $(CH_3)_3NAl(CH_3)_3$: 196 pm.

It has been suggested that the difference between the bridging and terminal bond distance in $[Al(N(CH_3)_2)_3]_2$ is due to the different coordination numbers of bridging and terminal N atoms, four and three respectively. The coordination numbers of bridging and terminal N atoms in $[Al(N{=}CPh_2)_3]_2$, Ph = phenyl, have been reduced to three and two. Both bridging and terminal AlN bond distances in the unsaturated trisamide are 4 pm shorter than the corresponding bonds in $[Al(N(CH_3)_2)_3]_2$, but their difference remains constant. We suggest that the shortening by 4 pm is due to the different covalent bonding radii of the N atoms in the two compounds. In any case comparison of the two structures shows that the coordination number is a less important variable than the magnitude of the dative character of the bonds.

A monomeric compound of composition RAlNR´ would be referred to as an aluminum imide. Such compounds are known but are always found to form oligomers, most often tetramers or hexamers. The structures of two such compounds are shown in Fig. 12. Each Al atom is presumably bonded to the external H atom or methyl group through a normal single covalent bond. The bonding within each cage must then be described in terms of canonical forms in which each Al or N atom is joined to two neighboring atoms through covalent bonds and to a third neighbor through a dative bond. The dative character of each bond in the cage is thus 1/3. The Al–N bond distance estimated as the 2:1 weighted average of our reference values for covalent and dative bonds is 191 pm, in good agreement with the observed distances.

Finally we note that the AlN bond distance in crystalline aluminum nitride is 190 pm. This bond may be described as 1/4 dative, and the 3:1 weighted average of the covalent and dative reference bond distances is 189 pm, again in good agreement with the observed value. Earlier in this section, we have used the mean bond energy in aluminum nitride, 277 kJ mol^{-1}, to demonstrate that the dative N→Al bond in $(CH_3)_3NAl(CH_3)_3$ is very weak. We have seen that the observed bond distance in AlN may be estimated as the 3:1 weighted average of the covalent and dative reference bond distances. If one makes a similar assumption regarding bond energies, one may estimate the bond energy of a 100% single covalent Al–N bond: 327 kJ mol^{-1}.

7.7 *Some Coordination Compounds of Zinc and Silicon*

One of the most interesting complexes of Zn may be the dipyridine complex of the bisamide Zn(1,4-dihydropyridin-yl)$_2$ (Fig. 13a). The Zn atom is bonded to two N atoms through normal covalent bonds and to two more N atoms trough dative bonds. The sizes and shapes of the four ligands are very nearly equal, so bond distances and valence angles at the metal atom are presumably determined by electronic effects alone. The dative bonds are found to be 19 pm longer than the covalent, and the angle spanned by the two covalent bonds is 26° larger than the angle spanned by the dative bonds.

Similarly the dative Zn→O bond distances in the complex between the Zn bis-aryloxide and tetrahydrofuran (**B**) is found to be 19 pm longer than the covalent, and the angle spanned by the two covalent bonds is 28° larger than the angle spanned by the two dative bonds. The four Zn–O bonds in Zn bis(acetylacetonate) (**C**) are all equal. The bond distances in each ZnO_2C_3 ring can be rationalized in terms of two canonical forms each with one covalent and one dative ZnO bond and alternating single and double CO and CC bonds around the ring: The ZnO bonds are thus 50% dative and 50% covalent. The observed bond distance is 4 or 5 pm shorter than the 1:1 average of the ZnO bond distances in **B**. The Zn atoms in crystalline ZnO are surrounded by four O atoms at the corners of a distorted tetrahedron. The average bond distance, 198 pm, is indistinguishable from the average Zn–O bond distance in the aryloxide complex **B**.

The structure of a complex where the central Si atom is bonded covalently to one (amide) N atom and datively to another (pyridine) N atom (**D**) is shown in Fig. 14. As expected, the datively bonded N atom occupies an axial position, and the dative bond is 27 pm longer than the covalent.

Dimethylaminosilane, $H_3SiN(CH_3)_2$, forms nitrogen-bridged pentamers in the solid state (**E**). The coordination geometries of the Si atoms are distorted trigonal bipyramidal with both axial positions occupied by N atoms. All Si–N bond distances are equal and must therefore be described as 50% covalent and 50% dative. The Si–N bond distance, 198 pm, is 14 pm longer than the average of the covalent

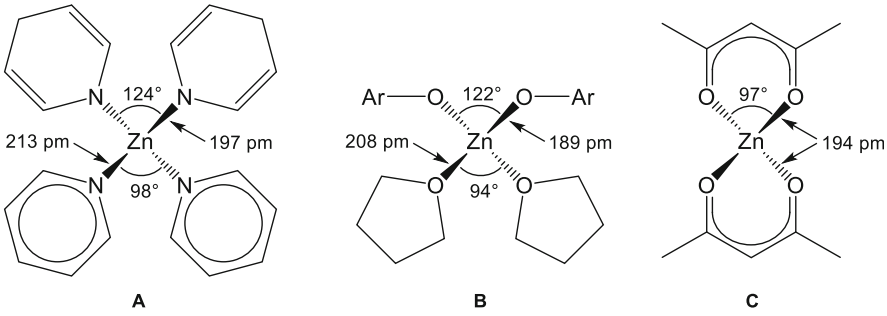

Fig. 13 The molecular structures of bis(1,4-dihydropyridin-yl)-bis(pyridine)Zn, $((CH_2)_4O)_2Zn(OAr)_2$, Ar=phenyl-2,4,6-tri-*tert*-butyl, and bis(acetylacetonate)Zn, $Zn(O_2(CCH_3)_2CH)_2$

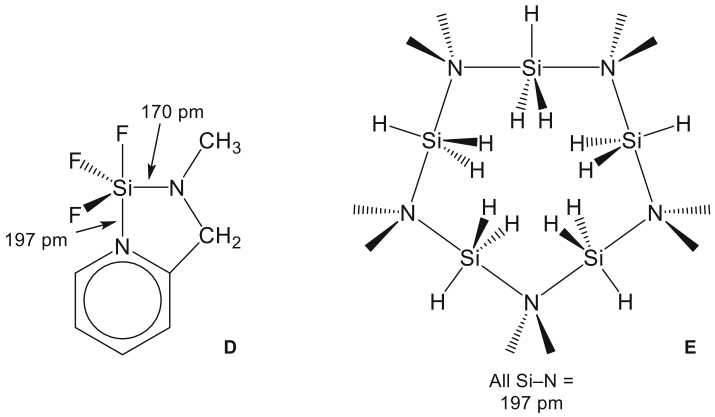

Fig. 14 The molecular structures of $F_3SiN(CH_3)(CH_2)C_5H_4N$ (**D**) and $[H_3SiN(CH_3)_2]_5$ (**E**)

and dative bond distances in **D**. Each Si atom in **E** carries three H atoms, and the Si atom in **D** carries three F atoms. We suggest, therefore, that the bond distances in the latter are shortened by inductive effects.

7.8 Anionic Complexes

The conceptually simplest anionic complex for which structural or thermodynamic information is available is the chlorotrihydroborate anion, $[H_3BCl]^-$. Minimum-energy atomization of the free ion leads to the formation of a boron atom, three H atoms, and a chloride ion. (Atomization to yield a H^- or B^- anion would require more energy.) We therefore describe it as a complex between a neutral BH_3 molecule and a chloride anion. The structure of the $[H_3BCl]^-$ ion with $[Ph_3PNPPh_3]^+$ as counterion has been determined by both X-ray and neutron diffraction. The coordination geometry was distorted tetrahedral with ∠ClBH valence angles equal to 105°. The B–H bond distances of 120 pm were unexceptional, but the dative $Cl^-\rightarrow B$ bond distance of 200 pm was substantially longer than the covalent bond distance in BCl_3, 174 pm. It was initially assumed that the long bond distance was due to the inclusion of a crystal impurity, but it has later been confirmed by several quantum chemical studies. The structure of the tetrachloroborate ion $[BCl_4]^-$ is tetrahedral with B–Cl bond distances equal to 184 pm. We consider these bonds to be 75% covalent and 25% ionic, and the observed bond distance is in very good agreement with the 3:1 weighted average of the covalent bond distance in BCl_3 and the dative Cl→B bond distance in $[H_3BCl]^-$, 183 pm.

Gallium forms a series of chloromethyl gallate ions: $[Cl_nGa(CH_3)_{4-n}]^-$, $n = 1$ to 4 (Fig. 15). Since the electron affinity of a Cl atom is greater than that of a methyl radical, we describe the GaCl bond in the monochloro gallate ion as a dative

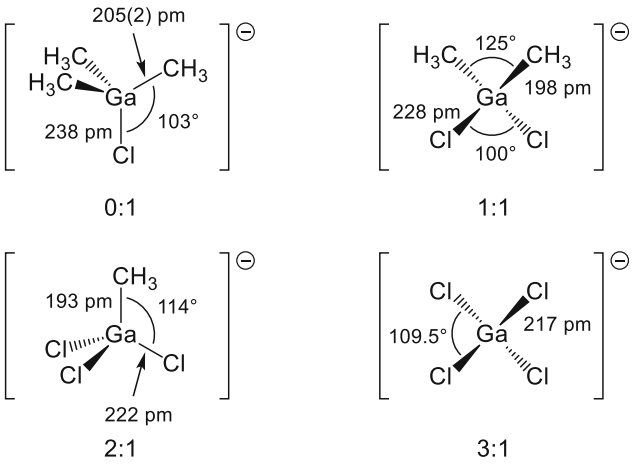

Fig. 15 The structures of chloromethyl gallate ions determined by X-ray diffraction studies of crystals with $[(CH_3)_4As]^+$ or $[(CH_3)_4Sb]^+$ counterions. The ratio between covalent to dative bonding contributions to the Ga–Cl bonds is shown under the respective structures

$Cl^- \rightarrow Ga$ bond and the three Ga–C bonds as covalent. This dative $Cl^- \rightarrow Ga$ bond distance is 27 pm longer than the terminal, covalent Ga–Cl distance in dimeric $GaCl_3$.

The ratio between the covalent and dative bonding contribution to GaCl bonds in $[Cl_2Ga(CH_3)_2]^-$ is 1:1, in $[Cl_3Ga(CH_3)]^-$ 2:1, and in $[Cl_4Ga]^-$ 3:1, and the GaCl bond distances in the four ions decrease monotonically from 238 pm in $[ClGa(CH_3)_3]^-$ to 217 pm in $[Cl_4Ga]^-$. The Ga–C bond distance in $[ClGa(CH_3)_3]^-$ has not been determined with accuracy, but it is certainly longer than in $[Cl_2Ga(CH_3)_2]^-$, 198 pm. The latter is indistinguishable from the bond distance in monomeric $Ga(CH_3)_3$. The monotonic decrease of Ga–C bond distances with increasing number of Cl atoms is presumably due to inductive effects.

The energy of the reaction

$$[GaCl_4]^-(g) = GaCl_3(g) + Cl^-(g),$$

calculated from the enthalpies of formation of reactant [72] and products, 358 kJ mol^{-1}, is indistinguishable from the mean Ga–Cl bond energy in $GaCl_3$. The dative bond in the free $[GaCl_4]^-$ ion is thus as strong as the covalent Ga–Cl bonds. It is perhaps not surprising that a negatively charged atom should be a better electron donor than a neutral atom embedded in a neutral molecule.

Similarly one might suspect that a singly, doubly, or triply charged metal cation is a much better electron acceptor than the same atom within a neutral molecule. We suspect, therefore, that the difference between covalent and dative bonds may be blurred in many ionic complexes.

8 Lewis-Valent and Subvalent Chlorides of the Group 13 and 14 Elements

8.1 The Inert Electron Pair

In his seminal article of 1916 Lewis remarked that the heavier elements in Groups 13 and 14 "form a class in which the atomic kernel is probably not neither uniquely determined nor invariable during chemical change." By the time that Sidgwick published his book *The Electronic Theory of Valency* in 1927, our understanding of the electronic structure of atoms was much further advanced, and the distinction between *s*- and *p*-electrons had been drawn [67]. "We now realize that the first two electrons in any group [. . .] correspond to the pair of electrons [. . .] in helium, and can have a certain completeness of their own [. . .]. We might thus anticipate that under some conditions the first two valence electrons in an element could [. . .] refuse either to ionize, or to form covalencies, or both. Why this inertness [. . .] should appear precisely where it does in the periodic table, we cannot say."

8.2 The Polar Covalent Chlorides of the Group 12 Metals

In Sect. 3 we used an ionic model to explore the nature of bonding in the gaseous, monomeric dihalides of the Group 2 and 12 metals. The formation of the molecular units from the separated atoms was then divided into two steps. In the first step the monoatomic ions were formed from the neutral atoms at infinite distance from one another, and in the second step the ions were brought together to form a molecular unit.

In the following we shall use a similar procedure to analyze the formation of the covalently bonded dichlorides, dibromides, and diiodides of the Group 12 metals from the separated atoms. In the first step, the electron pair in the valence shell *ns*-orbital of the free metal atom is broken up by exciting one of them to a valence shell *np*-orbital. The minimum energy required, $\Delta E^*(\mathrm{M})$, can be obtained from atomic spectral data [73]. In the second step the excited metal atom and the two halogen atoms are brought together to form the covalent bonds. Once the molecule has been formed, it may dissociate in such a manner that the metal atom is returned to the ns^1np^1 valence configuration. We denote half the energy required for this process as the mean bond energy for dissociation to the valence state, MBE^*(M–X). Alternatively, the molecule may dissociate in such a manner that the metal atom is left in the ns^2 ground-state electron configuration. The energy required is twice the mean M–Cl bond energy, MBE^0(M–X). Clearly

Table 12 Gaseous, monomeric dichlorides, dibromides, and diiodides of zinc, cadmium, and mercury

	$ZnCl_2$	$CdCl_2$	$HgCl_2$	$ZnBr_2$	$CdBr_2$	$HgBr_2$	ZnI_2	CdI_2	HgI_2
ΔE^*(M) (kJ mol^{-1})	389	367	471	389	367	471	389	367	471
*MBE**(M–X) (kJ mol^{-1})	512	462	457	462	416	420	398	376	381
MBE^0(M–X) (kJ mol^{-1})	318	273	224	269	232	184	203	192	145

ns^2 to ns^1np^1 electron excitation energies of the free metal atoms (ΔE^*); mean M–X bond energies for dissociation that leaves the metal atom in the excited ns^1np^1 valence state (*MBE**); and mean M–X bond energies for dissociation to yield the metal atom in the ns^2 ground state (MBE^0)

$$2MBE^0(\mathrm{M-X}) = 2\ MBE^*(\mathrm{M-X}) - \Delta E^*(\mathrm{M-X}). \tag{9}$$

The mean bond energy MBE^0(M–X) may be calculated from available thermochemical data, and *MBE**(M–X) may be calculated from Eq. (9).

The energy required to promote the metal atom from its ground state to the ns^1np^1 valence state decreases slightly from 389 kJ mol for M=Zn to 367 kJ mol^{-1} for M=Cd and then increases abruptly to 471 kJ mol^{-1} for M=Hg. For each dihalide, the mean bond energies for dissociation to the ns^1np^1 valence state (*MBE**) decrease significantly between Zn and Cd, but remain relatively unchanged between Cd and Hg. This is the trend expected from the variation of bond distances: Zn<Cd ≈ Hg (Table 2). The data in Table 12 thus indicate that the observed decrease of the mean M–X bond energies (MBE^0) between cadmium and mercury is due to the increased energy required for excitation of the metal from the ground state to the valence state.

8.3 The Group 13 Element Chlorides

The first four elements of Group 13 form trichlorides that are stable at normal temperatures and pressures. BCl_3 is a volatile liquid at room temperature and monomeric in the gas phase. $AlCl_3$, $GaCl_3$, and $InCl_3$ form solids at room temperature. Evaporation at moderate temperatures yields mixtures of monomeric and dimeric species. At higher temperatures all the gaseous trichlorides suffer partial decomposition to form monochlorides and Cl_2:

$$MCl_3(g) = MCl(g) + Cl_2(g).$$

At a given temperature and pressure, the equilibrium shifts to the right as the group is descended from B to In.

$TlCl_3$ has been synthesized and isolated as a solid, but decomposes at temperatures above 40°C to yield the solid monochloride and chlorine gas:

Table 13 Gaseous, monomeric mono- and trihalides of the Group 13 elements

	MX(g)		MX_3(g)			
M, X	R (pm)	D^0 (kJ mol^{-1})	R (pm)	MBE^0 (kJ mol^{-1})	ΔE*(M) (kJ mol^{-1})	MBE* (kJ mol^{-1})
B, Cl	172	508	174	440	345	555
Al, Cl	213	500	207	424	347	540
Ga, Cl	220	461	211	353	454	504
In, Cl	240	433	229	324	418	463
Tl, Cl	249	367	–	216 (est)	540	396 (est)
Tl, Br	262	330	–	176 (est)	540	356 (est)
Tl, I	282	266	–	107 (est)	540	287 (est)

M–X bond distances R and bond dissociation energies, D_0, of seven monohalides. Bond distances and mean bond energies, MBE^0, of the gaseous trichlorides of B, Al, Ga, and In. ns^2np^1 to ns^1np^2 electron excitation energies of the free metal atoms, ΔE*(M), and mean M–X bond energies for dissociation that leaves the metal atom in the excited ns^1np^1 valence shell electron configuration, MBE*. Estimated mean bond energies, MBE^0 and MBE*, of $TlCl_3$, $TlBr_3$, and TlI_3 (the dissociation energy of BCl(g) has been taken from [74])

$$TlCl_3(s) = TlCl(s) + Cl_2(g).$$

The mass spectra of the gas formed by evaporation of solid $TlCl_3$ show that it contains significant amounts of monochloride and chlorine in addition to trichloride. Neither the molecular structure nor the enthalpy of formation of gaseous, monomeric $TlCl_3$ has been determined.

$TlBr_3$ and TlI_3 may not exist. The former is only known as a crystalline tetrahydrate, presumably $[(H_2O)_4Tl]Br_3$, that decomposes on dehydration. A solid of composition TlI_3 was later shown to be the salt $Tl^+(I_3)^-$.

Before proceeding we pause to note that the bonds in the five monomeric, gaseous monochlorides as well as the bonds in the gaseous trichlorides of B, Al, Ga, and In are polar covalent rather than ionic. The experimental dipole moments of InCl and TlCl are less than 50% of those calculated for spherical ion models. Born–Landé calculations on an ionic model of the monochlorides yield dissociation energies that range from 55% (M=B) to 70% M=Tl) of the experimental value. Similar calculations on the trichlorides BCl_3, $GaCl_3$, and $InCl_3$ yield *negative* mean bond energies. The MBE of $AlCl_3$ is calculated to be positive, but is 80 % smaller than the experimental value.

The gas-phase molecular structures and dissociation energies of the seven monohalides MCl in Table 13 have all been determined by high-temperature spectroscopic studies. As expected, M–Cl bond distances increase, and the dissociation energies decrease as Group 13 is descended. Similarly Tl–X bond distances in the three thallium monohalides increase and the bond energies decrease as the halogen group is descended.

The molecular structures of the monomeric trichlorides MCl_3 (M=B, Al, Ga, and In) have been determined by gas-phase electron diffraction. The structures are all trigonal planar. Again M–Cl bond distances increase and bond energies decrease as Group 13 is descended. The bond distance in BCl_3 is slightly larger (2 pm) than in the monochloride, but the bond distances in the trichlorides of Al, Ga, and In are 6, 9, and 11 pm *shorter* than in the monochlorides. Comparing bond energies, one finds that the M–Cl bonds in the trichlorides are substantially weaker than in the monochlorides. The bonds in BCl_3 are 13% weaker than in BCl, and the difference increases as the group is descended. The weaker bonds in the trichlorides are unexpected, since the shorter bond is normally expected to be the stronger.

The ground-state valence shell electron configuration of the Group 13 elements is ns^2np^1. Formation of the first M–Cl bond may presumably take place without excitation to a higher energy valence state or hybridization of the bonding *np*-orbital on the metal atom. Formation of the trichlorides, however, requires that the ns^2 electron pair is broken up by promotion of one of the *ns*-electrons to a *np*-orbital. The lowest atomic state arising from an ns^1np^2 configuration is a ^4P state where the three valence electrons have parallel spins. The energies required to promote the Group 13 atoms from the ^2P ground state to the ^4P valence state, $\Delta E^*(M)$, are listed in Table 13 [73]. The promotion energies increase relatively slowly from 345 kJ mol^{-1} in B to 418 kJ mol^{-1} in In and then rises abruptly to 540 kJ mol^{-1} in Tl.

Formation of a gaseous MCl_3 molecule from the four separated atoms may be divided into two steps. In the first step the metal atom is promoted to the ^4P valence state; in the second step the three bonds are formed. Again we denote the mean bond energy for dissociation to the ns^1np^2 valence state of the metal atom as MBE^* (M–X):

$$MBE^*(\mathrm{M-X}) = MBE^0(\mathrm{M-X}) + \Delta E^*(\mathrm{M})/3. \tag{10}$$

The mean bond energies of BCl_3, $AlCl_3$, $GaCl_3$, and $InCl_3$ for dissociation to the valence state are listed in the seventh column of Table 13. As expected they decrease in a regular manner from B to In. Comparison with the dissociation energies of the corresponding monochlorides show that four MBE^*s are 7% to 9% larger. This fact was used to estimate the MBE^*s of $TlCl_3$, $TlBr_3$, and TlI_3 from the dissociation energies of the corresponding monohalides. Finally subtraction of $\Delta E^*(Tl)/3$ yielded the estimated mean bond energies MBE^0s of $TlCl_3$, $TlBr_3$, and TlI_3. The data in the table indicate that the reduction of the MBE^0 from 324 kJ mol^{-1} in $InCl_3$ to 216 kJ mol^{-1} in $TlCl_3$ is due to a combination of the increased excitation energy and a lower inherent M–Cl bond strength as witnessed by the lower dissociation energy of the monochloride. As expected the bonds in $TlBr_3$ and TlI_3 are predicted to be even weaker than in $TlCl_3$. As we have already pointed out, $TlBr_3$ and TlI_3 have never been isolated and may not exist.

Table 14 Gaseous monomeric dichlorides of the Group 14 elements

	ECl_2(g)			ECl_4(g)	
E	R (pm)	∠ClECl (°)	MBE^0 (kJ mol^{-1})	R (pm)	MBE^0 (kJ mol^{-1})
C	172	109[a]	373	177	323
Si	207	101	431	202	397
Ge	217	100	394	211	337
Sn	235	99	371	228	312
Pb	245	98	306	237	252

E–Cl bond distances, R; valence angles, ∠ClECl; and mean bond energies, MBE^0. Gaseous tetrachlorides of the Group 14 elements: E–Cl bond distances and mean bond energies (the bond distance and valence angle in CCl_2(g) has been taken from [75])

8.4 The Group 14 Element Chlorides

Germanium, tin, and lead form solid dichlorides, whereas the lighter species CCl_2 and $SiCl_2$ may be generated and studied in high-temperature vapors. Gas electron diffraction and spectroscopic studies show that all the dichlorides are angular with ClECl valence angles ranging from 109° in CCl_2 to 98° in $PbCl_2$. Bond distances, valence angles, and mean bond energies calculated from thermochemical data are listed in Table 14.

All the Group 14 elements form Lewis-valent tetrachlorides that are liquid at normal temperatures and pressures, but $PbCl_4$ decomposes at room temperature to yield Cl_2 gas and the solid dichloride and may detonate in vacuum. All the tetrachlorides have tetrahedral structures (Table 14).[2] Lead tetrabromide, $PbBr_4$, is reported to be significantly less stable than the tetrachloride, and it is doubtful that PbI_4 can exist at all.

The relationships between bond distances and bond energies are very similar to those observed for the Group 13 element chlorides:

1. Both Lewis-valent and subvalent E–Cl bonds become longer and weaker as the group is descended.

[2] $PbCl_4$ is a liquid at room temperature. At slightly higher temperatures, it decomposes – sometimes explosively – to solid $PbCl_2$ and Cl_2 gas. The decomposition reaction is clearly highly exothermic. The JANAF tables [30] list the standard enthalpy of formation of $PbCl_4$(g) at 298 K as –552 kJ mol^{-1} and the standard enthalpy of formation of $PbCl_2$(s) as –359 kJ mol^{-1}. These numbers yield a standard reaction enthalpy for the decomposition reaction $PbCl_4(g) = PbCl_2(s) + Cl_2(g)$ equal to $\Delta_{dec}H^0{}_{298} = +193$ kJ mol^{-1} corresponding to an *endothermic* reaction. One or both the enthalpies of formation listed by JANAF must clearly be in error! The Russian XUMUC tables [32] list the enthalpy of formation of $PbCl_2$(s) as –360 kJ mol^{-1}, i.e., in perfect agreement with the JANAF value. The enthalpy of formation of $PbCl_4$(g) is not listed, but for the liquid $\Delta_fH^0{}_{298} = -329$ kJ mol^{-1}, that is, 226 kJ mol^{-1} *higher* than the JANAF value for the gas. Using the XUMUC values for enthalpies of formation, the calculated reaction enthalpy for the decomposition reaction $PbCl_4(l) = PbCl_2(s) + Cl_2(g)$ is equal to $\Delta_{dec}H^0{}_{298} = -31$ kJ mol^{-1}. When calculating the mean Pb–Cl bond energy in $PbCl_4$, we have assumed that the molar enthalpy of vaporization of liquid $PbCl_4$ is equal to that of liquid $SnCl_4$, i.e., 40 kJ mol^{-1}.

2. The E–Cl bonds in the subvalent chlorides are stronger than in the Lewis-valent.
3. Except for the second period element (C), the E–Cl bonds in the subvalent chlorides are longer than in the Lewis-valent.

The shorter bond distances in the tetrachlorides of Si, Ge, Sn, and Pb may be rationalized as due to hybridization effects: The bonding molecular orbitals in the dichlorides are presumably formed from atomic orbitals with higher *p*-character.

The energy required to promote a Group 14 atom from the ^3P ground state to the lowest excited state with $ns^1np_x{}^1np_y{}^1np_z{}^1$ electron configuration (^5S) is unfortunately only known for C and Sn: $\Delta E^*(\mathrm{C}) = 403$ and $\Delta E^*(\mathrm{Sn}) = 474$ kJ mol^{-1}, respectively. This is, however, sufficient to show that the weaker E–Cl bonds in the C and Sn tetrachlorides are due to the energy required to break up the ns^2 electron pair before four E–Cl bonds can be formed. The energy required to promote a Pb atom from the ground-state to the valence-state electron configuration is not known, but comparison with In and Tl (Table 13) and Sn suggests a value of ΔE^*(Pb) between 590 and 600 kJ mol^{-1}.

As mentioned above, $PbCl_4$ may detonate in vacuum. The energy of the decomposition reaction

$$\mathrm{PbCl_4(g) = PbCl_2(s) + Cl_2(g),}$$

calculated from the enthalpies of formation reactants and products is $\Delta U^0{}_{\mathrm{dec}} = -21$ kJ mol^{-1}. If there had been no "inert pair effect," that means, if the $PbCl_4$ had not been destabilized by the nearly 600 kJ mol^{-1} spent to promote the metal atom to the valence state, the energy of the reaction would have been about +580 kJ mol^{-1}: Without the inert pair effect, there would have been no explosions!

9 Compounds of Hypervalent Main-Group Elements

According to the Lewis electron pair model for the single covalent bond, the atoms in Group 15 are expected to form three such bonds, the Group 16 atoms two, the Group 17 atoms one, and the Group 18 atoms none. At the time when Lewis' seminal paper was published in 1916, only two molecules, PCl_5 and SF_6, were known to form exceptions to this rule. When Sidgwick and Powell published their article on structural types in 1940, the number of exceptions had been increased by six: PF_5, PCl_3F_2, $(CH_3)_3SbF_3$, $TeCl_4$, SeF_6, and TeF_6. Today, 75 years later, the pentafluorides of P, As, Sb, and Bi are all known. The Group 16 elements S, Se, and Te are all known to form both tetra- and hexafluorides. The Group 17 elements Cl and Br are known to form tri- and pentafluorides, and iodine is known to form a penta- and a heptafluoride. The two noble gas atoms Kr and Xe form difluorides; in addition Xe also forms a tetra- and a hexafluoride. Only six atoms, As, Sb, Bi, Se, Te, and iodine, form homoleptic, hypervalent compounds with Cl atoms or methyl or phenyl groups as ligands.

The largest number of known hypervalent compounds carries fluorine or oxygen atoms as substituents. The ability of F and O to stabilize hypervalent compounds is probably due to the combination of their high electronegativity which is known to increase bond strength and their small radii which minimize steric repulsion between atoms spanning valence angles of 90° or less. The Cl atom is larger and less electronegative than the F atom, and the number of hypervalent chlorides is less than half the number of hypervalent fluorides. No hypervalent compound with a singly bonded Br or I atom as ligand appears to be known. The hydrogen atom is smaller than a fluorine atom, but no stable hypervalent compound with H atoms as substituents is known, perhaps because of its lower electronegativity.

There has been general agreement that bonds to fluorine, chlorine, methyl, or phenyl groups in hypervalent compounds should be described as single polar covalent bonds and that the central atoms therefore must accommodate more than four electron pairs in its valence shell. But there has been a curious reluctance to accept that bonds from the central atom to terminal oxygen atoms in the oxides or oxyacids of the Group 15, 16, or 17 elements, such as SO_2 SO_3, or H_2SO_4, are best described as double (two electron pair) bonds and that the central atoms in these compounds also must accommodate more than four electron pairs in their valence shells.

In the 1960 edition of *The Nature of the Chemical Bond* [68], Pauling presented the "older, conventional valence bond structure" for the sulfate ion with two single and two double SO bonds, but adds that such structures "have fallen into general disuse, in consequence of the suggestion originally made by Lewis [...] and accepted by most subsequent investigators, that the octet rule is to be applied to the sulfur atom" and other elements in the same or later rows. This rule would seem to imply that the four SO bonds in the sulfate ions should be described as single. Pauling himself suggested seventeen canonical forms that will "contribute largely to the normal state of the [sulfate] ion": four canonical forms with three single and one double SO bond, six forms with two single and two double SO bonds, four with one single and three double, and finally one canonical form with four double S=O bonds.

9.1 The Structures of Hypervalent Compounds of Phosphorus

Phosphorus forms a tri- and a pentafluoride (Fig. 16). The coordination geometry of the trifluoride is pyramidal and that of the pentafluoride trigonal bipyramidal as expected. The average bond distance in the pentafluoride is about 1 pm shorter, and the mean bond energy is 10% lower than in the trifluoride. [The reader might compare with the bond energies of divalent and tetravalent Group 14 element chlorides listed in Table 14. The bonds in the tetrachlorides are 8% to 18% weaker

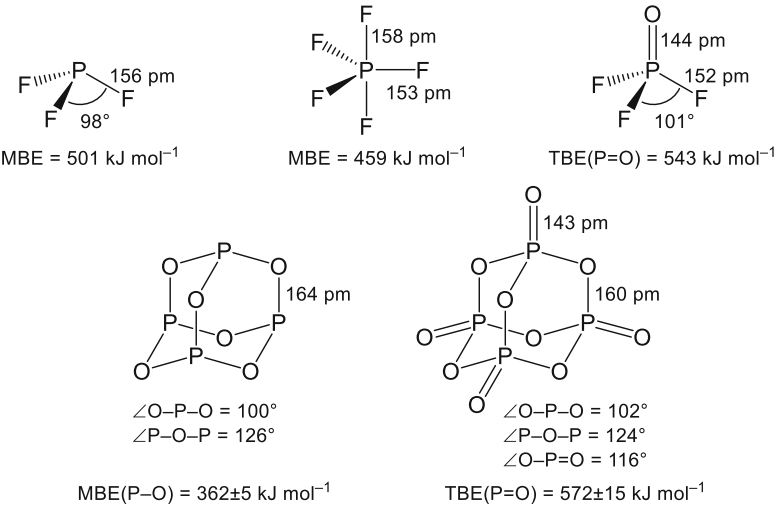

Fig. 16 The molecular structures and bond energies of PF_3, PF_5, F_3PO, P_4O_6, and P_4O_{10} in the gas phase

than the bonds in the dichlorides.] The nature of the P–F bonds in the Lewis-valent and hypervalent fluorides is clearly similar.

The simplest binary oxide is P_4O_6. The structure is highly symmetrical: The P atoms occupy the corners of a perfect tetrahedron while the O atoms occupy the corners of an octahedron. Each P atom is singly bonded to three O atoms and each O atom to two P atoms. The P–O bond distance is as expected for a single bond. The OPO valence angle is close to the FPF valence angle in PF_3. The large POP valence angles are presumably partly due to the larger size of the phosphorus atoms. The mean P–O bond energy, calculated as 1/12 of the energy of atomization, is 362 kJ mol^{-1} [76, 77].

The simplest higher oxide is P_4O_{10} where each P atom has added a terminal O atom at a distance of 143 pm, about 17 pm shorter than the single P–O bonds. The mean P=O bond energy calculated from the energy of atomization by transfer of the single bond energy from the hexaoxide is about 572 kJ mol^{-1} or 58% higher than for the single bond.

The P=O bond distance in the F_3PO molecule is 1 pm larger than in P_6O_{10}; the P=O bond energy is 5% smaller. We conclude that the phosphorus atoms in PF_5, P_4O_{10}, and F_3PO all contain five bonding electron pairs in their valence shell. The gas-phase structure of phosphoric acid is unfortunately unknown.

9.2 The Structures of Hypervalent Compounds of Sulfur

While the structure of sulfur difluoride is angular, the structure of the tetrafluoride is distorted trigonal bipyramidal with an equatorial atom missing (see Fig. 17). The coordination geometry and the distortions from the ideal trigonal bipyramidal valence angles are in full agreement with the VSEPR model. As expected, the axial S–F bond distances in SF_4 are about 11 pm longer than the equatorial. The *average* bond distance is, however, indistinguishable from that of SF_2. The structure of SF_6 is, as predicted by Lewis, perfectly octahedral. The S–F bond distance is about 3 pm *shorter* than in the difluoride. The mean bond energy in the tetrafluoride is 7% lower than in the difluoride; the mean bond energy in the hexafluoride is 10% lower. Thus the S–F bond distances and bond energies in the Lewis-valent and hypervalent compounds are approximately equal.

The S=O bond distance in SO is 148 pm as compared to the S–O single bond distance of 166 pm in HSOH. The double bond energy in SO, 519 kJ mol^{-1}, is larger than the double bond energies in the O_2 and S_2 molecules, 496 kJ mol^{-1} and 423 kJ mol^{-1}, respectively. The bond distance in the dioxide SO_2 is 143 pm, that is, 5 pm *shorter* than in the Lewis-valent monoxide; the bond energy is 3% higher. If the bond in the monoxide is double, so is the bond in the dioxide. It is our view that the terms single, double, or triple bonds should be used to describe the strength and length of the bonds. Lewis postulated that a single bond is associated with a shared electron pair, a double bond with two shared electron pairs, and a triple bond by three such pairs. The Lewis structure of SO_2 should therefore be drawn with two electron pairs between the S atom and each O. That would leave enough electrons to place two lone pairs on each O and one lone pair at the S atom. The S atom in SO_2, like the S atom in SF_4, has five electron pairs in the valence shell. According to the VSEPR model, the two electron pairs in each double bond occupy one domain. The

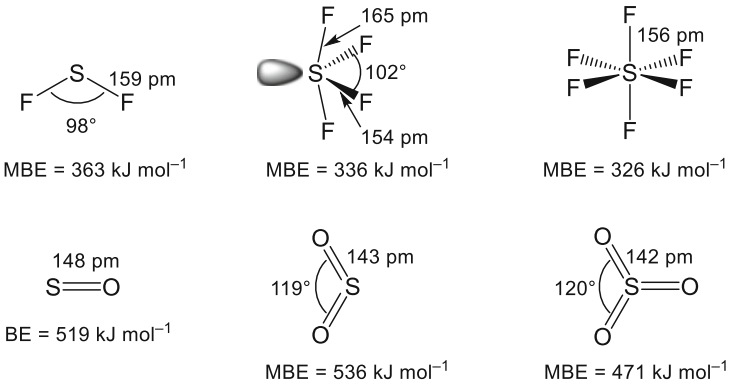

Fig. 17 *Above*: The molecular structures of SF_2, SF_4, and SF_6 determined by gas electron diffraction and mean bond energies (MBE) calculated from thermochemical data. *Below*: The molecular structures and bond energies of SO, SO_2, and SO_3

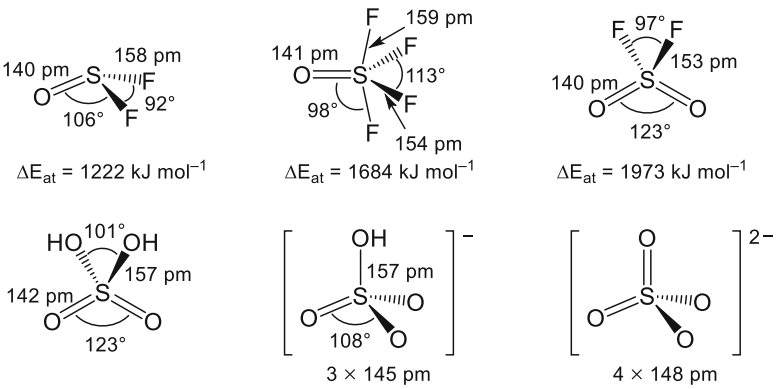

Fig. 18 *Top row*: The molecular structures of F_2SO, F_4SO, and F_2SO_2 determined by gas electron diffraction and atomization energies (ΔE_{at}) calculated from thermochemical data. *Second row*: The gas-phase molecular structure of the sulfuric acid molecule determined by MW spectroscopy and the structures of the hydrogen sulfate and sulfate ions determined by X-ray crystallography

electron lone pair on the sulfur should then lead to the angular structure that is observed.

The SO bond distance in SO_3 is 6 pm *shorter* than in SO; the mean bond energy is 10% lower. This is the same mean bond energy decrease as that observed between SF_2 and SF_6. We conclude that on the basis of the experimental bond distance and bond energy, the three bonds in SO_3 should be described as double. This implies that the S atom in SO_3, like the S atom in SF_6, has six electron pairs in the valence shell. According to the VSEPR model, repulsion between the three domains each containing two electron pairs should lead to the trigonal planar structure that is observed.

We now turn our attention toward mixed oxy-fluorides (Fig. 18). The S–F distance in the tetravalent compound F_2SO is about 2 pm shorter than the average S–F distance in SF_4, while the S=O bond distance is 3 pm shorter than in SO_2. The S atom in F_2SO, like the sulfur atoms in SF_4 and SO_2, has one nonbonding electron pair in its valence shell. The pyramidal coordination geometry and the magnitudes of the valence angles are thus in accord with the VSEPR model. The bond distances, valence angles, and coordination geometries of the two hexavalent compounds, F_4SO and F_2SO_2, are also fully consistent with the VSEPR model.

The atomization energies listed in Fig. 18 have been calculated from thermochemical data. The atomization energy of F_2SO may also be estimated by assuming that the S–F bond energy is equal to that of the tetrafluoride and that the S=O bond energy is equal to that of the dioxide. Similarly the atomization energies of the two hexavalent compounds, F_4SO and F_2SO_2, may be estimated by transferring bond energies from SF_6 and SO_3. The resulting estimated atomization energies are 1% below the experimental value for F_2SO, 10% lower for F_4SO, and 5% lower for F_2SO_2. We conclude that S–F and S=O bond distances and bond energies remain fairly constant from one compound to the next.

The structure of the sulfuric acid molecule in the gas phase is closely related to that of the F_2SO_2 molecule. The S=O distance is 2 pm shorter; the O=S=O valence angle is unchanged. The valence angles at sulfur spanned by the two singly bonded atoms (O or F) in the two compounds are indistinguishable. The S–O single bond distances are 15 pm longer than the double bond distances.

We conclude that all terminal O atoms in the gaseous sulfur oxides, in the four sulfur oxy-fluorides, and in gaseous sulfuric are joined to the sulfur atom through double bonds. If Lewis structures are drawn with double S=O bonds represented by two electron pairs, the coordination geometries of all these compounds are in accord with the VSEPR model. The sulfur atoms in all these molecules have five or six electron pairs in the valence shell.

The structure of the hydrogen sulfate ion has been determined by an X-ray diffraction study of crystalline $[H_3O]^+$ $[HSO_4]^-$. The bond length from the sulfur atom to the O atom carrying the H atom remains unchanged at 157 pm, while the bond distances from S to the three terminal O atoms have increased slightly to 145 pm.

The sulfate dianion is stable in the presence of counterions or in aqueous solution, but like many other doubly or triply charged oxoanions, it is unstable in the gas phase and emits a single electron [78]:

$$[SO_4]^{-2}(g) = [SO_4]^{-}(g) + e^- \quad \Delta E = -150 \pm 10 \text{ kJ mol}^{-1}.$$

X-ray diffraction studies of several salts show that the structure of the sulfate ion is tetrahedral with a SO bond distance of 148 pm. This SO bond distance is indistinguishable from that of the monoxide molecule SO. The might be taken to indicate that the four SO bonds in the ion are double. It should be clear, however, that the

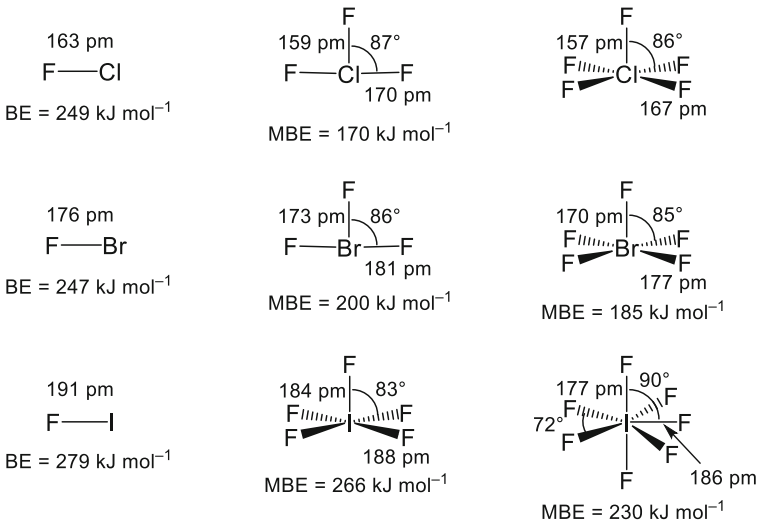

Fig. 19 The gas-phase molecular structures of hypervalent fluorides of Group 17 elements

electronic structure of the ion must be strongly influenced by the Coulomb interactions with the counterions that ensure its stability.

9.3 *Hypervalent Compounds of Group 17 Elements*

The second period element, F, stabilizes hypervalent compounds of elements in Groups 15, 16, 17, and 18, but does not itself display hypervalency (see Fig. 19). The central atoms in ClF_3 and BrF_3 must have two nonbonding electron pairs in their valence shell, and in accordance with the VSEPR model, they adopt T-shaped structures corresponding to trigonal bipyramids with the nonbonding pairs occupying equatorial positions. Similarly the central atoms in ClF_5, BrF_5, and IF_5 are left with one nonbonding electron pair in their valence shell and the compounds adopt structures corresponding to octahedrons with one corner occupied by the electron lone pair. The deviations from the ideal valence angles of 90° in all these molecules are in agreement with the VSEPR model.

The pentagonal bipyramidal structure of iodine heptafluoride is unique. There is however no need to formulate a VSEPR rule for compounds with seven electron pairs in the valence shell of the central atom: To the best of our knowledge, there is only one more such compound with a main-group element at the central position, and that compound, XeF_6, adopts distorted octahedral coordination geometry. As indicated in Fig. 19, there is a general tendency for the element to F bonds to become stronger as Group 17 is descended and weaker with increasing number of F substituents.

The molecular structures of the three chlorine oxides that are sufficiently stable to be investigated in the gas phase are shown in Fig. 20. The O–Cl bond distance and mean bond energy in OCl_2 provide reference values for single O–Cl bonds. The dioxide ClO_2 was one of the four molecules with an odd number of electrons that were mentioned by Lewis in his 1916 paper, and its properties continue to surprise: The O–Cl bond is 33 pm shorter than in OCl_2, but the bond energy is only 28% larger! The bond distances and valence angles in dichlorine heptoxide, Cl_2O_7, indicate that the bridging O atom is joined to the two Cl atoms through single bonds while the terminal ClO bonds are double. The energy of atomization of

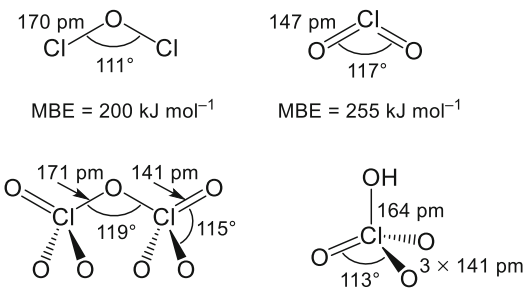

Fig. 20 The gas-phase structures of chlorine oxides and perchloric acid

gaseous Cl_2O_7 calculated from the enthalpy of formation is 1,691 kJ mol^{-1} [79], while the energy of atomization calculated from the ClO single and double bond energies in OCl_2 and ClO_2 respectively, is 1,930 kJ mol^{-1}. It seems probable that both the "single" and "double" ClO bonds in the heptoxide are weaker than in the two reference molecules!

The ClO bond distances to both the terminal and the two-coordinate O atoms in the perchloric acid molecule are similar to those in the anhydride Cl_2O_7. If the shorter ClO bonds are described as double bonds, this would imply that the Cl atoms in the two molecules have seven electron pairs in their valence shell.

9.4 Hypervalent Compounds of Xenon

The noble gas xenon forms a difluoride, a tetrafluoride, a hexafluoride, and a tetraoxide. Their structures and mean bond energies are summarized in Fig. 21. If we assume that the fluorides are kept together by covalent electron pair bonds, the Xe atom in the difluoride has five electron pairs in the valence shell, the Xe atom in the tetrafluoride six, and the Xe atom in the hexafluoride seven. The coordination geometries of XeF_2 and XeF_4 are as predicted by the VSEPR model. The structure of XeF_6 is that of an octahedron slightly deformed as if the seventh, nonbonding electron pair is pointed toward the center of a triangular face. Comparison with the I–F bond distances and bond energies in the hypervalent iodine fluorides show that the Xe–F bonds are about 10 pm shorter and about 50% weaker.

The coordination geometry of xenon tetraoxide is tetrahedral. The mean bond energy is 88 kJ mol^{-1} [80]. The low bond energy would seem to exclude double bonding and we propose a Lewis structure with eight electrons in the valence shell of the Xe atom and single electron pair bonds to each O atom. Since minimum-energy cleavage of the XeO bonds would proceed heterolytically to yield electrically uncharged atoms or XeO_n fragments, this Lewis structure implies that the single Xe–O bonds should be described as dative rather than covalent (see Sect. 7).

9.5 Nitrogen Oxides and Related Compounds

The reader may recall that two of the four molecules that Lewis referred to as having an odd number of electrons were NO and NO_2. In order to facilitate discussion of the bonding in these and related molecules, we begin by establishing benchmark values for bond distances and bond energies for N–N and N–O single bonds and for N=O double bonds. These were taken hydrazine, hydroxylamine, and nitrosyl oxide, respectively (see Fig. 22). The number of electrons in the NO molecule is one more than in N_2. The bond energy 189 kJ mol^{-1} is higher than our reference value for an N=O double bond, but 313 kJ mol^{-1} lower than the dissociation energy of the N_2 molecule. We therefore place the unpaired electron

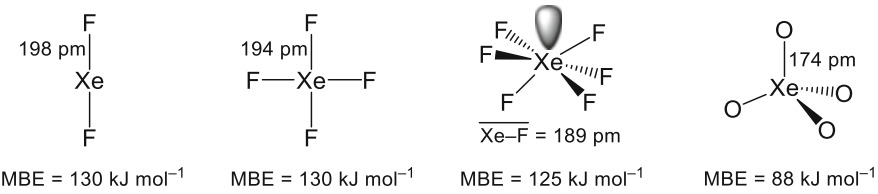

Fig. 21 The gas-phase structures of hypervalent compounds of xenon

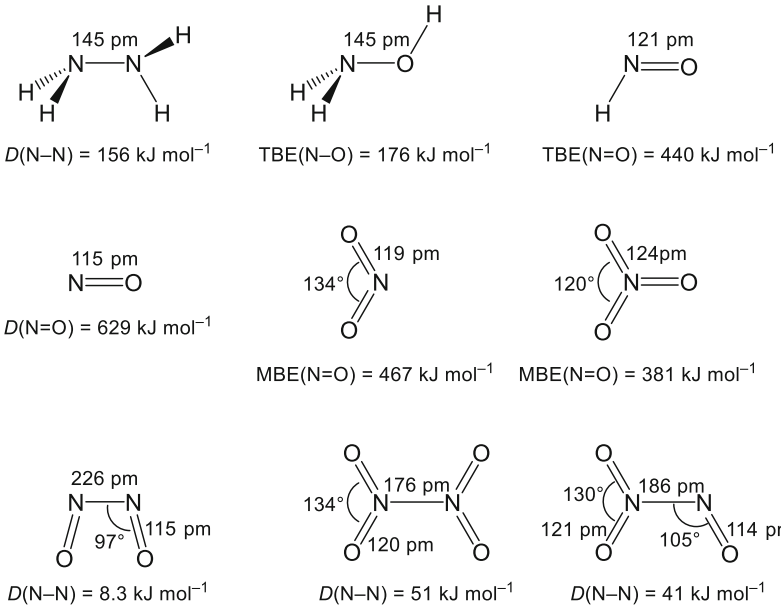

Fig. 22 *Upper row*: Bond distances and bond energies in prototype molecules with N–N and N–O single bonds and double N=O bonds. *Middle row*: Bond distances and NO bond energies in the three mononitrogen oxides. *Lower row*: Bond distances and N–N bond dissociation energies of three gaseous dinitrogen oxides

between the two nuclei and describe the NO bond as a 2½ bond. The NO bond distance is consistent with this description. If each of the two atoms is assigned two nonbonding electron pairs, the N atom contains nine electrons in the valence shell.

The structure of nitrogen dioxide is angular and the NO bond distance and bond energy are both close to our reference values for a double NO bond. According to Lewis' electron pair model, two electron pairs should then be placed between the N and each oxygen atom. If each O atom also carries two nonbonding electron pairs, the N atom is left with a single nonbonding electron. As in the NO molecule, the N atom has nine electrons in the valence shell.

The nitrogen trioxide molecule has never been isolated, but it has been generated in the gas phase and is sufficiently stable for the structure to be determined. The molecule is trigonal planar. The mean bond energy is 59 kJ mol^{-1} lower than the

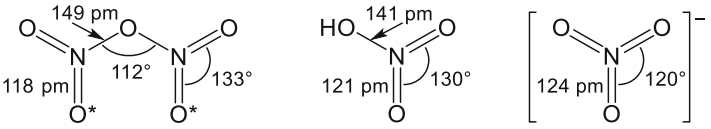

Fig. 23 The gas-phase structures of the dinitrogen pentoxide, nitric acid, dinitrogen oxide, and the structure of the nitrate anion determine by an X-ray diffraction study of the salt $[ONO]^+[NO_3]^-$

reference value for a double bond, but 205 kJ mol^{-1} higher than the reference value for a single bond. We therefore classify the three NO bonds as double bonds. This means that the central N atom has 12 electrons in the valence shell. Two oxygen atoms carry four nonbonding electrons while the third carries only three.

At low temperature, both nitrogen monoxide and nitrogen dioxide form crystalline NN bonded dimers. A mixed dimer, N_2O_3, has also been prepared. Evaporation yield mixtures of associated and unassociated species, and the structures of both monomers and dimers have determined by spectroscopic techniques.

All the dimers have planar structures. Both NO bond distances and ONO valence angles are very similar to those in the monomers. It is very easy to draw satisfactory Lewis structures for dimers where the unpaired electron on each monomer is used to form a single N–N bond. What surprises are the length and weakness of these bonds; the NN bond distance in N_2O_2 is 226 pm, in N_2O_4 it is 176 pm, and in N_2O_3 it is 186 pm. The energy of dissociation to monomers is 8.3 kJ mol^{-1} for N_2O_2, 51 kJ mol^{-1} for N_2O_4, and 41 kJ mol^{-1} for N_2O_3. The question "Why are the odd-electron molecules NO and NO_2 so stable?" has been transformed into another "Why are the single NN bonds in the dimers N_2O_2 and N_2O_4 so weak?" But we are no closer to a simple answer, and if there was one, it would probably have been articulated by now.

Gaseous N_2O_5 molecules consist of two planar NO_3 fragments joined by a common O atom. The NO_2 groups are however rotated some 30° out of the plane of the paper, presumably due to steric repulsion between the two O atoms marked by asterisks (see Fig. 23). Comparison of the terminal NO bond distances with our reference values in Fig. 22 clearly indicates that these bonds are double while the NO bonds to the central O atom are single. The energy of atomization calculated from thermochemical data is consistent with this view: The atomization energy calculated by the summation of the reference bond energies from Fig. 22 yields an atomization energy of 2,112 kJ mol^{-1}, only 2.5% below the thermochemical value. Following Lewis, we place two electron pairs between each N atom and the two terminal O atoms and one-electron pair between each N atom and the bridging O atom. If we assign two nonbonding electron pairs at each O, all electrons are accounted for. The number of electron pairs around N is *five*.

The bond distances and valence angles in the gaseous nitric acid molecule are clearly similar to those in the anhydride N_2O_5, and the enthalpy of atomization calculated from the reference bond energies in Fig. 22 plus the mean OH bond energy in H_2O reproduces the thermochemical value to within 2.8%. The best

Lewis structure is analogous to that of the anhydride, and the number of electron pairs around N is again *five*.

The bond distance in the trigonal planar nitrate ion is equal to the bond distance in NO_3 and slightly longer than the N=O double bonds in N_2O_5 or HNO_3.

The nitrate ion is stable in the gas phase, and Jenkins and Morris have determined its standard enthalpy of formation by combining the standard enthalpies of formation of the ionic crystals MNO_3, M=Li, Na, K, Rb, and Cs, with the results of elaborate lattice energy calculations: $\Delta H_f^0\left[NO_3^-(g)\right] = -320$ kJ mol^{-1} [81]. The mean N=O bond energy in the anion calculated as one third of the energy of the reaction

$$NO_3^-(g) = N(g) + 2O(g) + O^-(g),$$

is 413 kJ mol^{-1} or only 6% below the reference value for a N=O double bond. If we in consequence place two electron pairs between the N and each O atom, the former has *six* electron pairs in its valence shell.

9.6 d-*Orbitals or Not: Ab Initio Calculations and Electron Density Studies*

When the trigonal bipyramidal structures of PF_5 and PCl_5 and the octahedral structure of SF_6 were first established, the structures were commonly rationalized in terms of $sp^3d_z^2$ or sp^3d^2 hybridization of the central atoms [82]. There was, however, some doubt as to whether the outer presumably very diffuse *d*-orbitals were suitable for bond formation. An alternative description of the bonding in the phosphorus pentahalides in terms of three-center four-electron bonds avoided the use of *d*-orbitals: The P atom was assumed to be sp^2 hybridized and these hybrids were used to form normal two-center covalent bonds to the equatorial halogen atoms. The unhybridized p_z-orbital on the central atom was then combined with the p_z-orbitals of the two axial halogen atoms to form one bonding 3-center orbital, one nonbonding orbital centered on the halogen atoms, and one antibonding 3-center orbital. The bonding and the nonbonding orbitals were filled by two electrons each [83]. This scheme suggests that the two axial P–X bonds should be longer and weaker than the equatorial and that the axial halogen atoms should carry a larger net negative charge. Since this 3*c*-4*e* model confines one of the five valence electron pairs to the axial substituents, it appeared to be in better agreement with "the rule of eight." Bonding in SF_6 could be rationalized in a similar manner with two nonbonding electron pairs confined to the fluorine atoms.

Two important articles published in 1990 appeared to settle the discussion about the two alternative bonding models in favor of the 3*c*-4*e* model [84, 85]. Magnusson published the results of HF calculation on about 50 hypervalent or closely related Lewis-valent molecules using a double-z quality basis set including polarization

functions. The importance of the *d*-orbitals was assessed by their effect on the calculated electronic energies of both hypervalent compounds like PF_5 and SF_6 and Lewis-valent compounds like PF_3 and SF_2. The energy improvement per bond was found to be small in both cases, and *d*-orbitals added to the peripheral F atoms produced just as large energy improvement. Magnusson concluded that *d*-orbital contributions were small and that they acted as polarization functions allowing *s*- and *p*-orbitals to adjust to "the rapidly varying molecular potential in the space between the nuclei" [84]. Reed and Ragué von Schleyer studied of about sixty related molecules, many of them carrying doubly bonded oxygen atoms, and concluded that sp^3d or sp^3d^2 models were "inaccurate and misleading" [85].

Yet the properties (bond distances and bond energies) of hypervalent compounds are consistent with Lewis structures with five or six bonding electron pairs in the valence shell of the central atoms. What is the source of this discrepancy? The wavefunctions obtained by such ab initio calculations do not constitute exact solutions to the Schödinger equation and molecular orbitals; orbital energies and population parameters are nonobservable quantities that cannot be checked by experiment.

The total electron density in a molecule is, however, observable and may be examined by topological analysis. Molina and Dobado have carried out the topological analysis of the calculated electron densities of several related Lewis- and hypervalent molecules using the QTAIM approach [86]. Comparison of the electron densities at the bond critical points, their Laplacians, ellipticities, curvatures, and electronic energy densities indicate that the axial and equatorial bonds in PF_5 are very similar to one another as well as to the P–F bonds in the Lewis-valent compound PF_3. Similarly, the topological parameters of SF_6 (except the ellipticities which are determined by the symmetry) were close to those of SF_2. There appeared to be little difference between the bonds in related hypervalent and Lewis-valent molecules.

Noury, Silvi, and Gillespie[87] have studied the calculated electron densities in hypervalent molecules AX_5, with A=P or As and X=F, Cl, or methyl, using the topological analysis of the electron localization function *ELF* [88]. This topological analysis divides the space around each nucleus into a core basin containing all inner shell electrons, and several basins containing the electron lone pairs or bond pairs in the valence shell much like the domains envisaged in the VSEPR model. The charge within each basin ("the number of electrons") can be determined by integration. The central atoms in the pentavalent compounds studied by Silvi and coworkers carry no lone pairs, so the number of electrons in the valence shell (N_A) was determined by adding up the charges of the five A–X bond basins. For PMe_5 (which does not appear to exist), the calculated number of electrons in the valence shell of P was 9.42. The number of electrons in the valence shell was found to decrease strongly with increasing electronegativity of the ligating atoms: For PCl_5 the number is 7.13, and for PF_5 the number is 5.33. For $AsMe_5$ (which does exist) the number is $N_{As} = 9.68$, close to 10, the number expected if the central atom forms five nonpolar covalent single electron-pair bonds [87].

Tellurium, like arsenic, has an electronegativity coefficient very close to that of carbon. The hexamethyl derivative exists and is reasonably stable. *ELF* analysis of calculated electron densities indicates that the number of electrons in the valence shell of the Te atom is $N_{Te} = 11.10$, reasonably close to the value expected for six covalent single bonds. Silvi and coworkers concluded that "bonds in hypervalent compounds are not significantly different from the bonds in the corresponding non-hypervalent molecules." "The octet rule remains a useful rule for beginning students as an aid for writing Lewis structures provided it is recognized that there are many exceptions." And there the matter rests, at least for the time being!

10 Concluding Remarks

10.1 Electron Pairs and Electron Octets

Lewis' postulate that "an atom [in a molecule] tends to hold an even number of electrons in the [valence] shell" has been abundantly confirmed for main-group element compounds during the past century. Over the years a large number of unstable radicals have been generated and characterized, but the number of robust main-group element molecules with an odd number of electrons is still largely limited to two nitrogen oxides, NO and NO_2, and ClO_2. With the notable exception of the dioxygen molecule, all molecules with an even number of electrons, but with two of them un-paired, are all very unstable.

Langmuir's postulate that "any atom with atomic number less than 20, and with more than 3 electrons in its outside layer tends to take up enough electrons [through bond formation] to complete its octet" remains valid as far as it goes, but should not be allowed to obscure the fact that the elements in Groups 15 to 18 also form numerous covalently bonded, stable compounds with five, six, or more electron pairs in the valence shell of the central atom. If one includes datively bonded electron donor–acceptor complexes like $Cl_3Al[N(CH_3)_3]_2$ or F_4SiNH_3; anionic complexes like $[PF_6]^-$, $[SiF_6]^{2-}$, or $[AlF_6]^{3-}$; or coordination complexes like aluminum tris(acetylacetonate), the number of stable molecular units with more than four electron pairs in the valence shell of the central atom increases manifold. "The rule of eight" may be mentioned as a useful rule of thumb, but it should at the same time be made clear that there are numerous exceptions!

Acknowledgments We are grateful to Dr. Cina Foroutan-Nejad, Masaryk University (Brno), for allowing us to publish some of the results of his extensive calculations on the dihalides of the Group 2 and 12 metals and to Professor G. V. Girichev, Ivanovo State University of Chemistry and Technology, and Professor Pavel Karen, the University of Oslo, for helping us find relevant data on thermochemical properties or crystal structures.

References

1. Mingos DMP. Historical account of the development of the chemical bond. Struct Bond. doi:10.1007/430_2015_203
2. Lewis GN (1916) J Am Chem Soc 38:762–785
3. Kossel W (1916) Ann Physik 354:229–362
4. Langmuir I (1919) J Am Chem Soc 41:868–934
5. Brock WH (1992) The Fontana history of chemistry. Fontana Press, London, p 477
6. Lewis GN (1923)Valence and the structure of atoms and molecules. American chemical society monograph series, New York, pp 97–98, 101–103
7. Bragg WL (1913) Proc R Soc A 39:248–276
8. Born M (1923) Atomtheori des Festen Zustandes. Teubner, Leipzig
9. Born M, Landé A (1918) Ver Deut Phys Ges 20:210–216
10. Madelung E (1918) Physik Zeit 19:524
11. Sherman J (1932) Chem Revs 11:93–170
12. Huber KP, Herzberg G (1979) Molecular spectra and molecular structure, vol 4. Constants of diatomic molecules. Van Nostrand, New York
13. Rittner ES (1951) J Chem Phys 19:1030–1036
14. Hati S, Datta B, Datta D (1996) J Phys Chem 100:19808–19811
15. Haaland A (2008) Molecules and models. Oxford University Press, Oxford
16. Donald KJ, Hoffmann R (2006) J Am Chem Soc 128:11236–11249
17. Donald KJ, Hargittai M, Hoffmann R (2009) Chem Eur J 15:158–177
18. Bragg WL (1914) Proc R Soc Lond A 89:468–489
19. Buckley HE, Vernon WS (1925) Phil Mag 49:945–951
20. Ghalsasi P, Ghalsasi PS (2011) Inorg Chem 50:86–89
21. Morris DFC (1957) J Inorg Nucl Chem 4:8–12
22. Biltz WW, Klemm W (1926) Zeitschr Anorg Allg Chem 152:267–294
23. Ohmae K, Kuroda T (1968) Electrochem Soc Jpn 36:163–169
24. Grantham LF, Yosim SJ (1966) J Chem Phys 45:1192–1198
25. Redkin AA, Nikolaeva EV, Dedyukhin AE, Zaikov YP (2012) Ionics 18:255–265
26. Zeidler A, Salmon PS, Martin RA, Usuki T, Mason PE, Cuello GC, Kohara S, Fischer HE (2010) Phys Rev. B 82:104208–104208
27. Wharton L, Berg RA, Klemperer W (1963) J Chem Phys 39:2023–2031
28. Büchler A, Staufler JL, Klemperer W (1964) J Am Chem Soc 86:4544–4550
29. Hargittai M (2000) Chem Rev 100:2233–2301
30. NIST-JANAF Thermochemical tables – NIST chemical kinetics database, http://kinetics.nist.gov/janaf
31. Barin I (1989) Thermochemical data of pure substances, Pars I and II. VCH Publishers, Weinheim
32. Russian Education Resources Information Center: Electronic Database XuMuK (in Russian) http://www.xumuk.ru/
33. Frisch MJ, Trucks GW, Schlegel HB, Scuseria GE, Robb MA, Cheeseman JR, Scalmani G, Barone V, Mennucci B, Petersson GA, Nakatsuji H, Caricato M, Li X, Hratchian HP, Izmaylov AF, Bloino J, Zheng G, Sonnenberg DJ, Hada M, Ehara M, Toyota K, Fukuda R, Hasegawa J, Ishida M, Nakajima T, Honda Y, Kitao O, Nakai H, Vreven T, Montgomery JAJ, Peralta JE, Ogliaro F, Bearpark M, Heyd JJ, Brothers E, Kudin KN, Staroverov VN, Kobayashi R, Normand J, Raghavachari K, Rendell A, Burant JC, Iyengar SS, Tomasi J, Cossi M, Rega N, Millam NJ, Klene M, Knox JE, Cross JB, Bakken V, Adamo C, Jaramillo J, Gomperts R, Stratmann RE, Yazyev O, Austin AJ, Cammi R, Pomelli C, Ochterski JW, Martin RL, Morokuma K, Zakrzewski VG, Voth GA, Salvador P, Dannenberg JJ, Dapprich S, Daniels AD, Farkas Ö, Foresman JB, Ortiz JV, Cioslowski J, Fox DJ (2009) Gaussian 09 Revision A2. Gaussian, Wallingford
34. Cioslowsky J (1989) J Am Chem Soc 111:8333–8336

35. Landé A (1920) Zeitschrift für Physik 1:11–197
36. Wasastjerna JA (1923) Comm Phys Math Soc Sci Fenn 1:1–25
37. Pauling L (1939) The nature of the chemical bond, 1st edn. Cornell University Press, Ithaca. 2nd edn 1940
38. Pauling L (1927) Proc R Soc Lond A114:181–211
39. Slater JC (1930) Phys Rev 36:5–64
40. Shannon RD (1976) Acta Cryst A32:751–767
41. Witte H, Wölfel E (1955) Z Phys Chem 3:296–329
42. Schoknecht G, Naturf Z (1957) 12a:983–996
43. Bader RFW (1990) Atoms in molecules – a quantum theory. Oxford University Press, Oxford
44. Perrin CL (1991) J Am Chem Soc 113:2865–2868
45. Tsirelson VG, Avilov AS, Lepeshov GG, Kulygin AK, Stahn J, Pietsch U, Spence JCH, Phys J (2001) Chem B 105:5068–5074
46. Langmuir I (1919) J Am Chem Soc 41:129
47. Pauling L (1932) J Am Chem Soc 54:3570–3582
48. Bichowsky FR, Rossini FD (1936) The thermochemistry of the chemical substances. Reinhold Publishing Company, New York
49. Allred AL (1961) J Inorg Nucl Chem 17:215–221
50. Pauling L (1947) J Am Chem Soc 69:532–553
51. Allred AL, Rochow EG (1958) J Inorg Nucl Chem 5:264–268
52. Allen LC (1989) J Am Chem Soc 111:9003–9014
53. Bragg WH, Bragg WL (1913) Proc R Soc 89A:277–291
54. Brock WH (1992) The Fontana history of chemistry. Fontana Press, London, pp 258–261
55. Huggins ML (1926) Phys Rev 28:1086–1107
56. Pauling L, Huggins ML (1934) Z Krist 37:205–238
57. Mark H, Wierl R (1930) Naturwissenschaften 18:205
58. Schomaker V, Stevenson DP (1941) J Am Chem Soc 63:38–40
59. Heitler W, London F (1927) Z Physik 44:455–472
60. Pauling L (1931) J Am Chem Soc 53:1367–1400
61. Slater JC (1931) Phys Rev 37:481–489
62. Sidgwick NV, Powell HM (1940) Proc R Soc Lond A 176:153–180
63. Gillespie RJ, Nyholm RS (1957) Quart Rev Chem Soc 11:339–380
64. Gillespie RJ, Hargittai I (1991) The VSEPR model of molecular geometry. Allyn and Bacon, Boston
65. Haaland A (2008) Molecules and models. Oxford University Press, Oxford, pp 205–206
66. Haaland A, Green JC, McGrady GS, Downs AJ, Gullo E, Lyall MJ, Timberlake J, Tutukin AV, Volden HV, Østby K-A (2003) Dalton Trans 4356–4366
67. Sidgwick NV (1927) The electronic theory of valency. Oxford University Press, Oxford, pp 178–179
68. Pauling L (1960) The nature of the chemical bond, 3rd edn. Cornell University Press, Ithaca
69. Kaufman GB (1981) Inorganic coordination compounds. Heyden and Son Ltd., London, p 3
70. Haaland A (1989) Angew Chem Int Ed Engl 28:992–1007
71. Østby K-A, Haaland A, Gundersen G, Nöth H (2005) Organometallics 24:5318–5328
72. Jenkins HDB (1980) The standard enthalpy of formation of $[GaCl_4]^-$(g) is –1028 kJ mol^{-1}. Lattice energies. In: CHR handbook of chemistry and physics, CRC, Boca Roca; quoted by Dasent WE (1982) Inorganic energetics, 2nd edn. Cambridge University Press, Cambridge, p 80
73. Moore CE (1949) Atomic energy levels, vols 1–3. National Bureau of Standards, Circular 467, Washington
74. Hildenbrand DL (1996) J Chem Phys 105:10507–10510
75. Hansen N, Maeder H, Temps F (2001) Phys Chem Chem Phys 3:50–55
76. Hartley SB, McCoubrey JC (1963) Nature 198:476

77. Glushko VP ed (1978) Thermodynamic properties of specific substances. NAUP Publishers, Moscow
78. Stefanovich EV, Boldyrev AI, Truong TN, Simons J (1998) J Phys Chem B 102:4205
79. Martin JML (2006) J Mol Struct 771:19–26
80. Gunn SR (1965) J Am Chem Soc 87:2290–2291
81. Jenkins HDB, Morris DFC (1977) Phil Mag 35:1091–1097
82. Pauling L (1960) The nature of the chemical bond, 3rd edn. Cornell University Press, Ithaca, pp 147–153, 177–179
83. Rundle RE (1963) J Am Chem Soc 85:112–113
84. Magnusson E (1990) J Am Chem Soc 112:7940–7951
85. Reed AL, von Ragué Schleyer P, Am J (1990) Chem Soc 112:1434–1445
86. Molina JM, Dobado JA (2001) Theor Chem Acc 105:328–337
87. Noury S, Silva B, Gillespie RJ (2002) Inorg Chem 41:2164–2172
88. Becke AD, Edgecomb KE (1990) J Chem Phys 92:5397–5403

Struct Bond (2016) 170: 71–118
DOI: 10.1007/430_2015_197

Published online: 20 January 2016

Quantum Chemical Topology

Paul L.A. Popelier

Abstract In this frank and thought-provoking account, quantum chemical topology (QCT) is explained to the novice, leading up highlights of QCT's most recent findings and views. The difference between a topological atom and a quantum atom is explained. After some philosophical insights and historical material, equations start appearing in the second half, in order to explain topological energy partitioning. Special attention was paid to the clarity and completeness of these equations. This QCT approach is proposed as a minimal and reference-state-free method to interpret chemical bonding. The link between bond order and interatomic exchange energy is explicitly given and uses a multipole expansion. These two quantities are illustrated with quite a few numerical examples and the trends amongst them. Finally, the Laplacian of the electron density is briefly expounded, focusing on the so-called L-graph and how they heuristically support the Lewis pair model.

Keywords Bond order • Electron density • IQA • Laplacian • L-graph • Quantum atom • Quantum theory of atoms in molecules (QTAIM) • Topological atom

Contents

P.L.A. Popelier (✉)
Manchester Institute of Biotechnology (MIB), 131 Princess Street, Manchester M1 7DN, UK

School of Chemistry, University of Manchester, Oxford Road, Manchester M13 9PL, UK
e-mail: pla@manchester.ac.uk

Abbreviations

BCP	Bond critical point
cc-pVDZ	Correlation-consistent polarised valence-only double zeta
CCSD	Coupled-cluster singles and doubles
CISD	Configuration interaction single and double (excitation)
DFT	Density functional theory
DI	Delocalisation index
DMA	Distributed multipole analysis
EDA	Energy decomposition analysis
ELF	Electron localisation function
HF	Hartree–Fock
IQA	Interacting Quantum Atoms
MP2	Møller-Plesset second-order
QCISD	Quadratic configuration interaction single and double (excitation)
QCT	Quantum chemical topology
QCTFF	Quantum chemical topological force field
QTAIM	Quantum theory of atoms in molecules
SCF–MO–LCAO	Self-consistent field–molecular orbital–linear combination of atomic orbitals
VSEPR	Valence shell electron pair repulsion

1 Chemical Bonding Is Alive

This chapter is written as a collection of short sections, each built around a thought or an issue, or focusing on explaining one idea or fact. The number of equations in the current chapter has been deliberately suppressed unless where a verbal description alone would obfuscate the content. This decision did not apply to other chapters by the author's hand, that is, one chapter [1] containing a historical account of the development of the quantum theory of atoms in molecules (QTAIM) [2] and new didactic material, a very recent chapter [3] with refreshing and provocative philosophy, as well as an older, lengthy and dense chapter [4], written as an essay-like

critique but containing new results. Interested readers can always consult these other chapters for more detail.

Chemical bonding is a topic that is as alive today as it was a hundred years ago. One can debate if one should be sad or cheerful by this state of affairs. Let us start by thinking about why one could be cheerful. The continued interest in understanding chemical bonding brings joy because it means that chemistry is alive as a science. Chemistry makes an ever growing number of observations, of ever increasing quality, about the world of matter in broadly ambient conditions. Even better: Chemistry creates new worlds of matter, worlds in which it then makes new observations. In that sense, chemistry is a more complex science than Newtonian mechanics or equilibrium thermodynamics, for example. Those branches of science are mature and stable in that their principles and structure are established and provoke no further argument. However, in chemistry matters are different: an absolutely tiny fraction of all possible molecules has ever been synthesised (or calculated by ab initio methods, for that matter), and new bonding patterns may emerge. Moreover, new compounds and materials continue to appear, and some already defy the orthodox view on bonding. Examples come out on a regular basis in popularising magazines such as *Chemistry World* or *Chemical and Engineering News*. This continuous challenge to existing chemical bonding theory has been there for a long time, as can be deduced from utterances such as Coulson's "A chemical bond is not a real thing" (pp. 20–21 in [5]) or Pauling's admission of the ambiguities caused by his tautological "definition" of the chemical bond. Debates on the nature of the chemical bond keep being fuelled by new findings such as the emergence of boranes, noble gas compounds and more recent case studies such as beryllium bonds [6], quadruple bonding [7] in C_2, the "super van der Waals" interactions that are aurophilic bonds [8], boron–boron multiple bonding [9] and the first Be–B bond [10], to name a few. Even the hydrogen bond, supposedly a robust edifice of chemical bonding, was very recently redefined at IUPAC level [11]. The chemical bond is even more in flux than the aforementioned cases suggest: it all depends on one's starting point. These debates occur within the relative safety of the Born–Oppenheimer approximation, which actually allows chemistry to exist the way we learnt it. However, when this (robust) approximation breaks down [12] in experiments with dynamic control of quantum states, then a new vision of chemistry is warranted. Traditionally, molecules are seen as static entities, with an unambiguous architecture that is only "wiggled and jiggled" by thermal motion. However, ultrafast spectroscopies undermine this picture of a bond stretching around a well-defined equilibrium length. Finally, we observe that, during the last decade or so, large parts of chemistry have moved away from the single molecule to the molecular assembly (with the exception of analytical and spectroscopic techniques), as witnessed by the contemporary style of articles in the *Journal of the American Chemical Society*, for example. All this points towards

chemistry being far from closed as a science,[1] and the more types of species it studies, the more it demands a lucid and all-encompassing explanation for why they exist.

Now let us think about why one could be sad about the current state of affairs in which chemical bonding theory still being alive today. What is deplorable is that debates never seem to settle in favour of one solution or the other. The vigour[2] with which these debates are conducted makes the interested reader anticipate a clear conclusion in favour of one view or the other. Instead, the debates then fizzle out in an eerie compromise or rather status quo, which allows the contradictory views to coexist. Even if a debate reignites, it again leaves behind an unhappy coexistence of contradictions. Some scientists celebrate this situation, seeing this as a signature of richness, but of course in Newtonian mechanics an unresolved contradiction would be devastating. One cannot send a person to the moon successfully if the "option" $F = ma^2$ were used, instead of the "other option" $F = ma$, with which it would happily coexist. In chemistry, however, which appears to be different kind of science, a final and fully successful interpretation is still lacking. This chapter suggests that a potential candidate for that purpose is in the making. In fact, it has been around for a while, but the perspective that it offers needs to be urgently materialised and ideally falsified if possible. As such, there is no need to surrender to the view of Hoffmann that *any rigorous definition of a chemical bond is bound to be impoverishing*. This view causes an attitude allowing discussions to perpetuate without any prospect to ever being resolved. Is chemistry really this hopelessly complicated universe, preventing chemists to ever understand with a minimalistic toolbox? Can no future-proof insight ever be obtained? In this sense it is sad that the issue of chemical bonding is still open. Is this really the fate of interpretative theoretical chemistry? Is it incorrect to insist that one interpretation is wrong and the other is not?

The reader may point the finger at the text above, which appears to support the "contradiction" that one should be both sad and cheerful about the current state of affairs of chemical bonding. There is no contradiction when one carefully distinguishes two matters: the excitement of discovering new species (experimentally or computationally) and the way one conducts science. The qualifier "cheerful" refers to this excitement, while "sad" refers to the elusiveness of a clear and robust interpretation of chemical bonding. The qualifier "sad" applies even more to the unwillingness of some researchers to even look for this interpretation. It should be possible to do good science while exploring the new worlds that chemistry opens. In other words, armed with a minimal and rigorous method, one should explore bonding in the new worlds that chemistry opens. Perhaps more importantly, one

[1] Embryology, the science of the most marvellous and stunning molecular assembly ever, may well become a branch of Chemistry in a century or so if the current trend continues.

[2] Typically in the shape of "literature mudslinging", where the journal *Angewandte Chemie* appears to offer its services as an arena.

should make predictions with this trustworthy theory of chemical bonding. It appears that this goal has not been reached yet.

2 The Roots of the Chemical Bond

The history of the chemical bond is covered in detail in the chapter of Professor Mingos in this book but in this section we highlight a few ideas that will help the narrative of the current chapter. More than a century before quantum mechanics was established, researchers had already thought hard about the nature of matter (at ambient conditions), in particular how exactly various compounds are built from their constituent elements or atoms. The oldest concept necessary to understand the intuitive thinking behind the chemical bond is that of chemical affinity. Thanks to the work of the Belgian mathematical physicist Théophile de Donder, this concept has a precise definition, formulated within the context of thermodynamics and adopted by IUPAC. Chemical affinity is defined as the negative partial derivative of Gibbs free energy G with respect to extent of reaction ξ at constant pressure and temperature. Chemical affinity is positive for spontaneous reactions. The conceptual and mathematical precision of thermodynamics offers a great opportunity, probably even the best chance, to pinpoint an intuitive driving force behind changing matter. Indeed, in a pre-quantitative version, chemical affinity referred to the tendency of an atom (or compound) to combine with atoms or compounds, by chemical reaction. Later, chemical affinity became related to the *aggregation* or bonding of certain atoms.

This notion that matter can reorganise itself to become something else is very old: already in 1250 the term *affinitas* was used in the sense of a chemical reaction. Although the origin of chemical affinity is not easy to identify, what matters to us is the idea that, at the end of the process of change, the constituents are "happy sitting where they sit". Something attracted the constituents and created a stable aggregate that is held together for a long time. The next challenge is finding a pattern behind this aggregation: what holds the system together? This is a difficult question, which is why it is important to be perspicacious and clear.

Before addressing this key question, there are two important points to make about the nature of energetic stability of an aggregate, which have been discussed in more detail elsewhere [4]. The first point is the distinction between a force (first derivative of energy with respect to displacement) and Hessian (second partial derivatives of energy with respect to displacement). Mathematically the distinction is of course very clear, but verbal (i.e. non-mathematical) discussions can be confusing, in particular when talking about forces of attraction. One should bear in mind that in a stable molecule (i.e. at equilibrium), there are *no* forces on the nuclei. However, during molecular change, the forces on the nuclei are non-vanishing but at the end of this process, these forces do indeed vanish. If one perturbs the nuclear positions away from their equilibrium values, then forces will again emerge: the aggregate is *attractive* and will restore itself to its former equilibrium. The latter statement corresponds to the nature of the Hessian and not

the forces. Its eigenvalue spectrum (positive curvature in each dimension) will reveal that this equilibrium point in the potential energy surface is indeed a minimum. Note that if the aggregate is *compressed* compared to its equilibrium geometry, then *repelling* forces will emerge. Of course, if the aggregate is expanded from its equilibrium, then *attracting* forces will appear. In summary, it is important not to confuse *attracting* and *attractive*. The latter qualifier refers to the positive curvature in the potential energy surface at equilibrium; it is the signature of stability. The former qualifier refers to the process of formation, but again, the forces can be attracting or repelling and therefore cannot be used on their own to characterise if an aggregate is stable, let alone why. This apparently pedantic point can be the source of futile debates on chemical bonding, which is why it is raised here.

The second point is the reason for a molecular aggregate's stability, which can again fuel endless discussions. Chemists will agree that understanding follows from partitioning of the aggregate, most likely to atomic resolution. A bone of contention is *how* to partition exactly, and we have made a choice in this chapter. A second related sticking point is how to use this partitioned information. Inevitably, a molecule's stability is a *compromise* between opposing forces on all nuclei. These forces literally add up to a total of zero on each nucleus. Taking one force in isolation would lead to a different equilibrium geometry.

Alternatively, many chemists single out a few atoms in a system and ascribe the behaviour of the total system to the behaviour of these few atoms. For example, the stability of the global minimum geometry of the water dimer is ascribed to the O–H. . .O hydrogen bond. Even bolder, the energy stability of about 20 kJ/mol is ascribed to this hydrogen bond alone. Should not *all* atom–atom interactions be considered? Why does one ignore the changes, from monomer to complex, in the mono-atomic energies? While this view of hydrogen bonding may appear straightforward and innocent, it needs to be scrutinised by linking it rigorously to the underlying quantum mechanics. It has been known for decades that the stability of nucleic acid base pairs (guanine. . .cytosine versus adenine. . .thymine) cannot be explained by counting hydrogen bonds alone, although textbooks still hold on to this fallacy. The so-called secondary interaction hypothesis [13] addresses the cause of base pair stability by introducing interactions beyond hydrogen bonding. However, even this hypothesis cannot be justified [14] in the light of rigorous electrostatics. Another contentious example is the cause of the planar-to-non-planar torsional energy barrier in biphenyl: is it caused by a steric clash of the bay hydrogen atoms? We have accumulated unpublished evidence that this explanation is not correct, as confirmed by work of others [15].

Returning to the key question of the reason for the stability of aggregates, the 1850s saw the concept of valence as an important stepping stone. Frankland was one of the first to publish that the atoms of each elementary substance have a definite saturation capacity. As a result, the atoms can only combine with a certain limited number of the atoms of other elements. The subsequent theory of valency laid the foundations upon which modern structural chemistry rests. The combining power or affinity of an atom of an element was determined by the number of

hydrogen atoms that it combined with. In 1858 Couper visualised these relationships using dotted lines or dashes between the atoms in his formulae, thereby approximating the appearance of later formula styles, such as the Lewis diagram.

At this stage an important issue needs to be elucidated, usually ignored in textbooks, but one that helps clarifying why Lewis diagrams can run into trouble in their attempt to describe a bonding pattern, such as that of boranes. The cause of this trouble lies in the fact that valence is an atom-centred concept. An atom *A* is seen as a central object, which engages (i.e. bonds) with a number of objects around it. These objects are other atoms (elements), which act as ligands to the central atom. Although apparently sensible, this view puts the spotlight only on the interactions between the central atom and its ligands; the interactions between the ligands are ignored. The question is now whether this is safe. How do we know if the stability of the whole molecule should be ascribed to the stability of the interactions (i.e. bonds) between the central atom and its ligands only? In Sect. 12 on interatomic exchange energies in some simple molecules, we will return to this point with an example, after the methodology of quantum chemical topology (QCT) has been explained.

3 Lewis

In 1923 a prescient Faraday Discussion meeting took place, entitled "The electronic theory of valency". It was attended by Thomson (who discovered the electron), Sidgwick (a pioneer of the VSEPR model) and Lewis (proponent of the electron pair). It took more than 80 years before the next Faraday Discussion meeting [16] was held (Manchester, Great Britain, 2006) on a topic with overlapping content. The participants in 1923 discussed issues that are so commonplace and fundamental to chemistry, that one may forget they ever inspired debate. Remarkably, or perhaps not, they did so *before* the concept of the quantum spin had been proposed (in 1925). It is almost heartbreaking to see Lewis struggle to understand the chemical bond with phrases like "When two molecules (...) combine with one another, it is as though the two previously unpaired electrons were clamped together by some powerful mechanism. Quantum theory, so far as it has been developed hitherto, offers no interpretation of this fact, unless it is to be found in the very recent work of Sommerfeld in connection with his inner quantum number".

Here Lewis was trying to find a rigorous link between his own (correct) chemical intuition and physics. Such reconciliation of the physical and the chemical world is vital for the health of science. After all, nature does not care about the way science is organised by humans. While appreciating that we live in one world only it makes sense to construct a consistent and coherent picture of nature, cutting across the scientific disciplines. Unfortunately, research aiming to reconcile quantum mechanics and structural chemistry has met with variable success: too many debates are still open. This is partly due to the dislocation between mathematical simplicity and computational convenience on one hand, and conceptual intuition on the other.

Indeed, chemists think of atoms as the building blocks of molecules (and their assemblies), whereas the physically rooted Schrödinger equation thinks of molecules in terms of electrons and nuclei. Another example of such dislocation is the computationally convenient molecular orbital theory versus the chemically more intuitive valence bond theory. In this chapter we will introduce QCT, starting with QTAIM [2, 17, 18]. This theory will serve as a tool to bridge the gap between the numerical emptiness of modern wave functions and the wealth of chemical concepts. In an ideal world, chemical insight can indeed be safely extracted from modern wave functions. If this extraction persistently fails for a chemical concept such as aromaticity, for example, then the concept should be modified or abandoned.

Lewis was so convinced about the existence of the electron pair that he worried that the Coulomb law might not hold at atomic scale. In his famous 1916 paper [19], which reads as a stream of consciousness and lacks any mathematical formula while bearing the grand title *The Atom and the Molecule*, Lewis literally states that "Indeed it is evident that just as we have the law of universal attraction between particles at great distances, so *at small distances* we have the equally universal *law of repulsion*". He then muses about the then recent theory of Parson, which was built on the fundamental assumption that an electron is not merely a small charge but also a small magnet. Assuming therefore the existence of magnetic as well as electric forces between the different parts of the atom, Parson came to the conclusion that the most stable condition for the atomic shell is the one in which eight electrons are held at the corners of a cube. As always, great papers are inspired by lesser known work and draw much of their strength by enunciating, more clearly than anything before, what has been in the air before, or drawing it to its full conclusion. The other great inspiration to Lewis was the law of valence and countervalence of the Prussian chemist Richard Abegg, who formulated it a dozen years before Lewis's 1916 paper. Lewis used Abegg's rule as a basis for his theory of the cubical atom, which led to the octet rule.

Of course we now know that Coulomb's law does hold at very small distances but its effect is swamped by another effect that is an order of magnitude stronger and due to interacting quantum spins. The electrostatic repulsion between two electrons creates a Coulomb hole around each electron but the much stronger Fermi hole is caused by interaction between same-spin electrons: the closer in space that two same-spin electrons are, at any one time, the lower the probability of this event, reaching zero if the electrons occupy the same point. In principle, the Fermi hole offers a mechanism to create electron pairing but in a "passive way": a given α-spin electron will avoid another α-spin electron, while a β-electron will not feel the presence of this α-spin electron. As a result, there is a high probability of an α-spin electron being near to a β-spin electron. However, in the spirit of Lewis' wish of reconciliation, we should ask how the existence of electron pairs can be safely deduced from modern wave functions [20].

To end this brief section on Lewis, a note on his life. It appears that this book is primarily dedicated to Lewis's work. It is no coincidence that this book's publication timing of 2016 is exactly a century after that of Lewis's famous 1916 paper, which was not written earlier because Lewis worried about the exceptions to his

rule. Ironically, Langmuir with whom Lewis had a long rivalry now appears to take second stage in expositions on chemical bonding. If one looks up the name Lewis in a popular undergraduate textbook on general chemistry (e.g. Zumdahl's *Chemical Principles*), then the index returns several hits, including entries on Lewis structures, Lewis acids and bases and Lewis himself. Yet, at the time, Langmuir was socially more successful than Lewis, being awarded a Nobel Prize, for example (although Lewis had been nominated 35 times). Moreover, matters ended tragically for Lewis. One day, deadly fumes from his experiment with liquid hydrogen cyanide (HC≡N) had leaked into the laboratory. In spite of the coroner's report, some believe that it may have been a suicide. Whatever his depressed state of mind,[3] Lewis, being a deep and principled thinker, but perhaps too inflexible socially, emerges vindicated today, through the power and quality of his views.

4 The Electron Density

The first quantitatively successful formalism of quantum mechanics was Heisenberg's matrix mechanics. Although predictive, it was very cumbersome to do calculations with. Fortunately, a new formalism was invented soon afterwards, which was more practical, more intuitive, but, perhaps most importantly, computationally superior when applied to atomic physics and later chemistry. This newer version of quantum mechanics was invented by Schrödinger in response to Debije's call to finally see an equation matching all the talk about the wave nature of matter (as demonstrated by De Broglie). Ironically, the wave function, which is at the heart of this approach, is not intuitive when describing more than one particle. This is actually a consequence of the introduction of generalised coordinates, which assign a three-dimensional space to each particle. They feature in Hamiltonian mechanics, a formalism adopted by Schrödinger while constructing his immensely powerful equation. However, the origin of generalised coordinates lies in classical mechanics, in particular, the study of the rigid body dynamics of multibody systems. Generalised coordinates uniquely define a system's configuration relative to a reference configuration. When properly tailored to the problem at hand, they may simplify the equations of motion. Having said that, in quantum mechanics, a heavy price has been paid for transplanting generalised coordinates from classical mechanics to quantum mechanics. First, there is the problem of how to interpret the multibody wave function. Schrödinger struggled with this problem and had to wait until Born resolved it (from a practical point of view only) by introducing the electron density. For one single particle, Schrödinger got away with thinking that

[3] On the day he died, Lewis and Langmuir had met for lunch at Berkeley. Langmuir was on the Berkeley campus that day to receive an honorary degree. Lewis came back from lunch in a dark mood and played a miserable game of bridge after which he returned to work in his lab. An hour later, he was found dead by his graduate student Michael Kasha, who believed that the HCN incident was an accident (private communication, Prof. Alexis Bell).

the corresponding wave function was indeed an object in ordinary three-dimensional space, numerically expressing the wave nature of that particle. Already for two particles, this picture became untenable. The electron density links the multi-particle wave function back to real 3D space, but at the cost of introducing probability. One could argue that the original problem has been shifted from one place to another. A second aspect to the aforementioned heavy price is the failure of the early (and pure) versions of density functional theory (DFT) to be useful for chemistry. Indeed, at its inception, DFT did not embrace the idea of a multi-particle wave function, let alone a wave function. From the start, DFT operated in 3D space and thought of the electron density in the sense of statistical mechanics. Ever since, there has been a tension between multidimensional wave functions (abstract but quantitatively successful) and the three-dimensional electron density (more concrete but difficult to make numerically accurate).

Still, the electron density is an attractive starting point for the investigation of chemical concepts, such as the atom itself but then inside a molecule. The atom is perhaps the prime cornerstone of chemistry, before that of the bond. After all, atoms certainly exist within molecular or condensed matter systems but bonds are harder to pinpoint. The question is: what does an atom look like when it is inside a molecule (or molecular assembly)? QTAIM will provide an answer that is surprisingly minimal. Before showing how this is done, we end this section by clarifying why the electron density is an attractive starting point. First, it is an observable and can be measured by high-resolution X-ray crystallography. Secondly, the electron density is straightforward to imagine and study as it lives in 3D space. Thirdly, it can be obtained by various routes: (1) experimentally, (2) computationally using basis functions (of any type such as Gaussians, Slaters or plane waves) and (3) again computationally but then *without* basis functions (where the electron density is only known at grid points). As a result, if an atom is defined using the electron density only, then the atom will survive if one obtained it by another route, for example, by a Fourier expansion with crystallographic structure factors rather than by an SCF–MO–LCAO calculation using Gaussians. This independence of the route taken is an important advantage, both conceptually but also technically. As explained in the next section, the electron density naturally falls apart into (topological) atoms. Our definition of an atom and its properties (e.g. charge) survives if one would calculate the electron density with plane-wave basis functions compared to Gaussians. Population analyses such as Mulliken's or distributed multipole analysis (DMA) [21], for example, collapse if asked to return an atomic charge from a plane-wave expanded wave function. However, the charge of a topological atom still exists when using the latter.

5 The Topological Atom

Imagine a real and smooth landscape dominated by two dunes, each with a peak. Imagine picking a starting point in this landscape and finding out, in the immediate vicinity of this point, in which direction the elevation increases most. This direction is the direction of the *gradient vector* at that starting point. Following this gradient vector over a short distance leads to a new point at which the same question is asked: in which direction does altitude increase the fastest? A succession of short stretches of a gradient vector, which is constantly updated at each new point, forms a trajectory. This trajectory is called a *gradient path*. This is the path of steepest ascent in the landscape. Depending on where one started, the gradient path will reach one dune top or the other. Let us remember that a gradient path has a direction: it starts at a point and it terminates at another point.

Imagine that each starting point receives the label "dune A" or "dune B" depending on the terminus of the gradient path that originated at this starting point. The landscape then falls apart into two so-called basins, one for each dune, the top of which is called an *attractor*. This terminology is borrowed from the mathematical branch of dynamical systems.[4] Note how this way of partitioning the landscape naturally follows from the inherent shape of the landscape. In order to separate the dunes, no line was ever drawn in an arbitrary way or a priori; no parameter nor contour line had to be fixed at any stage.

The idea of the gradient path can easily be generalised to any dimension, but the case of three dimensions is the only one we need to define QTAIM atoms or *topological atoms* for short. Let us again pick a point, but now in 3D space, and evaluate the gradient of the electron density, denoted $\nabla\rho$, at this initial point. A succession of very short gradient vectors will again form a gradient path, in the smooth and continuous limit. The gradient path's curved trajectory is the route of maximum ascent in the electron density, starting at the given initial point and terminating at its natural attractor. The vast majority of electron density gradient paths terminate at a nuclear position. Together, they form a bundle of gradient paths that carves out a subspace, within the electron density, which belongs to a topological atom.

This result is illustrated in Fig. 1 for the simple case of the infamous molecule hydrogen cyanide, which consists of three topological atoms. Starting with nitrogen on the right, Fig. 1 shows a couple of dozen of gradient paths forming a web-like pattern, which spans the space allocated to nitrogen. The carbon is placed at the origin, while the square box in bold marks the horizontal and vertical boundaries of the plot (at −6 a.u. and +6 a.u). A special bundle of gradient paths starts at infinity and ends up at any of the little squares, which are so-called bond critical points. Their meaning will be explained later in a dedicated section.

[4] This branch was founded by the mathematician Henri Poincaré in the nineteenth century, as a result of his study of celestial mechanics. Essentially, a dynamical system is a means of describing how one state develops into another state over the course of time.

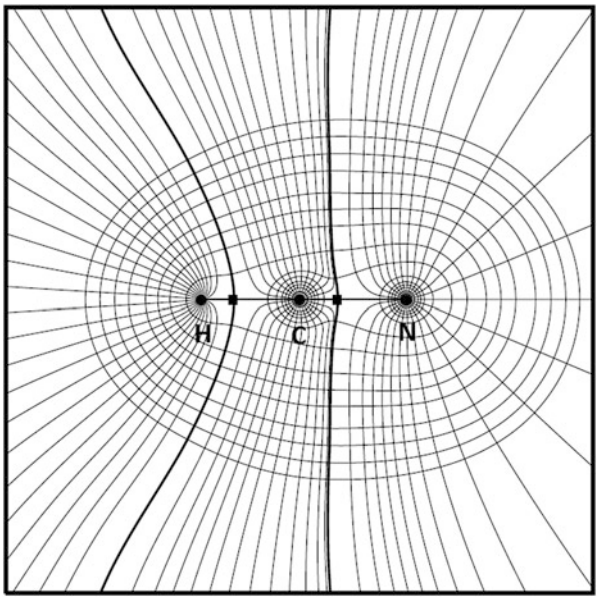

Fig. 1 A collection of gradient paths forming web-like patterns, which each span the subspace of each of the three topological atoms in HC≡N. Each atomic basin consists of an infinite multitude of gradient paths, here represented by a few dozen paths originating at infinity and terminating at the respective nuclei. Electron density contour plots are superimposed onto the field of gradient paths. The values of the contour lines start with 1×10^{-3} and continue with the sequence 2×10^{n}, 4×10^{n} and 8×10^{n} a.u., where n starts at -3 and increases with unity increments

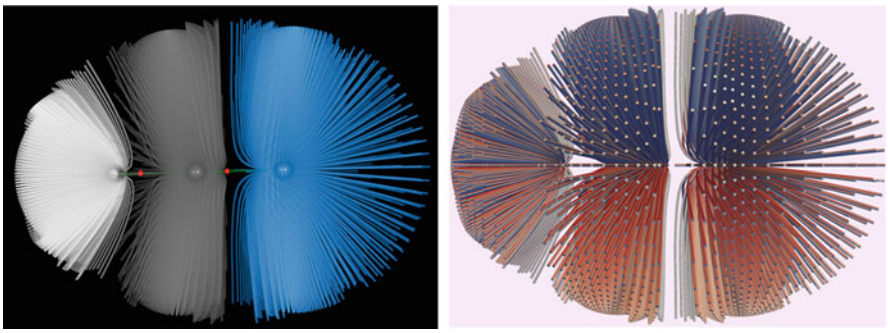

Fig. 2 A 3D view of a number of gradient paths in HC≡N, outlining the gradient vector field. Such image is vaguely reminiscent of masses warping space–time

Figure 2 shows a fuller representation of the information in Fig. 1, namely, a 3D view of the so-called gradient vector field (i.e. the collection of gradient paths) of HC≡N. This type of picture brings out a main feature of the topological atom: it is a subspace bounded in Cartesian space but unbounded in the space of the natural coordinates. These coordinates are the familiar (θ,ϕ) angles of the spherical polar coordinates (centred on the nucleus) and a path parameter s, which spans the full

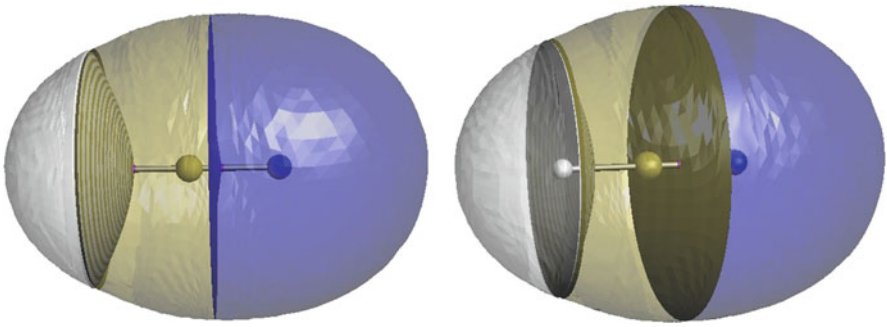

Fig. 3 Two views of the same 3D representation of the three topological atoms (*grey* = H, *brown* = C, *blue* = N) in HC≡N. An interatomic surface is a bundle of gradient paths originating at infinity and terminating at a bond critical point (*little purple sphere*)

interval $[-\infty,+\infty]$. The latter represents the progress along the unique gradient path through a given point on a sphere (centred at the nucleus), which is completely within the topological atom. More details can be found in Box 8.3 of [1].

Figure 3 shows a 3D view of the topological atoms in hydrogen cyanide. The solid curves appearing in Fig. 1, which run broadly vertically, are so-called interatomic surfaces. They reoccur in Fig. 2 as surfaces in 3D. These surfaces are the sharp boundaries between atoms inside a molecule. Note that the boundary between molecules within a molecular assembly is also sharp, because a molecule is simply the union of its topological atoms. A molecule in condensed matter is thus fully bounded by interatomic surfaces. It is clear that there are no gaps between the atoms and also that they do not overlap.

We emphasise again that the construction of an interatomic surface is parameter-free; one could say that the surface draws itself. The use of molecular contour surfaces of constant electron density is artificial and serves here the purpose of visualisation. Here, the practical edge of the molecule, when in the gas phase, is set to $\rho = 0.001$ a.u., which is a typical value. Finally, we note that a molecule in the gas phase, i.e., alone in the universe, is a fiction: sooner or later one will encounter another molecule, admittedly far away but one that still shares a topological boundary with the original "isolated" molecule. As a result, there is no need for a constant electron density surface to bound a molecule, that is, theoretically and philosophically in the gas phase and in the condensed phase, actually and practically. Any atom or collection thereof is always completely bounded by topological boundaries, which emerge naturally, without parameters.

6 The Nature of the Topological Partitioning

Quantum chemical topology (QCT) is a branch of theoretical chemistry that uses the language of dynamical systems (e.g. attractor, basin, gradient path, critical point and separatrix) to partition chemical systems and characterise them via associated

quantitative properties, e.g., atomic charge or bond order. The term QCT was first coined [22] in 2003, and the first symposium dedicated to it took place in 2013, in Mexico City. The full name has been justified in great detail in the 2003 paper (long footnote as [19] therein) and elsewhere [1, 4, 23], and the arguments will not be repeated here. The justification for the keyword "topology" has been elaborated separately in yet a different chapter [3].

This methodology can be applied to a variety of quantum mechanical functions, the oldest and most documented one being the electron density. In that case, one recovers QTAIM. The second oldest segment of QCT is the topological study of the Laplacian of the electron density [24, 25]. The Laplacian is an informative function for the "lighter" elements featuring in organic compounds and biomolecules. Because there is an extensive literature on its use and, being part of QTAIM as well, it will feature as the second segment of QCT, later in a dedicated section (Sect. 13). However, for heavier elements, the Laplacian fails to reveal the atomic shell structure beyond five atomic shells. A new quantum mechanical function, called electron localisation function (ELF) [26], was proposed to remedy this failure. Silvi and Savin were the first to study [27] ELF topologically, work that therefore constitutes the third segment of QCT. The chapter by Professor Silvi provides an extensive account of the topology of ELF. A fourth segment of QCT that will receive much attention in this chapter is called *interacting quantum atoms* (IQA) [28]. Details on the many other segments of QCT can be found in Box 8.1 of Chapter 8 in the book [1] edited by Frenking and Shaik. By bundling all these topological segments under the one umbrella of QCT, this approach is strengthened and competes better with the more traditional interpretative method quantum chemistry [21, 29–34]. This competition should ultimately lead to a falsification, annihilating contradictory interpretations of chemical phenomena given by QCT and non-QCT approaches.

In summary, the gradient vector is the key concept of QCT: it creates all the structure. It is important to spell out five hallmarks of QCT. First, QCT partitioning is parameter-free, as explained in Sect. 5. Secondly, topological atoms are defined in an *orbital-free* manner, as are other basins in QCT segment, for example, an ELF basin. When calculating exchange energies between topological atoms, one still needs orbitals but the shape and volume of the atoms themselves do not depend on these orbitals. The third and final QCT hallmark is its *reference-state-free* nature. Indeed, QCT analyses a single wave function to gain insight in the system at hand, without ever invoking a reference state. An example of such a reference state is a wave function that has not been anti-symmetrised and thereby violates the Pauli principle. Such reference state is crucial in the so-called energy decomposition analysis (EDA) [35, 36]. Another example is a promolecule, which is a simple superposition of free atoms, lacking any chemical hybridisation. Promolecules feature in the so-called deformation density, where were heavily used in high-resolution crystallography [37] before the application of QTAIM, and hence QCT, became standard in that field. Such reference states are artificial in that they cannot be realised in nature and hence cannot be measured, and they may require further parameters to be set. A fourth hallmark is that topological subspaces (i.e. basins in a

gradient vector field) do not overlap. In the case of the electron density, and hence topological atoms, this property has alluring repercussions [38, 39] in the area of intermolecular forces, where the thinking is still dominated by overlapping molecules. Many chemists are uncomfortable with the concept of a non-overlapping atom; yet, many objects in the world, conceptual or not, are non-overlapping: countries, the system and the surrounding in thermodynamics and living cells, for example. Finally, and fifthly, there are no gaps between topological basins: they exhaust space. In the case of the electron density, this fact has unexplored corollaries. Indeed, every point in space belongs to a topological atom; there is no "empty" (i.e. unallocated) space. The absence of the void has consequences for how one thinks about active and allosteric sites and other pockets in enzymes, for example. The familiar ball-and-stick, or even "helix–turn–sheet ribbon" representation of the protein modelling world, gives the impression that there is empty space. A molecular view according to topological atoms challenges [40] this impression. This new view interprets the entrance of a ligand into an enzymatic pocket as a deformation of it and the swarm of topological atoms surrounding the ligand, a process that comes with an energy cost. Steric hindrance then becomes a more gradual and continuous concept as opposed to the simple on–off picture purported by van der Waals radii.

7 The Quantum Atom

Let us forget about topological atoms for a moment. We now want to explore proposals for the definition of an atom from the point of quantum mechanics. We are interested in calculating the potential energy of electrons interacting with each other confined within an arbitrary subspace. Of course this subspace refers to a proposal for an atom. The aforementioned calculation is perfectly achievable by 3D integration, over this subspace's volume, of an integrand that is essentially the quantum equivalent of electron–electron Coulomb energy. Similarly, there are no conceptual problems if one wants to include the nuclear-electron potential energy. Moreover, one can calculate the potential energy between two subspaces.

However, there is a conceptual problem when one wants to calculate the kinetic energy of an arbitrary subspace. The integrand is then a kinetic energy density, which is a *local* kinetic energy or a point property; it is a kinetic energy at a particular point *per unit volume*. This quantity is thus a kinetic energy *density*, which, when integrated over a volume, gives the kinetic energy of the electrons in that volume. The trouble is that the kinetic energy density is not unique [41]: it is determined but for a constant factor times the Laplacian of the electron density. Now, integrating a kinetic energy density function over whole space returns a unique kinetic energy because integrating the Laplacian over whole space yields zero (for a mathematical discussion of this point and related ones see Box 8.2 of [1]). We now ask if there is subspace that shares the same property, namely, that of possessing a unique kinetic energy. The answer is yes and we call such a special

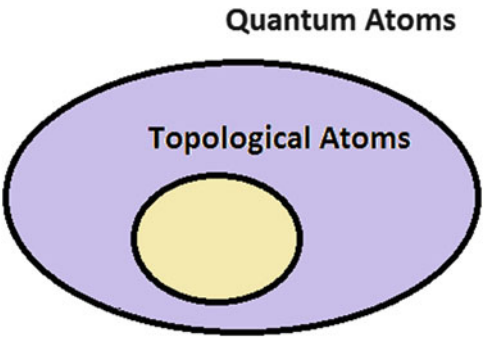

Fig. 4 Venn diagram showing that all topological atoms are quantum atoms but not vice versa

subspace a *quantum atom*. In summary, arbitrary subspaces have ill-defined kinetic energies but a quantum atom has a unique kinetic energy. This important result [42] has been known for more than four decades and was published in 1972.

Now, it can be proven mathematically that *a topological atom is a quantum atom*. For our purposes this statement suffices but it is useful to know that there are quantum atoms that are not topological atoms [43, 44]. Figure 4 makes this point crystal clear once and for all. So we are not interested in proving that topological atoms are *the* atoms of chemistry, nor do we claim that topological atoms are the only ones with a well-defined kinetic energy. Topological atoms are minimal and elegant objects by themselves, with the pleasant added property of having a unique kinetic energy, which opens an avenue towards a complete atomic energy partitioning.

Starting from Slater's molecular virial theorem, it was shown, early on, that a topological atom has its own virial theorem [45]. In general terms, a virial theorem is a fixed relationship between the kinetic and potential energy of system. Because of its existence, one only needs to know one type of energy in order to know the other type as well. In particular, the atomic potential energy can be deduced from the atom's kinetic energy. The latter is easier to calculate than the former, and this computational advantage has been exploited ever since the first atomic integration algorithms [46, 47] in 1981–1982. However, the problem is that the atomic virial theorem only holds provided there are no forces acting on the nuclei, which is the case at a stationary point in a molecular potential energy surface and hence for an equilibrium geometry. This undesirable restriction was lifted [48] in 2001, when it became possible to calculate the potential energy of an atom residing within a *non-equilibrium* molecular geometry. The concomitant algorithm involves an integration in six dimensions, that is, over two topological atoms. With the additional calculation of interatomic exchange energy [49], the analysis of torsional barriers became possible [50] in terms of a complete topological energy partitioning [51].

Inspired by the 2001 paper [48], Blanco et al. proposed [28] a new algorithm in 2005, leading to a series of interesting but dense papers [52–54] under a name the authors coined *Interacting Quantum Atoms* (*IQA*). This systematic work ran in parallel with the topological energy partitioning work by the current author and co-workers, but the latter were more interested in the development of a quantum

topological force field rather than the reinterpretation of chemical phenomena. The essential details of IQA will be explained in a later section. The principles [55] behind this truly novel force field, for now still called QCTFF, are based on the topological energy partitioning, polarisation treated by machine-learning and multipolar electrostatics [56]. Further discussion of QCT force field [38] is beyond the scope of this chapter.

The quantum atom was discovered [42] in 1972, which can be regarded as the birth of QTAIM. The roots of QTAIM thus lie in energy partitioning. It would take another 5 years before a second important component was added to QTAIM: the bond critical point, which is explained in the next section. In fact, the topological atom, other than being a quantum atom, emerged as a topological object sat in a wider context of chemical interpretability. As the Bader group looked at simple organic molecules, it discovered that the Lewis diagram naturally emerged from the electron density, via topological objects such a bond critical points and bond paths.

8 The Bond Critical Point (BCP)

Figure 5 presents an intuitive way to explain the bond critical point. This figure shows the outer constant-electron-density contour of $\rho = 0.001$ a.u., which can be taken as the practical edge of the molecule when in the gas phase. The $\rho = 0.001$ a.u contour is the boundary between the pink region ($\rho < 0.001$ a.u.) and the yellow

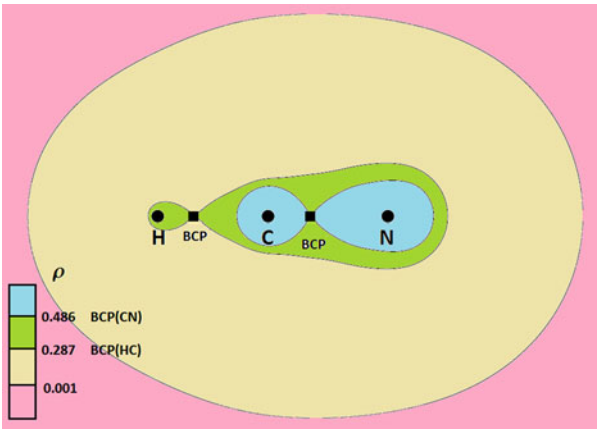

Fig. 5 The bond critical point (*little black square*) illustrated in HC≡N. The electron density (ρ) is represented by three constant-ρ contour lines, at $\rho = 0.001$, 0.287 and 0.486 a.u., which act as boundary values. The four colours used mark the regions bounded by each of three these boundaries; for example, the points in the *yellow region* have an electron density between 0.001 and 0.287 a.u. The electron density at the bond critical point (BCP) between H and C is 0.287 a.u., and this BCP marks the contact point between H and the C≡N fragment. The electron density at the BCP between C and N is 0.486 a.u., and this BCP is the contact point between C and N

region (0.001 a.u. $< \rho <$ 0.287 a.u.). If the electron density is increased beyond 0.287 a.u., then the hydrogen atom becomes disconnected from the rest of the molecule. In other words, this hydrogen, while still being inside the molecule, is now completely enclosed by its own contour lines (not shown). The value of the electron density at the bond critical point (BCP) between *H* and *C* is 0.287 a.u. This value is the highest electron density for which the hydrogen is still attached to the rest of the molecule while increasing the electron density, starting from 0.001 a.u. For any higher value than 0.287 a.u., the contours encompassing the whole molecule become disconnected.

An analogous disconnection process occurs when ρ increases above 0.486 a.u., which of course is the electron density at the second bond critical point. It is then that *C* and *N* also become disconnected. Now, all three atoms in HC≡N are fully encircled by their own contours (not shown). Overall, this process shows that bond critical points are "contact points" between certain atoms. *A bond critical point between two given atoms represents the transition point of the atoms being connected or disconnected*. When connected, they are encompassed by the same contours. When disconnected, the respective atoms have their own "atomic" contours.

The above introduction to the BCP is intuitive and potentially unexploited as an interpretation originally not given by the Bader group. However, this approach is reminiscent of the work [57, 58] of Paul Mezey, which yields a systematic description of chemical bonding and molecular shape, based on a simple density domain principle. A more mathematical (and rigorous) definition of a critical point in the first place is a point in 3D space where the gradient of the electron density vanishes. An attentive reader will remember that the gradient path has a direction. This is true except at a critical point of course. A gradient path always connects two critical points (or at least points infinitesimally close to them). More precisely, a gradient originates (very near) to a critical point (i.e. source) and terminates (very near) to another critical point (i.e. sink). It should be pointed out that a gradient path can always be characterised and classified by the *types* of the two critical points that it manifestly connects. This was done exhaustively [59] and for the first time in 2003. This classification focuses on how many gradient paths can originate from a source critical point and how many gradient paths can terminate at the sink critical point.

In order to characterise the bond critical point completely, one needs to look at the local curvature of the electron density at the critical point. For a maximum in the electron density ρ, the maximum is a maximum in any direction one approaches it and vice versa for a minimum. These are two of four possible types of critical points in 3D, which are easiest to understand. There are two more possible types of critical points in 3D. The BCP is a saddle point in that it is a maximum in two directions only (rather than three) and a minimum in the remaining direction. The direction of the minimum is the molecular axis of HCN. Indeed, a gradient path originates at a given BCP and terminates at one of the nuclear maxima. A second gradient path originates at the same BCP but at the opposite side and is attracted to the other nuclear maximum at that side. This pair of gradient paths is called an *atomic attraction line* [24]. When the forces on all nuclei vanish, as is the case for a

local energy minimum, then the atomic interaction line becomes a *bond path*. The set of all bond paths occurring a molecule (or molecular complex) is called a *molecular graph. It is this molecular graph that can be identified with a Lewis diagram.*

Note that a graph is a mathematical structure that models pairwise relations between objects, which in this case, are nuclei representing topological atoms. Such a relation is robust under moderate geometric deviations (shrinking and elongation) from the local energy minimum geometry. This is one of the reasons the keyword topology is justified [3] in the name quantum chemical topology.

A rigorous classification of the four types of critical points involves an inspection of the eigenvalues of the Hessian (more details in Box 8.4 of [1]). This piece of well-known mathematics can be paraphrased according to the aforementioned directional analysis of the electron density's curvature. All along we have assumed that this curvature does not vanish at the critical point, which makes it a *regular* (i.e. non-singular) critical point. Because the critical point has three non-vanishing curvatures, it is a *rank 3* critical point. Subsequent characterisation of the type of critical point is achieved by assigning a +1 for each direction in which the curvature is positive and −1 for each direction in which the curvature is negative. The next thing to do is adding these −1 and +1s. This sum is called the *signature* of the critical point. The signature of a maximum is clearly $(-1)+(-1)+(-1)=-3$, while that of a minimum is $1+1+1=+3$. When combined with their rank, the maximum and minimum critical points are designated (3,−3) and (3,+3), respectively. Within this nomenclature, a BCP is marked as (3,−1) because there are two negative curvatures and one positive one, or $(-1)+(-1)+1=-1$. The latter occurs in the direction of the atomic interaction line, which is simply the molecular axis in HCN. The former curvatures occur in the plane orthogonal to this axis. When moving away from the BCP, this plane becomes generally curved and is identified with the interatomic surface (see Fig. 3).

A BCP is a so-called *saddle* point because it has a mixed curvature, in the way a real saddle has (seen as a 2D surface embedded in 3D). For 2D manifolds, there is only one type of saddle point, but 3D manifolds possess two possible types. One type is of course the BCP, while the other type is the so-called ring critical point. This saddle point is a mirror image of the BCP because it has two positive curvatures in two directions and one negative curvature in the remaining direction. A ring critical point, which can also be considered as the dual of the BCP, connects topological atoms that topologically form a ring. This means that they all touch each other at the ring critical point.

From their inception, BCPs were taken up slowly (as is typical for truly novel concepts). BCPs appeared in sites within small and standard molecules where the paradigm of the Lewis diagram would expect them to appear. Even the initially controversial boranes and carboranes returned satisfactory molecular graphs [60], with their BCPs in uncontroversial positions. The first study [61] from the Bader group where challenging BCP patterns started popping up is one on van der Waals complexes. The potential energy surfaces of these simple complexes had been thoroughly investigated before and were well understood. This study located

atomic interaction lines and BCPs in the intermolecular regions of a total of 36 configurations of 11 van der Waals dimers and a trimer, none of which contained a hydrogen bond. The complexes comprised combinations of five moieties: argon atoms and the molecules C_2H_2, CO_2, OCS and SO_2. As a first example of the BCP patterns found, the C_s global energy minimum of the Ar...C_2H_2 complex has an atomic interaction line (and concomitant BCP) between one carbon and the argon. Secondly, depending on where the argon atom is situated with respect to OCS, a BCP appears between the argon and the carbon, the sulphur or the oxygen, depending on which energy minimum or transition state the configuration constitutes. Another example demonstrates that the C_{2h} transition state of the ethyne dimer has an atomic interaction line connecting two carbons. Finally, the most curious BCP patterns appear in the CO_2 dimer. In a sequence of dimer configurations, in which the two CO_2 molecules are parallel and slide over each other, a rich series of BCP patterns appears, including O...C, C...C, and O...O BCPs. One non-minimum configuration even has a double O...O BCP connection.

The area of non-covalent interactions[5] continues its path of increased prominent in chemistry as this central science investigates molecular assemblies more intensely than ever. This is the area where Lewis diagrams let the chemist down by remaining silent about how atoms are held together. This frustration is probably the main driver for an increasing number of researchers to scrutinise the BCP more than ever before. The meaning of the BCP is still a matter of debate [62–67] but a very promising explanation of it, not given in the original literature by Bader et al., was given [68] in 2007 in terms of the QCT energy partitioning. In order to understand it, the next section must be read because the explanation [1] involves a competition between interatomic exchange energies [69]. Note that even in Feb 2015, the chemical bond was still being debated in the popular press [70], and the meaning of the BCP clearly features in this debate.

9 Interacting Quantum Atoms (IQA)

A topological energy partitioning, independent of the atomic virial theorem (see Sect. 7), was proposed [48] in 2001. This innovation led to the development of a segment of QCT called *interacting quantum atoms* (*IQA*) [28]. Since its implementation in the computer program AIMALL [71], IQA has become an increasingly popular tool in the armoury of interpretative quantum chemical tools.

We start with the interatomic potential energy, a quantity that has received most attention, especially upon its expansion in a multipole series [56, 72, 73]. The calculation of the interatomic electrostatic potential energy V_{elec} involves a

[5] This term is actually too "black and white". The continuous energy gauge that we will introduce in the context of IQA will demonstrate that a bond can be in between a typical organic covalent bond and a "through space" interaction.

six-dimensional integral, over the volume of each of the two topological atoms A and B, or

$$V_{\mathrm{elec}}^{\mathrm{AB}} = \int_{\Omega_{\mathrm{A}}} d\mathbf{r}_1 \int_{\Omega_{\mathrm{B}}} d\mathbf{r}_2 \frac{\rho_{\mathrm{tot}}(\mathbf{r}_1)\rho_{\mathrm{tot}}(\mathbf{r}_2)}{r_{12}} \tag{1}$$

where the *total* charge density, $\rho_{\mathrm{tot}}(\mathbf{r})$, is the sum of the nuclear charge density and minus the electron density denoted $-\rho(\mathbf{r})$, while r_{12} is the distance between two infinitesimal pieces of charge density.

Note that $V_{\mathrm{elec}}^{\mathrm{AB}}$ actually consists of four contributions: the electron–electron Coulomb energy $V_{\mathrm{ee,coul}}^{\mathrm{AB}}$, the electron–nucleus attraction energy, denoted $V_{\mathrm{en}}^{\mathrm{AB}}$, its dual $V_{\mathrm{en}}^{\mathrm{BA}}$, and the nucleus–nucleus repulsion, $V_{\mathrm{nn}}^{\mathrm{AB}}$. Summing these four terms yields the full electrostatic interaction between two atoms A and B, $V_{\mathrm{elec}}^{\mathrm{AB}}$, or

$$V_{\mathrm{elec}}^{\mathrm{AB}} = V_{\mathrm{ee,coul}}^{\mathrm{AB}} + V_{\mathrm{en}}^{\mathrm{AB}} + V_{\mathrm{en}}^{\mathrm{BA}} + V_{\mathrm{nn}}^{\mathrm{AB}} \tag{2}$$

The electron–nucleus attraction energy is calculated as a 3D volume integral:

$$V_{\mathrm{en}}^{\mathrm{AB}} = -Z_{\mathrm{B}} \int_{\Omega_{\mathrm{A}}} d\mathbf{r} \frac{\rho(\mathbf{r})}{r_{1\mathrm{B}}} \tag{3}$$

where $r_{1\mathrm{B}}$ is the distance between an electron inside the volume of atom A and the nucleus of atom B. This calculation can also be performed if A=B, which features in the intra-atomic energy discussed below.

The energy $V_{\mathrm{ee,coul}}^{\mathrm{AB}}$ can be related to the second-order reduced matrix, $\rho_2(\mathbf{r}_1,\mathbf{r}_2)$. To understand how exactly, one needs to know the fine structure of $\rho_2(\mathbf{r}_1,\mathbf{r}_2)$, or

$$\begin{aligned}\rho_2(\mathbf{r}_1,\mathbf{r}_2) = \rho_2^{\mathrm{coul}} + \rho_2^{\mathrm{exch}} + \rho_2^{\mathrm{corr}} = \rho(\mathbf{r}_1)\rho(\mathbf{r}_2) \\ -\rho_1(\mathbf{r}_1,\mathbf{r}_2)\rho_1(\mathbf{r}_2,\mathbf{r}_1) + \rho_2^{\mathrm{corr}}(\mathbf{r}_1,\mathbf{r}_2)\end{aligned} \tag{4}$$

where the first term refers to the quantum-mechanically uncorrelated Coulomb-like pair density, the second term to the Fock–Dirac exchange (which is dominated by and associated with the Fermi hole), while the third term is at least an order of magnitude smaller [28, 54] than the second and connected with the Coulomb hole. The energy quantity $V_{\mathrm{ee}}^{\mathrm{AB}}$ is associated with the complete second-order matrix $\rho_2(\mathbf{r}_1, \mathbf{r}_2)$, which describes the three types of interactions that electrons experience when interacting with each other.

Figure 6 shows how each of the three contributions to the second-order matrix is associated with a type of energy: Coulomb (or electrostatic) energy, exchange energy and correlation energy. Note that accurate wave functions for H_2, as obtained [74] already in 1933 by James and Coolidge, and later refined [75] by Kołos and Wolniewicz, do not show a trace of either orbitals or exchange energy. In the words [76] of Coulson: "such concepts relate to our simplified mathematical

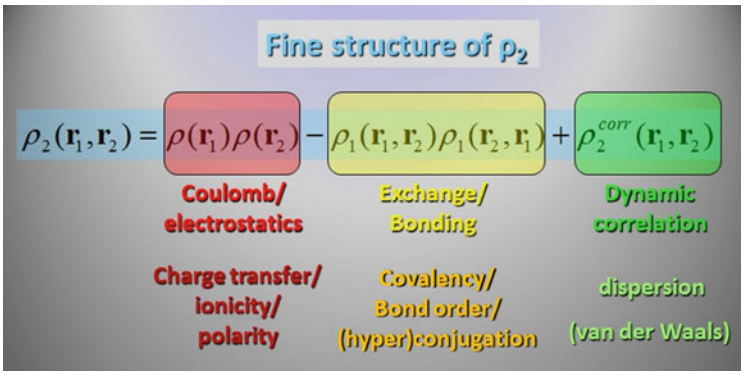

Fig. 6 Overview of the three contributions to the second-order reduced matrix, each with the specific chemical insight they offer

models for describing electrons, not to the electrons themselves". Still, with each of the aforementioned energy types can the chemist associate a concept that usefully characterises chemical bonds, such as charge transfer, ionicity and polarity, covalency, bond order and (hyper)conjugation and dispersion interactions (which feature in the modelling of protein and DNA/RNA oligonucleotides). In particular, there will be an energy contribution called V_{exch} (or sometimes abbreviated to V_x) that quantifies the covalent energy of a bond. Although this measure works well and makes sense as we will see in the next section, the potential worry is that this physical quantity may evaporate in the light of Coulson's comment. How do we know for sure which chemical concept relates to the electrons themselves rather than our models of them? This grave concern applies not in the least to the chemical bond itself.

Each term in Eq. (4) (and hence in Fig. 6) is associated with a type of potential energy, each associated with a chemical interpretation. As a result the corresponding fine structure of $V_{\text{ee}}^{\text{AB}}$ automatically follows, or

$$\begin{aligned} V_{\text{ee}}^{\text{AB}} &= \int_{\Omega_A} d\mathbf{r}_1 \int_{\Omega_B} d\mathbf{r}_2 \, \frac{\rho_2(\mathbf{r}_1,\mathbf{r}_2)}{r_{12}} = \int_{\Omega_A} d\mathbf{r}_1 \int_{\Omega_B} d\mathbf{r}_2 \, \frac{\rho(\mathbf{r}_1)\rho(\mathbf{r}_2)}{r_{12}} \\ &\quad - \int_{\Omega_A} d\mathbf{r}_1 \int_{\Omega_B} d\mathbf{r}_2 \, \frac{\rho_1(\mathbf{r}_1,\mathbf{r}_2)\rho_1(\mathbf{r}_2,\mathbf{r}_1)}{r_{12}} + \int_{\Omega_A} d\mathbf{r}_1 \int_{\Omega_B} d\mathbf{r}_2 \, \frac{\rho_2^{\text{corr}}(\mathbf{r}_1,\mathbf{r}_2)}{r_{12}} \\ &= V_{\text{ee,coul}}^{\text{AB}} + V_{\text{ee,exch}}^{\text{AB}} + V_{\text{ee,corr}}^{\text{AB}} \end{aligned} \tag{5}$$

The second term in Eq. (5) represents the exchange delocalisation energy, $V_{\text{ee,exch}}^{\text{AB}}$, which is present at Hartree–Fock level. This term teases out the interaction that keeps bonded atoms together. The degree to which atoms are bonded can be estimated by a non-energy measure, which is typically a quantum mechanical bond order. QCT offers such a measure [77]. However, it was shown by our lab [49] that

this bond order features only in the first term of the multipolar expansion of $V^{AB}_{ee,exch}$. Hence, the latter quantity contains more information than a bond order. The third term in Eq. (5), or $V^{AB}_{ee,corr}$, covers the effect of dynamic correlation and hence dispersion. It is absent at Hartree–Fock level, but was calculated for the first time [78], but as late as 2015, for CCSD/cc-pVDZ wave functions of H_2, N_2, H_2O and CO. The effect of dynamic correlation is dual: an increase in the magnitude of the nucleus–electron attraction energy and a decrease in the electronic repulsion.

The fourth and last energy contribution is intra-atomic, denoted E_{intra}. This quantity measures the intrinsic stability of an atom and cannot be written as "V" because this symbol is reserved for potential energy only. Indeed, E_{intra}, or the atomic "self-energy" [48], also contains kinetic energy, which is well defined for a topological atom. Many chemical phenomena such as rotation barriers, steric hindrance, the anomeric effect, the gauche effect or other stereo-electronic effects are controlled by E_{intra}. Collecting the three possible contributions to E_{intra} amounts to

$$E^{A}_{intra} = T^{A} + V^{AA}_{ee} + V^{AA}_{en} \tag{6}$$

where T^A is its kinetic energy. The intra-atomic energy E^A_{intra} is the energy that a single atom possesses inside a system, regardless of whether this system is a single molecule or a cluster of molecules (including even ions). Work from our lab (P. Maxwell and P.L.A. Popelier, Molecular Physics, unpublished) shows that an oxygen, nitrogen or carbon has the same energy, within maximum ~2 kJ mol^{-1}, when appearing in a tripeptide (three amino acids) compared to appearing in a pentapeptide. Of course these peptides' common nuclear skeleton stays in the same configuration in order to isolate the transferability of this mono-atomic energy. This energetic transferability was observed in seven test cases, i.e., the homo-oligopeptides of Ala, Ser, Thr, Gly, Val, Leu and Ile. This high degree of energetic transferability is an asset to QCT.

An extensive comparison [79] with alternative non-QCT methods showed that IQA (and hence QCT) gives a less distorted image of chemical phenomena, leading to smaller deformation and interaction energies, *thus better preserving the atomic identity from the energetic point of view*. This is a very important conclusion because it shows that the QCT atoms are appealing fragments, quantitatively expressing what chemists expect from atoms.

10 Applying IQA to Homonuclear Diatomics

The place to start are the homonuclear diatomics of period 1 and period 2 elements, whose binding energies have been analysed in great detail elsewhere [54]. Before we can look at data, we need a few more simple equations. First, for certain purposes, it makes sense to combine the two types of correlation (Fock exchange and electron Coulomb correlation) into a single quantity:

$$V_{\mathrm{xc}}^{\mathrm{AB}} = V_{\mathrm{ee,exch}}^{\mathrm{AB}} + V_{\mathrm{ee,corr}}^{\mathrm{AB}} \tag{7}$$

Secondly, the full interaction energy between two atoms A and B can be lumped together as follows:

$$V_{\mathrm{inter}}^{\mathrm{AB}} = V_{\mathrm{elec}}^{\mathrm{AB}} + V_{\mathrm{xc}}^{\mathrm{AB}} \tag{8}$$

Thirdly, the total molecular energy can be reconstructed from the intra-atomic energies (or self-energies) and these interatomic energies just defined:

$$E_{\mathrm{mol}} = \sum_{\mathrm{A}} E_{\mathrm{intra}}^{\mathrm{A}} + \sum_{\mathrm{A}} \sum_{\mathrm{B>A}} V_{\mathrm{inter}}^{\mathrm{AB}} \tag{9}$$

Fourthly, it is useful to compare the self-energy of a given atom with the energy of that atom in a free reference state, denoted E_0^{A}. This state is typically its ground state but one should keep in mind that the introduction of this reference is not an essential part of IQA because it is actually reference-state-free. One can then think of an atomic deformation energy, simply defined as

$$E_{\mathrm{def}}^{\mathrm{A}} = E_{\mathrm{intra}}^{\mathrm{A}} - E_0^{\mathrm{A}} \tag{10}$$

In this equation huge numbers are subtracted because period 2 elements have energies of the order of 10^5 kJ/mol. Clearly these are not energies in the chemical realm. This fact is to be expected because the construction of an atom, whether on its own or within a molecule, from its constituents (i.e. electrons and the nucleus) is not a chemical process. The latter involves intact atoms and focuses on the changes in the atoms' "alliances".

Fifthly, it is easy to retrieve and study the fine structure of the atomic deformation energy by using the equivalent of Eq. (6) for the free (isolated) atom:

$$E_0^{\mathrm{A}} = T_0^{\mathrm{A}} + V_{\mathrm{ee},0}^{\mathrm{AA}} + V_{\mathrm{en},0}^{\mathrm{AA}} \tag{11}$$

Although E_0^{A} is actually an intra-atomic energy, the label "intra" is dropped because the free atom obviously does not have an "inter" atomic component.

Combining this equation with Eqs. (6) and (10) yields

$$\begin{aligned} \Delta E_{\mathrm{intra}}^{\mathrm{A}} &= E_{\mathrm{intra}}^{\mathrm{A}} - E_0^{\mathrm{A}} = E_{\mathrm{def}}^{\mathrm{A}} = \left(T^{\mathrm{A}} + V_{\mathrm{ee}}^{\mathrm{AA}} + V_{\mathrm{en}}^{\mathrm{AA}}\right) - \left(T_0^{\mathrm{A}} + V_{\mathrm{ee},0}^{\mathrm{AA}} + V_{\mathrm{en},0}^{\mathrm{AA}}\right) \\ &= \Delta T^{\mathrm{A}} + \Delta V_{\mathrm{ee}}^{\mathrm{AA}} + \Delta V_{\mathrm{en}}^{\mathrm{AA}} \end{aligned} \tag{12}$$

Finally, after trite rearrangement, we can express the molecular binding energy as follows, using Eqs. (9) and (10):

$$
\begin{aligned}
E_{\text{bind}} &= E_{\text{mol}} - \sum_{\text{A}} E_0^{\text{A}} = \left(\sum_{\text{A}} E_{\text{intra}}^{\text{A}} + \sum_{\text{A}} \sum_{\text{B>A}} V_{\text{inter}}^{\text{AB}} \right) - \sum_{\text{A}} E_0^{\text{A}} \\
&= \sum_{\text{A}} \left(E_{\text{intra}}^{\text{A}} - E_0^{\text{A}} \right) + \sum_{\text{A}} \sum_{\text{B>A}} V_{\text{inter}}^{\text{AB}} \\
&= \sum_{\text{A}} E_{\text{def}}^{\text{A}} + \sum_{\text{A}} \sum_{\text{B>A}} V_{\text{inter}}^{\text{AB}}
\end{aligned}
\tag{13}
$$

It is now time to illustrate the meaning of the equations above by tabulating the various energy contributions for all ten diatomics announced. Table 1 provides the essential IQA information to understand the stability of these diatomics. All data shown there are calculated, but corresponding experimental data (equilibrium bond length R_{e} and dissociation energy $D_{\text{e}} = -E_{\text{bind}}$) as well as computational details can be found in [54].

The first remarkable observation is that all atomic deformation energies $E_{\text{def}}^{\text{A}}$ are positive. This means that an atom is destabilised when forming a homonuclear diatomic molecule, in the absence of any charge transfer between atoms, as is indeed the case for homonuclear diatomics. In other words, an atom "feels best" when it is on its own, free and isolated. The perturbation of forming a molecule increases any atom's self-energy, which is disadvantageous from its own point of view. How can a molecule then be a stable entity?

Looking at Eq. (13), it is clear that a negative binding energy, E_{bind}, which is the hallmark of a stable molecule, can only be achieved if the interatomic term is negative, or $\sum_{\text{A}} \sum_{\text{B>A}} V_{\text{inter}}^{\text{AB}} < 0$. This is the only way to compensate for the manifestly positive deformation energy. We note that in a diatomic molecule, there is only one term in this sum and hence $V_{\text{inter}}^{\text{AA}} < 0$. This deduction is indeed confirmed upon inspection of Table 1. In fact, Eq. (13) can be specified for homonuclear diatomics to Eq. (14),

$$
E_{\text{bind}} = -D_{\text{e}} = 2E_{\text{def}}^{\text{A}} + V_{\text{inter}}^{\text{AA}} \tag{14}
$$

which can be readily verified for a number of entries of Table 1. The most stable system, which is N_2, is held together by a massive negative interatomic energy, dominating a medium-valued atomic deformation energy. The interplay of $E_{\text{def}}^{\text{A}}$ and $V_{\text{inter}}^{\text{AA}}$ is complex as they each fail to show simple monotonic increases or decreases along an increasing atomic number Z. For example, the weak bond in Be_2 can be ascribed to a sudden dip in the magnitude of $V_{\text{inter}}^{\text{AA}}$, which hereby fails to compensate for the *steadily* increasing $E_{\text{def}}^{\text{A}}$ values as Z increases.

Equation 13 enables to reveal some fine structure in $E_{\text{def}}^{\text{A}}$. Ignoring the anomaly of Be_2, the absolute values of ΔT^{A}, $\Delta V_{\text{ee}}^{\text{AA}}$ and $\Delta V_{\text{en}}^{\text{AA}}$ monotonically increase from Li_2 to N_2. More precisely, the latter two quantities metaphorically battle each other: as the atom stabilises from increased attraction between its nucleus and swelling electron cloud, the atom also destabilises through increased electron–electron

Table 1 IQA analysis of homonuclear diatomics of period 1 and 2 elements (all values are calculated at high levels of theory [54], which agree sufficiently well with experimental data provided there)

Z	molecule	R_e[a]	D_e[a]	E^A_{def}	ΔT^A	ΔV^{AA}_{ee}	ΔV^{AA}_{en}	V^{AB}_{int}	V^{AB}_{cl}	V^{AB}_{xc}	δ^{AB}
1	H_2	0.741	452	33	222	398	-587	-519	111	-630	0.851
2	He_2	2.875	0	1	-0.4	1	+0.4	-3	0	-3	0.005
3	Li_2	2.674	116	70	22	273	-225	-256	3	-259	0.835
4	Be_2	2.523	17	111	12	239	-140	-238	10	-248	0.589
5	B_2	1.601	305	199	154	1079	-1034	-703	125	-828	1.368
6	C_2	1.254	617	203	293	2104	-2194	-1023	366	-1389	1.805
7	N_2	1.106	939	149	464	3129	-3444	-1238	575	-1813	1.952
8	O_2	1.219	514	213	276	2280	-2343	-941	361	-1302	1.541
9	F_2	1.399	177	191	66	1194	-1069	-558	139	-697	0.925
10	Ne_2	2.728	3	5	12	2	-9	-13	0	-13	0.034

[a]All energies are given in kJ/mol and the equilibrium internuclear distance (R^e) in Å.

repulsion. The majority of the values of ΔV^{AA}_{ee} and ΔV^{AA}_{en} are of the order 10^3 kJ/mol, while most E^A_{def} values are of the order of 10^2 kJ/mol. The smallness of this order of magnitude proves IQA's capacity to deliver a satisfactory quantification of the preservation of atomic identity inside molecules. In other words, a free atom deforms, while forming a molecule, by an amount that belongs to the energy scale of chemical change.

Before we discuss the V^{AB}_{xc} values of other simple molecules, we first digress, in the next section, and examine the important concept of bond order within the context of QCT.

11 Bond Order

The concept of bond order is old and deeply ingrained in the chemist's mind. The number of stripes two bonded atoms share in a Lewis diagram is automatically associated with the bond order of the bond linking these two atoms. Can these bond orders be linked to (modern) wave functions? Can they be computed through quantum mechanics? The answer is yes, and indeed for any pair of atoms, no matter the size of their separation. If the numerical values of the quantum mechanical (read QCT) bond order more or less coincide with those of the formal bond orders from Lewis diagrams (for typical covalent bonds), then QCT bond order values for more distant atoms pairs must be a meaningful extension of the Lewis diagram. In fact, there is a need for more creative versions of Lewis diagrams, which visualise the numerical information obtained from QCT bond orders. A variety of dotted,

dashed, dot-dash and other combinations may extend the current patterns of single, double, triple or even quadruple stripes. Mainly the hydrogen bond has contributed to the idea of extended Lewis diagrams, through its dotted line appearing alongside single stripes of monomeric single covalent bonds. The dative (covalent) bond or dipolar bond (with its curious arrow) is another example but surely there are more possible extensions, especially in the realm of molecular assemblies; QCT bond orders should be systematically analysed and fuel the extension of Lewis diagrams with a larger action radius.

For simplicity we only present the relevant formulae for a closed-shell Hartree–Fock wave function, but we note that they can be generalised to correlated (post-Hartree–Fock) wave functions [49, 80]. We start by recognising that there is no electron correlation energy in a Hartree–Fock wave function, so Eq. (7) becomes

$$V_{\mathrm{xc}}^{\mathrm{AB}} = V_{\mathrm{ee,exch}}^{\mathrm{AB}} + V_{\mathrm{ee,corr}}^{\mathrm{AB}} = V_{\mathrm{ee,exch}}^{\mathrm{AB}} = V_{x}^{\mathrm{AB}} \tag{15}$$

Work [49–51, 81] carried out in parallel to IQA's development introduced $E_{\mathrm{X}}^{\mathrm{AB}}$, which is equal to $2V_{\mathrm{x}}^{\mathrm{AB}}$ such that, drawing from Eq. (6)in [49], we have

$$V_{\mathrm{x}}^{\mathrm{AB}} = -\,2\int_{\Omega_{\mathrm{A}}} d\mathbf{r}_1 \int_{\Omega_{\mathrm{B}}} d\mathbf{r}_2 \sum_i \sum_j \frac{\psi_{\mathrm{i}}(\mathbf{r}_1)\psi_{\mathrm{i}}(\mathbf{r}_2)\psi_j(\mathbf{r}_1)\psi_j(\mathbf{r}_2)}{|\mathbf{R}+\mathbf{r}_2-\mathbf{r}_1|} \tag{16}$$

where i and j are summed throughout the molecular orbitals. Here $\mathbf{R} = \mathbf{R}_{\mathrm{B}} - \mathbf{R}_{\mathrm{A}}$ represents the internuclear vector, $\mathbf{R}_{\mathrm{A}}$ and $\mathbf{R}_{\mathrm{B}}$ the positions of the nuclei A and B in the global axis system, while $\mathbf{r}_1$ and $\mathbf{r}_2$ describe the electron density in the basins A and B, respectively. It is convenient to define the overlap function S at a point $\mathbf{r}$, which can be $\mathbf{r}_1$ and $\mathbf{r}_2$:

$$S_{ij}(\mathbf{r}) = \psi_i(\mathbf{r})\,\psi_j(\mathbf{r}) \tag{17}$$

Substituting Eq. (17) into Eq. (16) leads to

$$V_{\mathrm{x}}^{\mathrm{AB}} = -2\int_{\Omega_{\mathrm{A}}} d\mathbf{r}_1 \int_{\Omega_{\mathrm{B}}} d\mathbf{r}_2 \sum_{\mathrm{i}} \sum_{\mathrm{j}} \frac{S_{\mathrm{ij}}(\mathbf{r}_1)S_{\mathrm{ij}}(\mathbf{r}_2)}{|\mathbf{R}+\mathbf{r}_2-\mathbf{r}_1|} \tag{18}$$

A binomial Taylor expansion of $|\mathbf{R}+\mathbf{r}_2-\mathbf{r}_1|^{-1}$ and subsequent application of an addition theorem for regular spherical harmonics [82] factorise the electronic ($\mathbf{r}_1$, $\mathbf{r}_2$) and geometric ($\mathbf{R}$) coordinates as follows:

$$V_{\mathrm{x}}^{\mathrm{AB}} = -2\sum_{l_1=0}^{\infty}\sum_{l_2=0}^{\infty}\sum_{m_1=-l_1}^{l_1}\sum_{m_2=-l_2}^{l_2} T_{l_1 m_1 l_2 m_2}(\mathbf{R}) \sum_{ij} Q_{l_1 m_1}^{ij}(\Omega_{\mathrm{A}})\, Q_{l_2 m_2}^{ij}(\Omega_{\mathrm{B}}) \tag{19}$$

where the *exchange moments*, $Q_{lm}^{ij}(\Omega)$, unlike their Coulomb counterpart (the familiar atomic multipole moments), explicitly depend on the molecular orbitals:

$$Q_{lm}^{ij}(\Omega) = \int_{\Omega} d\mathbf{r}\ \ S_{ij}(\mathbf{r}) R_{lm}(\mathbf{r}) \tag{20}$$

Equation (19) can now be explicitly expanded term by term but we are only interested in the first term, or

$$V_x^{\mathrm{AB}} \cong \frac{-2}{R} \sum_{ij} Q_{00}^{ij}(\Omega_{\mathrm{A}})\, Q_{00}^{ij}(\Omega_{\mathrm{B}}) \tag{21}$$

where we have set $l = m = 0$ and used the facts that $R_{00}(\mathbf{r}) = 1$ and $T_{0000}(\mathbf{r}) = 1/R$, where $R = |\mathbf{R}|$ is the internuclear distance. The similarity of Eq. (21) with the simple and well-known expression of $q_A q_B/R$ for Coulomb energy is remarkable. Now we are interested in introducing the QCT bond order[6] denoted δ^{AB}. This important quantity is also called the delocalisation index (DI) and is defined (see Eq. (9) in [77] or Eq. (11) in [83]) as follows:

$$\delta^{\mathrm{AB}} = 4 \sum_{ij} S_{ij}(\Omega_{\mathrm{A}})\, S_{ij}(\Omega_{\mathrm{B}}) = 4 \int_{\Omega_{\mathrm{A}}} d\mathbf{r}_1 \int_{\Omega_{\mathrm{B}}} d\mathbf{r}_2 \rho_1(\mathbf{r}_1, \mathbf{r}_2) \rho_1(\mathbf{r}_2, \mathbf{r}_1) \tag{22}$$

where

$$S_{ij}(\Omega) \ = \int_{\Omega} d\mathbf{r}\ \ \psi_i(\mathbf{r}) \psi_{\mathrm{j}}(\mathbf{r}) = Q_{00}^{ij}(\Omega) \tag{23}$$

such that we obtain, after substituting Eq. (22) into Eq. (21),

$$V_x^{\mathrm{AB}} \cong -\frac{\delta^{\mathrm{AB}}}{2R} \tag{24}$$

This equation clearly shows that, if numerically obeyed within a reasonable error bar, V_x^{AB} is a measure of covalent energy because of its proportionality to bond order. This simple equation is a good approximation for sufficiently distant atoms. Many examples of the convergence of V_x^{AB} interactions are given in [49] where $(HF)_2$, $(H_2O)_2$, $(C_2H_2)_2$, butane, acrolein and 1,3,5-hexatriene were investigated. For example, the two unique V_x^{HO} energies, between atoms from different monomers in the water dimer (C_s symmetry: global minimum of $(H_2O)_2$), are converged within 0.1 kJ/mol at "monopole–monopole level". In other words, Eq. (24) is obeyed with an error bar of less than 0.1 kJ/mol.

[6] The definition of the delocalisation index DI in [85] is confusing due to the lack of a final and explicit formula for DI and because of scattering important technical information in the paper's main text. Fortunately, the numerical values reported in that paper for DI are in line with values published elsewhere.

Finally, it is worth pointing out that the QCT bond order is closely related to the covariance of the joint electron population distribution function [84], or

$$\delta^{AB} = -2\mathrm{cov}(N(A), N(B)) \tag{25}$$

The bond order, as a delocalisation index, measures the number of electron pairs shared between topological atom A and B. This index can be linked to the fluctuation of the electron population, denoted N, in both atoms.

A wealth of tabulated QCT bond orders can be found in [85, 86]. There is consistent evidence that, relative to the Hartree–Fock level, the typical effect of the conventional correlation methods is to decrease the value of δ^{AB} provided it refers to a covalent bond. The prototype of such a bond is H–H in H_2. Here, the Hartree–Fock QCT bond order is 1.000, but correlated levels (MP2, MP3, CISD, QCISD) reduce this value to 0.844–0.894. A more dramatic example is that of δ^{NN} in N_2, which contains a notoriously strong covalent bond. A typical Hartree–Fock calculation returns the formal bond order of 3 (more precisely 3.041 in [86]), but this value drops to 2.311 (MP2), 2.314 (MP4), 2.408 (CISD) or 2.312 (QCISD). It is clear that the values are stable with respect to the type of approximation generating the post-Hartree–Fock wave function. This effect is seen in many more systems [86]. This stability is an asset to QCT, as well as the stability with respect to a change in basis set, including diffuse functions. For example, δ^{NN} in N_2, again evaluated at Hartree–Fock level, amounts to 3.042, 3.037, 3.040 and 3.042 for 6-31G, 6-31G*, 6-311G(2d) and 6-311 + G(2d), respectively. In summary, the Lewis model is robustly recovered (independent of basis set) at Hartree–Fock level. Secondly, any post-Hartree–Fock method reduces the bond order by a largely similar amount and most so for the strongly covalent bonds.

Table 2 provides a quick tour of typical values of the QCT bond order δ^{AB} observed in simple molecules. Although when calculated at Hartree–Fock level these values best resemble the formal bond order of the Lewis diagrams, we report post-Hartree–Fock values only. The reason is that those values are more accurate, since the wave functions are more realistic. Indeed, the best numerical values need to inform Lewis diagrams not vice versa.

Van der Waals systems such as He_2 and Ne_2 show very small δ values, as expected. In spite of the anomalous behaviour of F_2 compared to the other dihalogens, and the quest of several groups (e.g. [87]) for an explanation of its bonding mechanism, the value of δ^{FF} is near unity and thereby underpins the confident single stripe in the Lewis diagram of F_2. In the hydrides, bond orders peak at δ^{CH} in CH_4, monotonically decreasing in both directions, that is, towards HF and LiH. The latter is an ionic compound, which ends up with a small bond order of only 0.199. As another standard example of an ionic system, LiF also adopts a small bond order value (0.185). Only in methane does the bond order comes close to unity, $\delta^{CH} = 0.85$. As the bond order "deteriorates" to $\delta^{OH} = 0.61$ in water, one may wonder if a full single stripe in the Lewis diagram can be justified. Or should one represent this bond with a dashed line? Kekulé developed an elaborate system for showing how bonds might be arranged in space, but since it

Table 2 Post-Hartree–Fock QCT bond orders of some simple molecules

Molecule	δ^{AB}	Molecule	AB	δ^{AB}	Molecule	AB	δ^{AB}	Molecule	AB	δ^{AB}
H_2	0.851	HF	HF	0.427	HCl	HCl	0.909	C_2H_2	CC	2.195
He_2	0.005	H_2O	OH	0.612	H_2S	SH	0.957		CH	0.857
Li_2	0.835		HH	0.009		HH	0.044	C_2H_4	CC	1.495
Be_2	0.589	NH_3	NH	0.793	PH_3	PH	0.765		CH	0.851
B_2	1.368		HH	0.018		HH	0.094	C_2H_6	CC	0.852
C_2	1.805	CH_4	CH	0.847	SiH_4	SiH	0.475		CH	0.833
N_2	1.952[a]		HH	0.035		HH	0.089	B_2H_6[b]	BB	0.057
O_2	1.541	BH_3	BH	0.521	AlH_3	AlH	0.384		BH_t	0.509
F_2	0.925		HH	0.113		HH	0.075		BH_b	0.300
Ne_2	0.034	BeH_2	BeH	0.276	MgH_2	MgH	0.369		H_bH_b	0.167
			HH	0.082		HH	0.030	CO_2	CO	1.171
		LiH	LiH	0.199	NaH	NaH	0.389		OO	0.228
		LiF	LiF	0.185				CO	CO	1.442
		BF_3	BF	0.298				NO^+	NO	1.997
			FF	0.172				CN^-	CN	1.916

[a]Note that this value (calculated at with the standard TZV(2d,f) basis set of the computer program GAMESS) is suddenly much smaller than the value of 2.3 in the main text, obtained with a triple-zeta basis set (6-311++G(2d,2p) with CISD/6-311++G(2d,2p) optimised geometries)

[b]Diborane has two types of hydrogens: four terminal ones (H_t) and two bridging ones (H_b)

was too cumbersome, it was quickly replaced by another system suggested earlier by Couper. He proposed that bond between two atoms be represented by a short line. This system is still in existence today but one could speculate about a slightly more informed system drawing from clusters of δ^{AB} values.

There is a non-negligible bond order ($\delta^{HH} = 0.113$) between the hydrogen atoms in BH_3 but this value reduces steadily to only 0.009 in H_2O, where δ^{HH} is only twice as large as δ^{HeHe} in He_2. The relatively large bond order values between two ligands rather than those between the central atom and a ligand will be taken up again in Sect. 12. The question is again if there should not be a signature of bonding between ligands in an extended Lewis diagram, if the ratio of δ^{CL}/δ^{LL} is becoming low, where L is the ligand and C the central atom. Indeed, in water $\delta^{OH}/\delta^{HH} = 68$, this ratio dropping to 44 in ammonia, further dropping to 24 in methane and only 5 in borane. In BF_3 the bond order ratio is as low as 1.73. In textbooks, this molecule is often represented by a bizarre resonance canonical involving a flickering $B^-{=}F^+$ pattern. Not only does this interpretation undermine the electronegativity of F and the electropositivity of B (according to whichever electronegativity scale) but it is also incompatible with the very low value of the BF bond order ($\delta^{BF} = 0.3$), which is not hinting at any double bond character (even when multiplied by three).

The third row hydrides behave quite differently compared to their second row counterparts. The δ^{EH} bond orders of the lower Z species (NaH, MgH_2, AlH_3 and SiH_4) average around 0.4. At PH_3 there is a crossing point where the bond order is almost the same as that in NH_3. For higher Z, the species (H_2S and HCl) are much more covalent than their second row counterparts. The δ^{EH}/δ^{HH} ratios are generally lower than in the second row.

The series ethane, ethane and ethyne presents the classic formal bond order between carbons. At Hartree–Fock level, one recovers, respectively, 0.99, 1.88 and 2.87, for the C–C single, double and triple bond. Rounded off to a single digit, these numbers confirm the formal bond order of 1, 2 and 3. However, at correlated level, these values are attenuated to become 0.85, 1.50 and 2.20, respectively. In this short series of hydrocarbons, transferability of bond order can be seen for the first time, where δ^{CH} averages to 0.847 ± 0.012. Similar transferability is also seen for BH bond orders in BH_3 and B_2H_6 where δ^{BH} averages to 0.515 ± 0.008. The BH_b bond in diborane where H_b is a bridging hydrogen is much weaker though ($\delta^{BH} = 0.300$). Finally, it is clear that the BB interaction is much weaker (about three times) than the H_bH_b interaction.

Finally, the formal C=O bond in CO_2 is much nearer to a single bond than to a double bond, but the non-negligible OO bond order (of 0.228) suggests the system is best regarded as one enjoying 3c–4e bonding. This is also the case for BH_3, SO_2 and SO_3 (the latter two not shown in Table 2). The isoelectronic systems CO, NO^+ and CN^-, which all contain 14 electrons, fall apart into a singlet $\delta^{CO} = 1.44$ (intermediate between single and double bond) and a doublet $\delta^{NO} = 2.00$ and $\delta^{CN} = 1.91$.

12 Interatomic Exchange Energies (V_x^{AB}) in Some Simple Molecules

The previous section showed how a bond order only approximates the full energetic interaction between any pair of atoms. The full interaction itself is quantified by the QCT interatomic energy, which can be expanded by a multipole expansion. This leads to the bond order curiously appearing as the equivalent of "charge on A times charge on B″ in the simple point charge formula of Coulomb energy. Note, however, that the bond order cannot be written as a product of a quantity purely depending on A and another purely depending on B.

An informative study [88], published in 2013, shows how the interatomic exchange energy V_x^{AB} behaves as a function of the elements A and B and their internuclear distance, for 31 small covalent molecules (including ions) and 3 van der Waals complexes. This paper shows that V_x^{AB} values aggregate in clusters and that the largest V_x^{AB} values constitute the covalently bonded pairs. As such, the molecular graph for a given compound draws itself from this first cluster of largest V_x^{AB} values. An example is the structure of diborane, (B_2H_6), which was controversial prior to 1951, when Longuet-Higgins proposed the now universally accepted structure (which Pauling got wrong). The ball-and-stick diagram of B_2H_6 automatically follows from the eight highest $\left|V_x^{AB}\right|$ values, all for BH pairs. At HF/6-311G(d,p) level, the two largest (absolute) values are 385 and 222 kJ mol^{-1}, corresponding to the covalent bonds $BH_{terminal}$ and BH_{bridge}, respectively. The next strongest interaction is that between the bridging hydrogens (117 kJ mol^{-1}), which is more than three times larger than the value between the two borons (34 kJ mol^{-1}). This observation is consistent with that made in connection with bond orders (see previous section). Although this fact was already observed in 1999 and discussed in a paper [85] entitled the "Lewis model and beyond", many a practitioner of the molecular orbital paradigm may spontaneously point out that the HH interaction is something new to her, or more modernly to him, and that a generous pinch of BB bonding is easier to understand. This is an example of QCT offering an interpretation diametrically opposed to that offered by the MO model.

Figure 7 shows the dependence of V_x^{AB} for all atom pairs in the global energy minimum of the water dimer. It is immediately clear that the various interatomic energies bunch up in non-overlapping clusters, about an order of magnitude apart from each other. The yellow cluster is the one with the highest absolute values. The next strongest interaction is the H. . .O hydrogen bond at around 30 kJ/mol, closely followed by V_x^{OO}. This surprising closeness suggests that the hydrogen bond is best seen as an interaction between three atoms really, in other words like a [O–H. . .O] system. In very strong hydrogen bonded systems such as [F–H. . .F]$^-$, the V_x^{FH} value is as high as 159 kJ/mol, while V_x^{FF} is 96 kJ/mol.

Table 3 shows a handful of molecules sampled from [88], where more data can be inspected, albeit in the unfortunate unit of kcal/mol. As anticipated from the bond order data in Table 3, the CH bond has the highest $\left|V_x^{AB}\right|$ value of all *EH*

interactions in the second row hydrides (E=Li, Be, B, C, N, O or F). In contrast to the conduct seen with bond orders, the highest central-ligand to ligand–ligand ratio (V_x^{CL}/V_x^{LL}) now occurs in water $\left(V_x^{OH}/V_x^{HH} = 176\right)$, monotonically decreasing over methane's value $\left(V_x^{CH}/V_x^{HH} = 50\right)$ to BeH_2 where it is only 7. In the boron-containing series, BH_3, BCl_3, BF_3 and BO_3^-, the ratio is 6, 4, 3 and 2.4, respectively, showing the sizable ligand–ligand delocalisation. Other relatively small ratios are found in four more oxides in Table 3 NO_3^-, CO_3^{2-}, PO_3^- and SO_3^- corresponding to V_x^{EO}/V_x^{OO} values of 16, 5, 7 and 9, respectively.

A look at hydrocarbons leads first to the C–C bonds in the classic series of ethyne, ethane and ethane, where the respective proportionality of the successive V_x^{CC} values is 2.5:1.7:1.0. Clearly, the formal Lewis diagram proportionality of 3:2:1 is not recovered. The V_x^{CH} value in ethane is 749 kJ/mol, a value conserved within 4 kJ/mol (i.e. 0.5%) in a host of saturated hydrocarbons (not shown in Table 3). Even in CH_3F, the C–H exchange energy is still 745 kJ/mol. This extraordinary transferability is echoed in the small difference (13 kJ/mol or 3%) in V_x^{BH} values in BH_3 and B_2H_6. In this context it is also remarkable to find that V_x^{CH} is 766 kJ/mol, both in benzene and in ethene. The weakest CH bonds are those in ethyne and in formic acid (both 707 kJ/mol). Interestingly, these correspond to the only cases in which the QCT charge of hydrogens bonded to carbon atoms is positive, referring to acidic hydrogen atoms. In all other cases, even in CH_3F and

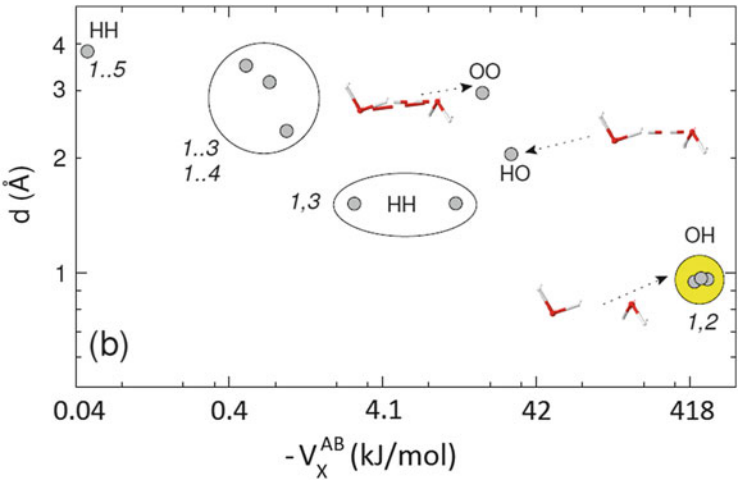

Fig. 7 The interatomic exchange energies found in the C_s global minimum energy configuration of the water dimer calculated at CAS(6,5)/6-311G(d,p) level of theory. The (*solid* or *dashed*) *coloured stripes* in the Lewis diagrams connect the atoms involved in the interaction. Three different (by C_s symmetry) V_x^{OH} values, appearing within each of the water monomers, cluster within the *yellow disc*. The next strongest interaction is the H. . .O hydrogen bond at around 30 kJ/mol, closely followed by V_x^{OO}. This surprising closeness suggests that the hydrogen bond is best seen as an interaction between three atoms really, [O–H. . .O]

Table 3 Interatomic exchange energies of some simple molecules at HF/6-311G(d,p)//HF/6-311G(d,p) level

Molecule	AB	$\lvert V_x^{AB}\rvert$	Molecule	AB	$\lvert V_x^{AB}\rvert$	Molecule	AB	$\lvert V_x^{AB}\rvert$	Molecule	AB	$\lvert V_x^{AB}\rvert$
HF	HF	372	BF_3	BF	276	B_2H_6[a]	BB	34	CH_3F	CH	745
H_2O	OH	527		FF	92		BH_t	385		CF	573
	HH	3	BCl_3	BCl	326		BH_b	222		FH	31
NH_3	NH	707		ClCl	88		H_bH_b	117		HH	13
	HH	6	BO_3^-	BO	293		H_bH_t	54	FHF^-	FH	159
CH_4	CH	753		OO	121	C_2H_2	CC	1,979		FF	96
	HH	15	CO_3^{2-}	CO	661		CH	707	HCN	CN	2,243
BH_3	BH	372		OO	121	C_2H_4	CC	1,385		HC	778
	HH	63	NO_3^-	NO	1,356		CH	766		HN	63
BeH_2	BeH	176		OO	84	C_2H_6	CC	795			
	HH	27	PO_3^-	PO	607		CH	749			
LiH	LiH	92		OO	84	C_6H_6	CC_o	1,096			
			SO_3^-	SO	866		CC_m	26			
				OO	96		CC_p	24			
							CH	766			

[a]Diborane has two types of hydrogens: four terminal ones (H_t) and two bridging ones (H_b)

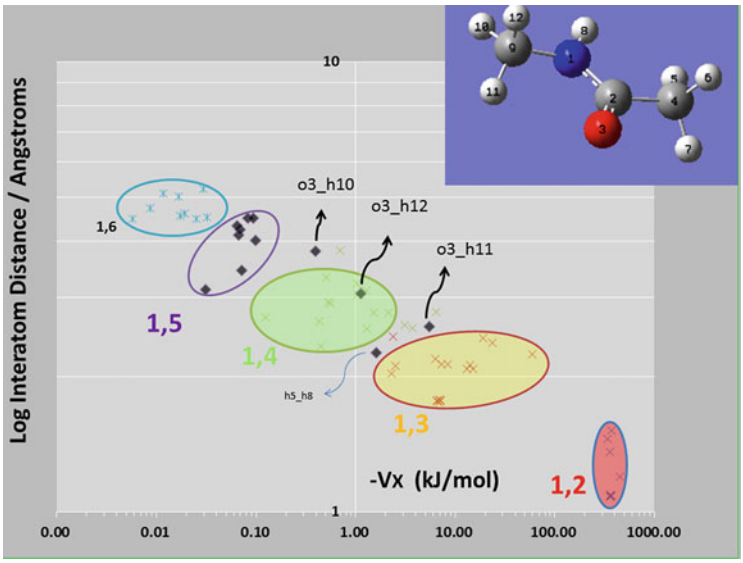

Fig. 8 The interatomic exchange energies found in *N*-methylacetamide as a function of internuclear distance

$C_3H_3^+$, the charge on hydrogen is negative. Similarly, the strongest CH bond (787 kJ/mol), found in methyllithium, corresponds to the most hydridic (i.e. negative) hydrogen.

Looking at benzene, the V_x^{CC} value between C_{ipso} and C_{ortho} is intermediate between that of ethane and ethene, as expected, the proportionality being 1.7 (ethene):1.4 (benzene):1.0 (ethane). The V_x^{CC} value between C_{ipso} and C_{meta} is 42 times smaller than that between C_{ipso} and C_{ortho}. Whereas this serious plunge is expected, what is perhaps more surprising is that the V_x^{CC} value between C_{ipso} and C_{para} is about the same as that between C_{ipso} and C_{meta}. This effect is a signature of strong 1,4 (ipso-*para*) delocalisation in the benzene ring, perhaps reminiscent of Dewar benzene.

The highest value found in Table 3 is that of the cyano group in HCN, or 2,243 kJ/mol. Only in N_2 does one find a higher value, that is, 2,427 kJ/mol. In HCN the V_x^{CH} value is still an almost invariant 778 kJ/mol, which deviates by barely 4% from the average of 749 kJ/mol.

More plots of V_x^{AB} versus internuclear distance (see Fig. 7) have been [88] published and should continue to be published because they reveal important chemical phenomena (e.g. hydrogen bonding). Figure 8 shows another (unpublished) example of how the onset of an intramolecular hydrogen bond can be detected. In *N*-methylacetamide, which is a well-studied prototype molecule for the peptide bond, there is a set of remarkable interactions between the oxygen and the hydrogen atoms of the more distant methyl group. The O3–Hn ($n = 10, 11, 12$) interactions are 1,5 interactions because there are four covalent bonds between O3

and Hn. There is a clearly separated, non-overlapping cluster of 1,5 interactions (in purple) spanning internuclear distance of 3 Å to just under 5 Å, with V_x^{OH} values under 0.1 kJ/mol. The O3–Hn ($n = 10, 11, 12$) interactions escape from this cluster with O3–H10 and O3–H12 adopting V_x^{OH} values up to an order of magnitude larger than the average cluster value but still falling within the [3Å, 5Å] interval. The O3–H11 interaction reaches an internuclear distance under 3 Å and a V_x^{OH} value of just over 5 kJ/mol. The position of this interaction indicates an unusually high degree of delocalisation, which is a signature of covalency. There is no bond critical point between O3 and H11 but a small deformation resulting from bringing the atoms slightly closer would lead to a bond critical point.

The sudden presence or absence of a bond critical point depending on the minute changes in nuclear positions is seen as a problem. Of course the yes/no character of chemical bonding has to be ultimately conceded in a reaction, where bonds are made or broken. However, many a chemist is uncomfortable with the binary nature of the bond critical point's presence. This is why some introduced [89] the so-called NCI method. Essentially this is a way of weakening the concept of a bond critical point and plotting contour plots of regions where it is *about* to appear. Two alternatives to this arbitrary route are known: either one looks at clusters of bond critical points in a dynamical picture [90], for example, in ethanol–water clusters sampled from a molecular dynamics simulation of a liquid mixture, or one studies *global* QCT properties (i.e. atomic self-energies and interaction energies) as opposed to *local* properties[7] (i.e. the presence of a bond critical point and properties evaluated at its position). Focusing on anomalies in plots of V_x^{AB} versus AB distance, as done in Fig. 8, is an important way forward and more reliable than NCI.

Finally, we discuss an interesting effect seen in saturated hydrocarbons, from ethane to pentane. In the staggered conformation of ethane, V_x^{HH} values were compared between a hydrogen of one methyl group with a hydrogen in the other methyl group. In particular, the $|V_x^{HH}|$ value of two hydrogen atoms in a planar HCCH arrangement (i.e. *trans*) was several times larger than that of two hydrogens in a non-planar arrangement. This effect is repeatedly confirmed along the methylene chain, throughout the series of hydrocarbons. From this consistent set of observations, a simple rule can be drawn, thereby making "back-of-the-envelope" predictions possible. Note that no explanation of this effect in terms of dated concepts such as hyperconjugation is necessary. One simply has to give the effect a name and apply it (within an appropriate action radius).

There is a need to systematically study patterns in V_x^{AB} values computed in molecular crystals and condensed matter assemblies where hitherto unnamed interactions, based on simple observations in the Cambridge Structural Database

[7] Local properties, which are very cheap to compute, should not be dismissed if they are used in an informed way and in close relationship with experiment. For example, the electron density at the bond critical point marking a hydrogen bond shows very close similarity with the increase in infrared intensity on hydrogen-bond formation (see [107]).

and the Protein Data Bank, are still lurking [91], in spite of considerable QCT progress [92] in the area of non-molecular ionic crystals.

13 The Laplacian of the Electron Density: The Atomic L-Graph

Much has been written [2, 17, 24, 25, 93–101] about the Laplacian of the electron density, denoted $\nabla^2\rho$, but here we revise just enough in order to communicate the results of an overlooked paper [102] cataloguing so-called L-graphs, which extract lone pairs and bonded pairs from modern wave functions. The Laplacian of the electron density is the second segment of QCT, an old function already studied in the 1980s. It thus predates the topological study [27] of the electron localisation function (ELF). In 1996 it was shown [103] that ELF and minus the Laplacian or the L-function are, in general, homeomorphic: the patterns of critical points in the two functions can be brought into 1–1 correspondence. ELF exploits the fact that the kinetic energy density contains information regarding the spatial localisation of the electrons. The Laplacian of the electron density, however, recovers this localisation completely empirically.

The Laplacian itself is a mathematical entity, proposed long before the birth of quantum mechanics, measuring the local curvature of a function in three dimensions. However, as stated above, it is more natural to use its negative (i.e. L(**r**)) because then this L-function is then *positive* when the function is locally *concentrated*, and L(**r**) is *negative* when it is locally depleted. The property allows it to reveal the shell structure of an atom (correctly up to and including period 4 elements), with only its electron density as input. The latter capacity makes L(**r**) a popular tool in X-ray crystallography although L(**r**) demands very accurate electron densities because it acts as a magnifying glass and thus reveals shortcomings. Calculated electron densities are more robust and accurate than experimental ones, thus inviting the Laplacian to act on calculated ones, especially in the molecular case.

Let us take methanal (H_2CO) as an example. Figure 9 shows a progression of four panels, starting from a detailed 2D contour plot and leading to an abstract yet complete object, called the L-graph. The latter is a collection of four *atomic L-graphs* in this case. Each atomic L-graph shows the maxima in $L(\mathbf{r}) = -\nabla^2\rho(\mathbf{r})$, each of which can be associated with a lone (electron) pair or a bonded (electron) pair. This protocol shows how the Lewis model can be extracted from modern wave functions.[8]

[8] The paper from which this information is drawn found that the B3LYP/6-311+G(2d,p) level of theory offers a good compromise between CPU time and wave function quality. The topological graphs remain invariant for basis sets of triple-zeta quality or higher.

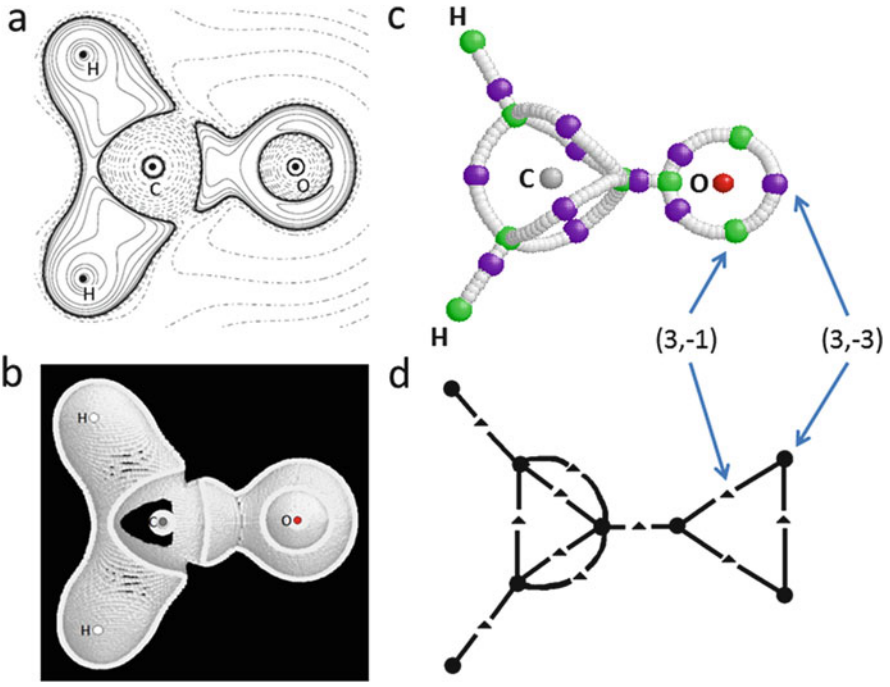

Fig. 9 Representations of minus the Laplacian of the electron density or the L-function in methanal: (**a**) constant value contour plots (*solid lines* for positive values) in the molecular plane; the K shell of the C and O atoms is very close to the respective nuclear positions; (**b**) slice through a 3D envelope of the L-function being zero; (**c**) the critical points (maximum = *purple* = (3,−3) and saddle point = *green* = (3,−1)) in the *valence shell charge concentration* (VSCC) region and (**d**) L-graph, schematically showing the connectivity (*edges*) between the maxima (at the *vertices*)

Figure 10 shows all the atomic L-graphs encountered in the 31 molecules investigated. As shown in Fig. 10a, the hydrogen L-graph consists only of an edge connecting two vertices, a maximum approximately coincident with the hydrogen nucleus and a (3,−1) critical point. In a full L-graph (spanning an entire molecule), the latter (3,−1) critical is superimposed onto the (3,−1) critical point of a neighbouring atomic L-graph, representing an atom to which the hydrogen is bonded. The superposition of (3,−1) critical points is the universal way of building an L-graph from atomic L-graphs, except when atoms are connected by triple bonds.

Figure 11 displays graphs of seven molecules containing only C, H and N: ammonia, methylamine, hydrazine, methanimine, ethanimine, *N*-methylpropanimine and ethanenitrile (acetonitrile). Ammonia consists of three hydrogen atomic L-graphs and one new atomic L-graph, that of tri-coordinated nitrogen. This

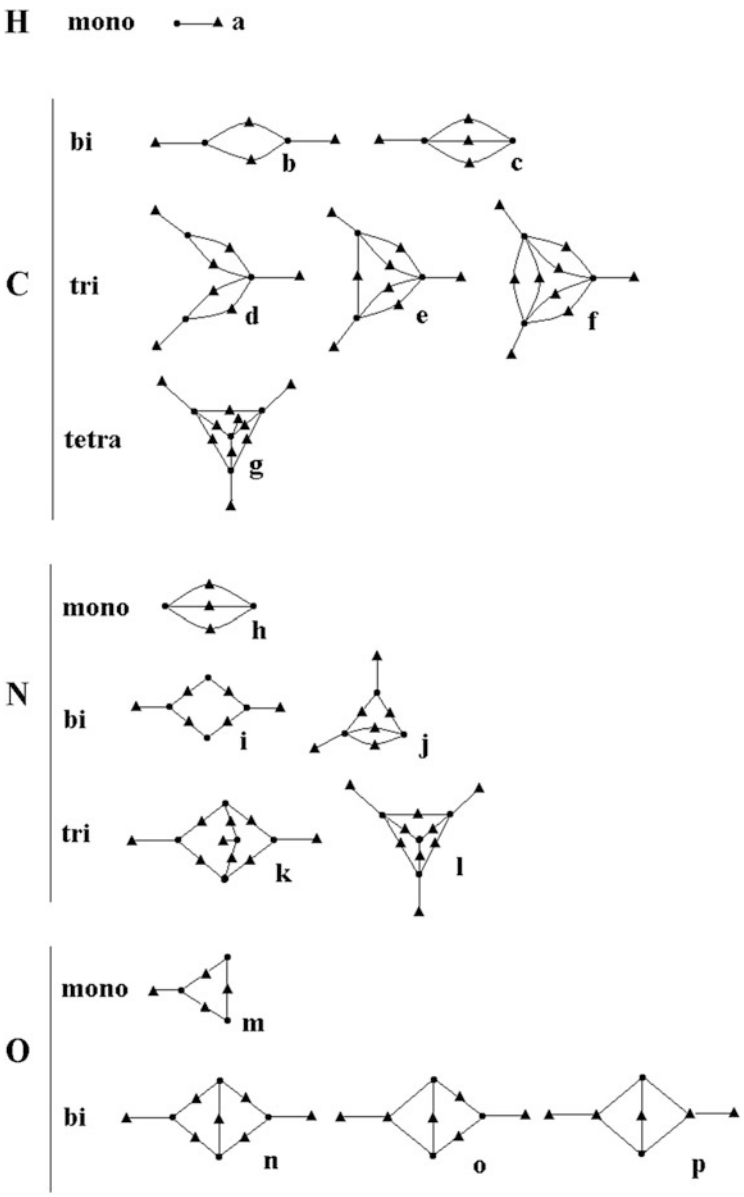

Fig. 10 Atomic L-graphs. (*a*) mono-coordinated (i.e. singly bonded) hydrogen, (*b*) bi-coordinated carbon (in ketene), (*c*) bi-coordinated carbon (in triple bond), (*d*) tri-coordinated carbon (in ketene), (*e*) tri-coordinated carbon (in keto), (*f*) tri-coordinated carbon (in O–C=O), (*g*) tetra-coordinated carbon, (*h*) mono-coordinated nitrogen, (*i*) linear bi-coordinated nitrogen, (*j*) non-linear bi-coordinated nitrogen, (*k*) "(near) planar" tri-coordinated nitrogen, (*l*) "non-planar" tri-coordinated nitrogen, (*m*) mono-coordinated oxygen, (*n*) bi-coordinated oxygen (alcohol, carboxyl, enol, ester, ether), (*o*) bi-coordinated oxygen (oxime) and (*p*) bi-coordinated oxygen (oxirane)

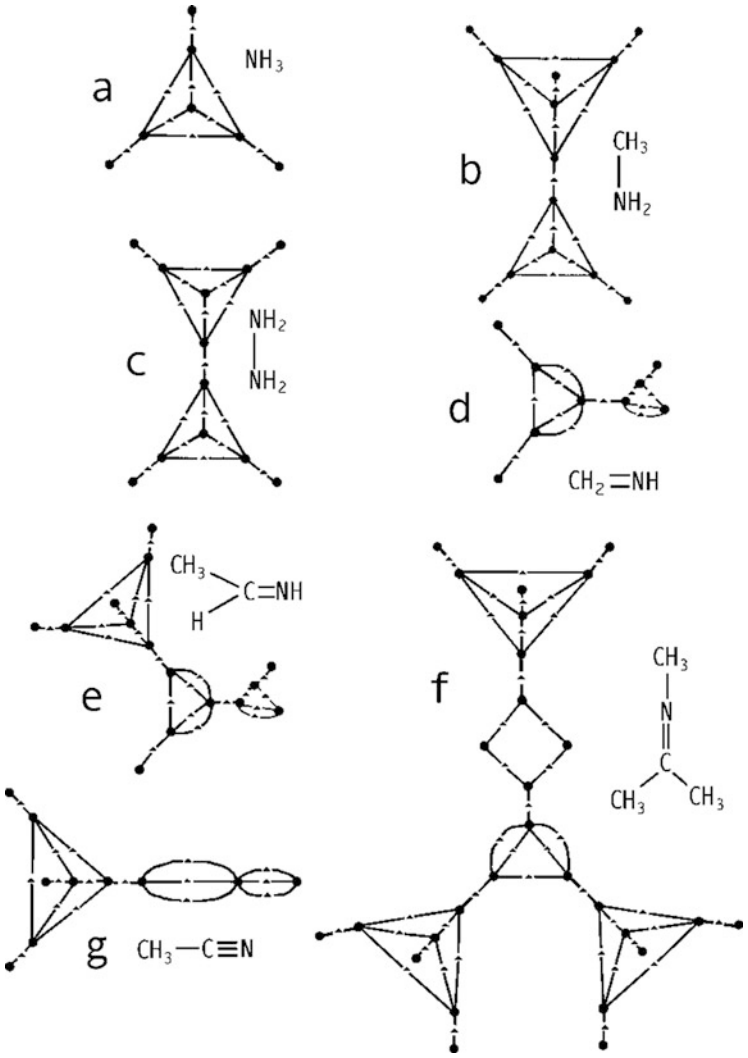

Fig. 11 L-graphs of molecules containing only C, H and N: (**a**) ammonia, (**b**) methylamine, (**c**) hydrazine, (**d**) methanimine, (**e**) ethanimine, (**f**) *N*-methyl-2-iminopropane and (**g**) ethanenitrile (acetonitrile)

atomic L-graph, shown in Fig. 10l, has been extensively discussed before [100] as part of a dynamical study of the full topology of the Laplacian in ammonia's umbrella inversion. This study showed that a nitrogen in a nearly planar environment adopts the atomic L-graph of Fig. 10k, while a moderately non-planar nitrogen adopts the atomic L-graph of Fig. 10l. In the latter graph, the central vertex should be associated with the lone pair. This atomic L-graph is preserved in

methylamine (Fig. 11b), where it is straightforwardly combined with the ubiquitous atomic L-graph of tetra-coordinated carbon (Fig. 10g). The graph of the non-planar molecule hydrazine (H_2NNH_2, Fig. 11c) is a simple juxtaposition of two atomic L-graphs of tri-coordinated nitrogen. The Schiff base methanimine, shown in Fig. 11d, is the first example of a bi-coordinated nitrogen. The atomic L-graph of the (non-linear) iminic nitrogen is shown in Fig. 10j. The CNH fragment in ethanimine (Fig. 11e) is also non-linear and exhibits the same atomic L-graph. However, the CNC fragment in *N*-methyl-2-iminopropane (Fig. 11f) is linear and leads to a different atomic L-graph for bi-coordinated nitrogen, shown in Fig. 10i. The imine functional group is the nitrogen analogue of the carbonyl group. This fact is reflected in the observation that the L-graphs of all three molecules (Fig. 11d, e and f) that contain the imine functional group have an atomic L-graph of carbon (Fig. 10e), identical to that in methane (Fig. 9d). The cyano group of ethanenitrile (acetonitrile, Fig. 11g) contains two almost identical atomic L-graphs, one for the carbon (Fig. 10c) and one for the nitrogen (Fig. 10h). This is a case where the two atomic L-graphs are not connected via a common (3,−1) critical point but via a (3,−3) critical point, as also seen in CH_3–C≡CH.

14 Atomic Charges

This section will be very short in an attempt to increase the impact of the main message. In order to minimise overlap with other contributions of the author, this chapter has so far remained silent on QTAIM as a method to provide atomic charges. Ironically, many casually observing computational chemists still perceive QTAIM primarily as (yet) another population analysis. They thus might expect a few words on the QTAIM charge, especially on how it compares with other charge generators.

There are papers that try to settle the difficult question which atomic charge is "better" than another (e.g. [104]). This literature will not be reviewed here. In the numerical range of charge values for atoms in polar bonds, QTAIM charges typically appear at the end of large magnitudes, while the (original) Hirshfeld charges show up at the other end, that is, of small magnitude. Curiously, the iterative Hirshfeld scheme [105], which was set up to avoid a well-known shortcoming of the original method, returns charges of much larger magnitude, thereby veering towards the QTAIM side.

The electronic population of a topological atom is obtained by integrating the electron density within its volume. After correction for the nuclear charge, one then obtains the net atomic charge. For example, the oxygen in water will have a net atomic charge of about −1.1e. This number expresses the charge transfer inside water. One can say that, on average, oxygen pulls towards itself the charge of just over one electron. In a literal sense, this electronic charge belongs to this oxygen. This charge has been obtained by adding (i.e. integrating) all the little bits of electronic charge density inside the oxygen's volume, in the same way that one

can calculate the total air content of a room. *The atomic charge is a signature of charge transfer*, *no more*, *no less*.

The atomic charge does not say much at all about the shape of the atom, or more precisely, how electronic charge is distributed within the atomic volume. This is the role of atomic multipole moments [72]. The dipole moment, for example, measures how much the centroid of the electronic charge is shifted from the nucleus and in which direction. Higher multipole moments gauge increasingly more complex and subtle features of charge distribution within the atom. The most direct and natural way to know the features of the atomic electron density is to inspect its multipole moments and use them in the calculation of electrostatic interaction. To demand that a single atomic point charge captures [106] all the complexities of an atomic electron density is futile. In fact, if one tries to do so anyway [40], then the original, authentic meaning of an atomic charge as a measure of charge transfer is destroyed.

In summary, QTAIM provides robust and meaningful atomic charges, which express the patterns of charge flow within a molecule, or ionic or molecular assemblies. At long range these charges are sufficient to describe how a topological atom interacts electrostatically with another atom, but at short range higher multipole moments must be used.

15 Conclusion

Quantum chemical topology (QCT) is a highly original way of partitioning and characterising a quantum mechanical system, whether a single molecule, a molecular assembly, an ionic crystal or any piece of condensed matter. An innocuous paper in 1972 marked the birth of this truly novel approach in theoretical chemistry, called QTAIM, which is the first and hence oldest segment of QCT. QCT has witnessed a very long incubation period in its uptake by a larger community, which is due to various reasons: (1) its novelty, (2) its computational cost, (3) imperfect robustness of integration algorithms, (4) the polarising character of QTAIM's originator and his reduced interest (5) in solving real chemical problems, (6) in diplomatic and didactic dissemination of chemical results and (7) creating user-friendly and efficient computer programs.

Today, many people have heard of QCT but it is still often confused with just being another population analysis. Some of those who understand QCT better than that have attacked it on various scientific grounds, with varying success. Overall, leaving alone unresolved issues and statements that still need work, the edifice that is QCT has withstood the test of time. In fact, in high-resolution crystallography, QCT has been mainstream for a decade. However, at a more ambitious level, one could ask when, if ever, QCT will feature in undergraduate textbooks.

Although there is still a lot of work to do, anyone with an appreciation for clear and minimal thinking will be attracted to what QCT has achieved so far and what it will offer in the future. Unless chemistry is really this hopelessly complex universe that can never be rationalised, let alone elegantly, one should strive for a falsifiable bottom-up rationalisation. Such a research program should start from modern

quantum mechanical wave functions and discover one chemical concept after another, or at least correct (or modify) existing concepts.

Lewis died long before the birth of QCT but, based on his way of thinking, he would probably have liked QCT as an approach to rigorously recover his insights from modern wave functions and to then go beyond what he had achieved.

Acknowledgments I thank the EPSRC for the award of an Established Career Fellowship and am grateful to Prof. Ibon Alkorta for providing the bond order data on BF_3 and for his comments on the manuscript and to Mr. Peter Maxwell for generating Fig. 8. Dr. Matthew Mills is thanked for his help in creating Fig. 2.

References

1. Popelier PLA (2014) The quantum theory of atoms in molecules. In: Frenking G, Shaik S (eds) The nature of the chemical bond revisited. Wiley-VCH, Weinheim, pp 271–308, Chapter 8
2. Bader RFW (1990) Atoms in molecules. A quantum theory. Oxford University Press, Oxford
3. Popelier PLA (2016) On quantum chemical topology. In: Alikhani E, Chauvin R, Lepetit C, Silvi B (eds) Challenges and advances in computational chemistry and physics dedicated to "applications of topological methods in molecular chemistry". Springer
4. Popelier PLA (2005) Quantum chemical topology: on bonds and potentials. In: Wales DJ (ed) Structure and bonding. Intermolecular forces and clusters, vol 115. Springer, Heidelberg, pp 1–56
5. Coulson CA (1953) The spirit of applied mathematics. Clarendon, Oxford
6. Yanez M, Sanz P, Mo O, Alkorta I, Elguero J (2009) Beryllium bonds, do they exist? J Chem Theory Comput 5:2763–2771
7. Shaik S, Danovich D, Wu W, Su P, Rzepa HS, Hiberty PC (2012) Quadruple bonding in C2 and analogous eight-valence electron species. Nat Chem 4:195–200
8. Pyykkö P (2008) Theoretical chemistry of gold. III. Chem Soc Rev 37:1967–1997
9. Braunschweig H, Dewhurst RD (2014) Boron–boron multiple bonding: from charged to neutral and back again. Organometallics 33:6271–6277
10. Arnold T, Braunschweig H, Ewing WC, Kramer T, Mies J, Schuster JK (2015) Beryllium bis (diazaborolyl): old neighbors finally shake hands. Chem Commun 51:737–740
11. Arunan E, Desiraju GR, Klein RA, Sadlej J, Scheiner S, Alkorta I, Clary DC, Crabtree RH, Dannenberg JJ, Hobza P, Kjaergaard HG, Legon AC, Mennucci B, Nesbitt DJ (2011) Definition of the hydrogen bond (IUPAC Recommendations 2011). Pure Appl Chem 83:1619–1641
12. Ball P (2011) Beyond the bond. Nature 469:26–28
13. Jorgensen WL, Pranata J (1990) Importance of secondary interactions in triply hydrogen bonded complexes: guanine-cytosine vs uracil-2,6-diaminopyridine. J Am Chem Soc 112:2008–2010
14. Popelier PLA, Joubert L (2002) The elusive atomic rationale for DNA base pair stability. J Am Chem Soc 124:8725–8729
15. Eskandari K, Van Alsenoy C (2014) Hydrogen–hydrogen interaction in planar biphenyl: a theoretical study based on the Interacting Quantum Atoms and Hirshfeld atomic energy partitioning methods. J Comput Chem 35:1883–1889
16. Popelier PLA (2007) Preface. Faraday Discuss 135:3–5
17. Popelier PLA (2000) Atoms in molecules. An introduction. Pearson Education, London

18. Matta CF, Boyd RJ (2007) The quantum theory of atoms in molecules. From solid state to DNA and drug design. Wiley-VCH, Weinheim
19. Lewis GN (1916) The atom and the molecule. J Am Chem Soc 38:762–785
20. Luechow A (2014) Maxima of |psi|**2: a connection between quantum mechanics and Lewis structures. J Comput Chem 35:854–864
21. Stone AJ (1981) Distributed multipole analysis, or how to describe a molecular charge distribution. Chem Phys Lett 83:233–239
22. Popelier PLA, Aicken FM (2003) Atomic properties of amino acids: computed atom types as a guide for future force field design. ChemPhysChem 4:824–829
23. Popelier PLA, Brémond ÉAG (2009) Geometrically faithful homeomorphisms between the electron density and the bare nuclear potential. Int J Quantum Chem 109:2542–2553
24. Bader RFW, Essen H (1984) The characterization of atomic interactions. J Chem Phys 80:1943–1960
25. Bader RFW, Gillespie RJ, MacDougall PJ (1988) A physical basis for the VSEPR model of molecular geometry. J Am Chem Soc 110:7329–7336
26. Becke AD, Edgecombe KE (1990) A simple measure of electron localization in atomic and molecular systems. J Chem Phys 92:5397–5403
27. Silvi B, Savin A (1994) Classification of chemical bonds based on topological analysis of electron localization functions. Nature (London) 371:683–686
28. Blanco MA, Pendas AM, Francisco E (2005) Interacting quantum atoms: a correlated energy decomposition scheme based on the quantum theory of atoms in molecules. J Chem Theory Comput 1:1096–1109
29. Webster B (1990) Chemical bonding theory. Blackwell, Oxford
30. Reed AE, Curtiss LA, Weinhold F (1988) Intermolecular interactions from a natural bond orbital, donor-acceptor viewpoint. Chem Rev 88:899–926
31. Mulliken RS (1955) Electronic population analysis on LCAO-MO molecular wave functions. I J Chem Phys 23:1833–1840
32. Pearson RG (2007) Applying the concepts of density functional theory to simple systems. Int J Quantum Chem 108:821–826
33. Kovacs A, Esterhuysen C, Frenking G (2005) The nature of the chemical bond revisited: an energy-partitioning analysis of nonpolar bonds. Chem Eur J 11:1813–1825
34. McWeeny R (1992) Methods of molecular quantum mechanics, 2nd edn. Academic, San Diego
35. Morokuma K (1971) Molecular orbital studies of hydrogen bonds. III C=O. . .H-O hydrogen bond in H2CO. . .H2O and H2CO. . .2H2O. J Chem Phys 55:1236–1244
36. von Hopffgarten M, Frenking G (2012) Energy decomposition analysis. WIREs Comput Mol Sci 2:43–62
37. Koritsanszky TS, Coppens P (2001) Chemical applications of x-ray charge-density analysis. Chem Rev 101:1583–1627
38. Popelier PLA (2012) Quantum chemical topology: on descriptors, potentials and fragments. In: Banting L, Clark T (eds) Drug design strategies: computational techniques and applications, vol 20. Royal Society of Chemistry, Cambridge, pp 120–163, Chapter 6
39. Popelier PLA (2012) A generic force field based on quantum chemical topology. In: Gatti C, Macchi P (eds) Modern charge-density analysis, vol 14. Springer, Berlin, pp 505–526
40. Popelier PLA (2012) New insights in atom-atom interactions for future drug design. Curr Top Med Chem 12:1924–1934
41. Cohen L (1978) Local kinetic energy in quantum mechanics. J Chem Phys 70:788–799
42. Bader RFW, Beddall PM (1972) Virial field relationship for molecular charge distributions and the spatial partitioning of molecular properties. J Chem Phys 56:3320–3329
43. Anderson JSM, Ayers PW, Hernandez JIR (2010) How ambiguous is the local kinetic energy? J Phys Chem A 114:8884–8895
44. Fletcher TL, Kandathil SM, Popelier PLA (2014) The prediction of atomic kinetic energies from coordinates of surrounding atoms using kriging machine learning. Theor Chem Acc 133 (1499):1–10
45. Bader RFW (1985) Atoms in molecules. Acc Chem Res 18:9–15

46. Biegler-Koenig FW, Nguyen-Dang TT, Tal Y, Bader RFW, Duke AJ (1981) Calculation of the average properties of atoms in molecules. J Phys B 14:2739–2751
47. Biegler-Koenig FW, Bader RFW, Tang TH (1982) Calculation of the average properties of atoms in molecules. 2. J Comput Chem 3:317–328
48. Popelier PLA, Kosov DS (2001) Atom-atom partitioning of intramolecular and intermolecular Coulomb energy. J Chem Phys 114:6539–6547
49. Rafat M, Popelier PLA (2007) Topological atom-atom partitioning of molecular exchange energy and its multipolar convergence. In: Matta CF, Boyd RJ (eds) Quantum theory of atoms in molecules, vol 5. Wiley, Weinheim, pp 121–140
50. Darley MG, Popelier PLA (2008) Role of short-range electrostatics in torsional potentials. J Phys Chem A 112:12954–12965
51. Rafat M, Popelier PLA (2007) Atom-atom partitioning of total (super)molecular energy: the hidden terms of classical force fields. J Comput Chem 28:292–301
52. Pendás AM, Blanco MA, Francisco E (2006) The nature of the hydrogen bond: a synthesis from the interacting quantum atoms picture. J Chem Phys 125:184112-1-20
53. Pendas AM, Blanco MA, Francisco E (2009) Steric repulsions, rotation barriers, and stereoelectronic effects: a real space perspective. J Comput Chem 30:98–109
54. Pendas AM, Francisco E, Blanco MA (2006) Binding energies of first row diatomics in the light of the Interacting Quantum Atoms approach. J Phys Chem A 110:12864–12869
55. Popelier PLA (2015) QCTFF: on the construction of a novel protein force field. Int J Quantum Chem 115:1005–1011
56. Cardamone S, Hughes TJ, Popelier PLA (2014) Multipolar electrostatics. Phys Chem Chem Phys 16:10367–10387
57. Mezey PG (1990) Molecular surfaces. In: Lipkowitz KB, Boyd DB (eds) Reviews in computational chemistry. VCH, New York, pp 265–294
58. Mezey PG (1993) Shape in chemistry. An introduction to molecular shape and topology. VCH, New York
59. Malcolm NOJ, Popelier PLA (2003) An improved algorithm to locate critical points in a 3D scalar field as implemented in the program MORPHY. J Comput Chem 24:437–442
60. Bader RFW, Legare DA (1992) Properties of atoms in molecules—structures and reactivities of boranes and carboranes. Can J Chem 70:657–676
61. Bone RGA, Bader RFW (1996) Identifying and analyzing intermolecular bonding interactions in van der Waals molecules. J Phys Chem 100:10892–10911
62. Cerpa E, Krapp A, Vela A, Merino G (2008) The implications of symmetry of the external potential on bond paths. Chem Eur J 14:10232–10234
63. Cerpa E, Krapp A, Flores-Moreno R, Donald KJ, Merino G (2009) Influence of endohedral confinement on the electronic interaction between He atoms: a He2@C20H20 case study. Chem Eur J 15:1985–1990
64. Wang S-G, Qiu Y-X, Schwarz WHE (2009) Bonding or nonbonding? Description or explanation? "Confinement bonding" of He@adamantane. Chem Eur J 15:6032–6040
65. Poater J, Sola M, Bickelhaupt FM (2006) Hydrogen–hydrogen bonding in planar biphenyl, predicted by atoms-in-molecules theory, does not exist. Chem Eur J 12:2889–2895
66. Bader RFW (2009) Bond paths are not chemical bonds. J Phys Chem A 113:10391–10396
67. Dem'yanov P, Polestshuk P (2012) A bond path and an attractive Ehrenfest force do not necessarily indicate bonding interactions: case study on M2X2 (M = Li, Na, K; X = H, OH, F, Cl). Chem Eur J 18:4982–4993
68. Pendas AM, Francisco E, Blanco MA, Gatti C (2007) Bond paths as privileged exchange channels. Chem Eur J 13:9362–9371
69. Tognetti V, Joubert L (2013) On the physical role of exchange in the formation of an intramolecular bond path between two electronegative atoms. J Chem Phys 138:024102
70. Alvarez S (2015) What we mean when we talk about bonds. In: Chemistry world. Royal Society of Chemistry, Cambridge, pp 36–37
71. AIMAll Todd A. Keith (2014) TK Gristmill Software, Overland Park KS, USA (aim.tkgristmill.com)

72. Popelier PLA, Joubert L, Kosov DS (2001) Convergence of the electrostatic interaction based on topological atoms. J Phys Chem A 105:8254–8261
73. Rafat M, Popelier PLA (2006) A convergent multipole expansion for 1,3 and 1,4 Coulomb interactions. J Chem Phys 124:144102-1-7
74. James HM, Coolidge AL (1933) The ground state of the hydrogen molecule. J Chem Phys 1:825–835
75. Kolos W, Wolniewicz L (1964) Accurate adiabatic treatment of the ground state of the hydrogen molecule. J Chem Phys 41:3663–3673
76. McWeeny R (1979) Coulson's valence. Oxford University Press, Oxford
77. Angyan JG, Loos M, Mayer I (1994) Covalent bond orders and atomic valence indices in the topological theory of atoms in molecules. J Phys Chem 98:5244–5248
78. Chávez-Calvillo R, García-Revilla M, Francisco E, Martín Pendás A, Rocha-Rinza T (2015) Dynamical correlation within the Interacting Quantum Atoms method through coupled cluster theory. Comput Theor Chem 1053:90–95
79. Pendas AM, Blanco MA, Francisco E (2007) Chemical fragments in real space: definitions, properties, and energetic decompositions. J Comput Chem 28:161–184
80. Pendas AM, Francisco E, Blanco MA (2005) Two-electron integrations in the quantum theory of atoms in molecules with correlated wave functions. J Comput Chem 26:344–351
81. Rafat M, Popelier PLA (2007) Long range behaviour of high-rank topological multipole moments. J Comput Chem 28:832–838
82. Varshalovich DA, Moskalev AN, Khersonskii VK (1988) Theory of angular momentum. World Scientific, Singapore
83. Poater J, Sola M, Duran M, Fradera X (2002) The calculation of electron localization and delocalization indices at the Hartree–Fock, density functional and post-Hartree–Fock levels of theory. Theor Chem Acc 107:362–371
84. Francisco E, Pendas AM, Blanco MA (2007) Electron number probability distributions for correlated wave functions. J Chem Phys 126:094102,1-12
85. Fradera X, Austen MA, Bader RFW (1999) The Lewis model and beyond. J Phys Chem A 103:304–314
86. Wang YG, Matta CF, Werstiuk NH (2004) Comparison of localization and delocalization indices obtained with Hartree-Fock and conventional correlated methods: effect of Coulomb correlation. J Comput Chem 24:1720–1729
87. Forslund LE, Kaltsoyannis N (2003) Why is the F-2 bond so weak? A bond energy decomposition analysis. New J Chem 27:1108–1114
88. Garcia-Revilla M, Francisco E, Popelier PLA, Martin-Pendas AM (2013) Domain-averaged exchange correlation energies as a physical underpinning for chemical graphs. ChemPhysChem 14:1211–1218
89. Johnson ER, Keinan S, Mori-Sanchez P, Contreras-Garcia J, Cohen AJ, Yang W (2010) Revealing noncovalent interactions. J Am Chem Soc 132:6498–6506
90. Mejía SM, Mills M, Shaik MS, Mondragon F, Popelier PLA (2011) The dynamic behaviour of a liquid ethanol-water mixture: a perspective from quantum chemical topology. Phys Chem Chem Phys 13:7821–7833
91. Paulini R, Mueller K, Diederich F (2005) Orthogonal multipolar interactions in structural chemistry and biology. Angew Chem Int Ed 44:1788–1805
92. Pendas AM, Francisco E, Costales A (2013) Perspectives for quantum chemical topology in crystallography. Phys Scr 87:048106
93. MacDougall PJ, Hall MB, Bader RFW, Cheeseman JR (1989) Extending the VSEPR model through the properties of the Laplacian of the charge-density. Can J Chem 67:1842–1846
94. Bader RFW, MacDougall PJ, Lau CDH (1984) Bonded and nonbonded charge concentrations and their relation to molecular-geometry and reactivity. J Am Chem Soc 106:1594–1605
95. Gillespie R, Johnson SA (1997) Study of bond angles and bond lengths in disiloxane and related molecules in terms of the topology of the electron density and its Laplacian. Inorg Chem 36:3031–3039

96. Gillespie RJ (2000) Improving our understanding of molecular geometry and the VSEPR model through the ligand close-packing model and the analysis of electron density distributions. Coord Chem Rev 197:51–69
97. Gillespie RJ, Bytheway I, Dewitte RS, Bader RFW (1994) Trigonal bipyramidal and related molecules of the main-group elements - investigation of apparent exceptions to the VSEPR model through the analysis of the Laplacian of the electron-density. Inorg Chem 33:2115–2121
98. Gillespie RJ, Popelier PLA (2001) Chemical bonding and molecular geometry from Lewis to electron densities. Oxford University Press, New York
99. Malcolm NOJ, Popelier PLA (2003) The full topology of the Laplacian of the electron density: scrutinising a physical basis for the VSEPR model. Faraday Discuss 124:353–363
100. Malcolm NOJ, Popelier PLA (2001) On the full topology of the Laplacian of the electron density II: umbrella inversion of the ammonia molecule. J Phys Chem A 105:7638–7645
101. Popelier PLA (2000) On the full topology of the Laplacian of the electron density. Coord Chem Rev 197:169–189
102. Popelier PLA, Burke J, Malcolm NOJ (2003) Functional groups expressed as graphs extracted from the Laplacian of the electron density. Int J Quantum Chem 92:326–336
103. Bader RFW, Johnson S, Tang TH, Popelier PLA (1996) The electron pair. J Phys Chem 100:15398–15415
104. de Oliveira AE, Haiduke RLA, Bruns RE (2000) Atomic mean dipole moment derivatives and GAPT charges. J Phys Chem A 104:5320–5327
105. Bultinck P, Van Alsenoy C, Ayers PW, Carbó-Dorca R (2007) Critical analysis and extension of the Hirshfeld atoms in molecules. J Chem Phys 126:144111
106. Yuan Y, Mills MJL, Popelier PLA (2014) Multipolar electrostatics for proteins: atom-atom electrostatic energies in crambin. J Comput Chem 35:343–359
107. Rozenberg M (2014) RSC Adv 4:26928

Struct Bond (2016) 170: 119–168
DOI: 10.1007/430_2015_186

Published online: 27 October 2015

Electron Pairs in Position Space

M. Kohout

Who is right? Questions such as these, involving not facts but ways of looking at facts, can lead to hatred and bloodshed when they touch human emotions.
– Hermann Weyl

Abstract The electron pair is a central object in chemist's view of the chemical bond. The definition and description of the electron pair in the position space is a complex problem within the quantum chemistry. Several different possibilities of how to accomplish this task, i.e., how to describe the localizability of an electron and electron pair, are given in a historical survey. The derivation of the electron localizability indicator (ELI) is presented and the application of ELI for the bonding analysis is examined for few systems. The importance of the ELI-q describing the singlet-coupled electron pairs and its connection to Lewis idea of bonding is highlighted.

Keywords Correlation • Electron localizability • Electron pair • ELI • Fermi hole

Contents

M. Kohout (✉)
Max Planck Institute for Chemical Physics of Solids, Nöthnitzer Str. 40, 01187 Dresden, Germany
e-mail: kohout@cpfs.mpg.de

1 Introduction

A molecule or solid is a system build up from atomic nuclei and the corresponding number of electrons. With an appropriate Hamiltonian $\hat{H}$, such system is described by a wave function Ψ, the solution of the eigenvalue problem $\hat{H}\,\Psi = E\Psi$. For fixed position of the nuclei (Born–Oppenheimer approximation), the wave function is a $3N$-dimensional mathematical object describing the movement of N electrons. The many-electron wave function is usually expressed as expansions using products of one-electron functions (orbitals) possibly expanded with chosen set of primitive functions (Slater functions, Gauss functions, plane waves, etc.). Even for time-independent nonrelativistic wave function, it is very difficult to perform an analysis of the system without further approximations or reductions.

The properties of a system can be inferred from the (approximate) wave function corresponding to the chosen Hamiltonian. Due to the high dimensionality of the wave function, the analysis of the system is often performed in the (Hilbert) space of the basis functions, i.e., adopting certain "mean field" point of view. With this, the influence of the contributing basis functions on the form of the wave function is examined, trusting in a meaningful relationship between the chosen basis (Ansatz) and more or less well-defined "physical" objects (atoms, groups, bonds, lone pairs). Such an analysis extends from the comparison of orbital energies (Aufbau principle), over the examination of the contribution weights (Mulliken population analysis), up to the inspection of the spatial form of the orbitals (orbital overlap, bond directions).

The expectation value of an operator $\hat{A}$ is given by the integral over the whole space. For $\langle \hat{A} \rangle = \int \Psi^* \hat{A}\, \Psi \mathrm{d}V$ operators acting on 2 particles at most, the 2-matrix

$\Gamma^{(2)}$ can be utilized to determine the expectation value $\langle \hat{A} \rangle = \int \hat{A}\, \Gamma^{(2)} \mathrm{d}V$, where the integration runs over the spin space coordinates of 2 particles. With this at hand, realizing the integration over regions of interest, the analysis of the system can be performed in real space (momentum space) without the explicit reference to the basis. Moreover, the results are independent of a unitary rotation of the basis. It is possible to examine the distribution of the 2-particle function $\hat{A}\Gamma^{(2)}$ itself, possibly fixing the coordinate of 1 particle (conditional property density) or integrating one coordinate over chosen region (e.g., in case of the domain-averaged Fermi hole [1]). Integrating one coordinate over the whole space yields a single-particle property density (corresponding to the chosen operator $\hat{A}$) which again can be examined, either itself or as integrals over chosen regions of space, an approach utilized in the analysis of electron density Laplacian, respectively to calculate the atomic charges [2].

Thus, various electron (pair) density functions can be evaluated in real space (also termed the coordinate space, position space, physical space, or direct space) in manifold ways. The analysis of property values at certain positions and search for topologically interesting locations or special paths in the gradient fields are few of possible applications. Some important approaches rely on the partitioning of the examined system into separate spatial fragments, which are often aimed to represent chemically important descriptors like atomic regions, bonds, or lone pairs. To perform the desired space partitioning, procedures are applied which determine in one or more steps the volume or the boundaries of the fragments, like the location of a bond critical point and the corresponding zero-flux surfaces in the electron density gradient in case of QTAIM [2].

In the following a special class of functions, termed electron localizability indicators [3–8], based on simultaneous evaluation of electron density and electron pair density will be described. This combination is utilized with the aim to analyze the correlation of electronic motion [9]. Apart from the density function point of view, the energy of a molecule can be thought as stemming from two parts – a one-particle terms in wide sense derived from the electron density and a two-particle terms derived from the electron pair density (of course, the full 2-matrix is still necessary today). The interplay between the electron density on the one hand and the electron pair density on the other hand could thus elucidate the situation in the molecular system.

Another aspect concerns the connection of the abovementioned electron localizability with the formation and description of an electron pair. The electron pair is the most important entity in the view and approach of G. N. Lewis to the chemical bonding [10]. In his seminal paper Lewis formed the idea of chemical bonding based on sharing of electron pairs. His idea of atoms consisting of a kernel and a shell in the position space found nowadays a remarkable support in the examination of atomic shell structure by different functions [11–25]. The electron pairing is in modern chemistry connected mainly with a pair of opposite-spin electrons occupying single orbital [26–28]. However, Lewis apparently thought of electron pairs located at specific positions in space. Possibly, the Old Master would be very excited by the inspection of an electron localizability indicator diagram of a molecule.

2 Short Survey on Localizability

New ideas and approaches are founded on discoveries and developments of the past. The building of present-time knowledge is erected on the knowledge and achievements of previous generations. Often, what is thought to be a new idea is just another viewpoint of an old powerful concept, like Lewis idea of chemical bonding based on electron pairs. With the novel insight, the already established concept can possibly grow to a new theory. Some of the developments that had an impact on the spatial analysis of atoms, molecules, and crystals, especially concerning the localizability of electrons, are more or less loosely and by far not complete, briefly listed in the following sections.

2.1 Event Probabilities and Loges

The partitioning of the real space into regions with localized groups of electrons was investigated already in the 1950s by Daudel and coworkers [29, 30]. The regions, called loges, were defined as those of minimal missing information function $I(\Omega)$ [31, 32]:

$$I(\Omega) = -\sum_n P_n(\Omega)\ln P_n(\Omega), \tag{1}$$

with the *event* probabilities $P_n(\Omega)$ to find n electrons within the region Ω and the remaining $(N-n)$ electrons exclusively outside Ω in the disjoint region Ω' (with $\Omega+\Omega'=\mathbf{R}^3$):

$$P_n(\Omega) = \binom{N}{n}\int_\Omega d\mathbf{r}_1 \ldots \int_\Omega d\mathbf{r}_n \int_{\Omega'} d\mathbf{r}_{n+1} \ldots \int_{\Omega'} \Gamma^{(N)}(\mathbf{r}_1, \ldots \mathbf{r}_N) d\mathbf{r}_N, \tag{2}$$

where the N-matrix $\Gamma^{(N)}(\mathbf{r}_1,\ldots\mathbf{r}_N) = \Psi^*(\mathbf{r}_1,\ldots\mathbf{r}_N)\Psi(\mathbf{r}_1,\ldots\mathbf{r}_N)$ is integrated. The event probabilities also determine the average number of electrons $\overline{N}(\Omega)$ (the electron population) as well as the average number of electron pairs $\overline{D}_2(\Omega)$ (the pair population) in Ω:

$$\begin{aligned} \overline{N}(\Omega) &= \sum_n^N nP_n(\Omega) \\ \overline{D}_2(\Omega) &= \frac{1}{2}\sum_n^N n(n-1)P_n(\Omega). \end{aligned} \tag{3}$$

Daudel connected the *localizability* of electrons with the correlation between the positions of electrons as measured by the event probabilities P_n. He attempted to

establish the loges as basis of a formalism for the bond description closely related to Lewis [10] representation of bonding [33].

2.2 Correlation of Electronic Motion

The idea of loges was adopted in 1974 by Bader and Stephens [9, 34] who used the fluctuation $\Lambda(\Omega)$ in the particle number in region Ω instead of the missing information function $I(\Omega)$ utilized by Daudel. The $\Lambda(\Omega)$ is the difference between the average of squares $\overline{N(\Omega)^2}$ and the squared average number of electrons $\overline{N}(\Omega)^2$:

$$\Lambda(\Omega) = \overline{N(\Omega)^2} - \overline{N}(\Omega)^2 = \sum_n n^2 P_n(\Omega) - \left[\sum_n n P_n(\Omega)\right]^2. \tag{4}$$

This expression can be conveniently rewritten using the electron and pair populations:

$$\Lambda(\Omega) = \overline{D}_2(\Omega) + \overline{N}(\Omega) - \overline{N}(\Omega)^2. \tag{5}$$

The authors reasoned that within a loge, where the fluctuation $\Lambda(\Omega)$ is minimized, the *correlation of electronic motion* is maximized. The minimal value $\Lambda(\Omega) = 0$ is found for the so-called pure pair population which is described by a single event that exactly m electrons are inside Ω, yielding $\overline{D}_2(\Omega) = 1/2m(m-1)P_m(\Omega)$, i.e., that all other event probabilities $P_2(\Omega)$ to $P_N(\Omega)$ are zero.

The integration of the so-called Fermi hole over the region Ω was connected by Bader and Stephens with the localization $F(\Omega)$ of electrons in the region. This can be easily expressed by:

$$F(\Omega) = \overline{D}_2(\Omega) - \overline{N}(\Omega)^2 \tag{6}$$

which shows that such electron localization describes the difference between the pair population and the population of quasi-independent electron pairs. With Eq. (5) a connection between the localization and fluctuation can be written as $\Lambda(\Omega) = F(\Omega) + \overline{N}(\Omega)$.

For few atoms and molecules, the procedure (utilizing the high symmetry of the system) yielded space partitioning into loges which could be connected with atomic cores, bonds, and lone pairs with electron populations close to the expectation of a chemist. It was concluded by Bader and Stephens [34]:

> The theory and results given here determine and illustrate the effect of Pauli exclusion principle on the distribution of electronic charge in real space. It has been demonstrated that the localization of charge in real space is determined by the localization of the Fermi correlation in pair space and that the extent of pairing and localization proceed hand in hand.

At that time, this appealing idea did not spread over the chemical community dealing with the interpretation of bonding situation, probably due to the difficulties to apply the method to more complex systems (of low symmetry). However, later this treatment of electron pairing culminated in the elaboration of the localization and delocalization indices [35].

2.3 Fermi Hole Mobility Function

In a study in 1982, Luken and Culberson analyzed the change of the Fermi hole shape with respect to the position of reference electron to gain information about the spatial localization of electrons [36]. The Fermi hole density is derived from the same-spin pair density and describes the probability density to find an electron at given position, when another same-spin electron is localized at the reference position with all the other electrons located somewhere in the space. Like in Sect. 2.2, it shows how the electronic motion of electrons creating a same-spin pair is correlated. For a closed-shell Hartree–Fock wave function, the so-called Fermi hole mobility function $F(\mathbf{r})$:

$$F(\mathbf{r}) = \frac{2}{\rho(\mathbf{r})^2} \sum_{i>j} \left[\phi_i \nabla \phi_j - \phi_j \nabla \phi_i\right]^2, \tag{7}$$

with the electron density ρ and the orbitals ϕ, measures the sensitivity of the Fermi hole to the change of the reference electron position. The authors assumed that low values of $F(\mathbf{r})$ render regions dominated by a single orbital. However, besides minima around the nuclei, it does not exhibit any significant structure. It was found that the comparison of $F(\mathbf{r})$ to the Fermi hole mobility function of a uniform electron gas $F_0(\mathbf{r})$:

$$F_0(\mathbf{r}) = \frac{3\pi}{4} \left(\frac{\rho(\mathbf{r})}{2}\right)^{2/3}, \tag{8}$$

revealed spatial regions which could be related to cores, bonds, and lone pairs. The authors have chosen the difference $F(\mathbf{r}) - F_0(\mathbf{r})$ as the analyzed measure. For molecules the regions of positive values, i.e., where $F(\mathbf{r}) > F_0(\mathbf{r})$, resembled the boundaries between loges proposed by Daudel [32]. This very interesting proposal, examined in more detail in later study [37], remained more or less unnoticed without a deeper impact until its "reincarnation" within the formulation of the electron localization function by Becke and Edgecombe [38].

2.4 Correction Term for Kinetic Energy Density

A year later, in 1983, Deb and Ghosh investigated an expression for the kinetic energy density t consisting of the full von Weizsäcker term together with the Thomas–Fermi term modified by a position-dependent correction term $f(\mathbf{r})$ [39]:

$$t = -\frac{1}{4}\nabla^2\rho + \frac{1}{8}\frac{(\nabla\rho)^2}{\rho} + \frac{3}{10}\left(3\pi^2\right)^{2/3} f(\mathbf{r})\ \rho^{5/3}. \tag{9}$$

The authors examined $f(\mathbf{r})$, which is a function of the electron density, with the goal to reproduce the kinetic energy density of atoms. Although the correction term nicely showed the atomic shell structure in real space, the work was not noticed by the community dealing with the real-space analysis of the bonding situation in molecules. Today we can recognize that, at the 1-determinantal level where $t = 1/2\sum_i |\nabla\phi_i|^2 - 1/4\nabla^2\rho$, the correction term $f(\mathbf{r})$ of Deb and Ghosh resembles the kernel of the electron localization (ELF) function proposed 7 years later (more specifically, the kernel of Savin's formulation of ELF [40]).

2.5 Electron Localization Function of Becke and Edgecombe

In a paper in 1990, Becke and Edgecombe proposed to describe the electron localization by a measure related to the Fermi hole [38]. Their electron localization function (ELF) was based on the conditional probability density to find a σ-spin electron close to another same-spin electron at the examined reference position. This probability density depends on the curvature of the Fermi hole. The authors connected the electron localization with the flatness of the Fermi hole. They stated that the electron localization is related to the expression:

$$D_\sigma = \sum_i^\sigma |\nabla\phi_i|^2 - \frac{1}{4}\frac{(\nabla\rho_\sigma)^2}{\rho_\sigma}. \tag{10}$$

However, instead of using D_σ as the localization measure, a calibration was included to "extract" more desirable features:

$$\chi_\sigma = D_\sigma / D_\sigma^0, \tag{11}$$

using the expression $D_\sigma^0 = \mathrm{c_F}(2\rho_\sigma)^{5/3}$ valid for a uniform electron gas with the density ρ_σ (and the Fermi constant $c_\mathrm{F} = \frac{3}{10}(3\pi^2)^{2/3}$). This kernel of the $\mathrm{ELF_{BE}}$ formula was transformed to the final expression:

$$\eta_{\mathrm{BE}} = \frac{1}{1+\chi_{\sigma}^{2}}, \tag{12}$$

with ELF values η_{BE} bound between 0 and 1 (the subscript BE – for Becke and Edgecombe – is used here to discriminate between the later modifications of ELF). Of course, there is no "physical" content in the final Lorentzian transformation. The purpose of the transformation was to get diagrams showing similar shape for regions of interest, irrespective of the participating atoms.

In certain sense $\mathrm{ELF}_{\mathrm{BE}}$ can be seen as a modified version of the approach of Luken and Culberson (cf. Sect. 2.3). Both approaches refer to the Fermi hole curvature and both need a reference system, chosen to be the uniform electron gas. However, there are two major differences between the approaches. Although the Fermi hole mobility function of Luken and Culberson is governed by the Fermi hole curvature, in their model the sensitivity of the Fermi hole shape to the change of the position of the reference electron is analyzed, whereas Becke and Edgecombe ask for the probability density to find an electron with respect to examined reference position (with simple words, in case of $\mathrm{ELF}_{\mathrm{BE}}$ the reference electron is not meant to move). Moreover, Luken and Culberson chose the subtraction for the comparison with the uniform electron gas, whereas Becke and Edgecombe preferred the division.

$\mathrm{ELF}_{\mathrm{BE}}$ is based on the same-spin pair density. Interestingly, in the study of Becke and Edgecombe, only closed-shell systems were examined. It was not mentioned there how to deal with spin-polarized systems (for which two $\mathrm{ELF}_{\mathrm{BE}}$ diagrams, separately for each spin, were necessary to comply with the derivation given in the paper). Additionally, the reason for the arbitrary calibration with the uniform electron gas was not given. It was not clearly stated that without the calibration, the desired structure of the ELF diagrams would disappear.

2.5.1 Interpretation of Dobson

Soon after the appearance of the ELF, some interesting interpretations and remarks were given by Dobson [41]. He stated that the kernel of the ELF formula (cf. Eqs. (10) and (11)) is valid for states with zero Schrödinger current density, which explicitly means that time dependency would change the formula. Additionally, Dobson connected the Fermi hole curvature with the kinetic energy of the relative motion of same-spin electron pairs.

In another interpretation Dobson pointed out that the Fermi hole curvature is related to the conditional number of same-spin electrons within a small sphere of radius R around the reference electron. This number of other same-spin electrons is given by the integral of conditional pair density within the sphere. The integral can be determined from the Taylor expansion of the pair density around the reference position. In this way the particle numbers enter the scene, replacing the probability

densities. However, the necessity of the uniform electron gas comparison remained hidden by veil of silence.

2.6 Electron Localization Function of Savin

The ELF_{BE} is based on electron pair interactions, which are not explicitly accessible within the density functional theory (DFT). Formally it is possible to extract the pair density from the Kohn–Sham (KS) wave function Ψ_{KS} by the reduction of $\Psi^*_{KS}\Psi_{KS}$ to a 2-particle function. But one must be aware that the pair interactions are not properly reproduced by the resulting 2-matrix (as the single-determinantal KS wave function refers to a noninteracting system under the action of an exchange–correlation functional).

To circumvent this uncomfortable situation, Savin proposed in a study submitted in 1991 to reformulate ELF using kinetic energy densities [40]. In DFT the electron density $\rho = \sum_i \phi_i^2$ as well as the kinetic energy density $\tau = 1/2\sum_i |\nabla \phi_i|^2$ are given via the Kohn–Sham orbitals (assumed to be real valued). With this, the numerator D_σ of Eq. (11) can be formally seen as the Pauli kinetic energy density t_P:

$$t_P = \tau - \frac{1}{8}\frac{(\nabla\rho)^2}{\rho}, \tag{13}$$

which can be interpreted as the increase of kinetic energy density due to the Pauli principle. Interestingly, in the abovementioned study of Savin et al., the reformulation of the ELF kernel was given for the total electron density, i.e., including both spins:

$$\chi_S = t_P/t_{P,h}, \tag{14}$$

where $t_{P,h} = c_F\,\rho^{5/3}$ is the kinetic energy density of a uniform electron gas with the electron density ρ. This was later probably the source of certain "irritations" resulting in the proposal to formulate ELF for each spin separately [42], which is of course given already by the original formulation of Becke and Edgecombe. ELF_S of Savin with the values

$$\eta_S = \frac{1}{1+\chi_S^2}, \tag{15}$$

bound between 0 and 1, yields for closed-shell systems at single-determinantal level results identical with η_{BE}.

In the case of open-shell systems, several choices are possible. An obvious recipe is to evaluate ELF for each spin channel separately. As mentioned above, this corresponds to the formulation of Becke and Edgecombe, yielding two ELF

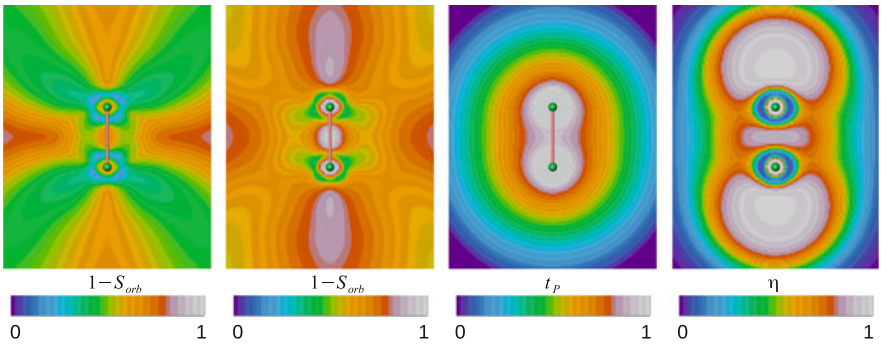

Fig. 1 Orbital localization measured by the orbital-contribution entropy S_{orb} for the Hartree–Fock calculation of the N_2 molecule. From *left* to *right*: *1*, canonical orbitals; *2*, natural localized orbitals; *3*, Pauli kinetic energy density t_{P}; *4*, ELF

diagrams. If one insists on single diagram, then either the total quantities τ and ρ can be fed into $\mathrm{ELF_S}$ (cf. Eqs. (13) and (14)) or the kinetic energy densities for the spin-polarized case can be used, e.g., $t_{\mathrm{P,h}} = 2^{2/3} c_{\mathrm{F}} \left(\rho_\alpha^{5/3} + \rho_\beta^{5/3} \right)$, cf. Kohout and Savin [16]. Of course, at a position with pronounced spin density, those ELF formulas will not deliver identical η values.

From Eq. (13) it can be inferred that in region dominated by a single orbital (e.g., after Foster–Boys localization), the t_{P} will be close to zero. With this argumentation, ELF should show regions dominated by localized orbitals. While this can be schematically shown for nearly perfectly localized orbitals [43, 44], for real systems the t_{P} does not manifest such evident localization dependency. To express the spatial extent of orbital localization for all m occupied orbitals ϕ_i of the N-electron system at once, let us define the orbital-contribution entropy S_{orb}:

$$S_{\mathrm{orb}} = -\frac{1}{\ln N} \sum_i^m \phi_i^2/\rho \, \ln\left(\phi_i^2/\rho\right). \tag{16}$$

If at the position $\mathbf{r}$ the electron density $\rho(\mathbf{r}) = \phi_i(\mathbf{r})^2$, then $S_{\mathrm{orb}} = 0$ and the region is dominated by the orbital ϕ_i. Thus, the localization extent can be conveniently given by the function $1 - S_{\mathrm{orb}}$. The first diagram in Fig. 1 shows the localization extent for the canonical orbitals from the Hartree–Fock calculation of the N_2 molecule. Although the presence of the orbitals corresponding to the respective σ, π, and lone-pair orbitals can be recognized, the localization extent come up to somewhat above 0.5 only. Using the natural localized orbitals created by the isopycnic localization [45, 46], the localization extent is much higher showing regions of $1 - S_{\mathrm{orb}}$ close to 1 (cf. the second diagram of Fig. 1). However, the Pauli kinetic energy density, which is invariant with respect to a unitary rotation of the orbitals, does not exhibit any pronounced structure in the bonding or lone-pair region, respectively (cf. the third diagram of Fig. 1). Thus, the lone pairs and bond (only

single localization feature present for the σ and π bonds) shown in ELF are explicitly due to the rescaling of t_P by the homogeneous gas value $t_{P,h}$.

2.7 Variations on ELF

With the success of ELF as an appealing bonding descriptor of chemical situation in molecules and solids [47, 48], some modifications of ELF appeared, based mainly on Savin's viewpoint using kinetic energy densities. The connection to the kinetic energy made it desirable to search for modifications enabling to evaluate ELF directly from the electron density without resorting to the orbitals (an approach somewhat in between was given for the Be atom, where the KS orbitals were computed from the experimental electron density [49]). Additionally, some special aspects connected with the wave function representation, like momentum space or time dependency, were examined. Later, functions describing electron localization that were in wide sense related to ELF, respectively formulated in the spirit of ELF, emerged.

2.7.1 Removing the Orbital Dependency

To avoid the dependence on orbitals when computing ELF, Gadre et al. [50] proposed in 1993 to utilize an approximate construction of the 1-matrix by the application of a nonlocal density approximation. At the 1-determinantal level of theory, the pair density is recovered from the knowledge of the 1-matrix. This allows to follow the procedure of Becke and Edgecombe and finally arrive at purely electron density-based variant of ELF. The so-called DELF shows topology similar to the one of ELF.

The objective to formulate ELF without orbitals was also undertaken few years later by Fuentealba [51]. He used for the kinetic energy density τ an approximation incorporating beside the electron density also the exchange energy density and the electrostatic potential. ELF including this expression for τ was thus formally independent of the orbitals. The modified version termed ESP-ELF exhibits topology similar to the original ELF, with behavior somewhat deviating from ELF_S close to the atomic nucleus (where ESP-ELF approaches zero – the same is valid at large distances).

The attempt to determine ELF directly from the experimental electron densities was realized in 2002 by Tsirelson and Stash [52]. Again, the ELF formulation of Savin was used with τ replaced by second-order expansion of the kinetic energy density (Kirzhnits approximation [53]). The proposed modification of ELF is dependent only on the electron density and its derivatives. This modified ELF reveals the atomic shell structure. However, due to a deformation of the atomic shell shape toward the nucleus, a saddle point emerges at the position between the bonded atoms, where the original ELF displays a maximum. Several different

approximations for the kinetic energy density within the ELF formulation were also examined in 2005 by Ayers [54].

2.7.2 Consideration of Wave Function Representation

Both ELF_{BE} and ELF_S were originally defined for single-determinantal time-independent wave functions in the real-space representation. Already in 1994 an attempt to analyze electron localization in momentum space was undertaken by Kulkarni [55]. The proposed electron momentum localization function (EMLF) was defined in complete analogy to the real-space ELF formula (without an explicit momentum space equation given for ELF). The electron momentum localization function (EMLF) definition was supposed to be applicable to closed-shell systems only. EMLF showed the atomic shell structure with spurious discontinuities in the EMLF gradient. This artifact as well as some structural EMLF features for molecules could not be reproduced later using the electron localizability indicator [7].

The influence of time dependency on the ELF was examined in 2005 by Burnus et al. [56] who applied the time-dependent orbitals within the ELF_{BE} formalism. The resulting expression for D_σ was formulated using τ_σ and $(\nabla\rho_\sigma)^2/\rho_\sigma$ (similarly to Savin's formulation), in which case an additional term emerged. This term, $-j_\sigma^2/\rho_\sigma$, is proportional to the current density j. The current density term also appears in case of imaginary wave function, like in the presence of magnetic fields [57]. The time-dependent electron localization function (TDELF) is suitable to analyze, for instance, the scattering processes.

2.7.3 ELF for Separate Contributions

The original definition of ELF was based on the same-spin pair density, i.e., considering the electron localization with respect to another electron of identical spin. The ELF formulation of Savin opened not only the possibility to apply ELF to the DFT using KS orbitals but also to take into account the total electron density. Savin did not express the equations explicitly for separate spin contributions (as this was obvious). Possibly this was the reason for Madsen et al. [58] and later also Melin and Fuentealba [42] to propose in 1999 and 2003, respectively, to use ELF_α and ELF_β for free radical systems and to state that it is possible to evaluate ELF separately for the ρ_α and ρ_β densities (which of course is already given by the original ELF). Melin and Fuentealba correctly mentioned that the sum of the spin-dependent functions does not yield the total ELF (the possibilities on how to include both spins within total ELF for spin-polarized systems were analyzed in 1996 by Kohout and Savin [16]).

Santos et al. [59] proposed in 2004 to formulate ELF separately for the σ and π components of the wave function. The authors reasoned that this is possible because the kinetic energy is additive and can be decomposed into the aforementioned parts.

However, the sum of such (separated) localization functions again does not yield total ELF. Moreover, ELF_σ and ELF_π have no connection to the original formulation of Becke and Edgecombe. It should be emphasized that ELF_π does not reveal any significant information if only single π orbital is present in the system (e.g., in ethylene).

2.8 Localized Orbital Locator

The ratio $\tau_\sigma^{\mathrm{LSDA}}/\tau_\sigma^{\mathrm{exact}}$, where the numerator and denominator are the (σ-spin dependent) kinetic energy density in the local spin density approximation and the noninteracting KS kinetic energy density, respectively, was used in 2000 by Schmider and Becke [60] as indicator of the chemical bonding situation. It differs from the ELF kernel by the absence of the von Weizsäcker term $\frac{1}{8}(\nabla\rho_\sigma)^2/\rho_\sigma$. With convenient transformation of the above ratio, projecting the values within the range 0 to 1, the localized orbital locator (LOL) was defined. The name was rationalized from the idea that the kinetic energy density is invariant with respect to unitary transformation of the orbitals. Hence, one is free to choose localized orbitals. The kinetic energy density $\tau_\sigma^{\mathrm{exact}} = \sum|\nabla\phi_\sigma|^2$ is low at the position of the maximum of a localized orbital (if the contributions of all other orbital gradients are negligible). LOL can be understood as tool for locating the localized orbitals. Interestingly, it shows all the topological features of ELF, although the LOL kernel is just a part of the ELF kernel.

2.9 Probability Distributions and Maximal Probability Domains

Daudel's approach of event probability experienced in 2002 a revival in a study of Savin [61]. In this study, the radii r of spheres around the atomic nucleus such that the probability $P_n(r)$ to find n electrons outside the sphere is maximal were analyzed. The highest outermost probability marked the radius of core–valence separation with electron populations in good agreement with the periodic table. A comparison to the event probabilities valid for independent particles was used to enhance the probability information.

In the case of molecules, the determination of the domains of maximal probability was a challenging task [62]. The results for some simple molecules (e.g., LiH, BH, C_2H_4) show that the regions of maximal event probabilities $P_n(\Omega)$ seem to be connected with "chemical" descriptors, like cores, bonds, and lone pairs [63–65].

2.10 Integrals of Pair Density

Following Dobson's interpretation [41], Savin used in a paper in 1997 [47] reasoning based on integrals of conditional pair density to introduce the $\rho^{5/3}$ denominator in ELF independently of the uniform electron gas. The number of electrons surrounding the reference electron in a small sphere of radius R is approximately given by the expression:

$$\frac{1}{2}\frac{4\pi R^5}{5}D_\sigma(\mathbf{r}), \tag{17}$$

for D_σ cf. Eq. (10). If the radius R is chosen such as to keep the electron population within the sphere constant, i.e., with $4\pi R^3\rho(\mathbf{r})/3 = \text{const}$, the 5/3 power for the density reference is recovered. Here, the arguments were used to explain the scaling. Later the argumentation with electron density and electron pair density integrals were used to interpret ELF in terms of event probabilities as the intrusion of other electrons to the (constant) population within the small sphere [66].

In 2002 two studies were submitted independently by Silvi [67] and Kohout [3], respectively, proposing to use particular integrals of electron pair density over specific regions as indicators of the electron localization. Although very similar in the formalism, the two approaches follow different philosophy considering the underlying definition as well as the statements concerning the "physical" meaning.

Silvi defined the so-called spin-pair composition $c_\pi(\mathbf{r})$ as the ratio of the number of parallel spin pairs to the number of antiparallel spin pairs (actually, c_π is proportional to this ratio). The number of electron pairs was determined by the integral of the corresponding electron pair density over an *arbitrary* volume around the examined reference point. For very small volumes, this ratio can be evaluated using an approximate expression, e.g., in the case of closed-shell HF wave function:

$$c_\pi(\mathbf{r}) \approx \frac{\nabla^2 P^{\alpha\alpha}_{\text{cond}}\left(\mathbf{r}\middle|\mathbf{r}'\right)}{3\rho^{5/3}(\mathbf{r})} \tag{18}$$

with the conditional same-spin electron pair density $P^{\alpha\alpha}_{\text{cond}}\left(\mathbf{r}\middle|\mathbf{r}'\right)$. In this case the spin-pair composition is formally proportional to the ELF kernel. The advantage of this approach is that, in contrast to ELF, the $\rho^{5/3}$ denominator is not related to the uniform electron gas. Instead, it ensues from the approximate expression for the number of (HF, i.e., uncorrelated) antiparallel spin pairs within the examined volume. The actual volume of the arbitrary chosen region, needed to derive the above expression, was deduced from the electron density integral.

The definition of the electron localizability indicator (ELI) of Kohout was based on a different approach (inspired by Savin's suggestion [47] of a "breathing sphere" enclosing constant charge as well as Bader's proposition of correlation of electronic motion [9]). For ELI, first the whole space is partitioned at once into nonoverlapping compact regions (called *micro-cells*) enclosing a fixed electron

population ω_q – an approach termed the ω-restricted space partitioning (ωRSP) [68]. Then, the electron pair population in each *micro-cell* is determined, thus yielding a discrete distribution of values. The so-called ELI-q (with the q emphasizing the fixed charge condition) is proportional to such distribution of pair populations.

On the other hand, fixing the electron pair population at the value ω_D in each *micro-cell* and sampling the charge (electron population) within the *micro-cells* of the resulting space partitioning yields the localizability indicator ELI-D (emphasizing the fixed electron pair condition ω_D). Formally, in case of closed-shell HF wave function, ELI-q is identical with c_π. However, in ELI-q the $\rho^{5/3}$ denominator is neither related to the uniform electron gas nor to the number of antiparallel spin pairs. It stems from the fixed charge condition. ELI is discussed in detail later in Sect. 4. It is worth noting that the spin-pair composition can easily be redefined within the ωRSP scheme (yielding, in case of correlated functions, formulas clearly departing from Silvi's definition of the spin-pair composition).

Although based on integration over small volumes, the spin-pair composition yields a continuous function (i.e., the integration volumes overlap). In contrast, ELI is a discrete distribution of values, which formally can be made continuous in the so-called limit after rescaling (cf. Sect. 4). Formally, the spin-pair composition of Silvi could be seen as being based on the q-restricted space partitioning, i.e., as ratio of same-spin and opposite-spin pairs in *micro-cells* enclosing fixed electron population.

2.11 Electron Pair Localization Function

An interesting approach analyzing the pairing of electrons was presented in 2004 by Scemama et al. [69]. There, the basic ingredients are the average distances $d_{\sigma\sigma}(\mathbf{r})$ and $d_{\sigma\bar{\sigma}}(\mathbf{r})$ between an electron located at ($\mathbf{r}$) and the closest same-spin and opposite-spin electron, respectively (computed from quantum Monte Carlo approach). The electron pair localization function (EPLF) is defined as follows:

$$\mathrm{EPLF}(\mathbf{r}) = \frac{d_{\sigma\sigma}(\mathbf{r}) - d_{\sigma\bar{\sigma}}(\mathbf{r})}{d_{\sigma\sigma}(\mathbf{r}) + d_{\sigma\bar{\sigma}}(\mathbf{r})}. \tag{19}$$

For EPLF close to zero, the average distances between spin-like and spin-unlike electrons are similar. The minimal EPLF value of -1 is reached in regions where the opposite-spin electrons are much closer than the same-spin ones (and vice versa for the maximal EPLF value of 1). EPLF reveals the shell structure of atoms. It was used to describe the bonding situation in molecules. As stated by Amador-Bedolla et al. [70], EPLF is a relative measure in the sense that it depends only on the ratio $d_{\sigma\sigma}/d_{\sigma\bar{\sigma}}$ and not on the actual average distance between the electrons.

2.12 Measure of Covariance

A relation between the ELF kernel and a local measure of covariance was outlined in 2005 by Ayers [54]. Let the number of electron pairs formed between two disjoint regions Ω_i and Ω_j be $\overline{N}_{ij}$. The electron populations within the regions are $\overline{N}_i$ and $\overline{N}_j$, respectively. The covariance σ_{ij}^2 of the number of electrons in the two regions is given by $\sigma_{ij}^2 = \overline{N}_{ij} - \overline{N}_i\overline{N}_j$. The author proposed to use distinct very small regions "covering" the molecule and compute the covariances σ_{ij}^2 between the region Ω_i at the position $\mathbf{r}_i$ and all the other regions Ω_j as well as the fluctuations σ_{kk}^2 (like the covariances, but applied to single region Ω_k). From this the correlation matrix is formed:

$$R_{ij} = \frac{\sigma_{ij}^2}{\sqrt{\sigma_{ii}^2}\sqrt{\sigma_{jj}^2}}. \tag{20}$$

The electron populations in Ω_i and Ω_j are thought to be independent if $R_{ij} = 0$. As a measure of local fluctuation, the sum of squared correlation matrix elements per electron was used. For volumes Ω approaching zero, this can be approximated by:

$$\lim_{V(\Omega)\to 0} \frac{1}{\overline{N}_i}\left(\sum_{j\neq i} R_{ij}^2\right) = \int \rho_\sigma(\mathbf{r}_j) h_{\sigma\sigma}^2(\mathbf{r}_i, \mathbf{r}_j)\ \mathrm{d}\mathbf{r}_j. \tag{21}$$

This index, with the hole correlation function $h_{\sigma\sigma}^2(\mathbf{r}, \mathbf{r}')$, was stated to be a natural "local representation" of the "minimum fluctuation" criterion for the electron localization. Here, in certain sense, the fluctuation in electron population (per electron) within very small region is related to the extent of correlation of electron populations between the chosen region and all the remaining (very small) regions. It was shown that the index given by Eq. (21) (raised to the 2/3rd power) is inversely proportional to the ELF kernel.

3 Some Remarks to ELF

During the last 20 years since the introduction by Becke and Edgecombe, the ELF has grown into a valuable tool for the analysis of chemical bonding. It is my personal opinion that this "rise" of ELF would never be realized without the enthusiastic engagement of A. Savin. As manifested in previous section, the label ELF was attached to different functions (like the original ELF and the function of Tsirelson), sometimes even to functions only defined in sort of "ELF manner" with meaning definitely departing from that of the original definition (like ELF for the π contributions). Despite the usefulness of all the ELF-like descriptors, the meaning

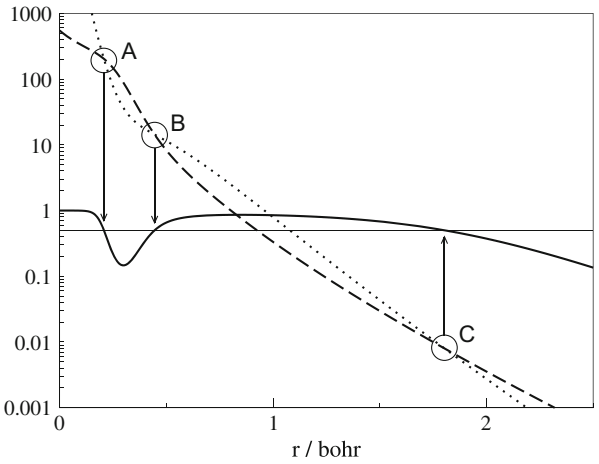

Fig. 2 Data for the Ne atom using the wave function of Clementi and Roetti. *Solid line*, ELF (the *horizontal line* indicates $\eta = 0.5$); *dashed line*, Pauli kinetic energy density t_P; *dotted line*, $t_{P,h} = c_F \rho^{5/3}$. The *circles*, marked by *capital letters*, highlight the situation where $t_P = t_{P,h}$. The *arrows* point to the corresponding positions with $\eta = 0.5$

of the particular ELF variant used should be clearly stated [43]. In the following some comments [71] to ELF are given.

3.1 ELF Does Not Mirror Pauli Repulsion

As mentioned in Sects. 2.5 and 2.6, the electron localization in sense of ELF was connected with the flatness of Fermi hole [38], respectively with the magnitude of Pauli repulsion [40]. However, the statement often found in literature that high ELF values are characteristic for regions of low Pauli repulsion can easily be refuted. To see this, let us analyze the typical situation for an atom. Figure 2 shows ELF (solid line) for the Ne atom computed using the wave function of Clementi and Roetti [72]. Two atomic shells separated by an ELF minimum (logarithmic scale) are visible, with the first shell populated by 2.2 electrons [16]. Approaching the Ne nucleus ELF attains its maximal value 1, i.e., the electrons are highly localized around that position. However, in contrast with the above statement suggesting very low Pauli repulsion, the t_P (dashed line) reaches at the nucleus the maximal value as well. The ELF value is close to 1 only because near the nucleus t_P is much smaller than the kinetic energy of the uniform electron gas $t_{P,h}$ (dotted line). It can nicely be seen that for the Ne atom, both curves, t_P and $t_{P,h}$, decay monotonically with the distance from the nucleus, not mirroring the sign change of the ELF slope [49].

When focusing at positions of identical ELF values, for instance, $\eta = 0.5$, it can be shown that the magnitude of Pauli repulsion, given by the t_P, cannot be inferred from the ELF value alone (cf. Fig. 2). At each of the positions for which $\eta = 0.5$ (marked A, B, and C), the t_P equals $t_{P,h}$ (cf. Eqs. (14) and (15)), i.e., the corresponding curves cross each other. However, going from the positions A to C, the value of t_P itself changes by several orders of magnitude. Thus, from the

information that ELF equals 0.5, it cannot be deduced whether this corresponds to the situation that, for instance, $t_P/t_{P,h} = 100/100$ or $t_P/t_{P,h} = 0.01/0.01$, respectively.

3.2 Uniform Electron Gas Calibration

The most important ingredient in ELF seems to be the curvature of the Fermi hole (respectively the value of Pauli kinetic energy density). However, the respective functions itself do not show the rich structure so typical for ELF. It is exclusively the calibration with respect to the uniform electron gas that generates all the desired features. Thus, the ELF values depend on the function used for the calibration, which was arbitrarily chosen to be the kinetic energy density of the uniform electron gas. This arbitrariness of the choice was often criticized, e.g., by Bader [73]. Another calibration function was examined by Ayers [54]. He used nearly free electron gas, but found the results much less satisfactory.

The uniform electron gas calibration is a very suggestive choice. Nevertheless, the ELF value $\eta = 0\ 5$ only indicates the fact that the magnitude of the Fermi hole curvature (respectively the Pauli kinetic energy density) at the examined position in the system equals the one in the reference uniform system of the same electron density. It is not appropriate to extend this coincidence to other features, especially when concerning the uniformity of the electron gas. From Fig. 2 it is clear that close to the nucleus (cf. the position A), the density gradient is very large, i.e., far away from zero as dictated by a uniform distribution. Moreover, $\eta = 0.5$ is not connected with kind of "perfect" delocalization [74, 75]. This would demand for very inconvenient classification of ELF values below 0.5 (for instance, calling this "regions of low electron density," as wrongly stated in Burdett and McCormick [74] and Sun et al. [75]).

3.3 Calculations with Pseudopotentials

For single-determinantal wave function, the kinetic energy density τ and the electron density ρ are computed from the orbitals $\{\phi_i\}$:

$$\tau = \sum_i |\nabla \phi_i|^2 \quad \rho = \sum_i \phi_i^2. \tag{22}$$

Thus, the above densities can be evaluated separately for disjoint subsets $\{\phi_i\}_\kappa$, whereby the total densities are recovered by summing up the partial quantities. For instance, the orbital space can be splitted into σ and π contributions $\{\phi_i\}_\sigma$ and $\{\phi_j\}_\pi$, the corresponding partial τ_σ, τ_π and ρ_σ, ρ_π calculated, with $\tau = \tau_\sigma + \tau_\pi$ and $\rho = \rho_\sigma + \rho_\pi$.

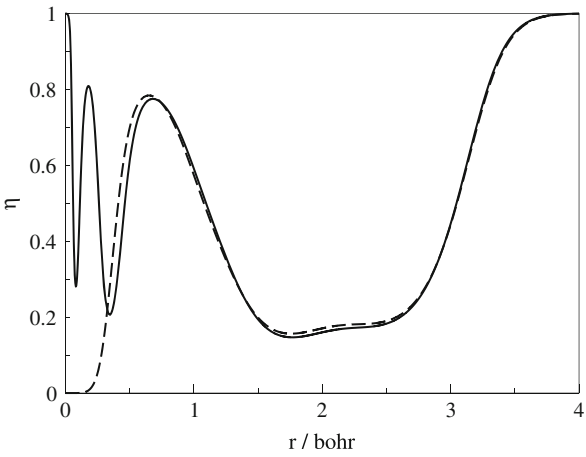

Fig. 3 ELF for the Zn atom using 6-311G basis. *Solid line*: ELF for the total 30-electron wave function. *Dashed line*: ELF for the 20-electron valence (SDD pseudopotential replacing 10 core electrons)

The ELF kernel χ_S (cf. Eq. (14)) is based on the Pauli kinetic energy density which contains the von Weizsäcker term $(\nabla\rho)^2/8\rho$. It is obvious that this term cannot be in general written as a sum of contributions in the form:

$$\frac{1}{8}\frac{(\nabla\rho)^2}{\rho} \neq \frac{1}{8}\sum_{\kappa}\frac{(\nabla\rho_\kappa)^2}{\rho_\kappa}. \tag{23}$$

Only when in some spatial region the contribution ρ_λ is much smaller than the total density ρ and at the same time $\nabla\rho_\lambda$ is much smaller than the total density gradient, the λ terms can safely be omitted in the respective total quantities:

$$\frac{1}{8}\frac{(\nabla\rho)^2}{\rho} \approx \frac{1}{8}\frac{\left(\sum_{\kappa\neq\lambda}\nabla\rho_\kappa\right)^2}{\sum_{\kappa\neq\lambda}\rho_\kappa} \qquad \rho_\lambda \ll \rho \wedge \nabla\rho_\lambda \ll \nabla\rho. \tag{24}$$

If additionally $\tau_\lambda \ll \tau$ (with τ_λ computed from the set $\{\phi_i\}_\lambda$), then the influence of the λ set on χ, i.e., the ELF value, is negligible in that spatial region.

Thus, the evaluation of calculations with electrons replaced by pseudopotentials must be performed with great caution. Figure 3 shows ELF for the Zn atom computed with Gaussian03 using the 6-311G basis set. ELF for the total 30-electron wave function (cf. the solid line) displays all four spatial shells (for the shell electron populations, cf. Kohout and Savin [16]). If the 10 core electrons are replaced by the SDD pseudopotential, the two innermost ELF peaks vanish (cf. the dashed line). At distances larger than roughly 0.8 bohr from the nucleus, the two lines almost coincide. Thus, only in regions outside the "pseudopotential hole" it is safe to compute ELF from the valence wave function only [49]. Otherwise, the ELF topology could possibly be changed in the region of interest. Note that the

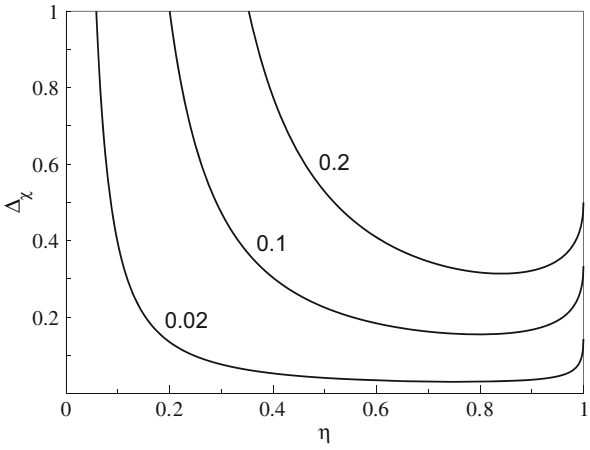

Fig. 4 Dependence of the difference Δ_χ of the ELF kernel on the ELF values η. The difference Δ_χ is computed for the (fixed) difference between the ELF values η and $(\eta - \Delta_\eta)$. Each *line* is marked by the chosen ELF difference Δ_η

electron populations of ELF basins close to the "pseudopotential hole" will change when compared to the data computed from the total wave function.

3.4 Differences of ELF Values

Usually only the qualitative aspect of ELF is taken into account; for instance, by the inspection of the ELF topology when mainly the positions of critical points $\nabla\eta = 0$ are of interest, respectively the ELF basins are determined. Due to the Lorentzian scaling (cf. Eq. (12)), proper care should be exercised in the case of quantitative evaluation of ELF, especially when considering the differences between ELF values [71]. As an example let us assume the difference $\Delta_\eta = 0.2$ between the ELF values η and $(\eta - \Delta_\eta)$. The differences Δ_χ of the corresponding ELF kernel values are not constant, but strongly depend on η (cf. the upper line in Fig. 4). The η dependence is less pronounced for smaller Δ_η (cf. the lower line in Fig. 4), except for very low ELF values where the kernel differences Δ_χ again rapidly increase. The difference $\Delta_\eta = 0.1$ seems to be a moderate change of ELF values (actually, 10% of the scale range). If taken between $\eta = 0.8$ and $\eta = 0.7$, it corresponds to the absolute difference of $\Delta_\chi \approx 0.15$ for the corresponding ELF kernel values. But when taken between $\eta = 0.2$ and $\eta = 0.1$, the change of the ELF kernel values increases above $\Delta_\chi = 1$, i.e., around 6 times the previous value. This means that it is not sufficient to specify just the magnitude of the difference between two ELF values. It should also be stated at which ELF value the difference was taken, because the relevant quantity is possibly the ELF kernel (or the inverse of it, due to the inverse relationship between χ and the localization) and not the ELF value affected by the Lorentzian scaling.

3.5 ELF for Correlated Wave Functions

For a single-determinantal time-independent wave function, both ELF_{BE} and ELF_S are formally given by an identical expression. The expressions will deviate from each other (even at the single-determinantal level) when the time dependency is taken into account, as already mentioned in Sect. 2.7.2. To make the formulas identical again (at that level), the current density term must be included into the ELF_S [56].

The situation is even more complicated for explicitly correlated wave functions, like those from a configuration interaction (CI) calculation. To extend the approach of Becke and Edgecombe to the correlated level, the Laplacian of spherically averaged correlated conditional same-spin pair density needs to be computed. Consistently, at the same time the calibration should be performed using the correlated uniform electron gas as well, an aspect that was not taken into account in any ELF analysis of correlated wave functions. Of course, the expression for "fully correlated" ELF_{BE} would deviate from the original (HF) ELF_{BE} formula.

Using the approach of Savin, it would be necessary for ELF_S to determine the Kohn–Sham orbitals corresponding to the correlated electron density. From those orbitals, the kinetic energy density τ of noninteracting electrons as well as the Pauli kinetic energy density t_P could be evaluated. Another route is conceivable by the replacement of τ with the interacting kinetic energy density $G = \sum n_i |\nabla \varphi_i|^2$ computed from the natural orbitals φ with the natural occupations n_i [76]. Then the Pauli kinetic energy density t_P is replaced by the term $G/2 - (\nabla\rho)^2/8\rho$, which is however not equal to the Laplacian of the correlated conditional pair density. Consistently, the kinetic energy density of the correlated uniform electron gas should be used as the calibrating system. The resulting "fully correlated" ELF_S formula would be different from the expression given by Savin. Moreover, even the meaning would change (because the noninteracting system is no more used in this case). With the abovementioned replacement of t_P, but retention of the expression $c_F\rho^{5/3}$ for the (noninteracting) uniform calibration, one can arrive at formulation, abbreviated ELF_{SI} in Kohout et al. [5], which is something in between the "fully correlated" and the original expression. At this stage it is clear that there are many possibilities for choosing the definition of "correlated" ELF.

In a study dedicated to ELF at correlated level, Matito et al. [77] proposed to use as the kernel the sum of the conditional same-spin pair density Laplacians (up-spin and down-spin):

$$\frac{\nabla_s^2 \gamma^{(2)\alpha\alpha}(\mathbf{r}, \mathbf{r}+\mathbf{s})\big|_{s=0} + \nabla_s^2 \gamma^{(2)\beta\beta}(\mathbf{r}, \mathbf{r}+\mathbf{s})\big|_{s=0}}{2c_F\ \rho^{8/3}}. \tag{25}$$

It was claimed that this formulation follows Silvi's approach of spin-pair composition (cf. Sect. 2.10). Indeed, the Laplacian terms are connected with the number of (correlated) same-spin electron pairs in small arbitrary chosen region. However, the division by the factor $\rho^{8/3}$ reveals that this is compared to the number of

uncorrelated opposite-spin pairs, which seems to be somewhat inconsistent with the intended attempt to formulate ELF at correlated level. Possibly, because ELI was incorrectly reproduced in the abovementioned paper, the authors were not aware that Eq. (25) actually corresponds (in the ELI terminology, cf. next section) to the distribution of same-spin electron pairs in infinitesimally small regions enclosing fixed amount of (total) electron population.

4 Electron Localizability Indicator

The expectation value in quantum mechanics is given by the integral of (possibly) many-particle function (which results from the action of given many-particle operator on appropriate density matrix) over the whole space. The integration over the whole space can be formally decomposed into the sum of integrals over separate nonoverlapping space-filling regions of chosen space partitioning. Such decomposition transforms the examined continuous function into a discrete distribution of integral values, the number of which depends on the granularity of the partitioning. On one end of the granularity scale, there is the integral over the whole space (expectation value). This is followed by the coarse-grained partitioning, which yields few integral values for relatively large regions (like the atoms in molecules of Bader [2]). Such partitioning is the basis of the interacting quantum atoms energy partition method introduced by Pendás et al. [68, 78, 79]. On the other end of the scale, there is what could be called the fine-grained space partitioning into infinitesimally small regions, yielding a discrete distribution of huge number of integral values, almost effacing the difference between continuous and discrete. The latter partitioning was used within the approach of ω-restricted space partitioning (ωRSP) [68].

The ωRSP is the most important ingredient for the definition of whole family of functionals, one of which is the electron localizability indicator (ELI) [3]. The functionals are derived from the integrals of the so-called *sampling* function over the regions of the ωRSP, which in turn is based on integrals of the so-called *control* function.

The transition from continuous to discrete (and the conception of quasi-continuous distribution) as well as the ωRSP with the interplay between the sampling and control function and the derivation of ELI is described in more detail in next sections.

4.1 From Continuous to Discrete

The partitioning of the coordinate space can be performed in various ways depending not only on the chosen rules but the dimensionality of the space as well. In the following, the partitioning operates on n-dimensional coordinate space

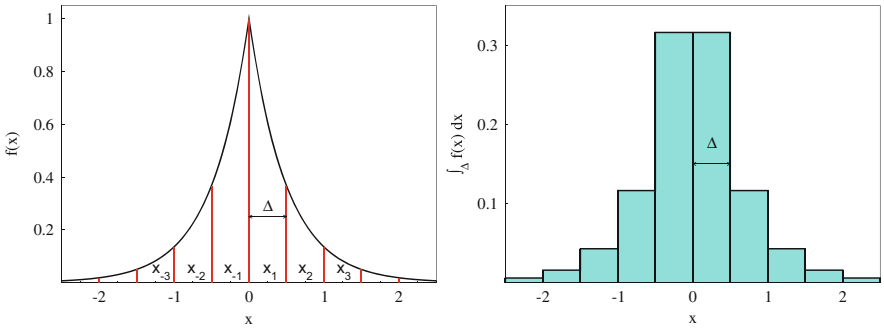

Fig. 5 Integration of one-dimensional Slater function over intervals. *Left*: *black line* $f(x) = \mathrm{e}^{-2|x|}$; *vertical red lines* mark the intervals of constant width $\Delta = 0.5$. *Right*: the height of the bars represents the value of the $f(x)$ integral over the corresponding interval in the *left diagram*

X^n, which can be either the whole space or specified part of it, e.g., a unit cell for solid state systems. The partitioning into the regions μ_i obeys at least the two rules:

- $\mu_i \cap \mu_j = \varnothing \quad \forall\ i \neq j$
- $X^n = \cup_i \mu_i$

Thus, the regions of the space partitioning are nonoverlapping and space filling, i.e., there are no gaps between the regions. Of course, additional rules that allow to determine the number or the size of the regions μ_i are necessary. Even then, this often still allows for infinite number of possible partitioning schemes.

4.1.1 One-Dimensional Space

The black line in the left diagram of Fig. 5 shows the one-dimensional Slater function $f(x) = (\zeta/2)\ \mathrm{e}^{-\zeta|x|}$, with $\zeta = 2$, which integrates to unity, $\int_{-\infty}^{\infty} f(x)\mathrm{d}x = 1$. Let us partition the whole x range into equidistant nonoverlapping intervals centered at the positions x_i as illustrated in the left diagram by the red vertical lines using the interval width $\Delta = 0.5$. Then, the total integral over the whole x range can be decomposed into the sum of integrals F_i over the (infinite number of) intervals. The bars in the right diagram of Fig. 5 represent the integrals of $f(x)$ over the intervals of the left partitioning. The height of each bar corresponds to the integral value as given by:

$$F_i = \int_{x_i - \Delta/2}^{x_i + \Delta/2} f(x)dx = e^{-\zeta|x_i|}\sinh(\zeta\Delta/2). \tag{26}$$

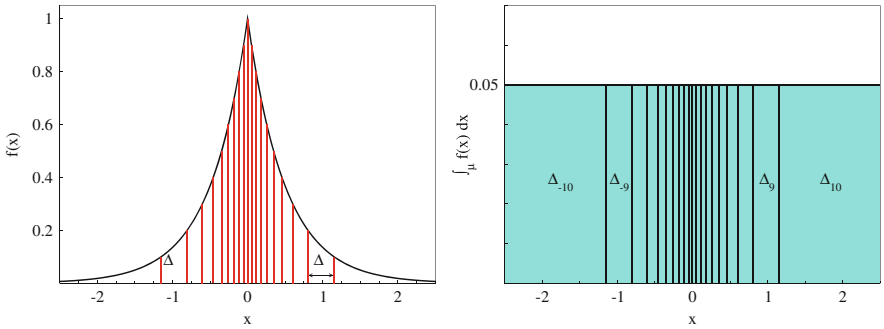

Fig. 6 Integration of one-dimensional Slater function over intervals. *Left*: *black line* $f(x) = e^{-2|x|}$; *vertical red lines* mark 20 intervals of such width Δ_i that the integral $F_i = 1/20$. *Right*: the height of the bars represents the value F_i of the $f(x)$ integral over the corresponding interval in the *left diagram* (i.e., the constant value 1/20)

The integrals F_i form a discrete distribution of values which can be approximated for sufficiently small interval width by $F_i \approx f(x_i)\Delta$. Thus, for very fine partitioning, the integral values are proportional to the function values, i.e., the resulting discrete distribution $\{F_i\}$ will mimic the function $f(x)$ because the width Δ is constant.

The integral values F_i over the intervals crucially depend on the chosen partitioning. As a special case let us perform the partitioning of the whole x range into κ intervals Δ_i such that $\int_{\Delta_i} f(x)\mathrm{d}x = 1/\kappa$, i.e., $\{F_i\}$ is a discrete distribution of constant values. Figure 6 shows exemplary such partitioning of $f(x) = e^{-2|x|}$ into 20 intervals, each yielding the integral $F_i = 1/20$. Note that in contrast to the previous example, now the number of regions is finite, with the outermost intervals (intervals Δ_{-10} and Δ_{10} in the right diagram) of infinite size.

In case of one-dimensional function, only the starting interval possibly needs to be chosen. All other intervals are then unequivocally determined by the given rule and can be found successively one after another (for nonoverlapping space-filling partitioning).

4.1.2 Compactness and Locality of Effects

The situation differs for two- and higher-dimensional space. There can be an infinite number of possibilities on how to partition the two-dimensional space into nonoverlapping space-filling regions μ_i (obeying additional rules, e.g., fixed volume or fixed integral value), even when the first region is known. This is because now the shape of μ_i becomes relevant.

Consider, for simplicity, the partitioning of a surface into nonoverlapping space-filling regions μ_i such that all the regions have the same volume (cf. the two schematic diagrams in Fig. 7 showing just seven regions of the total surface).

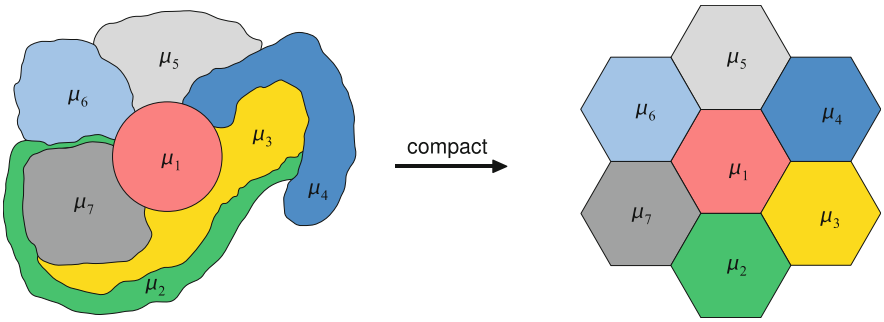

Fig. 7 Schematic picture of space partitioning into regions μ_i of identical volumes. The regions in the *right diagram* are more compact than in the *left diagram*

The regions μ_i can be of different shape (cf. the left diagram), starting from a circle (i.e., very compact one – region μ_1) to extremely narrow parts (cf. μ_2), twining around the other regions. Especially in the latter case, it would be difficult to decide to which spatial location the desired property (effect), connected with the region μ_2, should be assigned to. However, for the spatial analysis the locality of effects is important, which means that the regions should preferably be as compact as possible.

As a suitable measure of compactness in 2 dimensions can be utilized, for instance, the variance $v_i = \int_{\mu_i} (\mathbf{r} - \overline{\mathbf{r}}_i)^2 \, \mathrm{d}S$ of the positions $\mathbf{r}$ within the surface S_i of the region μ_i around the average position $\overline{\mathbf{r}}_i = \int_{\mu_i} \mathbf{r} \, \mathrm{d}S/S_i$. The smallest variance v_i° is given when the region μ_i forms a circle. Thus, let us express the compactness of a region by $c_i = v_i^\circ / v_i \leq 1$ and the compactness of the space partitioning as $\overline{c} = (1/m) \sum_i^m c_i \leq 1$, where the sum runs over all regions with finite surface (for infinite space there is always at least one infinite large region).

The compactness of the regions in the left diagram of Fig. 7 is low (except μ_1 for which $c_1 = 1$). In contrast, the right diagram shows very compact space partitioning into hexagonal regions of identical surface size (with $c_i = 0.992$). One can imagine that for such partitioning the effects connected with the respective regions act more locally then in case of the left partitioning.

Of course, real molecular and solid state systems occupy three-dimensional space. In this case the space partitioning is formed by sufficiently small nonoverlapping space-filling regions μ_i, called micro-cells, having the volumes V_i. Like in the two-dimensional case, the shape of the micro-cells needs to be restricted for proper account of the locality of the space partitioning. In 3 dimensions the variance of coordinates v_i scaled by the coordinate variance of a sphere v_i° can be used as the compactness measure c_i of the micro-cell μ_i:

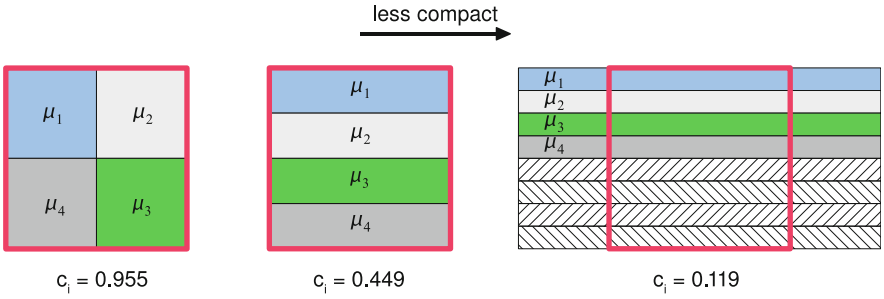

Fig. 8 Number of regions μ_i of identical volumes in chosen region Ω of space (*red square*). *Left*: 4 micro-cells of quadratic shape within Ω. *Middle*: the micro-cells (volumes unchanged) are less compact than in the *left diagram*, but all four are still within Ω. *Right*: the micro-cells (volumes unchanged) are just partially in Ω; four more micro-cells were necessary to fill the region Ω

$$c_i = \frac{v_i^\circ}{v_i} \leq 1 \qquad v_i = \int_{\mu_i} (\mathbf{r} - \overline{\mathbf{r}}_i)^2 \mathrm{d}\mathbf{r}; \qquad v_i^\circ = \frac{3}{5}\left(\frac{3}{4\pi}\right)^{2/3} V_i^{5/3}. \tag{27}$$

The compactness $\overline{c}$ of the space partitioning is the average compactness of all micro-cells with finite volumes:

$$\overline{c} = \frac{1}{m}\sum_i^m c_i \quad \forall\ i : V_i < +\infty. \tag{28}$$

The compactness of the distribution also guarantees that the number of micro-cells located in some larger region (a hint on the density of micro-cells) can be deduced from the micro-cell volumes. This would not be the case for long stretched micro-cells participating only partially on the volume of the examined region. This is elucidated in Fig. 8. The left scheme shows arbitrary chosen region Ω, represented by the red square with the volume V_Ω. The region encloses 4 quadratical micro-cells (for simplicity assumed as the most compact shape; $c_i = 0.955$) of identical volumes $V_\Omega/4$. The micro-cells in the middle scheme are "deformed" to a rectangular shape with side ratio 1:4, without changing the micro-cell volumes. The compactness drops to $c_i = 0.449$, but all 4 micro-cells are still within Ω, i.e., local to the region Ω. In the right scheme the micro-cells are further "deformed" to rectangles with side ratio 1:16, resulting in relatively low compactness of $c_i = 0.119$. The elongated micro-cells leak out from Ω and participate only with 1/2 of the micro-cell volume to V_Ω. Now, parts of eight micro-cells (note the additional 4 shaded micro-cells) are needed to fit the volume V_Ω, i.e., more than the V_Ω/V_i micro-cells deduced from the micro-cell volumes.

For a given compactness, many space-partitioning schemes are conceivable. Let us assume such compact partitioning that the (finite) volume of the largest micro-cell is smaller than a chosen value $V_{\max}$. The diameter of such micro-cell,

roughly $\sqrt[3]{V_{\max}}$, is approximately the range within that the shape of each micro-cell of the partitioning can be "deformed." Thus, an increasing refinement of the space partitioning leads to stable situation for the distribution of the micro-cells.

4.1.3 Compact Space Partitioning Around an Atom

In case of spherical symmetry, for example, considering an isolated atom, it is convenient to utilize micro-cells μ_i following the spherical symmetry as well (in the sense that all micro-cells at the same distance from the center will have the same shape). The micro-cells will be positioned in subsequent shells of the thickness Δ_i, confined between an inner sphere with the radius $r_i - \Delta_i/2$ and an outer sphere with the radius $r_i + \Delta_i/2$. If there are κ_i micro-cells in the shell, then each micro-cell in the shell has the same volume V_i:

$$V_i = \frac{1}{\kappa_i}\frac{4}{3}\pi \left(3r_i^2\Delta_i + \frac{1}{4}\Delta_i^3\right). \tag{29}$$

If the division is fine enough, i.e., for very high κ_i, the two-dimensional closest packing (cf. the right diagram of Fig. 7) within the shell can be chosen, resulting in hexagonal prismatic micro-cell shape. The inner and outer bases of each hexagonal prism are parts of the delimiting spheres forming the shell. For such micro-cells μ_i, the compactness requires that $\Delta_i = \sqrt[6]{25/27}\sqrt[3]{V_i}$, i.e., approximately $\Delta_i \approx \sqrt[3]{V_i}$ (with the compactness $c_i = 0.948$). For a given volume V_i, this yields the condition for the thickness Δ_i of the shell as well as the number κ_i of micro-cells in the shell at the distance r_i.

To perform an actual partitioning of the space, the prescription controlling the micro-cell volumes V_i must be specified. For instance, choosing volumes V_i yielding constant number κ of micro-cells in any of the consecutive shells. If the number κ of micro-cells in a shell is sufficiently high, then the shape of the micro-cells μ_i becomes almost regular hexagonal prism with the volumes $V_i \approx \Delta_i \; 4\pi r_i^2/\kappa$, i.e., the κth part of the shell volume. To fulfill the condition of compactness, the volumes of the micro-cells μ_i must increase with increasing shell radius r_i, in accordance with $\Delta_i \approx r_i\sqrt{4\pi/\kappa}$, i.e., the expression $\kappa\Delta_i^2$ recovers the surface of the sphere with the radius r_i. The two-dimensional section through such partitioning is schematically shown in the left diagram of Fig. 9 (of course, only up to certain shell, because the partitioning extends to infinity).

The above partitioning can be "evaluated" by the integration of another field over the micro-cells of the partitioning. For instance, the integration of the electron density $\rho(\mathbf{r})$ over the volumes V_i of the micro-cells μ_i yields the discrete distribution of electron populations $\{q_i\}$ with:

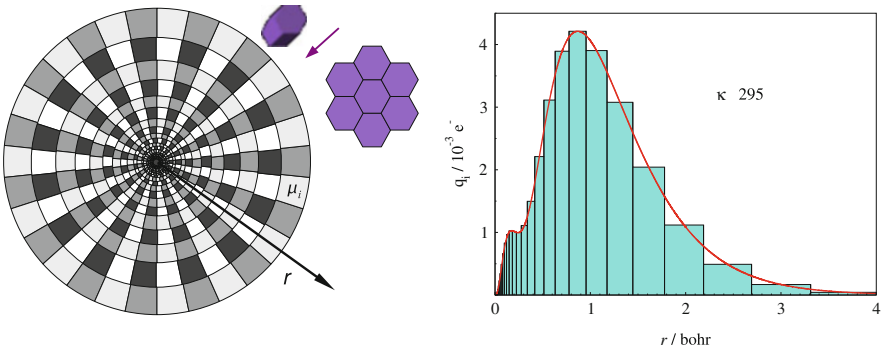

Fig. 9 Space partitioning in case of spherical symmetry. *Left*: schematic diagram of section through the space partitioning with constant number κ of micro-cells in each shell. *Right*: the height of the bars corresponds to the electron population in the micro-cells (space partitioning with $\kappa = 295$) for the Ne atom [72]; the *red solid line* is $r^3\rho(r)$, scaled by $(4\pi/\kappa)^{3/2}$ to match the bars

$$q_i = \int_{\mu_i} \rho(\mathbf{r}) d\mathbf{r} \approx \rho(\mathbf{r}_i) \;\; V_i \propto \mathbf{r}_i^3 \;\; \rho(\mathbf{r}_i). \tag{30}$$

Thus, for infinitesimally small volumes V_i of the micro-cells μ_i, i.e., very large κ, the (discrete) distribution $\{q_i\}$ yields the same topology as $\mathbf{r}^3\rho(\mathbf{r})$. In the right diagram of Fig. 9, the number of micro-cells in every spherical shell was set to $\kappa = 295$, and the electron density of the Ne atom [72] was integrated over the micro-cells. The width of the bars corresponds to the width of the micro-cells (Δ_i) of the space partitioning. The height of the bars shows the electron populations q_i in the micro-cells μ_i. The red solid line, given by $(4\pi/\kappa)^{3/2}\mathbf{r}^3\rho$, highlights the proportionality between the distribution $\{q_i\}$ and the expression $\mathbf{r}^3\rho$.

There is an additional interesting issue. The diagrams for both the function $\mathbf{r}^3\rho$ (properly scaled) and the distribution $\{q_i\}$ for infinitesimally small volumes will be practically identical (as the distance between the discrete q_i values is infinitesimally small). But in contrast to the total integral $\int \mathbf{r}^3\rho(\mathbf{r})d\mathbf{r}$ of the continuous expression, yielding the expectation value $\langle r^3 \rangle$, the distribution $\{q_i\}$ must be summed up giving $\sum q_i = N$, the number of electrons in the system. Also, it should be emphasized that the space partitioning was performed applying a geometrical prescription, i.e., in contrast to the space partitioning described in the following section, without any field involved.

4.2 ω-*Restricted Space Partitioning*

An appealing prescription for the space partitioning is such one that yields micro-cells describing objects of same "quality." This is comparable to a procedure in

laboratory, where all samples have certain identical property, for instance, the same volume, weight, resistivity, etc. Let us attribute the term "quality" to the integral of chosen n-particle function $f_c(\mathbf{r}_1, \cdots, \mathbf{r}_n)$ over the volume V_i of the micro-cell μ_i:

$$ {}^nF_i = \int_{\mu_i} \mathrm{d}\mathbf{r}_1 \cdots \int_{\mu_i} f_c(\mathbf{r}_1, \cdots, \mathbf{r}_n) d\mathbf{r}_n \tag{31} $$

The micro-cells are assumed to be of the same "quality" with respect to the so-called *control* function f_c when for the micro-cells μ_i the integrals ${}^nF_i$ have the same value ω. This assumption can be utilized to control the volume and the number of the micro-cells, i.e., the space partitioning (which explains the designation "control function"). In Martín Pendás et al. [68], the ω-restricted space partitioning (ωRSP) was defined as the decomposition of the volume into compact nonoverlapping space-filling regions that obey the restriction that the integral of the control function over each region yields the fixed value ω.

If the control function is a nonzero constant $f_c \equiv \xi$, then all micro-cells of the ωRSP have the same volume $V_i = \omega/\xi$. Otherwise, a suitable control function should be real valued and everywhere positive (everywhere negative) to avoid cancelations during the integration of f_c over the micro-cell volume. Thus, the ωRSP follows the rules (for $\overline{c}$ and ${}^nF_i$, cf. Eqs. (28) and (31)):

- $\mu_i \cap \mu_j = \varnothing \quad \forall\ i \neq j$
- $X^n = \cup_i \mu_i$
- $\delta\overline{c} = 0$
- ${}^nF_i = \omega \qquad \forall\ i$

4.2.1 1-Particle Control Function

For the 1-particle control function $f_c(\mathbf{r})$ with the integral over the whole space yielding the finite value F_c and the μ_i integrals evaluating to ${}^1F_i$:

$$ F_c = \int f_c(\mathbf{r}) \mathrm{d}\mathbf{r} = \sum_i^{\kappa} \int_{\mu_i} f_c(\mathbf{r}) \mathrm{d}\mathbf{r} = \sum_i^{\kappa} {}^1F_i = \kappa\omega, \tag{32} $$

where the number κ of micro-cells can easily be determined. If the value of the restriction Ω is so small that the integrals over μ_i of Eq. (32) yielding Ω can be approximated by

$$\omega = \int_{\mu_i} f_c(\mathbf{r})\mathrm{d}\mathbf{r} \approx f_c(\mathbf{r})V_i, \tag{33}$$

then the volumes V_i of the micro-cells μ_i can be approximately determined from (i.e., utilizing the zeroth term of Taylor expansion of f_c):

$$V_i \approx \omega / f_c(\mathbf{a}_i) \tag{34}$$

where $\mathbf{a}_i$ is a position within the micro-cell volume V_i, e.g., conveniently the average coordinate $\bar{\mathbf{r}}_i$ (cf. Sect. 4.1.2 and Eq. (27)). Of course, for $f_c(\mathbf{a}_i) = 0$, the volume must be determined from the integral representation (for approximate expression, using higher terms of Taylor expansion of f_c).

An example of 1-particle control function is the electron density $\rho(\mathbf{r})$. The ωRSP controlled by the electron density of an N-electron system will consist of $\kappa = N/\omega_q$ micro-cells, with each micro-cell μ_i restricted to enclose the fixed amount of electron population (charge) ω_q. For the restriction ω_q small enough to apply the approximation in Eq. (33), the volumes of micro-cells μ_i will be given by $V_i = \omega_q/\rho(\bar{\mathbf{r}}_i)$.

4.2.2 2-Particle Control Function

The situation is somewhat different for a 2-particle control function $f_c(\mathbf{r}_1, \mathbf{r}_2)$. In this case only a part of the total integral F_c is recovered by the sum of all ${}^2F_i$ values (cf. the general Eq. (31) for n particles):

$$F_c = \sum_{i,j} \int_{\mu_i} \mathrm{d}\mathbf{r}_1 \int_{\mu_j} f_c(\mathbf{r}_1, \mathbf{r}_2) d\mathbf{r}_2 = \sum_{i \neq j} \int_{\mu_i} \mathrm{d}\mathbf{r}_1 \int_{\mu_j} f_c(\mathbf{r}_1, \mathbf{r}_2) d\mathbf{r}_2 + \sum_{i}^{\kappa} {}^2F_i. \tag{35}$$

Of course, the sum of the ${}^2F_i$ values equals $\kappa\omega$ as dictated by the ωRSP. But the number κ of micro-cells cannot be inferred from the F_c value alone, without the knowledge of the sum of terms with integrals over differing micro-cells.

If the restriction ω is small enough, then the integrals ${}^2F_i$ can be approximated by integrals over Taylor expansions around chosen position (e.g., $\bar{\mathbf{r}}_i$) within the micro-cell volume V_i:

$${}^2F_i = \int_{\mu_i} \mathrm{d}\mathbf{r}_1 \int_{\mu_i} f_c(\mathbf{r}_1, \mathbf{r}_2) d\mathbf{r}_2 = t_c(\bar{\mathbf{r}}_i)\ V_i^{\vartheta_c} + \varepsilon_c(\bar{\mathbf{r}}_i). \tag{36}$$

The function $t_c(\bar{\mathbf{r}}_i)$ and the parameter ϑ_c are determined by the first non-vanishing term of the applied Taylor expansion. The correction term $\varepsilon_c(\bar{\mathbf{r}}_i)$ ensures the fulfillment of the integral value (the correction is specific to the micro-cell μ_i). The micro-cell volume V_i can be approximated by:

$$V_i = \left[\frac{\omega - \varepsilon_c(\bar{\mathbf{r}}_i)}{t_c(\bar{\mathbf{r}}_i)}\right]^{1/\vartheta_c} \approx \left[\frac{\omega}{t_c(\bar{\mathbf{r}}_i)}\right]^{1/\vartheta_c}, \tag{37}$$

because the correction term $\varepsilon_c(\bar{\mathbf{r}}_i)$ becomes negligibly small with respect to $t_c(\bar{\mathbf{r}}_i)$ $V_i^{\vartheta_c}$ for sufficiently small ω. This approximation is of course valid also for 1-particle control function.

As the 2-particle control function can serve, for instance, the same-spin electron pair density, $\rho_2^{\sigma\sigma}(\mathbf{r}_1, \mathbf{r}_2)$ normalized to the total number of σ-spin electron pairs $N_\sigma(N_\sigma - 1)/2$. The integral of the same-spin pair density over each micro-cell volume yields the number of same-spin pairs $D_i^{\sigma\sigma}$ in the micro-cell. As will be shown later, the number of pairs D_i can be approximated by the integral of the pair density Laplacian (in which case $\vartheta_c = 8/3$ and $t_c(\bar{\mathbf{r}}_i)$ is the Fermi hole curvature). The number of micro-cells with $D_i^{\sigma\sigma}$ restricted to the value ω_D could be determined if the number of pairs formed *between* the micro-cells would be known as well.

4.3 From Discrete to Quasi-continuous

The micro-cells of an ωRSP play the role of objects of the same "quality." Then, the micro-cells μ_i can be "evaluated" by the integrals of an m-particle *sampling* function $f_s(\mathbf{r}_1, \cdots, \mathbf{r}_m)$ over the micro-cell volumes V_i yielding the sampling values ${}^m\zeta_i$:

$${}^m\zeta_i = \int_{\mu_i} d\mathbf{r}_1 \cdots \int_{\mu_i} f_s(\mathbf{r}_1, \cdots, \mathbf{r}_m) d\mathbf{r}_m. \tag{38}$$

The discrete distribution $\{{}^m\zeta_i\}$ shows how the chosen sampling property propagates through the particular spatial configuration (inherent to the examined system) of the micro-cells. Each ${}^m\zeta_i$ value indicates which amount of the sampling property is connected to a fixed amount of the control property at the examined position (micro-cell) in the system.

Note that unlike the "breathing sphere" of Savin [47] (enclosing constant charge), the examined micro-cell is not continuously moved through the system during the evaluation of the sampling property. Instead, with ωRSP first the whole space is at once partitioned and then the sampling function is evaluated yielding a discrete distribution (observe that the "breathing sphere" approach results in a continuous function). In case of 1-particle sampling function, connected to an expectation value of an operator, the corresponding distribution $\{{}^1\zeta_i\}$ shows how the expectation value is divided among the "probes" (i.e., micro-cells) of the same "quality."

Using the Taylor expansion of the sampling function f_s, the integral ${}^m\zeta_i$ can be replaced by the expression:

$$ {}^{m}\zeta_i = t_{\mathrm{s}}(\overline{\mathbf{r}}_i)\ V_i^{\vartheta_{\mathrm{s}}} + \varepsilon_{\mathrm{s}}(\overline{\mathbf{r}}_i) \tag{39} $$

where the function $t_{\mathrm{s}}(\overline{\mathbf{r}}_i)$ and the parameter ϑ_{s} follow from the first non-vanishing term the Taylor expansion around the position $\overline{\mathbf{r}}_i$ in the micro-cell volume V_i. With the correction term $\varepsilon_{\mathrm{s}}(\overline{\mathbf{r}}_i)$, the exact integral value for the micro-cell μ_i, as given by Eq. (38), is recovered.

The approximate expression for ${}^{m}\zeta_i$ has not only the advantage of a simple formula for the calculation of the integral over the chosen region (with small volume), but more importantly the connection to the micro-cell volume restricted by the ωRSP procedure can easily be established. This is done by replacing the volume V_i in Eqs. (39) from (37):

$$ {}^{m}\zeta_i = t_{\mathrm{s}}(\overline{\mathbf{r}}_i)\ \left[\frac{\omega - \varepsilon_{\mathrm{c}}(\overline{\mathbf{r}}_i)}{t_{\mathrm{c}}(\overline{\mathbf{r}}_i)}\right]^{\vartheta_{\mathrm{s}}/\vartheta_{\mathrm{c}}} + \varepsilon_{\mathrm{s}}(\overline{\mathbf{r}}_i) = t_{\mathrm{s}}(\overline{\mathbf{r}}_i)\ \left[\frac{\omega}{t_{\mathrm{c}}(\overline{\mathbf{r}}_i)}\right]^{\vartheta_{\mathrm{s}}/\vartheta_{\mathrm{c}}} + \varepsilon(\overline{\mathbf{r}}_i) \tag{40} $$

with all the corrections included in $\varepsilon(\overline{\mathbf{r}}_i)$. For sufficiently small restriction ω (for which ε becomes very small), the sampling values can be approximated by:

$$ {}^{m}\zeta_i \approx \omega^{\vartheta_{\mathrm{s}}/\vartheta_{\mathrm{c}}}\ t_{\mathrm{s}}(\overline{\mathbf{r}}_{ii})\left[\frac{1}{t_{\mathrm{c}}(\overline{\mathbf{r}}_i)}\right]^{\vartheta_{\mathrm{s}}/\vartheta_{\mathrm{c}}} \tag{41} $$

From the above expression, it is clear that for the micro-cell μ_i (centered at the position $\overline{\mathbf{r}}_i$), the sampling value ${}^{m}\zeta_i$ depends only on (is scaled by) the choice of the value for the restriction ω, which controls the volume of the micro-cell. That is, the approximate values for the whole distribution $\{{}^{m}\zeta_i\}$ are uniquely preset by the functions t_{s} and t_{c}. The value of the restriction ω determines the actual size (and the number) of micro-cells and thus specifies the scale for the sampling values (i.e., more precisely the multiplicator $\omega^{\vartheta_{\mathrm{s}}/\vartheta_{\mathrm{c}}}$).

Let us apply the ωRSP to the Ne atom using the basis set of Clementi and Roetti [72]. The left diagram of Fig. 10 shows a section through the micro-cells of the space partitioning restricted to enclose $\omega_D = 10^{-8}$ same-spin electron pairs. It can be seen that each spherical shell contains different number of micro-cells. It should be emphasized that there are no micro-cells outside the outermost shell (with the largest micro-cells) shown in the diagram. There is just one additional huge region with ω_D pairs extending to infinity (thus not compact), i.e., the total number of regions is finite. This is in contrast to the space partitioning discussed in Sect. 4.1.3 (cf. Fig. 9), with infinite number of micro-cells. Observe that only if the space partitioning is based on control function normalized to finite F_{c} value (total number of same-spin pairs in case of the Ne atom), the number of micro-cells will be finite as well.

In each micro-cells of the above space partitioning, the σ-spin electron density of the Ne atom can be sampled, yielding the discrete distribution of charges $\{q_i^{\sigma}\}$ (cf. the right diagram of Fig. 10). The width of the bars corresponds to the width of

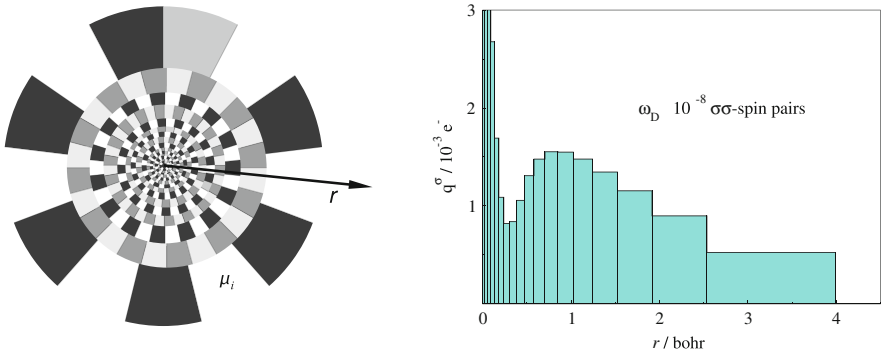

Fig. 10 ωRSP for Ne atom [72, 80] with micro-cells restricted to enclose 10^{-8} same-spin electron pairs. *Left*: schematic diagram of section through the space partitioning. *Right*: the height of the bars corresponds to the electron population in micro-cells

the micro-cells centered at the distance r from the Ne nucleus and the height represents the charge (population) q_i^σ within the micro-cell. The electron population q_i^σ of the micro-cell μ_i is given by:

$$q_i^\sigma = \int_{\mu_i} \rho^\sigma(\mathbf{r}) d\mathbf{r} \approx \rho^\sigma(\overline{\mathbf{r}}_i) \; V_i. \tag{42}$$

Thus, the charge in each micro-cell can be approximated by the product of the electron density at the position $\overline{\mathbf{r}}_i$ and the volume of the micro-cell centered at this position (i.e., $t_s \equiv \rho^\sigma$ and $\vartheta_s = 1$ in Eq. (39)).

The volumes of the micro-cells are determined by the restriction ω_D, i.e., a change of the ω_D value implies the change of the micro-cell volumes in accordance with Eq. (37). In case of micro-cells restricted to enclose a fixed amount ω_D of same-spin electron pairs, the distribution of electron populations will scale with ω_D as follows (with $\vartheta_c = 8/3$, cf. Eq. (41) and Sect. 4.4):

$$q_i^\sigma \approx \omega_D^{3/8} \rho^\sigma(\overline{\mathbf{r}}_i) \left[\frac{12}{t_c(\overline{\mathbf{r}}_i)} \right]^{3/8}. \tag{43}$$

The left diagram of Fig. 11 shows the discrete distributions of charges resulting from the sampling of electron density ρ^σ of the Ne atom over micro-cells restricted to enclose the fixed amount of same-spin pairs ω_D equal 10^{-8}, 10^{-9}, and 10^{-16}, respectively. The circles show the electron population in the micro-cells centered at the marked distances $\overline{\mathbf{r}}_i$ from the nucleus. The large black circles represent the distribution for $\omega_D = 10^{-8}$ same-spin pairs. The micro-cells are relatively large (cf. also Fig. 10), which gives rise to the sparse distribution of the circles. The electron populations are given in units of 10^{-3} electrons (the left side scale).

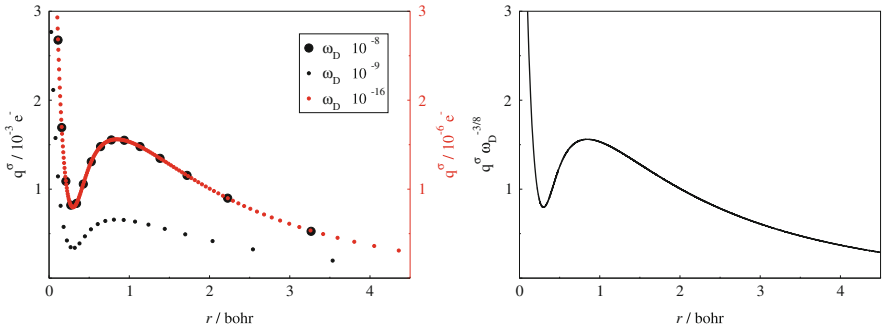

Fig. 11 Electron populations for the Ne atom [72, 80]. *Left*: the micro-cells, centered at distances marked by *circles*, are restricted to enclose the amount ω_D of same-spin pairs. The values for the *black circles* refer to the left side scale and for the *small red circles* to the *red scale* on the right side of the diagram. *Right*: electron populations rescaled by ${\omega_D}^{3/8}$. The distribution is so dense (with ω_D not explicitly specified) that the positions are no more distinguishable (but discrete)

Reducing the restriction to $\omega_D = 10^{-9}$ same-spin pairs diminishes the electron populations as well (cf. the small black circles), due to the reduction of the micro-cell volumes. And vice versa the number of micro-cells has increased as reflected by the denser spacing of the circles along the distance from the nucleus. Further reduction to $\omega_D = 10^{-16}$ same-spin pairs yields much smaller micro-cells as shown by the dense distribution of the small red circles in the diagram. The populations in the micro-cells of this distribution are seemingly of same value as for the $\omega_D = 10^{-8}$ restriction. However, observe that the charges for the $\omega_D = 10^{-16}$ restriction are related to the scale on the left side of the diagram given in 10^{-6} electrons. This is due to the scaling with the factor ${\omega_D}^{3/8}$ in Eq. (43) for the approximate electron population.

Let us divide the sampling values ${}^m\zeta_i$ by the factor $\omega^{\vartheta_s/\vartheta_c}$:

$$\frac{1}{\omega^{\vartheta_s/\vartheta_c}}\,{}^m\zeta_i = \frac{1}{\omega^{\vartheta_s/\vartheta_c}}\int_{\mu_i} \mathrm{d}\mathbf{r}_1 \cdots \int_{\mu_i} f_s(\mathbf{r}_1, \cdots, \mathbf{r}_m) d\mathbf{r}_m. \tag{44}$$

In such a way rescaled sampling values can be approximated by a position-dependent function (determined by the Taylor expansion) (cf. Eq. (41)):

$$\frac{1}{\omega^{\vartheta_s/\vartheta_c}}\,{}^m\zeta_i \approx t_s(\overline{\mathbf{r}}_i)\left[\frac{1}{t_c(\overline{\mathbf{r}}_i)}\right]^{\vartheta_s/\vartheta_c}, \tag{45}$$

i.e., the function does not include the ω value. The exact rescaled sampling values are still dependent on the ω value (however, the differences between the exact and approximate values decrease with ω). The limit of the distribution of rescaled sampling values:

$$\lim_{\omega\to 0}\left\{{}^{m}\zeta_i\ \ \omega^{-\vartheta_s/\vartheta_c}\right\} \approx t_s(\mathbf{r})\left[\frac{1}{t_c(\mathbf{r})}\right]^{\vartheta_s/\vartheta_c} = t_s(\mathbf{r})\ \ \widetilde{V}^{\vartheta_s}(\mathbf{r}) \tag{46}$$

is a continuous function. $\widetilde{V}(\mathbf{r})$ is the so-called volume function given by the limit of the micro-cell volume rescaled by ω^{1/ϑ_c} (cf. Eq. (37)).

Thus, rescaling all the sampling values (charges) shown in Fig. 11 with the corresponding $\omega_D^{3/8}$ would result in data points closely gathered around the curve given by:

$$\lim_{\omega\to 0}\left\{q_i\ \ \omega_D^{-3/8}\right\} \approx \rho^{\sigma}(\mathbf{r})\left[\frac{1}{t_c(\mathbf{r})}\right]^{3/8} = \rho^{\sigma}(\mathbf{r})\ \ \widetilde{V}_D(\mathbf{r}), \tag{47}$$

with pair–volume function $\widetilde{V}_D(\mathbf{r})$ representing the rescaled volume of a fixed fraction of the same-spin electron pair. The rescaled distribution of charges $\left\{q_i\ \ \omega_D^{-3/8}\right\}$ can be formed for any nonzero value ω_D. For infinitesimally small ω_D, the rescaled charges will become practically indistinguishable from the limit after rescaling [Eq. (47)]. However, the number of the members of the distribution $\left\{q_i\ \ \omega_D^{-3/8}\right\}$ will still be finite (and determined by ω_D). With suitable nonzero ω_D, the rescaled distribution can be made as dense as desired, but never continuous. In other words, one can compute the rescaling sampling values at any chosen discrete set of positions, similarly to a continuous function, with the confidence that the data will be members of a distribution determined by certain (unknown) nonzero ω_D. Data set with such behavior is termed a *quasi-continuous* distribution [8, 68]. The diagram on the right side of Fig. 11 shows the discrete distribution of rescaled charges. The distribution (with ω_D not explicitly given) is so dense that the actual positions of the corresponding micro-cells cannot be recognized. Here, without the knowledge of ω_D, it is not even possible to count the micro-cells. The diagram of the distribution appears to be like that for a continuous function (ω_D is so small that the situation does not change for any magnification, i.e., ω_D is infinitesimally small). Of course, strictly speaking, any center of the contributing micro-cell is a point isolated from other micro-cell centers. Finally, it cannot be truly adjudged from the right diagram of Fig. 11 whether the reader is not cheated by the continuous curve for the limit after rescaling (cf. Eq. (47)).

4.4 The Electron Localizability Indicator

On the basis of the ωRSP, various discrete distributions can be created based on the choice of the control and sampling functions. Both the control and sampling functions depend on the coordinates of one or more electrons (cf. Sects. 4.2 and 4.3). If the sampling function depends on 1 electron only, then the sum of all

sampling values yields the corresponding expectation value. An appealing choice for a single-electron sampling function is the electron density which gives after the application of the ωRSP a discrete distribution of electron populations (charges), with the sum of all values equal to the number of electrons in the system. After the rescaling (cf. Sect. 4.3), the resulting quasi-continuous distribution can be analyzed. Of course, the topology as well as the interpretation of such distribution crucially depends on the choice of the control function.

4.4.1 ELI-D and ELI-q

An interesting choice for the control function is, among others [25, 81], the electron pair density (respectively a specific part of it). Then, the ωRSP describes micro-cells enclosing fixed pair population. The procedure in which the distribution of certain variant of populations (e.g., the electronic charges) is determined over micro-cells controlled by (fixed) value of another population variant (e.g., electron pair population) is termed the *restricted populations approach* [68]. The electron localizability indicator ELI-D is a quasi-continuous rescaled distribution of charges over micro-cells enclosing fixed amount ω_D of electron pairs:

$$\Upsilon_D^{\sigma}(\mu) = \frac{1}{\omega_D^{p}} \int_{\mu} \rho^{\sigma}(\mathbf{r}) \; \mathrm{d}\mathbf{r} : \quad \omega_D = \iint_{\mu} \rho_2^{\sigma\sigma}(\mathbf{r}_1, \mathbf{r}_2) \; \mathrm{d}\mathbf{r}_1 \mathrm{d}\mathbf{r}_2 = \text{const.} \tag{48}$$

The ELI-D values are represented by the symbol Υ_D^{σ}, where σ indicates for which spin the localization was computed. This can be either the α spin or β spin, when the electron density was derived from the $\alpha\alpha$-spin and $\beta\beta$-spin pair density, respectively. Another possibility, especially convenient for spin-polarized systems, is to split the total pair density into two parts, $\rho_2^{(t)}$ and $\rho_2^{(s)}$, for electron pairs coupling to triplet and singlet, respectively [8]. Then, for $\Upsilon_D^{(t)}$ and $\Upsilon_D^{(s)}$, the population of electrons coupling to a triplet (singlet) in micro-cells enclosing fixed amount of tripled (singlet) pairs is analyzed. The exponent p in Eq. (48) depends on the chosen spin components. This is due to the mathematical procedure on how the integrals of electron density and pair density are evaluated. The integrals in Eq. (48) can be in principle exactly evaluated whenever the electron density and pair density are available. However, as described in Sects. 4.2 and 4.3, for very small micro-cells, the integrals can be replaced by the Taylor expansion around a chosen position **a** in the micro-cell. The electron population in micro-cell μ with the volume V_μ is approximately:

$$\int_{\mu} \rho^{\sigma}(\mathbf{r}) \; \mathrm{d}\mathbf{r} \approx \rho^{\sigma}(\mathbf{a}) V_{\mu}, \tag{49}$$

whereby for sufficiently small micro-cells the error approaches zero. The micro-cell volume can be determined from the ω_D integral that can be in case of same-spin pair density (respectively for the triplet-coupled pairs) approximated by [8]:

$$\omega_D = \iint_{\mu} \rho_2^{\sigma\sigma}(\mathbf{r}_1, \mathbf{r}_2) \; \mathrm{d}\mathbf{r}_1 \mathrm{d}\mathbf{r}_2 \approx \frac{1}{12} g^{\sigma}(\mathbf{a}) \; V_{\mu}^{8/3}, \tag{50}$$

with the Fermi hole curvature $g^{\sigma}(\mathbf{a})$ at the position $\mathbf{a}$ in the micro-cell. Thus, the micro-cell volume can be approximated by $V_{\mu} = [12\omega_D / g^{\sigma}(\mathbf{a})]^{3/8}$, and choosing $p = 3/8$ for the exponent in Eq. (48) ensures that in the limit after rescaling the ELI-D for this spin variant will converge to the value:

$$\widetilde{\Upsilon}_D^{\sigma}(\mathbf{r}) = \lim_{\omega \to 0} \left[\Upsilon_D^{\sigma}(\mu) \right] = \rho^{\sigma}(\mathbf{r}) \; \left[\frac{12}{g^{\sigma}(\mathbf{r})} \right]^{3/8}. \tag{51}$$

ELI-D in the limit after rescaling $\widetilde{\Upsilon}_D^{\sigma}(\mathbf{r})$ is a continuous function, whereas $\Upsilon_D^{\sigma}(\mu)$ is a quasi-continuous distribution.

The scaling exponent p is different for ELI-D based on singlet-coupled electron pairs. The reason for this is that the probability density for two opposite-spin electrons placed on top of each other is usually nonzero. The integral of the singlet-pair density $\rho_2^{(s)}(\mathbf{r}_1, \mathbf{r}_2)$ over a micro-cell can be approximated by [8]:

$$\omega_D = \iint_{\mu} \rho_2^{(s)}(\mathbf{r}_1, \mathbf{r}_2) \; \mathrm{d}\mathbf{r}_1 \mathrm{d}\mathbf{r}_2 \approx \rho_2^{(s)}(\mathbf{a}, \mathbf{a}) \; V_{\mu}^2. \tag{52}$$

Now the micro-cell volume can be approximated by $V_{\mu} = \sqrt{\omega_D / \rho_2^{(s)}(\mathbf{a}, \mathbf{a})}$, and choosing $p = 1/2$ for the exponent in Eq. (48) ensures that in the limit after rescaling the ELI-D for the singlet-coupled electrons will converge to the value:

$$\widetilde{\Upsilon}_D^{(s)}(\mathbf{r}) = \lim_{\omega \to 0} \left[\Upsilon_D^{(s)}(\mu) \right] = \rho^{(s)}(\mathbf{r}) \; \left[\frac{1}{\rho_2^{(s)}(\mathbf{r}, \mathbf{r})} \right]^{1/2}. \tag{53}$$

Observe that in the above expression, the density of singlet-coupled electrons is integrated. Additionally, only for explicitly correlated wave function, the so-called on-top value $\rho_2^{(s)}(\mathbf{r}, \mathbf{r})$ will differ from the product of $\rho^{\alpha}(\mathbf{r})\rho^{\beta}(\mathbf{r})$ of the spin densities. This means that a reasonable evaluation of ELI for singlet-coupled electron pairs can be applied only to correlated wave functions, because $\Upsilon_D^{(s)}$ yields a constant value for single-determinantal wave functions.

For all the abovementioned spin variants, the electron density can be chosen as the control function. The resulting electron localizability indicator ELI-q is a quasi-continuous rescaled distribution of pair populations over micro-cells enclosing fixed charge ω_q:

$$\Upsilon_q^{\sigma\sigma}(\mu) = \frac{1}{\omega_q^p}\iint_\mu \rho_2^{\sigma\sigma}(\mathbf{r}_1,\mathbf{r}_2)\ \mathrm{d}\mathbf{r}_1\mathrm{d}\mathbf{r}_2 : \quad \omega_q = \int_\mu \rho^\sigma(\mathbf{r})\ \mathrm{d}\mathbf{r} = \text{const.} \tag{54}$$

Using Eq. (49) the volume of the q-restricted micro-cell can be approximated by $V_\mu = \omega_q/\rho^\sigma(\mathbf{a})$. Approximating the same-spin (respectively triplet-coupled) pair density integral by the expression in Eq. (50) and taking $p = 8/3$ yields for the limit after rescaling:

$$\widetilde{\Upsilon}_q^{\sigma\sigma}(\mathbf{r}) = \lim_{\omega\to 0}\left[\Upsilon_q^{\sigma\sigma}(\mu)\right] = \frac{1}{12}g^\sigma(\mathbf{r})\ \left[\frac{1}{\rho^\sigma(\mathbf{r})}\right]^{8/3}. \tag{55}$$

The comparison of the above expression with Eq. (51) shows the straightforward connection between the ELI values for the D-restricted and q-restricted space partitioning. The same procedure applied to the singlet-coupled electron pairs (using the approximate expression of Eq. (52) together with $p = 2$) gives in the limit after rescaling the corresponding ELI-q:

$$\widetilde{\Upsilon}_q^{(s)}(\mathbf{r}) = \lim_{\omega\to 0}\left[\Upsilon_q^{(s)}(\mu)\right] = \rho_2^{(s)}(\mathbf{r},\mathbf{r})\left[\frac{1}{\rho^{(s)}(\mathbf{r})}\right]^2. \tag{56}$$

Again, there is a simple connection between $\Upsilon_q^{(s)}$ and $\Upsilon_D^{(s)}$ (cf. Eq. (53)). For convenience, the above ELI-q expression is used with a scaling factor 1/4 $[(N-2)/(N-1)]^2$ with the effect that the ELI-q value reaches 1 for uncorrelated pairs.

4.4.2 ELI-D or ELI-q?

Which of the ωRSP should be used for the ELI, the D-restricted or q-restricted approach? To decide this, the meaning of the distribution must be understood. Loosely speaking, ELI-D is proportional to the charge needed to form an electron pair. The higher the Υ_D^σ value is, the more charge is needed to form the electron pair, i.e., the electronic motion is more correlated and the same-spin electrons are avoiding each other to higher extent. It can be also shown that Υ_D^α is proportional to the event probability $P_1^\alpha(\mu)$ which shows how "alone" an electron is in the micro-cell μ. The $P_1^\alpha(\mu)$ is the probability to find exclusively single electron inside the micro-cell (with all remaining electrons outside the micro-cell) [30, 32]. From the derivation of ELI-D and ELI-q, it is clear that both are in an inverse proportional relationship (besides differing exponents), with ELI-q indicating how much electron pairs can be formed from the fixed amount of charge.

High ELI-D values for the Υ_D^α, Υ_D^β, and $\Upsilon_D^{(t)}$ variants are found in regions attributed to atomic shells, bonds, and lone pairs as such regions are particularly characteristic for the reluctance to form a same-spin and triplet-coupled electron

pair, respectively. In case of the singlet coupling, the ELI-q variant $\Upsilon_q^{(s)}$ is more suitable as a bonding descriptor, because the singlet-coupled (opposite-spin) pairs are expected to be formed in the bonding regions and removed by the correlation outside the shells, bonds, and lone pairs. The $\Upsilon_q^{(s)}$ approach is nicely in accord with Lewis idea of a chemical bond represented by an (opposite-spin) electron pair. Nowadays the notion of a Lewis pair is usually connected with a doubly occupied orbital (in the independent particle model). However, in his famous paper, Lewis did not consider occupation of levels and orbitals. Instead, he used very emphatic and vivid description of electron pairs clearly located in coordinate space, e.g., at the edges of a cube around the nucleus. From this viewpoint, the $\Upsilon_q^{(s)}$, describing a particular sort of spatial extent of opposite-spin pairing, would be the preferred descriptor for the analysis of the bonding situation in a molecule or solid.

Unfortunately, this concept has very stringent limitation dictated by the independent particle model, which is the most used one in the computational chemistry. In this model, the motion of the opposite-spin electrons is fully uncorrelated, i.e., the probability density to find two opposite-spin electrons at the positions $\mathbf{r}_1$ and $\mathbf{r}_1$ (and all the other electrons somewhere in space) is simply the product of the electron densities $\rho^{\alpha}(\mathbf{r}_1)\rho^{\beta}(\mathbf{r}_1)$. Then, the ωRSP with the restriction of fixed charge yields for $\Upsilon_q^{(s)}$ identical pair populations in each micro-cell, and there is nothing to be analyzed. The $\Upsilon_q^{(s)}$ is a very sensitive tool to inspect the influence of correlation, but the access to explicitly correlated wave functions is heavily computer resource demanding.

For the majority of the ELI analyses, the ELI-D variant has to be used. Do we see the opposite-spin pairing in this case? In certain sense yes, but not explicitly. As mentioned above, the Υ_D^{α} is proportional to the $P_1^{\alpha}(\mu)$ event probability. For closed-shell wave function, it is proportional to the $P_1^{\beta}(\mu)$ as well. For single-determinantal wave functions, the opposite-spin pair population is, for sufficiently small regions μ, given mainly by the product $P_1^{\alpha}(\mu)P_1^{\beta}(\mu)$. In this case the squared Υ_D^{α} distribution reproduces the data for the (uncorrelated) opposite-spin pairs. This assertion is not exact for correlated wave functions. Even more, whereas the explicit inclusion is decisive for the $\Upsilon_q^{(s)}$ distribution for the singlet coupling, there are only minute changes in the topology of $\Upsilon_D^{(t)}$ for the triplet coupling [82].

For complete comparison, the spin-pair composition of Silvi [67] is also evaluated for the examples described in the following sections. To the best of my knowledge, the spin-pair composition was derived and used only for the independent particle model. In this case, as described in Sect. 2.10, the spin-pair composition c_{π} is proportional to the ELF kernel. The spin-pair composition can be derived on the basis of the q-restricted ωRSP. For the independent particle, the only difference to the derivation of Silvi would be that with the ωRSP approach, the spin-pair composition is a quasi-continuous distribution instead of a continuous function. From Eqs. (50) and (52), it can be seen that the ratio of the same-spin and opposite-spin pairs in a micro-cell is proportional to cell volume $V_{\mu}^{2/3}$. Replacing

the micro-cell volume by $V_\mu = \omega_q/\rho$ (cf. Eq. (49)) yields for independent particles the factor $\rho^{5/3}$ used by Silvi. Similar procedure can be consistently applied to the ratio of the triplet-coupled to singlet-coupled electron pairs computed for correlated wave function:

$$c_\pi(\mu) = \frac{\iint_\mu \rho_2^{(t)}(\mathbf{r}_1, \mathbf{r}_2)\ \mathrm{d}\mathbf{r}_1 \mathrm{d}\mathbf{r}_2}{\iint_\mu \rho_2^{(s)}(\mathbf{r}_1, \mathbf{r}_2)\ \mathrm{d}\mathbf{r}_1 \mathrm{d}\mathbf{r}_2}. \tag{57}$$

Using the approximate expressions from Eqs. (50), (52), and (49), it follows:

$$c_\pi(\mu) \approx \frac{1}{\omega_q^p}\frac{1}{12}\frac{g^{(t)}(\mathbf{a})\ V_\mu^{8/3}}{\rho_2^{(s)}(\mathbf{a},\mathbf{a})\ V_\mu^2} = \frac{1}{\omega_q^p}\frac{1}{12}\frac{g^{(t)}(\mathbf{a})}{\rho_2^{(s)}(\mathbf{a},\mathbf{a})}\ \frac{\omega_q^{2/3}}{\rho(\mathbf{a})^{2/3}} \tag{58}$$

and choosing $p = 2/3$ yields for the limit after rescaling the expression

$$\widetilde{c}_\pi(\mathbf{r}) = \lim_{\omega\to 0}\left[c_\pi(\mu)\right] = \frac{1}{12}\frac{g^{(t)}(\mathbf{r})}{\rho_2^{(s)}(\mathbf{r},\mathbf{r})}\frac{1}{\rho(\mathbf{r})^{2/3}}, \tag{59}$$

with the Fermi hole curvature $g^{(t)}(\mathbf{r})$ for the triplet-coupled electron pair, the singlet-pair on-top density $\rho_2^{(s)}(\mathbf{r},\mathbf{r})$, and the total electron density $\rho(\mathbf{r})$. For the same-spin and opposite-spin pairs at single-determinantal level, the above expression recovers Silvi's formulation. Following the original paper, the spin-pair composition is used with the Lorentzian scaling, i.e., $1/\left[1 + c_\pi^2\right]$. However, in the spirit of the ωRSP approach, it would be more consistent to directly use the c_π, but defined as the ratio of the singlet-coupled to the triplet-coupled electron pairs. The inclusion of the singlet-pair on-top density ensures that the proper number of correlated electron pairs will be taken into account.

4.5 ELI for Ionic Bond

The LiH molecule is a classical example of an ionic system due to the relative large electronegativity difference. The description as Li^+H^- is also reflected in the position space analysis by the effective charge of Bader's atoms ($\pm 0.9e^-$) determined within the quantum theory of atoms in molecules (QTAIM) from the density gradient field [2]. They correspond to so-called QTAIM basins, which are defined as the manifold of all density gradient trajectories terminating at the so-called attractor which is a density maximum. The integral of the electron density over a basin yields the basin population. If the basin encloses an atomic nucleus, then the effective charge of this atom is given by the subtraction of the nuclear charge from

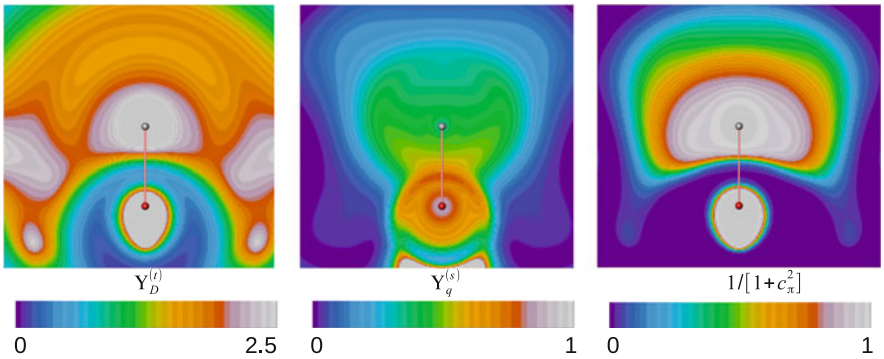

Fig. 12 CISD/CCTC calculation of the LiH molecule. *Left*: ELI-D for triplet-coupled pairs. *Middle*: ELI-q for singlet-coupled pairs. *Right*: singlet–triplet spin-pair composition

the electron population. The method of basin determination and evaluation can be applied also to another fields, for instance, to ELI (however, then without the physical reasoning given for the QTAIM basins).

For the LiH molecule a CISD calculation was performed with the GAMESS program [83] using the CCTC basis set and exiting 4 electrons in 47 orbitals. The 2-matrix was created and ELI computed with the DGrid program [80]. The left diagram in Fig. 12 shows ELI-D for the triplet-coupled electron pairs $Y_D^{(t)}$. The core shell of the Li atom is clearly manifested by high ELI-D values. The corresponding basin contains 2.0 electrons. High localization is found also around the hydrogen nucleus. The additional ELI-D localization domains are located in low electron density region – an effect due to the "splitting" of the basis set. Because the hydrogen does not have a core region, the polarity of the bond can hardly be judged from the population of the "valence basin." Instead of separate bond basin, as usual for all other elements, the electron population is fully ascribed to the H atom. Thus, from the viewpoint of the $Y_D^{(t)}$ basin population, there is almost no difference between the Li–H and C–H bond. Further analysis involving the localization (LI) and delocalization (DI) indices [35] can help to discriminate between the bonds to hydrogen. The delocalization index $\delta(A,B)$ between the basins A and B is defined as the integral of the exchange–correlation part of the pair density over the two basins:

$$\frac{1}{2}\delta(A,B) = \int_A \rho(\mathbf{r}_1)\ \mathrm{d}\mathbf{r}_1 \int_B \rho(\mathbf{r}_2)\ \mathrm{d}\mathbf{r}_2 - \int_A \mathrm{d}\mathbf{r}_1 \int_B \rho_2(\mathbf{r}_1,\mathbf{r}_2)\ \mathrm{d}\mathbf{r}_2. \qquad (60)$$

The localization index $\lambda(A)$ results for $A = B$. For the dimer the sum $\lambda(A) + \delta(A,B)/2 = \overline{N}(A)$. The DI amounts to the number of electron pairs shared between the basins. For the QTAIM basins, the DI can be related to the bond order [84]. In case of an ionic bond, the DI is relatively small [85], e.g., $\delta(\mathrm{Li,\ H}) = 0.19$

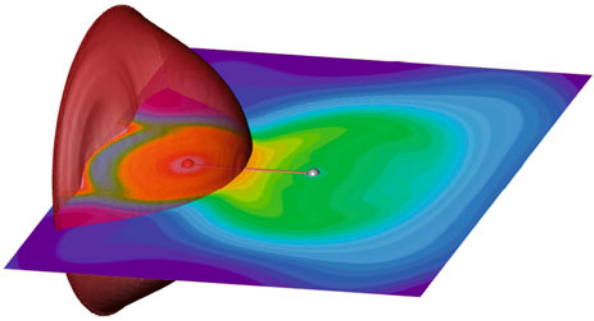

Fig. 13 CISD/CCTC calculation of the LiH molecule. The slice shows $\Upsilon_q^{(s)}$. The red-colored QTAIM basin for the Li atom encloses the $\Upsilon_q^{(s)}$ maximum between Li and H

for the QTAIM basins, and it drops to 0.12 for the ELI-D basins (sharing between the Li core basin and the rest of the dimer). This also means that almost all the electrons in the Li core basins are localized within this basin and correspondingly for the electrons in the H basin. For comparison, the hydrogen basin of a C–H bond has also around 2 electrons in the ELI-D basin, but the LI is much smaller because of larger extent of electron sharing with other basins.

Because $\Upsilon_D^{(t)}$ shows how "alone" an electron is, it could be inferred that the high ELI-D values around the hydrogen position describe a located opposite-spin electron pair (both α-spin and β-spin electrons are alone and there are 2 electrons in the H basin, which for independent particle would correspond to a pair). The inspection of the mid ELI-q diagram of Fig. 12 for the singlet coupling $\Upsilon_q^{(s)}$ reveals that, somewhat unexpected, the formation of a singlet pair is enhanced in the region between the Li core and the H nucleus (and not only around the hydrogen) reminiscent of a covalent/polar bond. Possibly this behavior is again due to the absence of a core for the hydrogen atom. The ELI-q basin for this $\Upsilon_q^{(s)}$ maximum between Li and H encloses the hydrogen nucleus and contains 2.1 electrons. Interestingly, the $\Upsilon_q^{(s)}$ maximum is located within the QTAIM basin of Li atom (cf. Fig. 13).

Considering the singlet–triplet spin-pair composition c_π as based on the q-restricted ωRSP, it is clear that for single-determinantal wave functions it shows the $\Upsilon_D^{(t)}$ topology (because the number of singlet-coupled pairs is a constant for fixed charge condition). c_π indicates the excess of singlet-coupled pairs over the triplet-coupled pairs. A comparison of the right diagram of Fig. 13 with the mid one shows that the domain of high $\Upsilon_q^{(s)}$ values between Li and H is not reproduced in the c_π diagram. Apparently, although the singlet pairs are preferably formed in that region, they are overruled by the triplet pairs. The singlet-coupled pairs are clearly dominating the regions around the Li and H nuclei. It seems that c_π recovers most of the $\Upsilon_D^{(t)}$ features of the triplet coupling, not monitoring the strong influence of the correlation like in case of the $\Upsilon_q^{(s)}$ for the singlet coupling.

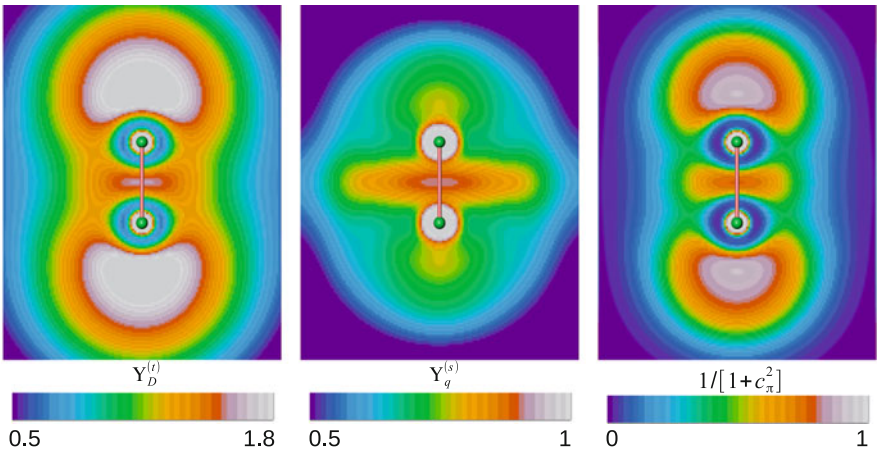

Fig. 14 CISD/CCT calculation of the N_2 molecule. *Left*: ELI-D for triplet-coupled pairs. *Middle*: ELI-q for singlet-coupled pairs. *Right*: singlet–triplet spin-pair composition

4.6 ELI for Covalent Bond

The analysis of a covalent bond was performed exemplary for the N_2 molecule. In the CISD calculation with the CCT basis set, 10 valence electrons and 58 orbitals were used. Two symmetry-equivalent QTAIM basins, each enclosing a nitrogen nucleus, are present. The DI between the QTAIM basins, which in case of a HF calculation yields the bond order 3.03, is reduced by the correlation to the value $\delta(\mathrm{N,N}) = 2.22$ [35, 86] (the DI for the same-spin pair contribution only amounts to 2.85). The strong decrease of the bond order is somewhat in contrast to chemical intuition and is due to the decrease of the contributions of the ionic structures [86]. The ELI-D for the N_2 molecule, shown in the left diagram of Fig. 14, displays the core regions as well as an $\Upsilon_D^{(t)}$ maximum at the bond midpoint and two large lone-pair regions. Qualitatively the diagram does not differ much from a diagram for a HF calculation [5, 87], and in both cases, each nitrogen core basin $\mathcal{C}_\mathrm{N}$ is populated by 2.1 electrons. The bond basin $\mathcal{B}_{\mathrm{NN}'}$ contains only $3.6\mathrm{e}^-$ ($3.9\mathrm{e}^-$ for HF), which is too low when assuming a Lewis-pair-like contribution of 2 electrons per bond order for the ELI-D basin population. Of course, the population of the lone-pair basins $\mathcal{L}_\mathrm{N}$ is with $3.1\mathrm{e}^-$ ($2.9\mathrm{e}^-$ for HF) correspondingly too high.

Closer inspection of the DIs between the ELI-D basins enables deeper view into the bonding situation. As usual, the core basins do not share much electrons with the surrounding. Especially the sharing between the two core basins as well as the core basin and the lone pair of the other nitrogen is negligible (cf. Table 1). Although the distance between the two lone-pair regions is large, the electron sharing $\delta(\mathcal{L}_\mathrm{N}, \mathcal{L}_{\mathrm{N}'}) = 0.374$ (with 0.494 for HF) is significant and larger than the sharing with the closest core basin $\delta(\mathcal{C}_\mathrm{N}, \mathcal{L}_\mathrm{N}) = 0.294$. There is also considerable electron sharing between the lone-pair basin and the bond basin $\delta(\mathcal{L}_\mathrm{N}, \mathcal{B}_{\mathrm{NN}'}) = 1.159$.

Table 1 Delocalization indices $\delta(b_1,b_2)$ between the ELI-D basins b_1 and b_2 for the N_2 molecule from the CISD and HF calculation

b_1	b_2	$\delta(b_1,b_2)_{CI}$	$\delta(b_1,b_2)_{HF}$	$\delta(b_1,N')_{CI}$	$\delta(b_1,N')_{HF}$
$\mathcal{C}_N$	$\mathcal{C}_{N'}$	0.003	0.008	0.082	0.148
	$\mathcal{L}_{N'}$	0.022	0.052		
	$\mathcal{L}_N$	0.294	0.253		
	$\mathcal{B}_{NN'}$	0.239	0.246		
$\mathcal{L}_N$	$\mathcal{L}_{N'}$	0.374	0.494	0.775	1.107
	$\mathcal{B}_{NN'}$	1.159	1.271		
$\mathcal{B}^N_{NN'}$	$\mathcal{B}^{N'}_{NN'}$	0.930	1.128	1.365	1.778
	$\mathcal{C}_{N'}$	0.057	0.089		
	$\mathcal{L}_{N'}$	0.379	0.561		

The $\delta(b_1,N')$ is the DI with the neighboring nitrogen basin

The electron sharing between the QTAIM basins (connected with the bond order) can be decomposed into separate contributions of ELI-D basin parts contained within the corresponding QTAIM basins. The ELI-D basin parts are obtained by the intersection between the QTAIM and ELI-D basins – technique originally used for the evaluation of bond polarity [88]. In case of the N_2 molecule, the $\mathcal{L}_N$ and $\mathcal{C}_N$ ELI-D basins are completely inside the nitrogen QTAIM basin. The bond basin $\mathcal{B}_{NN'}$ is cut into half by the QTAIM basins yielding the basin parts $\mathcal{B}^N_{NN'}$ and $\mathcal{B}^{N'}_{NN'}$, each in separate nitrogen basin (labeled by the superscript). Table 1 shows that the main part of the bond order $\delta(N,N') = 2.22$ (3.03 for HF) is given by the sharing between the nitrogen QTAIM basin and the (other nitrogen) lone-pair basin $\delta\left(\mathcal{L}_N, N'\right) = 0.775$ (1.107 for HF) as well as the intersection part of the bond basin $\delta\left(\mathcal{B}^N_{NN'}, N'\right) = 1.365$ (1.778 for HF), respectively. Additionally, only around 40% of the bond order is recovered by the sharing between the two halves of the bond basin $\delta\left(\mathcal{B}^N_{NN'}, \mathcal{B}^{N'}_{NN'}\right) = 0.930$. In view of the ELI-D bond analysis, it demonstrates that the bonding between the atoms cannot be attributed exclusively to the bonding basin.

The core regions of high $\Upsilon^{(s)}_q$ values in the mid ELI-q diagram of Fig. 14 are clearly evident, because the core electrons were not included in the active space of the CISD, i.e., they exhibit HF-like pairing. The bond between the nitrogen atoms is identifiable by the $\Upsilon^{(s)}_q$ localization domain between the cores. In this region the pairing of the opposite-spin electrons is favored. However, ELI-q does not reveal separate maxima that would mark the lone pairs behind the cores. Certainly, a shoulder in $\Upsilon^{(s)}_q$ is perceivable, but this is not enough to define a lone-pair basin. The absence of lone-pair maxima for some molecules is the major drawback for the bonding analysis with ELI-q for singlet-coupled electron pairs performed up to now [87, 89]. It is still not clarified, whether ELI-q is not able to "correctly" discern all

bonding features or if the level of correlation is not high enough to reach the final view.

The right diagram of Fig. 14 displays the singlet–triplet spin-pair composition for the correlated N_2 calculation. Although the correlated opposite-spin pairs are involved in the derivation of c_π, the diagram exhibits the same topology as the ELI-D distribution $\Upsilon_D^{(t)}$. The only difference is that the bond basin is now populated by $4.0e^-$ and the lone pairs contain 2.9 electrons each.

4.6.1 The C_3H_6 Molecule

It could be suspected that for hydrocarbons, the influence of correlation is not as much important as for other compounds. Then, possibly, the ELI-q for the singlet-coupled electrons would be of minor importance for the bonding analysis. To examine the extent of opposite-spin electron pairing in case of the C–C and C–H bonds, the C_3H_6 was analyzed. The CISD calculation of the cyclopropane molecule was performed with the triple-zeta basis CCT using 18 electrons excited into 75 orbitals. The correlated 2-matrix was used to compute the electron density as well as the ELI (and the spin-pair composition).

The QTAIM basin populations $\overline{N}(\mathrm{H}) = 1.0e^-$ and $\overline{N}(\mathrm{C}) = 6.0e^-$ confirm the covalent character of the bonding (the HF results differ by less than $0.05e^-$). The correlated delocalization indices $\delta(\mathrm{C,C}) = 0.806$ and $\delta(\mathrm{C,H}) = 0.812$ show the somewhat reduced bond order with respect to the bond order deduced from the HF results 0.978 and 0.948, respectively. The bond order reduction is mainly due to the influence of opposite-spin correlation (the correlated same-spin DIs are just slightly reduced).

The left diagram of Fig. 15 displays the topology of ELI-q for singlet-coupled electron pairs for the C_3H_6 molecule. The spherical 0.8-localization domains of $\Upsilon_q^{(s)}$ around the carbon nuclei are due to the exclusion of the carbon core electrons from the CISD active space (i.e., showing HF-like pairing of the opposite-spin electrons). The C–H bonds are indicated by the disklike localization domains of enhanced opposite-spin pairing located between the carbon and hydrogen atoms. Proper representation of the C–C bonds is more difficult to achieve. The domains between the carbon atoms cannot be reduced to a $\Upsilon_q^{(s)}$ maximum close to the bond line. Instead, there are maxima above and below the carbon plane and an additional maximum in the middle of the carbon triangle. The ELI-q topology for cyclopropane heavily depends on the extent of the correlation recovered by the CI calculation. A simple CASSCF calculation using smaller active space exhibits $\Upsilon_q^{(s)}$ distribution that can hardly be connected with meaningful bonding analysis. This apparently unsatisfactory behavior of ELI-q could be possibly turned into advantage, when searching for the origin and influence of the opposite-spin correlation.

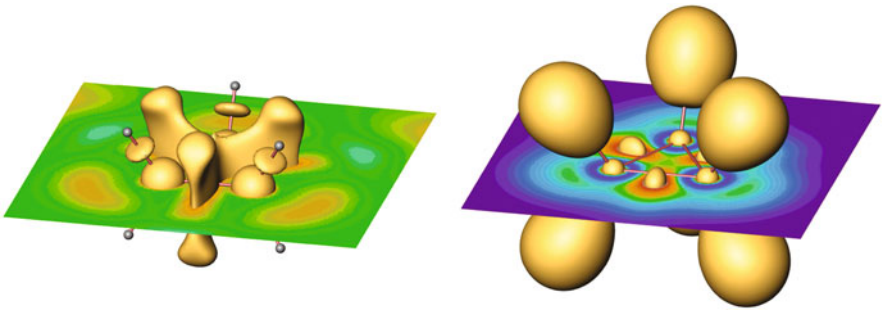

Fig. 15 CISD/CCT calculation of the C_3H_6 molecule. *Left*: ELI-q for singlet-coupled pairs with the 0.8-localization domains of $\Upsilon_q^{(s)}$. *Right*: singlet–triplet spin-pair composition with the 0.8-localization domains of c_π

Assuming that $\Upsilon_q^{(s)}$ should recover proper "chemical" description, because chemical bonding is intrinsically connected to spin pairing, could help to tune the correlated wave function or find better approach.

Considering instead of ELI-q, the correlated spin-pair composition reveals that for this descriptor the extent of opposite-spin correlation is of minor importance. The spin-pair composition can be seen, similarly to ELI-q, as being based on the q-restricted space partitioning. However, the ratio between the opposite-spin and same-spin electron pairs behaves like the independent opposite-spin pairs would be taken into account (which in this view would in certain sense be proportional to the $\Upsilon_D^{(t)}$ values of ELI-D; see below).

The bonding situation described by the correlation of electronic motion of triplet-coupled electrons is shown by means of the $\Upsilon_D^{(t)}$ indicator in the left diagram of Fig. 16. The localization domains between the carbon atoms represent the C–C bonds. The corresponding bond basins are populated by 1.8 electrons. The core regions are given by the small spherical domains around the carbon nuclei. The C–H bonds are indicated by single ELI-D domains around the hydrogen positions – description closely resembling the situation for LiH. The ELI-D basin for the C–H bond encloses 2.0 electrons, which is the same value as for the population outside the Li core in the LiH molecule. The combined analysis with intersections between the ELI-D and QTAIM basins clarify this obstacle. The right diagram of Fig. 16 shows the QTAIM basin of the carbon atom intersected by the ELI-D basins. The two hydrogen ELI-D basins intersect the atomic basin of carbon and yield two intersections of the same size each containing $1.08e^-$. Thus, the hydrogen ELI-D basin is almost equally distributed between the atomic QTAIM basins of the hydrogen and carbon atoms, i.e., the C–H bond is covalent and nonpolar [88].

Inside the carbon QTAIM basin is the ELI-D core basin $\mathcal{C}_C$ enclosing 2.1 electrons (cf. the small black-colored sphere for the neighboring carbon core in Fig. 16). The electron sharing between the core basin and the closest QTAIM atom is very low (cf. Table 2). The bond basin $\mathcal{B}_{CC'}$ is cut by the carbon atoms into two

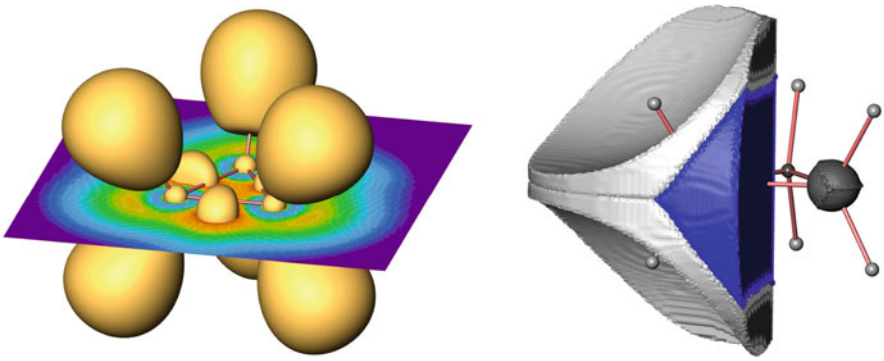

Fig. 16 CISD/CCT calculation of the C_3H_6 molecule. *Left*: ELI-D for triplet-coupled pairs with the 1.5-localization domains of $Y_D^{(t)}$. *Right*: ELI-D core basin (*black*) together with the carbon QTAIM basin (cropped by 0.001 a.u. electron density isosurface) intersected by the ELI-D basins (intersections with the bond and hydrogen basins in *blue* and *gray*, respectively)

Table 2 Delocalization indices $\delta(b_1,b_2)$ between the ELI-D basins b_1 and b_2 for the C_3H_6 molecule from the CISD and HF calculation

b_1	b_2	$\delta(b_1,b_2)_{CI}$	$\delta(b_1,b_2)_{HF}$	$\delta(b_1,C')_{CI}$	$\delta(b_1,C')_{HF}$	$\delta(b_1,H)_{CI}$	$\delta(b_1,H)_{HF}$
$\mathcal{C}_C$	$\mathcal{B}_{CC'}$	0.104	0.096	0.029	0.045	0.030	0.048
$\mathcal{B}^C_{CC'}$	$\mathcal{B}^{C'}_{CC'}$	0.360	0.377	0.531	0.599	0.048	0.074
$\mathcal{B}^H_{CH}$	$\mathcal{B}^C_{CH}$	0.624	0.663				

The $\delta(b_1,C')$ and $\delta(b_1,H)$ are the DIs with the closest carbon and hydrogen basins

parts ($\mathcal{B}^C_{CC'}$, marked by blue color in Fig. 16, and $\mathcal{B}^{C'}_{CC'}$). The electron sharing between these bond parts $\delta\left(\mathcal{B}^C_{CC'}, \mathcal{B}^{C'}_{CC'}\right) = 0.360$ amounts to only about 45% of the total bond order. The contribution to the C–C bond order increases to 66% when the sharing of the intersection part with the whole atomic basin of the carbon, $\delta\left(\mathcal{B}^C_{CC'}, C'\right) = 0.531$, is considered. In contrast, the C–C bond part $\mathcal{B}^C_{CC'}$ does not contribute much to the C–H bond order (with $\delta(\mathcal{B}_C, H) = 0.048$).

The ELI-D basin $\mathcal{B}_{CH}$ representing the C–H bond can be split by the intersection with the involved carbon and hydrogen QTAIM basins into the parts $\mathcal{B}^C_{CH}$ (one of the gray-colored basin parts in 16) and $\mathcal{B}^H_{CH}$. The electron sharing between the parts $\delta(\mathcal{B}^C_{CH}, \mathcal{B}^H_{CH}) = 0.624$ recovers already 77% of the C–H bond order, which means that the bonding basin $\mathcal{B}_{CH}$ is a reasonable description of the C–H bond. Of course, the DI between the carbon QTAIM basin and $\mathcal{B}^H_{CH}$ returns the C–H bond order because $\mathcal{B}^H_{CH}$ is actually the full hydrogen QTAIM basin.

5 Conclusions

Although not an observable, it is obvious that the concept of bonding between atoms is of paramount importance in chemistry. The structure of molecules and solids is visualized and perceived in the usual three-dimensional coordinate space. It seems to be natural that also the analysis of the bonding situation should be performed in the coordinate space. A starting frame for such analysis is surely the QTAIM approach of Bader based on the evaluation of the electron density and its derivatives. However important and useful this method is, it does not describe electron pairs, which are the paradigm and focus of Lewis idea of chemical bond. This information is accessible through the pair density.

In the preceding sections, the electron localizability indicator (ELI) was presented and applied to few systems. ELI includes in its definition integrals of both the electron density and the pair density. With this at hand, it is connected with the correlation of electronic motion, which is in certain sense a local description of electron pairing. It can be expected that specific ELI patterns will able to visualize (and possibly quantify) the bonding situation. This ability strongly depends on the ELI variant used to examine the system.

The ELI variant $\Upsilon_D^{(t)}$ (ELI-D) based on the correlation between same-spin electrons (described by the Fermi hole) is a robust bonding descriptor directly connected with the Pauli principle. Thus, it can be used already at the independent particle level of theory. ELI-D displays high values in spatial regions that can be connected with the conception of atomic shells, lone pairs, and bonds. In analogy to the QTAIM approach, basins can be determined with the aid of the $\nabla \Upsilon_D^{(t)}$ field. This gives access to the spatial extent and evaluation of electronic population of atomic shells, lone pairs, and bonds. It should be stressed out that the qualitative as well as almost quantitative spatial description of atomic shells, closely following the patterns deduced from the periodic table, is the most important prerequisite for the application of ELI-D to the analysis of bonding situation. Somewhat unpleasant drawback of ELI-D is that it does not directly refer to opposite-spin electron pairs. The local pairing of opposite-spin electrons, attribute that a chemist is immediately associating with the notion of chemical bond, is not included in the $\Upsilon_D^{(t)}$ definition.

This is clearly the playground of the ELI-q variant $\Upsilon_q^{(s)}$ describing the correlation of motion of singlet-coupled electrons. ELI-q shows the regions of space where the opposite-spin pairing is not suppressed by the correlation. Such regions of high $\Upsilon_q^{(s)}$ values could be connected with the position of a Lewis pair. As was expounded in this chapter, in case of independent particles, the ELI-q yields a distribution of constant values. Only for explicitly correlated density matrices, some structure of the $\Upsilon_q^{(s)}$ distribution will emerge that is worthwhile to be analyzed. Additionally, the level of correlation captured by the wave function calculation must be high enough to reveal reasonable topological characteristics that can be associated with bonding descriptors. Detailed study of the atomic shell structure represented by ELI-q variant $\Upsilon_q^{(s)}$ is still not available. Moreover, the approximate expression for $\Upsilon_q^{(s)}$ is based on the

opposite-spin on-top density. If for perfectly correlated wave function the on-top density would be zero everywhere in space, the corresponding approximate ELI-q formula would exhibit the same scaling behavior as ELI-D. Further investigation of $\Upsilon_q^{(s)}$ is necessary to unfold the potentiality of this descriptor.

References

1. Ponec R (1997) J Math Chem 21:323
2. Bader RFW (1990) Atoms in molecules. Oxford University Press, Oxford
3. Kohout M (2004) Int J Quantum Chem 97:651
4. Kohout M (2007) Faraday Discuss 135:43
5. Kohout M, Pernal K, Wagner FR, Grin Y (2004) Theor Chem Acc 112:453
6. Kohout M, Pernal K, Wagner FR, Grin Y (2005) Theor Chem Acc 113:287
7. Kohout M, Wagner FR, Grin Y (2006) Int J Quantum Chem 106:1499
8. Kohout M, Wagner FR, Grin Y (2008) Theor Chem Acc 119:413
9. Bader RFW, Stephens ME (1974) Chem Phys Lett 25:445
10. Lewis GN (1916) J Am Chem Soc 33:762
11. Bader RFW, Essén H (1984) J Chem Phys 80:1943
12. Bader RFW, MacDougall PJ, Lau CDH (1984) J Am Chem Soc 106:1594
13. Boyd RJ (1978) Can J Phys 56:780
14. Hunter G (1986) Int J Quantum Chem 29:197
15. Kohout M (2001) Int J Quantum Chem 83:324
16. Kohout M, Savin A (1996) Int J Quantum Chem 60:875
17. Sagar RP, Ku ACT, Smith VHJ, Simas AM (1988) J Chem Phys 88:4367
18. Schmider HL, Sagar RP, Smith VHJ (1992) Can J Chem Phys 70:506
19. Sen KD, Gayatri TV, Toufar H (1996) J Mol Struct (Theochem) 361:1
20. Sen KD, Slamet M, Sahni V (1993) Chem Phys Lett 205:313
21. Shi Z, Boyd RJ (1988) J Chem Phys 88:4375
22. Simas AM, Sagar RP, Ku ACT, Smith VHJ (1988) Can J Phys 66:1923
23. Sperber G (1971) Int J Quantum Chem 5:189
24. Waber JT, Cromer DT (1965) J Chem Phys 42:4116
25. Wagner K, Kohout M (2011) Theor Chem Acc 128:39
26. Heitler W, London F (1927) Z Phys 44:455
27. London F (1928) Z Phys 46:455
28. Pauling L (1939) The nature of the chemical bond. Cornell University Press, Ithaca
29. Daudel R (1953) C R Hebd Seances Acad Sci 237:601
30. Daudel R, Brion H, Odiot S (1955) J Chem Phys 23:2080
31. Aslangul C, Constanciel R, Daudel R, Kottis P (1972) Adv Quantum Chem 6:93
32. Daudel R (1968) The fundamentals of theoretical chemistry. Pergamon, Oxford
33. Daudel R, Bader RFW, Stephens ME, Borrett DS (1974) Can J Chem 52:1310
34. Bader RFW, Stephens ME (1975) J Am Chem Soc 97:7391
35. Fradera X, Austen MA, Bader RFW (1999) J Phys Chem A 103:304–314
36. Luken WL, Culberson JC (1982) Int J Quantum Chem Symp 16:265
37. Luken WL, Culberson JC (1984) Theor Chim Acta 66:279
38. Becke AD, Edgecombe KE (1990) J Chem Phys 92:5397
39. Deb BM, Ghosh SK (1983) Int J Quantum Chem 23:1
40. Savin A, Jepsen O, Flad J, Andersen OK, Preuss H, von Schnering HG (1992) Angew Chem Int Ed Engl 31:187
41. Dobson JF (1991) J Chem Phys 94:4328
42. Melin J, Fuentealba P (2003) Int J Quantum Chem 92:381

43. Savin A (2005) J Mol Struct (Theochem) 727:127
44. Savin A (2005) J Chem Sci 117:473
45. Cioslowski J (1990) Int J Quantum Chem S24:15
46. Cioslowski J (1991) J Am Chem Soc 113:4142
47. Savin A, Nesper R, Wengert S, Fässler TF (1997) Angew Chem Int Ed Engl 36:1808
48. Silvi B, Savin A (1994) Nature 371:683
49. Kohout M, Savin A (1997) J Comput Chem 18:1431
50. Gadre SR, Kulkarni SA, Pathak RK (1993) J Chem Phys 98:3574
51. Fuentealba P (1998) Int J Quantum Chem 69:559
52. Tsirelson V, Stash A (2002) Chem Phys Lett 351:142
53. Kirzhnits DA (1957) Sov Phys JETP 5:64
54. Ayers PW (2005) J Chem Sci 117:441
55. Kulkarni SA (1994) Phys Rev A 50:2202
56. Burnus T, Marques AL, Gross EKU (2005) Phys Rev A 71:010501(R)
57. Räsänen E, Castro A, Gross EKU (2008) Phys Rev B 77:115108
58. Madsen GKH, Gatti C, Iversen BB, Damjanovic L, Stucky GD, Srdanov VI (1999) Phys Rev B 59:12359
59. Santos JC, Tiznado W, Contreras R, Fuentealba P (2004) J Chem Phys 120:1670
60. Schmider HL, Becke AD (2000) J Mol Struct (Theochem) 527:51
61. Savin A (2002) In: Sen KD (ed) Reviews of modern quantum chemistry: a celebration of the contributions of Robert G. Parr. World Scientific, Singapore, p 43
62. Cancès E, Keriven R, Lodier F, Savin A (2004) Theor Chem Acc 111:373
63. Gallegos A, Carbó-Dorca R, Lodier F, Cancès E, Savin A (2005) J Comput Chem 26:455
64. Menendéz M, Martín Pendás A, Braïda B, Savin A (2015) Comput Theor Chem 1053:142
65. Scemama A, Caffarel M, Savin A (2007) J Comput Chem 28:442
66. Savin A (2004) J Phys Chem Solids 65:2025
67. Silvi B (2003) J Phys Chem A 107:3081
68. Martín Pendás A, Kohout M, Blanco MA, Francisco E (2012) In: Gatti C, Macchi P (eds) Modern charge-density analysis. Springer, Dordrecht
69. Scemama A, Chaquin P, Caffarel M (2004) J Chem Phys 121:1725
70. Amador-Bedolla C, Salomón-Ferrer R, Lester WA Jr, Vázquez-Martínez JA, Aspuru-Guzik A (2007) J Chem Phys 126:204308
71. Kohout M, Wagner FR, Grin Y (2002) Theor Chem Acc 108:150
72. Clementi E, Roetti C (1974) At Data Nucl Data Tables 14:218
73. Bader RFW, Johnson S, Tang TH, Popelier PLA (1996) J Phys Chem 100:15398
74. Burdett JK, McCormick TA (1998) J Phys Chem A 102:6366
75. Sun Q, Wang Q, Yu JZ, Kumar V, Kawazoe Y (2001) Phys Rev B 63:193408
76. Savin A, Silvi B, Colonna F (1996) Can J Chem 74:1088
77. Matito E, Silvi B, Duran M, Solà M (2006) J Chem Phys 125:024301
78. Blanco MA, Martín Pendás A, Francisco E (2005) J Chem Theory Comput 1:1096
79. Francisco E, Martín Pendás A, Blanco MA (2006) J Chem Theory Comput 2:90
80. Kohout M (2015) DGrid 5.0. Radebeul
81. Finzel K, Grin Y, Kohout M (2012) Theor Chem Acc 131:1106
82. Bezugly V, Wielgus P, Wagner FR, Kohout M, Grin Y (2008) J Comput Chem 29:1198
83. Schmidt MW, Baldridge KK, Boatz JA, Elbert ST, Gordon MS, Jensen JH, Koseki S, Matsunaga N, Koseki S, Matsunaga N, Nguyen KA, Su SJ, Windus TL, Dupuis M, Montgomery JA (1993) J Comput Chem 14:1347
84. Ángyán JG, Loos M, Mayer I (1994) J Phys Chem 98:5244
85. Baranov AI, Kohout M (2011) J Comput Chem 32:2064
86. Francisco E, Martín Pendás A, Blanco MA (2007) J Chem Phys 126:094102
87. Bezugly V, Wielgus P, Kohout M, Wagner FR (2010) J Comput Chem 31:2273
88. Raub S, Jansen G (2001) Theor Chem Acc 106:223
89. Bezugly V, Wielgus P, Kohout M, Wagner FR (2010) J Comput Chem 31:1504

Struct Bond (2016) 170: 169–212
DOI: 10.1007/430_2015_179

Published online: 9 October 2015

New Landscape of Electron-Pair Bonding: Covalent, Ionic, and Charge-Shift Bonds

Sason Shaik, David Danovich, Benoit Braida, Wei Wu, and Philippe C. Hiberty

Abstract We discuss here the modern valence bond (VB) description of the electron-pair bond vis-à-vis the Lewis–Pauling model and show that along the two classical families of covalent and ionic bonds, *there exists a family of charge-shift bonds (CSBs) in which the "resonance fluctuation" of the electron-pair density plays a dominant role*. A bridge is created between the VB description of bonding and three other approaches to the problem: the electron localization function (ELF), atoms-in-molecules (AIM), and molecular orbital (MO)-based theories. In VB theory, CSB manifests by repulsive or weakly bonded covalent state and large covalent–ionic resonance energy, RE_{CS}. In ELF, it shows up by a depleted basin population with fluctuations and in AIM by a positive Laplacian. CSB is derivable also from MO-based theory. As such, CSB is shown to be *a fundamental mechanism that satisfies the equilibrium condition of bonding, namely, the virial ratio of the kinetic and potential energy contributions to the bond energy*. The chapter defines the atomic propensity for CSB and outlines its territory: Atoms

S. Shaik (✉) and D. Danovich
Institute of Chemistry and the Lise-Meitner Minerva Center for Computational Quantum Chemistry, The Hebrew University, Jerusalem 9190401, Israel
e-mail: sason@yfaat.ch.huji.ac.il; david.danovich@mail.huji.ac.il

B. Braida
Sorbonne Universités, UPMC Univ. Paris 06, UMR 7616, LCT, 75005 Paris, France
CNRS, UMR 7616, LCT, 75005 Paris, France

W. Wu
The State Key Laboratory of Physical Chemistry of Solid Surfaces, Fujian Provincial Key Laboratory of Theoretical and Computational Chemistry, and College of Chemistry and Chemical Engineering, Xiamen University, Xiamen, Fujian 361005, China

P.C. Hiberty (✉)
Laboratoire de Chimie Physique, UMR CNRS 8000, Groupe de Chimie Théorique, Université de Paris-Sud, 91405 Orsay Cédex, France
e-mail: philippe.hiberty@u-psud.fr

(fragments) that are prone to CSB are compact electronegative and/or lone-pair-rich species. As such, the territory of CSB transcends considerations of static charge distribution, and it involves (a) homopolar bonds of heteroatoms with zero static ionicity, (b) heteropolar σ- and π-bonds of the electronegative and/or electron-pair-rich elements among themselves and to other atoms (e.g., the higher metalloids, Si, Ge, Sn, etc.), and (c) electron-rich hypercoordinate molecules. Several experimental manifestations of charge-shift bonding are discussed.

Keywords AIM · Bonding · Charge-shift bonding · Covalent bonding · Electron pairing · Electronegativity · ELF · Ionic bonding · Lewis structures · Resonance energy · Valence bond

Contents

1 Introduction

The conceptual element from which an entire chemical universe can be constructed is the chemical bond [1]. As such, the bond is the "quantum building block" of the grand scheme of "LEGO" by which practicing chemists devise and control the formation of new molecules of ever-increasing complexity and beauty. In this respect, the chemical community owes a great debt to Lewis who was the first to define the chemical bond in terms of electronic structure [1], well before the quantum mechanical revolution transpired in physics and provided a rigorous basis for the Lewis concept in terms of what we call today valence bond (VB) theory [2]. This Lewis Centennial Volume is hence a tribute to one of the greatest chemists whose ideas are still the foundations of our way of thinking 100 years after their conception. This contribution recounts the new VB outlook of bonding with a focus on the two-electron bond as the most ubiquitous bonding form in nature.

As we shall show, the articulation of the bond paradigm requires that alongside the traditional covalent (polar-covalent) and ionic bonds, there should exist a third and a distinct class of bonding, the so-called charge-shift bonding (CSB) [3–15], which has unique experimental signatures. We shall describe these three classes and form bridges to other theories by demonstrating that CSB can be articulated also from theories based on electron density consideration, specifically the electron localization function (ELF) [16] and atoms-in-molecules (AIM) [17] theories, as well as from MO theory [14]. Other bond types, odd-electron and hypervalent bonds, which also belong to the CSB family, will be mentioned in passing.

The paper introduces initially Pauling's application of VB theory to derive the classical bond families outlined in the original Lewis paper [1]. The second part questions the underlying assumptions of Pauling's scheme and shows that waiving the key assumption naturally leads to the emergence of the CSB family along with the two traditional ones. Then modern VB theory [18] is used to support the existence of three bond families, covalent, ionic, and CSB. Details on modern VB theory can be found in review sources [18, 19]. In the third part of the paper, we show how the new family of CSB emerges also from ELF and AIM theories, as well as from MO theory. Subsequently, we discuss the physical origins of CSB and describe experimental manifestations of this new bond family. Finally, we try to trace the potential territory of CSB and where novel experimental articulations of the CSB theory may be productive.

2 The Development of the Notion of Electron-Pair Bonding

The concept of the electron-pair bond was formulated in a stroke of genius by Gilbert Newton Lewis in his famous 1916 JACS article, "The Atom and the Molecule" [20], in which he introduced the concept of the electron-pair bond as an intrinsic property that stretches between the covalent and ionic situations. This

work has eventually had its greatest impact in chemistry through the work of Irving Langmuir [21], who ably articulated the Lewis concept, coining new and catchy terms [22]. However, the mechanism whereby the electron pair could constitute a bond remained mysterious until 1927, when Walter Heitler and Fritz London published their seminal paper [23], which calculates the bonding energy in H_2. Using a modern terminology, the bond energy in H_2 was shown to arise from the resonance interaction between the two spin arrangement patterns, $H^{\uparrow}H^{\downarrow}$ and $H^{\downarrow}H^{\uparrow}$, required to generate a singlet electron pair [Φ_{cov} in Eq. (1)]. In the winter of 1928, London [24] drew the basic principles of the nonionic bond, and his theory was in essence a quantum mechanical articulation of Lewis' covalent bond:

$$\Phi_{cov}(H \bullet - \bullet H) = H^{\uparrow\downarrow}H \leftrightarrow H^{\downarrow\uparrow}H. \tag{1}$$

The Heitler–London papers mark the birth of VB theory [2], which was developed by Pauling as a quantum mechanical version of the Lewis model. This quantum mechanical articulation of Lewis' shared-pair model has culminated in a generalizing intellectual construct [25], which described the electron-pair bond A–X as a superposition of covalent (Φ_{cov}) and ionic forms, $\Phi_{A}{+}_{X}{-}$ and $\Phi_{A}{-}_{X}{+}$ [Eq. (2a) and (2b)].

$$\Phi(A - X) = A \bullet\!\!-\!\!\bullet X \leftrightarrow A^{+} : X^{-} \leftrightarrow A{:}^{-}X^{+}, \tag{2a}$$

$$= \Phi_{cov(A\bullet-\bullet X)} \leftrightarrow \Phi_{A^{+}X^{-}} \leftrightarrow \Phi_{A^{-}X^{+}}. \tag{2b}$$

This picture enabled a unified description of bonding in any molecule, in terms of VB theory. Slater and van Vleck showed [26, 27] that an MO treatment followed by complete configuration interaction is equivalent to the VB-based covalent–ionic scheme of Pauling. In retrospect, reading Lewis' paper shows that he anticipated the ideas that underlie the physical organic chemistry school [22, 28, 29] of Ingold and the resonance concept [28, 30] expounded by Pauling. Thus, the birth of VB theory in chemistry was an ingenious quantum chemical dressing of Lewis' seminal idea by Pauling and can be referred to as the Pauling–Lewis VB theory.

3 The Valence Bond Description of the Two-Electron Bond

3.1 The Pauling Covalent–Ionic Superposition Scheme of the Two-Electron Bond

Figure 1 describes the Pauling–Lewis perspective of electron-pair bonding in terms of VB mixing diagrams [9]. Three structures, one covalent, $\Phi_{cov(A\bullet-\bullet X)}$, and two ionic ones, $\Phi_{A^{+}X^{-}}$ and $\Phi_{A^{-}X^{+}}$, are required to describe an electron pair bond A-X, which may either be homo- or heteronuclear.

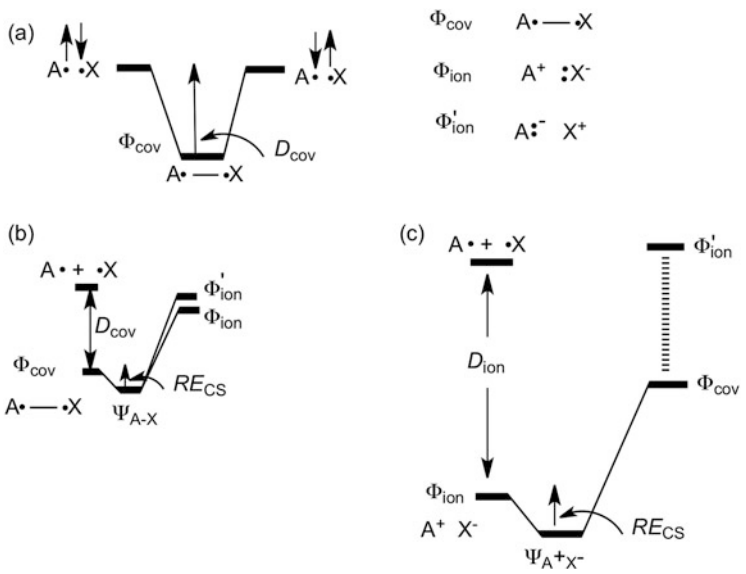

Fig. 1 Piecing up the A–X bond by means of VB mixing diagrams. (**a**) The covalent structure is stabilized by D_{cov} due to resonance between the two spin arrangement patterns required to create a singlet pair. (**b**) The covalent–ionic mixing for a polar-covalent A–X bond. (**c**) The covalent–ionic mixing for an ionic $A^+:X^-$ bond. D_{ion} is the difference of the electrostatic stabilization of the ionic structure less the energy needed to create the ions from the atoms. In both (**b**) and (**c**), RE_{CS} is the covalent–ionic resonance energy, so-called in this manuscript as the charge-shift resonance energy

The covalent structure Φ_{cov} (Fig. 1a) is stabilized by spin pairing due to the resonance of the $A^{\uparrow}X^{\downarrow}$ and $A^{\downarrow}X^{\uparrow}$ spin arrangement forms. This contributes to the covalent bond energy due to spin pairing, denoted as D_{cov}. For a dominantly covalent bond, where Φ_{cov} is the lowest VB structure (Fig. 1b), this stabilization energy D_{cov} is the covalent contribution to the total bonding energy. On the other hand, ionic structures are stabilized by electrostatic interactions, relative to the separated atoms by an amount D_{ion}. When an ionic form, e.g., $\Phi_{A^+X^-}$, is the lowest among the VB structures (Fig. 1c), the bond is ionic and the electrostatic stabilization energy is the dominant contribution to the bond energy. The covalent–ionic mixing results in a resonance energy contribution that augments, in principle, the bonding of either covalent or ionic bonds. The original literature refers to this quantity as the "charge-shift resonance energy," RE_{CS} [3–15], because the pair density inherent in the VB wave function shows that *covalent–ionic mixing is associated with fluctuation of the electron pair from the average electron population*. As we shall see later, the RE_{CS} quantity figures prominently in the charge-shift bonding (CSB) motif.

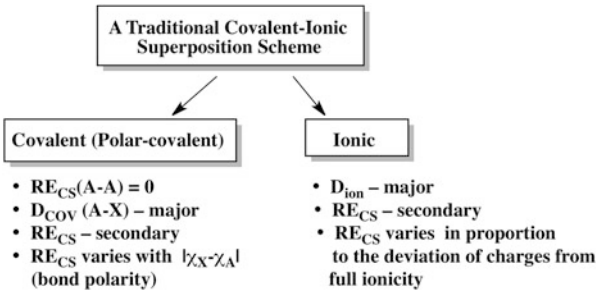

Scheme 1 The traditional covalent and ionic bond families based on Pauling's covalent–ionic superposition scheme. Reproduced from [9] with permission of Wiley-VCH

To use the scheme to calculate bond energies, Pauling assumed that for homonuclear bonds $RE_{CS} = 0$[1]. On the other hand, RE_{CS} was assumed to be nonzero for heteronuclear bonds A–X. In accord, the dissociation energy D_{AX} of an A–X bond was considered as being made of a purely covalent contribution, $D_{cov(A\bullet-\bullet X)}$, augmented by the resonance energy due to covalent–ionic mixing. The covalent contribution was estimated as the geometric average of the bond energies of the two corresponding homonuclear bonds, A–A and X–X, as in Eq. (3):

$$D_{cov(A\bullet-\bullet X)} = (D_{AA} \bullet D_{XX})^{1/2}. \tag{3}$$

Using Eq. (3), the remaining contribution to the actual bond energy, D_{AX}, was considered to be the resonance energy due to covalent–ionic mixing, and this value was used to gauge the electronegativity scale, as shown in Eq. (4):

$$D_{AX} - D_{cov(A\bullet-\bullet X)}\left(\text{kcal mol}^{-1}\right) = 23(\chi_x - \chi_A)^2, \tag{4}$$

where χ is the electronegativity. Furthermore, once the electronegativity is known, the "bond polarity" (δ) can be quantified as in Eq. (5), thereby providing the extent of ionic $A^+ X^-$ character in the bond:

$$\delta = 1 - \exp\left[-0.25(\chi_x - \chi_A)^2\right]. \tag{5}$$

As such, in practice, the Pauling covalent–ionic superposition scheme has traditionally become associated with two bond families, based on a criterion of static charge distribution; these are the covalent (polar-covalent) bond and ionic bond families in Scheme 1. In the first family, the major contribution to bonding comes from spin pairing. Importantly, in homopolar bonds, the RE_{CS} contribution was assumed – in Pauling's original scheme[1] and in subsequent treatments based on

[1] The use of RE_{CS} (A–A) ≈ 0 appears as a working assumption, e.g., on pages 73–100 (see also footnote 13 on page 73), in [25] where it is estimated that the ionic structures in, e.g., Cl_2 will contribute less than 2% to the total bond energy. A stricter assumption is used in Sanderson's treatment ([31] below), which neglects the resonance energy altogether.

it – to be very small and *was set to zero*. In heteropolar bonds, the primary contribution to bonding is normally considered to be the D_{cov} quantity[1], while the charge-shift resonance energy is of secondary importance, except for very polar bonds involving the very electronegative atoms. Furthermore, as shown by Eq. (4), the magnitude of RE_{CS} is considered to vary in proportion to the electronegativity difference of the fragments, A and X, much like the charge distribution, i.e., the "bond polarity" in Eq. (5).

In the second family, the major bonding contribution comes from the electrostatic energy in the dominant ionic structure, whereas RE_{CS} is a minor factor; its magnitude is supposed to vary in proportion to the deviation of the charge distribution from full ionicity.

As such, in the traditional classification of both bonding types, it is assumed that one can deduce the magnitude of the covalent–ionic resonance energy *by simply inspecting the static charge distribution of the molecule*.

Using MO theory, it is possible to transform the delocalized canonical MOs to a set of localized MOs (LMOs) that describe two-center bonds (for pioneering localization methods, see [32–37]). The LMOs retrieve the covalent–ionic superposition scheme as follows: The electron-pair bond is the LMO itself, while the covalent–ionic superposition can be quantified from the charge polarization of the LMO; namely, the relative size of the coefficients of the hybrids of the contributing fragments to the LMO determines the bond polarity. Accordingly, MO theory leads in principle to the same electron-pair bonding picture as the classical covalent–ionic paradigm of Pauling. In fact, both VB and MO descriptions are simply articulations of the original Lewis formulation of electron-pair bonding.

3.2 Limitations of the Pauling Scheme

Thus, our bonding paradigm is now 100 years old [20], and yet even a cursory search in the literature suggests that this is perhaps not the whole story. Just consider the bonds of silicon to electronegative atoms. By criterion of the static charge distribution, these bonds are virtually as ionic as, e.g., LiF or NaCl (e.g., $H_3Si^{+0.85}F^{-0.85}$ vs. $Li^{+0.94}F^{-0.94}$, $Na^{+0.91}Cl^{-0.91}$, etc.)[2] [38]. But, while Li^+F^- and Na^+Cl^- behave as genuine ionic bonds, the Si^+X^- bonds behave chemically as covalent bonds [39–45]. The bonds look so similar, yet they are so very different in their chemical behavior. Indeed, all Si–X bonds are more ionic than the corresponding C–X bonds [40] according to static charge distribution, and nevertheless, these are the C–X bonds that exhibit ionic chemistry in condensed phases, whereas the ionic Si–X chemistry is extremely rare [40–46] with a handful of exceptions [47, 48]. For example, trityl perchlorate, $Ph_3C^+ClO_4^-$, is an ionic

[2] Silvi B, AIM analysis, of SiH_3–F and Li–F using B3LYP/6-31+G* and B3LYP/6-31G* levels cited in [9] above

solid like NaCl [46], while the silicon analog is a covalent solid with a short Si–O bond [42]. It is apparent therefore that the static charge distribution is not a reliable indicator of the nature of bonding. *There must be an additional property of the bond that is missing in the traditional covalent–ionic superposition scheme*.

This property is RE_{CS}. In fact, the Pauling construct, in Fig. 1, Eqs. (3)–(5), and Scheme 1, considers the covalent and ionic structures to be generators of bonding families but overlooks their resonance energies as a potential generator of a third family. The major problem is associated with the assumption that for homonuclear bond $RE_{CS} = 0$. This assumption undermines the role of RE_{CS} and overestimates the magnitude of D_{cov}. As shown later, this assumption is factually incorrect, and its implementation leads to a loss of an entire bond family, the so-called *charge-shift bonds (CSBs)*.

4 A Modern VB Perspective of the Two-Electron Bond

These and many similar puzzles have prompted two of us (SS and PCH) in 1990 to reexamine the classical covalent–ionic paradigm using the tools of ab initio VB theory [3–15]. The interested reader in modern VB theory can consult a recent monograph and a review [18, 19]. Our first intriguing findings [3, 4] concerned the F–F bond, which has been intensely debated and which requires quite a high level of configuration interaction to yield a quantitatively correct bond energy[3] (see also [49–51]). By any known measure, the F–F bond would be defined as a "covalent bond." Firstly, it is a homonuclear bond, where ionicity should not matter. Secondly, the weight of its covalent structure is as large as that for the H–H bond [3, 4, 9]. Is the F–F bond really covalent as the H–H bond? The answer according to Fig. 2 is "no."

Figure 2 displays the dissociation energy curves of a few bonds showing the dominant VB structure of the bond alongside the "exact" ground state, which is a resonating combination of the covalent and ionic components, calculated by means of modern VB theory. Inspection of Fig. 2a, b makes it apparent that the bonding natures of the H–H and F–F bonds are very different. While in H_2 the covalent VB structure displays by itself a potential well, which is already a good approximation of the exact curve (Fig. 2a), the covalent component of F_2 is on the contrary purely *repulsive* (Fig. 2b). Thus, covalent spin pairing does not contribute anything to F–F bonding. *The bonding is in fact sustained by the very large charge-shift resonance energy* due to the mixing of the higher lying ionic structures (not shown in the Figure) into the repulsive covalent structure. Thus, although F–F may be formally a covalent bond according to its zero static charge distribution, this definition cannot

[3] As seen from Table 10.2 of [2], CASSCF/6-31G* or GVB/6-31G* lead to BDE values of ~16.0 kcal mol^{-1}, compared with the experimental value of 38.3 kcal mol^{-1}. Using MRCI/cc-pVTZ, the value is 35.9 kcal mol^{-1}.

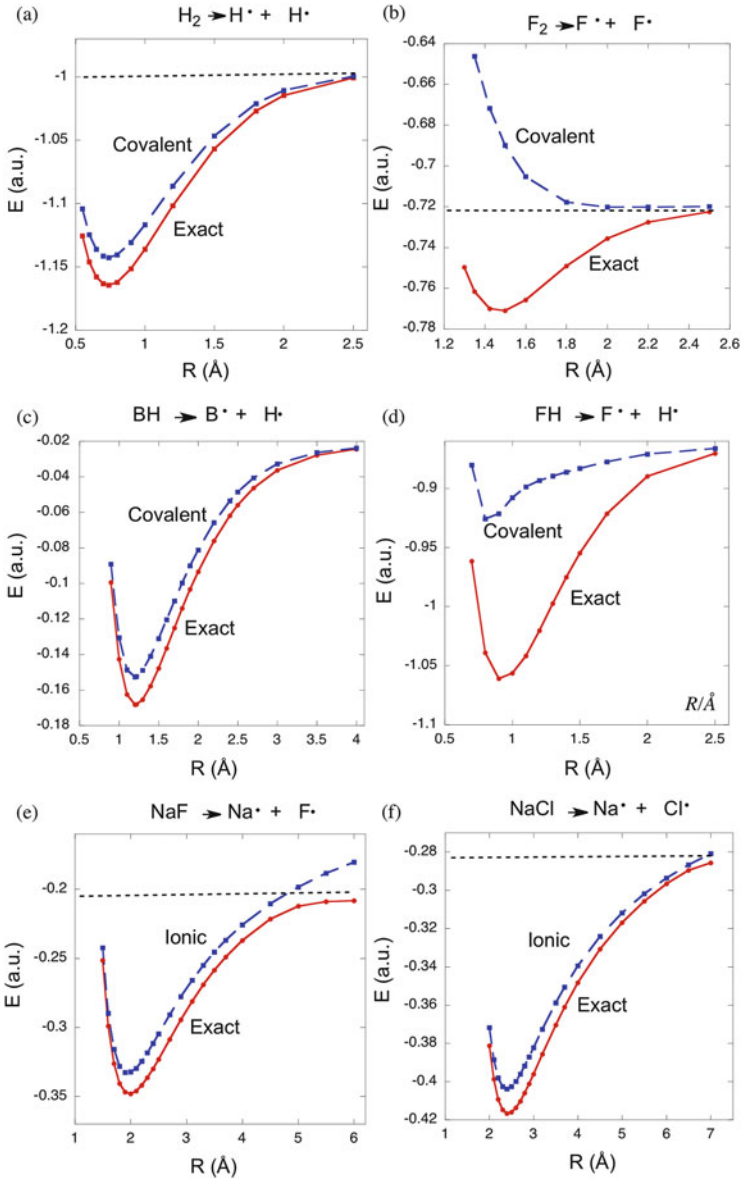

Fig. 2 Dissociation energy curves for (**a**) H_2, (**b**) F_2, (**c**) BH, (**d**) FH, (**e**) NaF, and (**f**) NaCl. The *blue lines with squares* show the purely covalent VB structures. *Red lines with squares* show the optimized covalent + ionic "exact" ground state. Reproduced from [12] with permission of *Nature Chemistry*

tag its true nature; the F–F bond is in fact a charge-shift bond (CSB), because *the bonding exists as a result of the ionic–covalent fluctuation of the electron-pair density*. This F–F case shows that the assumption underlying the classical Pauling scheme (Scheme 1) is incorrect; the covalent bonding by itself is not necessarily stabilizing even for homopolar bonds and even in case where the covalent structure clearly dominates the wave function, having the highest coefficient, as in F–F. Importantly, *homopolar bonds can have very large charge-shift resonance energies*. Moreover, the appearance of a repulsive covalent structure shows that these structures can be repulsive when the covalent spin-pairing energy is frustrated by Pauli repulsion (the same-spin interaction of the lone-pair electrons with the bonding electrons in the covalent structure). We shall elaborate this point later when we discuss the physical origins of CSB, and we shall see that once the assumption in Pauling scheme is removed, this enables to re-chart the mental map of the chemical bond.

However, CSB is not restricted to F–F, as can be seen by comparing Fig. 2d to c. It is clear that the B–H bond is classically covalent, while the F–H bond is not; its covalent structure is weakly bonded while the majority of the bonding energy in the exact VB wave function arises from the RE_{CS} due to the mixing of the ionic structures. Thus, here the Pauli repulsion weakens very much the covalent bonding, but not to the extent found in Fig. 2b for F–F.

Finally, Fig. 2e, f shows the NaF and NaCl bonds. It is clear that for both bonds, the dominant VB structure is ionic and it is very close to the exact covalent–ionic superposition curve, with a negligible RE_{CS} contribution. These two bonds are classically ionic.

As such, Fig. 2 reveals very nicely the two classical bond families, covalent and ionic, but alongside them, it reveals also the presence of a third bond type, *wherein the bonding does not arise from any one of the covalent or ionic structures, but rather from the resonance interaction, RE_{CS}, between them.* This is the charge-shift bonding (CSB) family. In recent years, a variety of σ- and π-bonds, both homo- and heteronuclear, were shown to share this property, thereby forming a growing family of CSBs [3–15], which we are going to focus upon in the remaining text.

5 Characterization of CSB by Other Theoretical Methods

The eventual acceptance of the CSB concept in chemistry ultimately depends on three conditions: (a) that the concept is proven to be robust and derivable from whichever theory one uses, (b) that manifestations of CSB in experimental data are found, and (c) that the concept leads to some testable predictions. We shall start by finding alternative theoretical probes for bonding and especially for the signatures of CSB.

5.1 VB Characterization of Bond Types

As discussed above, the emergence of three bonding families, covalent, ionic, and CS bonds, was originally derived from modern VB calculations [3, 4]. Thus, the VB wave function of an A–X bond was computed as a combination of the covalent form, Φ_{cov} (A•–•X), and the two ionic forms, Φ_{ion} (A^+X^-) and Φ'_{ion}(A^-X^+), shown in Fig. 1 and in Eq. (6):

$$\Psi(\mathrm{VB}) = c_1\Phi_{cov} + c_2\Phi_{ion} + c_3\Phi'_{ion}. \tag{6}$$

Equation (6) is identical to the Pauling wave function (see above), but all the terms are now computed by means of ab initio VB theory [18, 19]. The principal VB structure is the one having the lowest energy and hence also the largest coefficient among the three structures in Eq. (6). Its contribution to the total bond dissociation energy (D_e) is referred to as either D_{cov} or D_{ion}, wherein the subscript specifies the dominant VB structure. In all cases, the RE_{CS} is determined by reference to the bonding energy of the principal VB structure, as expressed by Eqs. (7a) and (7b):

$$D_e(\mathrm{polar-covalent}) = D_{cov} + RE_{CS}, \tag{7a}$$

$$D_e(\mathrm{ionic}) = D_{ion} + RE_{CS}. \tag{7b}$$

Note that Eq. (7a) covers both covalent and CSBs, depending on the magnitude of RE_{CS} vis-à-vis the total bond energy D_e. Similarly, Eq. (7b) covers both ionic and strongly polar CSBs, wherein the ionic structure dominates the wave function. These quantities characterize the bonding type as revealed from Fig. 2. Thus, in Fig. 2a, c, the principal VB structure for both H–H and B–H is Φ_{cov}, while the RE_{CS} quantity is small and much less significant than the large D_{cov}. In accord, these bonds are classical covalent and polar-covalent types, respectively. By contrast, F–H in Fig. 2d displays a weakly bound principal structure Φ_{cov}, and the major contribution to the bond comes from RE_{CS}; H–F is a CSB. An extreme CSB case is the F–F bond, in Fig. 2b, in which the principal structure Φ_{cov} is not even bonded, i.e., D_{cov} is *negative*, while RE_{CS} is even larger than the total bonding energy. Finally, in Na–F and Na–Cl (Fig. 2e and f), the principal VB structure is now Φ_{ion}, and the RE_{CS} quantity is a minor contributor, making both classical ionic bonds, where most of the bonding energy arises from the ionic structure.

5.2 ELF and AIM Characterization of Bond Types

An alternative way to characterize bonding uses electron density theories, like electron localization function (ELF) [16] and atoms in molecules (AIM) [17]. Will ELF and AIM show these three families? What will be the ELF and AIM signatures for CS bonds?

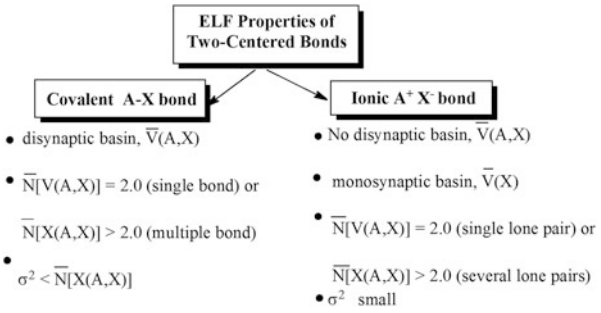

Scheme 2 Ideal covalent and ionic bonds and their expected ELF properties. Reproduced from [9] with permission of Wiley-VCH

5.2.1 ELF Characterization of Bond Types

The ELF approach uses a local function related to the Pauli repulsion to probe the separation of the different electron pairs and from this analysis carries out a partition of the molecular space into basins that correspond to the volumes occupied by core inner shells, bonds, and lone pairs. As in the Lewis model, a valence basin may either belong to a single atomic shell or be shared by several ones. In the first case, the basin is called monosynaptic and corresponds to a lone-pair region, and in the second case, it is polysynaptic and specifically disynaptic for a two-center bond that is of interest in this chapter.

A given basin is typified by a statistical analysis of the density. Thus, it is possible to calculate the basin population, $\overline{N}$, and its variance, σ^2, by integrating the one-electron and the pair density over the volumes of the corresponding basins. In the statistical theory of the basin populations, the variances measure the electron fluctuation in a given basin, and the covariances [9, 52] are thought to gauge directly the covalent–ionic fluctuations in terms of weights of ionic structures. However, since the covariance values exhibit similar trends to those of the variance [9], we shall focus only on the latter quantities.

For a classical covalent bond, the basin is disynaptic, its population is close to 2.0, and the variance (and covariance) is significantly smaller than the population, while a classical ionic bond like NaCl has only core and monosynaptic basins [9, 16, 53]. Scheme 2 summarizes these features, which defines only two electron-pair bond families, either covalent or ionic, in the original ELF formulations. Any bond with very different values, for the basin population and the corresponding fluctuation index, will not qualify as either covalent or ionic. However, as will be shown immediately, CSB possesses unique ELF characteristics, which foretell the repulsive (or slightly attractive) covalent density.

5.2.2 AIM Characterization of Bond Types

In AIM theory [17], a bond is generally characterized by a bond path, which defines a maximum density path connecting the bonded atoms. The point of the path at

which the density is at minimum is called the bond critical point (BCP), and the values of the density, $\rho(\mathbf{r}_c)$, and its Laplacian, $\nabla^2\rho(\mathbf{r}_c)$, at this point are characteristics of the interaction type in the bonding region. According to AIM, a classical covalent bond is typified by a significant $\rho(\mathbf{r}_c)$ value and a large negative $\nabla^2\rho(\mathbf{r}_c)$. By contrast, closed-shell interactions, suffering from Pauli repulsions (also known as overlap repulsion or exchange repulsion), as in ionic bonds or the He/He interaction, have characteristically a small critical density *and a positive Laplacian*. Note that the coexistence of a significant BCP density along with a positive Laplacian is not considered in the original AIM theory [17] and is viewed as an exception [54]. As will be seen below, this combination of features is in fact the signature of a homonuclear CS bond.

The Laplacian is especially telling quantity [17, 55], since it is connected to the kinetic and potential energy densities at BCP, $G(\mathbf{r}_c)$ and $V(\mathbf{r}_c)$, respectively, by the following local-virial theorem expression:

$$\frac{\hbar^2}{4m}\nabla^2\rho(\mathbf{r}_c) = 2G(\mathbf{r}_c) + V(\mathbf{r}_c). \tag{8}$$

Thus, a negative Laplacian means that the bonding region is dominated by lowering of the potential energy, while a positive Laplacian means that the interaction in the bonding region is typified by excess kinetic energy and is hence repulsive. All the AIM parameters for bonds in a molecule can be either calculated or derived from experimental density determination and are used by experimental chemists to characterize interactions within molecules [56, 57]. As such, we might expect AIM to reveal the presence of CSBs.

6 Common Trends of Bond Types Revealed by VB, AIM, and ELF

6.1 Common Conclusions in VB and AIM Analyses of Bonds

In order to provide a global picture of the various categories of bonds, we collected 27 bonds in Table 1 [3–15] and organized them into three groups, labeled as (**I**)–(**III**). The first group involves homonuclear bonds starting from H–H all the way to the "inverted" C–C bond in [1.1.1]propellane (see Scheme 3) [11]. Groups (**II**) and (**III**) involve heteronuclear bonds, starting from C–H all the way to Si–F.

Each bond in the table is characterized by five VB properties: the weight of the principal VB structure (ω_{cov} or ω_{ion}), the bonding energy of that structure (D_{cov} or D_{ion}), the full bond dissociation energy (D_e), the charge-shift resonance energy (RE_{CS}), and the relative resonance energy in percent units ($\%RE_{CS} = 100RE_{CS}/D_e$). For some of the bonds, we show AIM-derived quantities (ρ and $\nabla^2\rho$) as well as the

Table 1 Bonds and their VB and AIM properties: group (**I**) corresponds to homonuclear covalent and CS bonds, (**II**) to heteronuclear covalent and CS bonds, and (**III**) to ionic bonds

I.	**A–A**	ω_{cov}	D_{cov}	D_e	RE_{CS}	$\%RE_{CS}$	ρ	$\nabla^2\rho$	$\nabla^2\rho_{cov}$	$\nabla^2\rho_{res}$
1	H–H	0.76	95.8	105.0	9.2	8.8	0.27	−1.39	−0.70	−0.31
2	Li–Li	0.96	18.2	21.0	2.8	13.1	0.01	−0.01	−0.01	0.00
3	Na–Na	0.96	13.0	13.0	0.0	0.2	0.01	0.00	0.00	0.00
4	$H_3C–CH_3$	0.55	63.9	91.6	27.7	30.2	0.25	−0.62	−0.26	−0.36
5	$H_2N–NH_2$	0.62	22.8	66.6	43.8	65.7	0.29	−0.54	−0.02	−0.68
6	HO–OH	0.64	−7.1	49.8	56.9	114.3	0.26	−0.02	+0.46	−0.75
7	F–F	0.69	−28.4	33.8	62.2	183.9	0.25	+0.58	+1.00	−0.83
8	Cl–Cl	0.64	−9.4	39.3	48.7	124.1	0.14	+0.01	+0.14	−0.26
9	Br–Br[a]	0.71	−15.3	44.1	59.4	143.8	–	–	–	–
10	$C–C_{inv}(prop)$[b]	0.62	−2.2	~70.	72.2	>100	0.19[c]	+0.43[c]	–	–
11	$C–C_w(prop)$[b]	~0.55	–	–	–	–	0.25[c]	−0.51[c]	–	–
II.	**A–X**									
12	$H_3C–H$[a]	0.69	90.2	105.7	15.1	14.3	–	–	–	–
13	$H_3Si–H$[a]	0.65	82.5	93.6	11.1	11.9	–	–	–	–
14	B–H	0.71	78.2	89.2	11.0	12.3	0.19	−0.61	−0.59	−0.04
15	Cl–H	0.70	57.1	92.0	34.9	37.9	0.26	−0.81	−0.33	−0.42
16	F–H	0.52	33.2	124.0	90.8	73.2	0.38	−2.52	−1.82	−0.52
17	$H_3C–F$[a]	0.45	28.3	99.2	70.9	71.5	–	–	–	–
18	$H_3C–Cl$[a]	0.62	34.0	79.9	45.9	57.4	–	–	–	–
19	$H_3Si–Cl$[a]	0.57	37.0	102.1	65.1	63.8	–	–	–	–
20	$H_3Ge–Cl$[a]	0.59	33.9	88.6	54.7	61.7	–	–	–	–
21	F–Cl[a]	0.59	−39.7	47.9	87.6	182.9	–	–	–	–
22	Cl–Br[a]	0.69	−9.2	40.0	49.2	123.0	–	–	–	–

III.	$\mathbf{A}^{+}\,\mathbf{X}^{-}$	ω_{ion}	D_{ion}	D_{e}	RE_{CS}	$\%RE_{\text{CS}}$	ρ	$\nabla^2\rho$	$\nabla^2\rho_{\text{ion}}$	$\nabla^2\rho_{\text{res}}$
23	Li–F	0.76	93.3	104.5	11.2	10.7	0.07	+0.62	+0.51	−0.01
24	Na–F	0.72	77.0	86.0	9.0	10.4	0.05	+0.37	+0.27	+0.02
25	Li–Cl	0.56	76.8	88.5	11.7	13.3	0.04	+0.24	+0.16	0.00
26	Na–Cl	0.63	71.4	79.5	10.1	8.1	0.03	+0.18	+0.13	0.00
27	H_3Si–F[a]	0.36	103.8	140.4	36.6	26.1	–	–	–	–

[a]From [9, 12]. All other data are from [10] unless noted otherwise. Energies in kcal mol^{-1}, ρ in au $\left(\text{e}.a_o^{-3}\right)$, $\nabla^2\rho$ in au $\left(\text{e}.a_o^{-5}\right)$. The partial Laplacians are based on weights of the corresponding VB structures (see Eqs. (9)–(16) in [10])

[b]$C–C_{inv}$(prop) is the inverted bond in [1.1.1]propellane, and the $C–C_w$(prop) is one of the wing bonds of the same molecule. The VB data are from [10, 11]

[c]Experimental data [58] for a substituted [1.1.1]propellane derivative. The values for the wing bonds are averaged. Energies in kcal mol^{-1}, ρ in au $\left(\text{e}.a_o^{-3}\right)$, $\nabla^2\rho$ in au $\left(\text{e}.a_o^{-5}\right)$

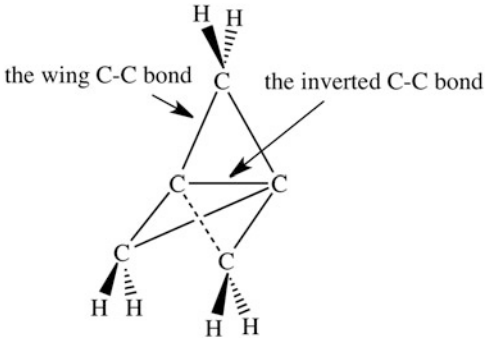

Scheme 3 The molecule [1.1.1]propellane and its two C–C bond types

Laplacian components in the BCP for bonding due to the principal structure of the bond ($\nabla^2\rho_{cov}$ or $\nabla^2\rho_{ion}$) and the covalent–ionic resonance ($\nabla^2\rho_{res}$) [10].

Let us first inspect the homonuclear bonds in (**I**), which by all definitions could not possess static bond ionicity. The bond energies in entries 1–4 are dominated by the covalent component with charge-shift resonance energy being the minor bonding contribution ($\%RE_{CS} < 50\%$). By contrast, the bonds in entries 6–10 all have a bonding energy dominated by RE_{CS} ($\%RE_{CS} > 100\%$), while the covalent structure is repulsive ($D_{cov} < 0$). The N–N bond, entry 5, is a borderline case, with $\%RE_{CS}$ accounting for 66.6% of the total bonding energy. Leaving aside the weak Na–Na and Li–Li bonds for which all AIM parameters are close to zero, there is an excellent correlation between the RE_{CS} quantities and the AIM parameters, especially within the same row of the periodic table. Thus, from C–C all the way to F–F (entries 4–7), the resonance component of the Laplacian ($\nabla^2\rho_{res}$) is more and more negative, in line with the increase of RE_{CS}, while the covalent component ($\nabla^2\rho_{cov}$) goes from negative to positive values, in line with the repulsive nature of the covalent structure in CS bonds. As a result, the total Laplacian $\nabla^2\rho$ is large and negative for classically covalent bonds and small or positive for CS bonds. Note that, according to the computed RE_{CS} and the experimentally derived $\nabla^2\rho$ values [58], the [1.1.1]propellane molecule displays the two categories of bonds, classically covalent for the wing bonds (entry 11) and CS bond for the "inverted" central bond (entry 10). Finally, the coappearance of small or positive total Laplacian $\nabla^2\rho$ hand in hand with a significant density, $\rho(\mathbf{r}_c)$ in homonuclear CS bonds (HO–OH, F–F, Cl–Cl), defines a new bonding category that was not anticipated in the original AIM theory. This is the CSB family.

The above relationships are illustrated more vividly in Fig. 3, which plot the covalent part of the Laplacian against the covalent bond energies, D_{cov}, for homonuclear bonds [10]. In the right lower quadrant, where $D_{cov} > 0$ and $\nabla^2\rho_{cov} < 0$, there are the bonds with stabilized covalent bonding. The second group, in the upper left quadrant, involves *electronegative and lone-pair-rich atoms and* "*inverted carbons*" which produce CSBs. It can be seen that this bonding type is associated with weakened covalent spin pairing ($D_{cov} < 0$), owing to lone-pair repulsion, which raises the kinetic energy as seen from the positive sign of

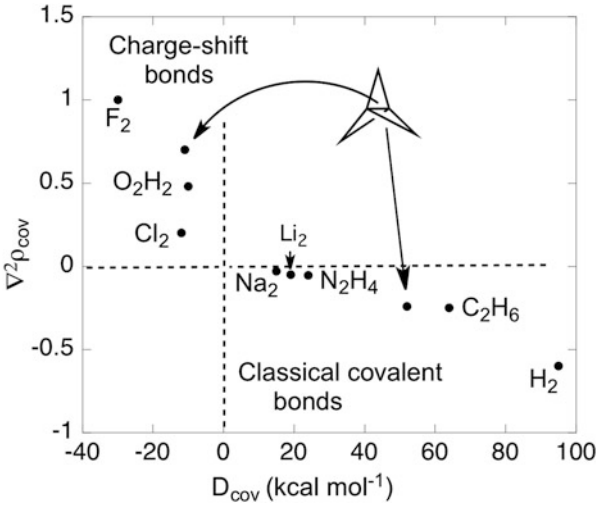

Fig. 3 Correlation of the covalent Laplacian (L) with the value of D_{cov} for homonuclear bonds. The CSBs are concentrated in the *upper left quadrant*, while the classical covalent bonds are in the *lower right quadrant*. Note the two bond types of [1.1.1] propellane, each belonging to a different quadrant. Reproduced from [10] with permission of Wiley-VCH

$\nabla^2\rho_{cov}$. Clearly, AIM and VB theory converge, both revealing the presence of a CSB family.

Turning to heteropolar bonds in (**II**) in Table 1, we note the following trends. While the covalent VB structure is the principal one for all these bonds, still the bonds fall into two distinct groups. Specifically, the bonds in entries 12–15 belong to the classical polar-covalent bond family based on their $\%RE_{CS}$ that is well below 50%. By contrast, the bonds in entries 16–22 all have weakly bonded covalent structures and large $\%RE_{CS}$ exceeding 50% and in some cases >100%.

In part (**III**) of the table, the principal VB structure of all bonds is ionic. The bonding energies in entries 23–26 are all dominated by the electrostatic contribution to bonding (D_{ion}), with small RE_{CS} contributions. These are classical ionic bonds. Finally, the Si–F bond in entry 27 is special; its principal VB structure is ionic; its static ionicity is large, but its RE_{CS} is significant, much larger than that in the classical ionic bonds in (**III**). VB theory predicts that this bond will be very different from ionic bonds. As already alluded to above, the Si–X bonds behave as though they were covalent despite their large ionic characters in terms of charge distribution. Here, in (**II**) and (**III**), these bonds and their heavier analogs are clearly marked either as CS bonds (Si–Cl, Ge–Cl) [6] or as bonds with a large CSB character (Si–F) [9]. A similar case to Si–F was noted recently for protonated methanol [15], wherein the bond wave function is dominated by the VB structure $H_3C^+ :OH_2$, but the bond energy is dominated by the RE_{CS} quantity due to resonance between $H_3C^+ :OH_2$ and the corresponding covalent structure, $H_3C\bullet - \bullet OH_2^+$.

The AIM analysis of the heteropolar bonds in (**II**) does not distinguish between the covalent and CSB cases, but the Laplacian components in the BCP show that the CSBs have more pronounced $\nabla^2\rho_{res}$ values [10], compared with the classical covalent bonds, in line with the dominant RE_{CS} quantity. Finally, the AIM analysis of the classical ionic bonds in (**III**) [10] shows the expected characteristics from

closed-shell interactions; all have positive Laplacians that are dominated by the ionic component, $\nabla^2\rho_{\text{ion}}$.

6.2 Common Conclusions in VB and ELF Analyses of Bonds

Table 2 collects the ELF results for a group of single bonds, reported in the original literature [9]. For covalent and CSB, we show the population of the disynaptic basin that corresponds to the A–X bond, $\overline{N}[V(A,X)]$, and its variance σ^2, which is a measure of the charge density fluctuation of the bonding electrons. For ionic bonds (entries 6, 7), the core population of the most electropositive atom A is reported instead of $\overline{N}[V(A,X)]$.

Table 2 exhibits three groups of bonds. Entries 1–5 show bonds with almost 2.0 electrons in the disynaptic basin, with weak to moderate fluctuation compared to the total population. These are the classical covalent bonds.

Entries 6 and 7 of Table 2 show two bonds, which do not exhibit any disynaptic basin but possess a basin for the bare core of sodium. The other basin, which is not shown, resides on the electronegative atoms Cl and F. In both entries, the population of the core basin of sodium is close to 10 e-, and the variance is rather small (0.11–0.12). These are classical ionic bonds.

Table 2 Populations $\overline{N}(\Omega)$ and population variance σ^2 in ELF basins [9]

Entry	Molecule	Basin	$\overline{N}(\Omega)$	σ^2	Bond type
1	H–H	V(H, H)	2.0	0.0	cov.
2	Li–Li	V(Li, Li)	2.0	0.17	cov.
3	CH_4	V(C, H)	1.97	0.63	cov.
4	SiH_4	V(Si, H)	2.0	0.46	cov.
5	C_2H_6	V(C, H)	2.0	0.63	cov.
		V(C, C)	1.81	0.96	cov.
6	NaCl	C(Na)	10.02	0.11	ion.
7	NaF	C(Na)	10.01	0.12	ion.
8	F_2[a]	V(F, F)	0.44	0.42	CS
9	Cl_2[a]	V(Cl, Cl)	0.73	0.59	CS
10	Br_2	V(Br, Br)	0.81	0.68	CS
11	FCl	V(F, Cl)	0.39	0.35	CS
12	FBr	V(F, Br)	0.28	0.26	CS
13	ClBr	V(Cl, Br)	0.67	0.54	CS
14	H_2O_2	V(O, O)	0.49	0.41	CS
15	N_2H_4	V(N, N)	1.16	0.77	CS
16	HF	V(H, F)	1.22	0.68	CS
17	CH_3F	V(C, F)	0.86	0.64	CS
19	SiH_3F	V(Si, F)	0.27	0.24	ion-CS

[a]V(F, F) and V(Cl, Cl) are the unions of two monosynaptic basins

The largest group in Table 2 corresponds to entries 8–17. In all of these bonds, the population of the A–X basin is of the order of 1 e^- or less, and the variances of these populations are large, almost of the same order as the population. The small populations of the disynaptic basins indicate that *these are not classical covalent bonds*, in which two spin-paired electrons are expected to dominate the bonding energy. In fact, at higher levels of calculations, in the cases of F–F and Cl–Cl, the disynaptic basins are split into two monosynaptic ones that are 0.2 Å apart, and the electrons in the bonding region behave as though the bonds were "dissociated" with significant Pauli repulsion between the electrons. This, together with the large variance, signifies that the bonding in these molecules is dominated by fluctuation of the charge density. This last group of bonds corresponds therefore to the same CSB type that emerges from the VB calculations.

The last entry in Table 2 corresponds to the Si–F bond. With the 6-31+G* basis set, this bond reveals a disynaptic Si–F basin, with a weak population and large variance, mostly due to the delocalization involving the fluorine lone pairs. Thus, ELF and VB agree that although this bond has high static ionicity, it is a borderline case lying in between the groups of ionic bonds and charge-shift bonds.

Clearly, therefore, much like the VB picture, the ELF analysis reveals the same distinction between the covalent and CS bond groups [9]. Bonds like H–H, C–C, Li–Li, etc., possess disynaptic basins with a population close to 2.0 electrons and small variances, whereas bonds like F–F, Cl–Cl, O–O, Br–Br, N–N, and the inverted C–C bond of [1.1.1]propellane possess small basin populations ($\leq$1.0) [59], with variances as large as the population.

The match between the predictions of the two methods is made vivid by inspecting the homonuclear bonds in Fig. 4, which shows a plot of the basin population bonds vis-à-vis the charge-shift resonance energy. The correlation is apparent; the smaller the basin population, the larger the charge-shift resonance energy. Furthermore, the heavy red circles in Fig. 4 show how the rate of variance

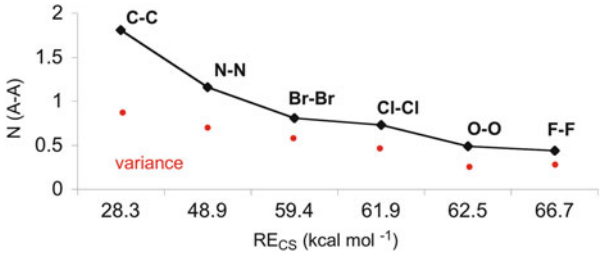

Fig. 4 A correlation between the ELF population of the disynaptic basin and the VB-calculated charge-shift resonance energy, for a series of homonuclear bonds. The *heavy red circles* show the change of the population variances (σ^2) of the bonds. Reproduced from [9] with permission of Wiley-VCH

over population increases as the RE_{CS} quantity increases and vice versa. It is apparent that the variance is less than half of the basin population for the covalent bond (C–C), but it gets gradually closer to the population for the CS bonds (from Br–Br to F–F), thereby showing again the connection between repulsive covalency, the fluctuating electron density, and the large charge-shift resonance energy. Recalling (Table 1) that all the bonds in Fig. 4 have very similar weights of covalent and ionic contributions to bonding, it is clear that the major feature of bonding that distinguishes this group is the RE_{CS} quantity that arises from the covalent–ionic fluctuation of the pair density.

The correlation in Fig. 4 indicates that both theories converge to the same conclusion, thereby substantiating the classification of CSB as a distinct bonding type that is supported by a dominant RE_{CS} quantity, due to covalent–ionic fluctuation. Furthermore, both theories show that *this group of bonds transcends considerations based on static charge distribution and is more concerned with the* "*dynamic bond ionicity*" (for "dynamic ionicity," see [60]).

6.3 Common Conclusions in VB, ELF, and AIM Analyses of Bonds

Figure 5 projects the distinction of the covalent and CSB families by the three theoretical approaches. The figure depicts the ELF molecular basins for $H_3C–CH_3$, F–F, and the two C–C bond types in [1.1.1]propellane, alongside their VB and AIM properties. It is seen that the C–C bond of ethane in Fig. 5a and the wing C–C bond in [1.1.1]propellane in Fig. 5c have nice cylindrical ELF basins with populations close to 2.0, highly negative Laplacians, and a small or moderate RE_{CS}. These are classical covalent bonds. By contrast, Fig. 5b, c shows that the disynaptic basins of F–F and the inverted C–C bond of [1.1.1]propellane are in fact two monosynaptic basins, much like dissociated bonds. The corresponding basin populations are tiny with variances being as large as the populations, the Laplacian is highly positive indicating repulsive covalent structures, and the RE_{CS} quantities are very large. Thus, the three methods diagnose the same classification of homonuclear bonds into two families. ELF and AIM diagnose the attractive/repulsive nature of the covalent "shared densities," while VB brings additional energetic insight that highlights the dominant role of the RE_{CS} energy in the CSB group. Furthermore, the experimentally derived AIM properties for [1.1.1]propellane clearly provide an experimental support for the notion of the CSB character of the inverted C–C bond.

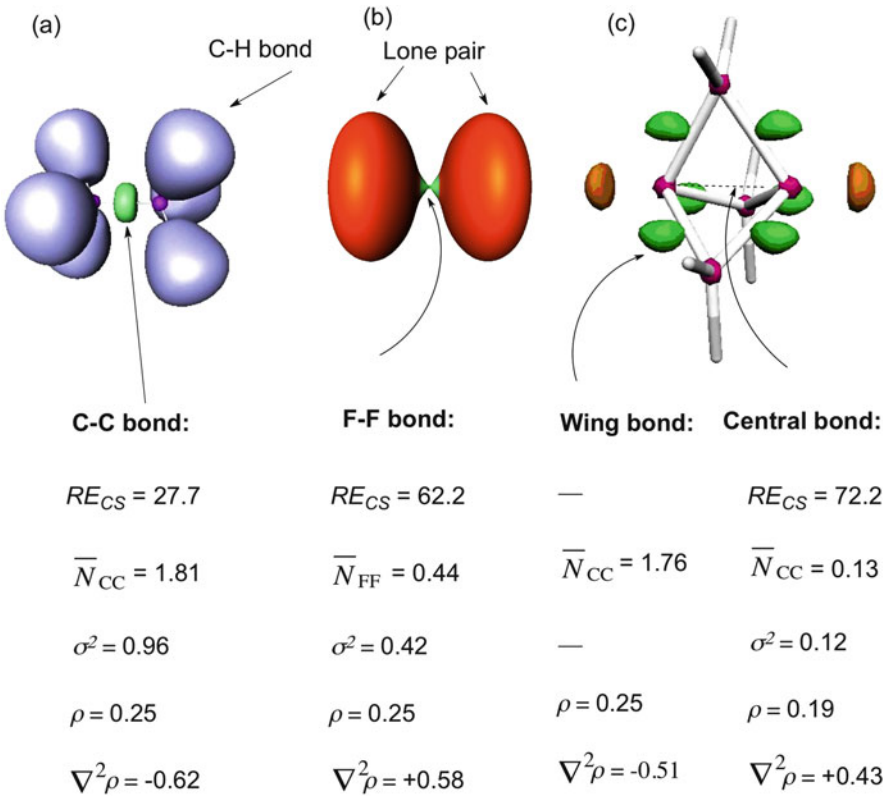

Fig. 5 Pictorial ELF representations of electron density in a few typical bonds: (**a**) the ELF disynaptic basin [9] for $H_3C–CH_3$, (**b**) the disynaptic and lone-pair basins for the F–F bond, and (**c**) disynaptic basins for the wing bonds of [1.1.1]propellane and two monosynaptic basins for the central inverted bond [59]. Each bond is further characterized by its covalent–ionic resonance energy RE_{CS}, the ELF basin population $\overline{N}$ and its variance σ^2, the density ρ at the bond critical point, and the corresponding Laplacian $\nabla^2\rho$ (energies are in kcal mol^{-1}, densities in ea_0^{-3}, Laplacians in ea_0^{-5}). For $H_3C–CH_3$ and F–F, the ELF and AIM parameters are taken from [9] and [11], respectively. For [1.1.1]propellane, the AIM parameters are experimental values [58] from the study of a substituted [1.1.1]propellane derivative. The ELF drawings in this Fig. (**a**) and (**b**) are reproduced with permission of Wiley-VCH from Figs. 3 and 4 in [9]. Copyright Wiley-VCH Verlag & Co. KGaA. The ELF drawing in this Fig. (**c**) is reproduced with permission from Fig. 1a in [59]. Copyright Wiley-Interscience

6.4 The Three Bonding Families

In summary, CSB emerges as a distinct class alongside the covalent and ionic bonds. In VB theory [3–15], CSB is typified by large covalent–ionic resonance energy, RE_{CS}, and in ELF, by a depleted basin population with large variance and covariance [9]. In addition, homonuclear CSB is characterized in AIM by a positive

or small Laplacian of the electron density which coappears with a significant value of the density itself, $\rho(\mathbf{r}_c)$ [11, 54]. It should be noted that the characterizations of CSB by AIM and ELF electron density analysis are independent of the level of calculation used to compute the wave function or electron density, e.g., MO bonding theory or density functionals [9, 11], showing that the non-VB-based methods effectively account for CSB, even if not in the explicit way achieved by VB theory.

7 How Does MO Theory Reveal CSB?

In MO theory, the covalent–ionic resonance energy is embedded into the total energy and is not an immediately apparent property. In addition, the reference state for MO theory is the Hartree–Fock (HF) wave function, which at the same time lacks electron correlation and also does not provide any bonding for F–F. It is therefore challenging to demonstrate that CSB emerges also from MO theory.

Recently, we addressed the challenge and showed that (a) MO-based theory also reveals the CSB family and (b) the bonding in F–F is due to the charge-shift resonance energy. The essential step in this demonstration is the definition of an MO-based reference state that would be identical to the covalent structure of VB theory. While the details appeared recently in the original literature [14], we would like to show here the essential results of the demonstration.

Figure 6 shows the energy curves for the dissociation of H–H (Fig. 6a, b) and F–F (Fig. 6c, d) using MO-based and VB theories. In the VB curves (Fig. 6b, d), the bond wave function is based on the covalent and ionic structures, while the reference state is the covalent structure as we showed already above. On the other hand, in the MO-based curves (Fig. 6a, c), the bond is described by a two-configuration SCF (TCSCF) wave function and has a reference two-configuration (RTC) state. The construction of RTC state is based on the fact [18] that a bond in the HF wave function, Ψ_{HF}, involves 50% covalent and 50% ionic characters and so does the corresponding doubly excited configuration, Ψ_D (where the two electrons in the σ-bond orbital are excited to the antibonding σ*). In a homonuclear bond, the only difference is the sign of the combination, $\Psi_{HF} = \text{cov} + \text{ion}$, while $\Psi_D = \text{cov} - \text{ion}$. Thus, the RTC state is constructed as the wave function obtained by subtracting: $\Psi_{HF} - \Psi_D$. It is seen from Fig. 6 that the so generated MO-based curves are entirely identical to the corresponding VB curves, one for H_2 showing a classical covalent bond, the other for F_2 showing CSB.

In fact, it is also possible to define the MO-based curves at higher levels and for other bonds as well. This is illustrated in Fig. 7, which shows the correlation of $\%RE_{CS}$ values obtained with TCSCF augmented with second-order perturbation theory (PT2) and those obtained with the BOVB method, for the C–C, N–N, O–O, and F–F bonds. The correlation is seen to be good and to involve covalent bonds ($\%RE_{CS} < 50$) and CSBs ($\%RE_{CS} >> 50$). Clearly, CSB is not peculiar to VB theory and it is derivable also from an MO-based theory. *It follows therefore that the charge-shift resonance*

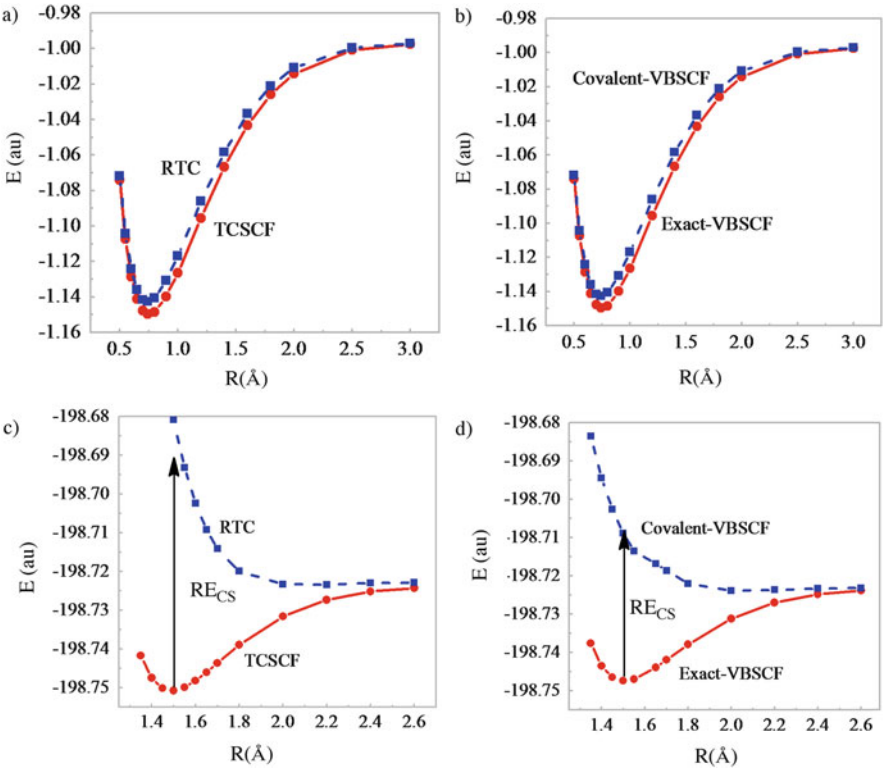

Fig. 6 Full state curves and reference state curves for H–H and F–F bonds. The MO-generated curves involve two-configuration self-consistent field (TCSCF) wave functions and reference two-configuration (RTC) states, while the VB curves are covalent and full covalent–ionic state curves: (**a**) and (**b**) show the dissociation curves for H–H. (**c**) and (**d**) show the corresponding curves for F–F. The *arrow* for F–F shows the magnitude of the RE_{CS} as the difference between the reference state (covalent or RTC) and the full state curve. Reproduced with ACS permission from [14]

energy is a fundamental property of the chemical bond that is not specific to any particular computational method or theory.

We can turn now to answer a frequently asked question, "Why do we say that the F–F is bonded by charge-shift resonance, isn't it bonded simply by electron correlation?" The MO-based conclusion that F–F is "bonded by electron correlation" is rooted at the fact that at the HF level the molecule is not bonded and electron correlation, which is brought about by configuration interaction (CI), is required to induce bonding. Let us recall that the HF wave function (Ψ_{HF}) for an electron-pair bond A–A is described by 50% covalent and 50% ionic characters, which means that there are identical probabilities for the two electrons to reside on the same atom or being separated apart, one on each atom. Thus, the two electrons in Ψ_{HF} are not correlated, and electron correlation is obtained by complementing

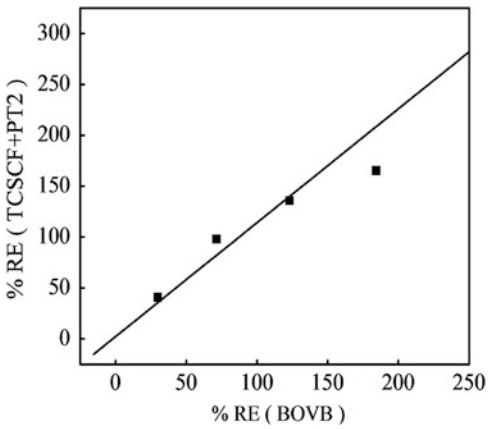

Fig. 7 A correlation of $\%RE_{CS}$ values ($\%RE_{CS} = 100RE_{CS}/D_e$) obtained at the TCSCF+PT2 level and the BOVB level, for the C–C, O–O, N–N, and F–F bonds, from *left* to *right*. Reproduced with ACS permission from [14]

Ψ_{HF} with CI. The CI raises the weight of the covalent character to ca. 70% while decreasing the ionic character to ca. 30%, thereby reducing the probability of two electrons to be on the same atom [18, 19]. By contrast, using the covalent structure as the reference state (either in VB or in MO, as in Fig. 6) causes the electrons to be *overly* correlated, and the charge-shift resonance energy stabilization brought about by mixing of the ionic structures augments the ionic character while reducing the covalent one. Hence, MO and VB theories start at opposite ends, such that RE_{CS} and the correlation energy are completely different physical quantities. However, when we use the same reference state for both VB and MO theories, as in Figs. 6 and 7, we can see clearly the fundamental role of RE_{CS} and of CSB. The usage of the artificially high-energy Ψ_{HF} state, which is fully delocalized (50–50% ionic/covalent), masks this fundamental property of the chemical bond.

8 Physical Origins of CSB

While the phenomenon of CSB is derived from four independent theoretical treatments, one would still like to base this bonding type on some fundamental principles. All the methods show that the emergence of CSB coincides with poor bonding by the shared-electron density of the electron pair. In VB calculations and MO method using a covalent-reference state, this manifests as a repulsive or weakly attractive covalent structure (Figs. 2b and 6c, d), in ELF this is shown by escape of the shared density from the disynaptic basin (Figs. 4 and 5), and in AIM one finds that the shared density has a positive Laplacian (Fig. 5) much as in cases which exhibit closed-shell repulsion, e.g., He_2. Coupling the AIM technique into VB shows that CS bonds have large resonance Laplacians (entry 7 in Table 1). Furthermore, AIM shows also that the positive Laplacian is associated with excess kinetic energy in the bonding region and the same is implied by the ELF definition. As such, we would like to articulate a physical mechanism that reveals the root causes

of weakly bonded or repulsive covalent structure and that links this repulsion to increase of kinetic energy of the electrons and the role of RE_{CS}. This is done in the following section.

8.1 CSB and Atomic Size

The large RE_{CS} quantity of CS bonds is an outcome of the mechanism necessary to establish equilibrium and optimum bonding during bond formation. This mechanism, based on the virial theorem, has been analyzed in the original literature in details [4, 9, 61], while here we present a simpler analysis.

By comparing the atomic and covalent radii in the periodic table, one finds that as a rule $r_{atom} > r_{cov}$. This means that as atoms (fragments) bind, they shrink [61]. The shrinkage causes a steep increase in the fragments' kinetic energy, which exceeds the lowering of the potential energy due to the diminished size [62–68]. Thus, the shrinkage tips the virial ratio of the kinetic (T) vs. potential (V) energies off equilibrium. At equilibrium, the ratio has to be $V/T = -2$. All resonance energy terms are (1) negative and (2) dominated by kinetic energy, and therefore, *the covalent–ionic resonance is a negative kinetic energy term that reduces the steep rise in the kinetic energy and restores the virial ratio* [4, 9, 61–68] and this is true for all bonds. The kinetic energy rise due to shrinkage is proportional to the compactness of bonding partners, and therefore, as the fragments in bonding become more compact, the kinetic energy rise due to the atomic/fragment shrinkage will get steeper, and a larger RE_{CS} quantity will be required to restore the equilibrium.

A simple demonstration of the atom compactness effect is Fig. 8 [4], which models the effect of orbital compactness by calculating the CS-resonance energy of

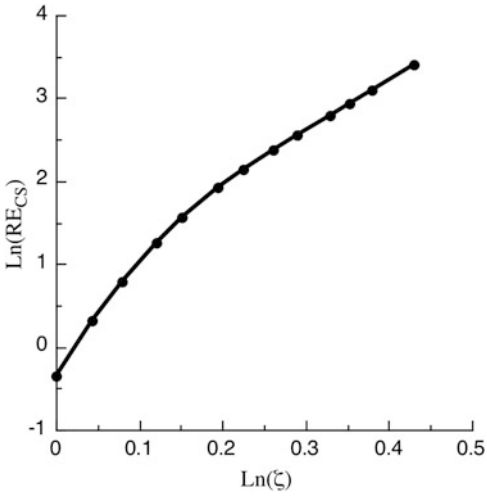

Fig. 8 A natural logarithm plot of the VB-computed [4] CS-resonance energy against the orbital exponent, ζ, for a pseudo-H'_2 molecule where the 1s orbitals of H′ have modified orbital exponent, ζ. Adapted with permission from [4]. Copyright 1992 American Chemical Society

an H'_2 molecule, where H′ is an atom with a variable orbital exponent, ζ. It is seen that as the orbital exponent increases, the CS-resonance energy increases. In the region $Ln(\zeta) = 0.2$–0.5, the relationship is linear following Eq. (9):

$$Ln(RE_{CS}) = 8.9Ln(\zeta) - 0.4. \tag{9}$$

The result in Fig. 8 and its expression in Eq. (9) are direct demonstrations of the role of the atomic size. Thus, as ζ increases, the orbital of H′ becomes more compact, leading to increase of the kinetic energy of the atoms, and hence, the CS-resonance energy increases in order to restore equilibrium for the bond.

8.2 The Pauli Repulsion Pressure as a Driving Force for CSB

Real atoms (fragments) are not merely pseudo-hydrogens. They bear also lone pairs or other electron pairs, which can interact with the "test bond" by Pauli repulsion. As we saw, in some bonds like F–F, Cl–Cl, O–O, etc., the spin pairing leads to a covalent structure that is either destabilized or only weakly stabilized relative to the dissociated atoms (Table 1). This failure of the covalent structure to provide significant bonding was quantified in VB terms [3–6, 9, 12] and found to originate primarily in *the Pauli repulsion between the bonding electrons and the lone pairs that have the same symmetry as the bond*. The repulsion between the lone pairs themselves contributes too but to a lesser extent [8]. Scheme 4 illustrates this repulsive interaction that counteracts[3] the spin-pairing stabilization in F–F [9, 49–51], using a cartoon.

Thus, as argued before [18, 69], and is reiterated in the textbox below, both the spin coupling energy as well as each of the 3-electron repulsion terms have the same expression but with opposite signs. Hence, the two Pauli repulsive terms add up to a larger quantity than the spin-pairing energy, and the covalent structure of F–F is repulsive (Fig. 2b) with a negative D_{cov} quantity [13]. The same considerations apply to other bonds, which bear lone pairs. In any case, the Pauli repulsion pressure will weaken the corresponding covalent bonding energy.

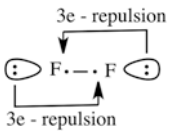

Scheme 4 The lone-pair bond-pair repulsion in the covalent structure of F–F. The bond pair is depicted as two electrons (*dots*) connected by a *line*

Textbox

Using the Hückel resonance integral β and the overlap S between the two hybrid atomic orbitals (HAOs), which participate in spin pairing, the covalent bonding in the F–F bond leads to the following stabilization energy [18, 69]:

$$\Delta E_{\mathrm{cov}} = 2\beta S; \quad \beta < 0. \tag{10}$$

Each of the Pauli repulsion terms in Scheme 4 has the same expression but with a negative sign:

$$\Delta E_{3\mathrm{e-Pauli}} = -2\beta' S'. \tag{11}$$

Therefore, the net D_{cov} becomes

$$D_{\mathrm{cov}} = -[\Delta E_{\mathrm{cov}} + 2\Delta E_{3\mathrm{e-Pauli}}] = -2\beta S + 4\beta' S' < 0. \tag{12}$$

Thus, D_{cov} will be net destabilizing if βS and $\beta' S'$ have comparable magnitudes.

This Pauli repulsion was pointed out originally by Sanderson [31], who termed this as the lone-pair bond-weakening effect (LPBWE). Since the Pauli repulsion has the same expression as the bonding energy but with a different sign [Eq. (11) in the textbox], its presence in a bond will raise the kinetic energy of the bond, and the effect will become more severe as the number of lone pairs on the atom increases. As the atoms (fragments) are brought together, the LPBWE augments the kinetic energy rise since all -βS terms are dominated by increase of the kinetic energy. This tips the virial ratio off-balance, and hence the only way for the molecule to restore the virial ratio and achieve equilibrium bonding is to augment the ionic-covalent mixing and increase thereby the CS-resonance energy[4] [4, 61], which reduces the kinetic energy in the bonding region.

[4] As seen from footnote 3 here, the F–F bond energy arising from CASSCF or from GVB wave functions is rather poor, 16.0 kcal mol^{-1}. These methods treat the covalent and ionic structures of the bond in a mean-field approximation. Only further extensive CI of the GVB and CASSCF wave functions allows the bond energy to get closer to experiment. The modern BOVB methods lead to the correct bond energy, ca 36 kcal mol^{-1}, by explicit treatment of the ionic structures, which are allowed to take on their particular set of orbitals. Thus bonding in F–F mainly originates from *the response of the electronic structure to the fluctuation of the electron-pair density from the average density*.

Since electronegative fragments are compact and also lone-pair rich, we might expect that in bonds of such fragments, the resonance energy that is required to restore the virial ratio will become necessarily very large, generating thereby bonds with weakened bonding in the covalent structures and large RE_{CS} quantities. Thus, CSB is associated with a fundamental mechanism that is necessary to adjust the kinetic and potential energy to the virial ratio at equilibrium, in response to the Pauli repulsive strain exerted on the bond and the shrinkage of the atoms (fragments) that occurs during bonding.

9 Trends in Electron-Pair Bonds

Understanding the roots of CS bonding allows us to outline some global correlations for the CS-resonance energy and bonding in general. Recalling that electronegative atoms have compact valence orbitals and are lone-pair rich, we might expect that the electronegativity of the atom or fragment (χ_A) will be an organizing quantity for RE_{CS} and in the absence of LPBWE also of D_e.

These global relationships are illustrated in Fig. 9 for RE_{CS}. Figure 9a shows the RE_{CS} quantities for homonuclear A–A bonds, plotted against the electronegativity (χ_A) of A. It is seen that in each period, RE_{CS} increases as the electronegativity increases. Figure 9b shows a plot of RE_{CS} vs. the sum of electronegativities of the fragments using both homonuclear and heteronuclear bonds [9], while Fig. 9c, d show, respectively, the same trend for π-bonds of doubly bonded and triply bonded molecules [7, 70]. It is apparent that the RE_{CS} quantity of the bond generally increases as the molecular electronegativity of the bond partners increases. We note that the scatter in the plots in Fig. 9b–d reflects in part the effect of the electronegativity difference, namely, the classical Pauling effect on the covalent–ionic resonance energy [see Eq. (4)]. Thus, for a given molecular electronegativity ($\chi_X + \chi_A$), the RE_{CS} quantity increases, to some extent, with increase of the electronegativity difference ($\chi_X - \chi_A$), thereby reflecting an incremental increase of RE_{CS} due to the stabilization of the ionic structure, A^+X^-, and its stronger mixing into the covalent structure. However, the electronegativity difference constitutes only a secondary influence. Indeed, in contrast to the behavior in Fig. 9b–d where a global correlation with ($\chi_X + \chi_A$) is apparent, no correlation whatsoever is observed when the RE_{CS} data is plotted against ($\chi_X - \chi_A$) alone. *The fundamental correlation is with the sum of electronegativities*, which gauges both the effects of the fragment compactness and the Pauli repulsion pressure on the shared density.

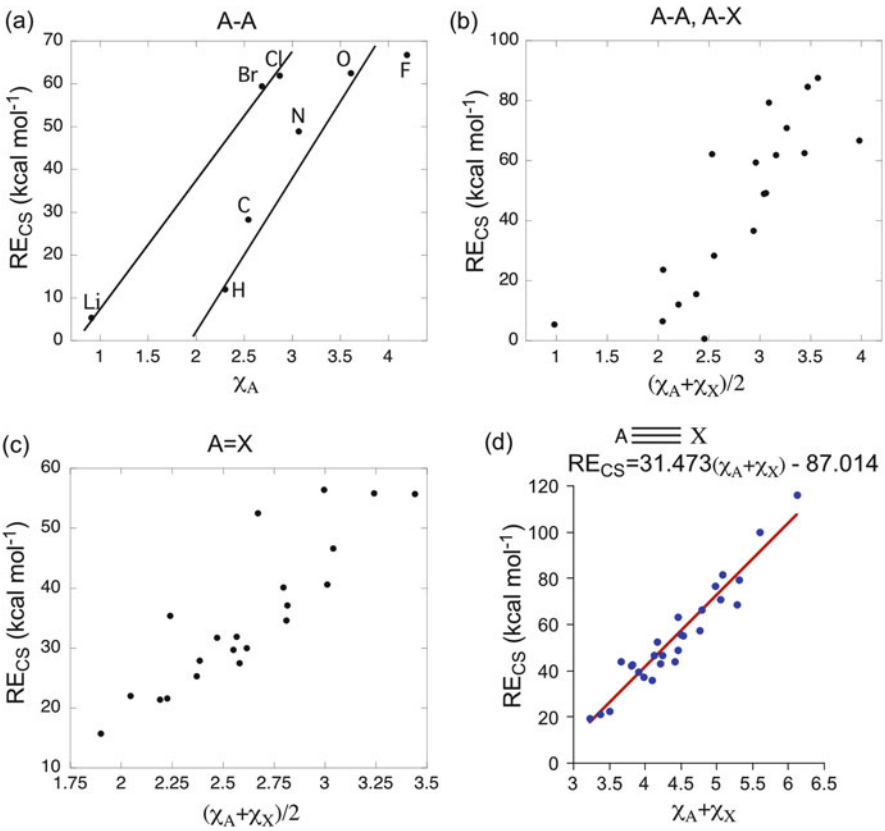

Fig. 9 Correlation of the charge-shift resonance energy (RE_{CS}) of a bond with the electronegativities (χ) of the bonded atoms or fragments. (**a**) A plot of RE_{CS}(A–A) vs. χ_A, the electronegativity of A, reproduced from [9] with permission of Wiley-VCH. (**b**) A plot of RE_{CS} for A–A and A–X bonds vs. the average electronegativity of the bond, reproduced from [9] with permission of Wiley-VCH. (**c**) A plot of RE_{CS} for π-bonds (of doubly bonded molecules, A=X) vs. the average electronegativity of the bond partners, reproduced from [9] with permission of Wiley-VCH. (**d**) A plot of RE_{CS} for two π-bonds (of triply bonded A≡X molecules) vs. the sum of electronegativities of the bond constituents, reproduced with permission from [70]. Copyright 2011 American Chemical Society. Permissions for (**a**)–(**c**) are by Copyright Wiley-VCH Verlag & Co. KGaA. Part (**d**) is reproduced with permission from [70]. Copyright 2011 American Chemical Society

Since π-bonds do not suffer from LPBWE, even their D_{cov} quantity correlates quite well with the sum of electronegativities of the fragments. This along with the dominance of bonding by the RE_{CS} means that one may expect that the total π-bond energy will also correlate with the sum of the fragment electronegativities rather than with their difference. Figure 10 shows this global correlation for the total π-bonding energy in triply bonded molecules, A≡X. Thus, *the bonding gets stronger as the molecular electron affinity increases.*

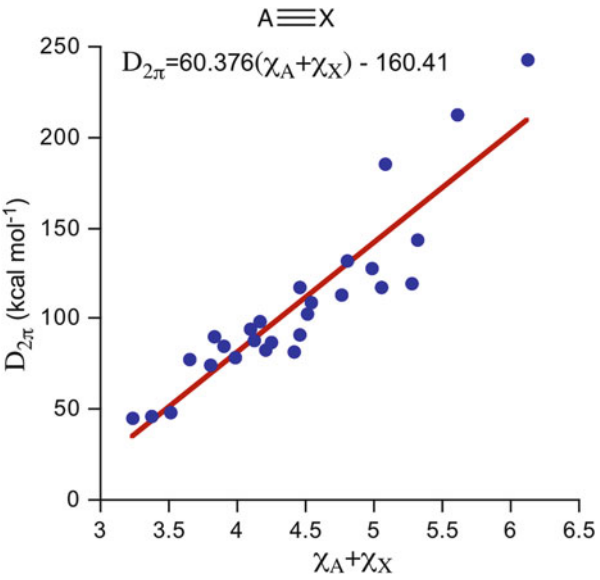

Fig. 10 A plot of VB-calculated sum of π-bond energies, $D_{2\pi}$, for A≡X molecules vs. the molecular electronegativity, $(\chi_A + \chi_X)$. Reproduced with permission from [70]. Copyright 2011 American Chemical Society

10 Additional Factors of CSB

The Pauli repulsion pressure that is associated with the lone pairs of electronegative fragments is not the only factor that can promote CSB. A recently identified additional factor [4–6, 9] was expressed in bonds between metalloids of group 14 and electronegative groups, like all the Si–F, Si–Cl, and Ge–Cl bonds in Table 1. The VB calculations for these bonds [6, 71] show that the corresponding ionic curve for, e.g., the Me_3Si–Cl bond is much deeper than that for the corresponding Me_3C–Cl bond [71]. Moreover, the ionic curve $Me_3Si^+Cl^-$ has a tighter minimum than Me_3C^+Cl in harmony with the fact that the charge is completely localized on Si in Me_3Si^+, while highly delocalized in Me_3C^+. Figure 11 shows the charge distribution in the two cations, and it is apparent that while the Me_3C^+ carries a tiny little charge on the central carbon, in the case of Me_3Si^+ all the positive charge is localized on the Si. This causes the ionic and covalent structures to be close in energy in Me_3SiCl, thus leading to a high RE_{CS} quantity, which is apparent from Table 1 for the Si–Cl bond.

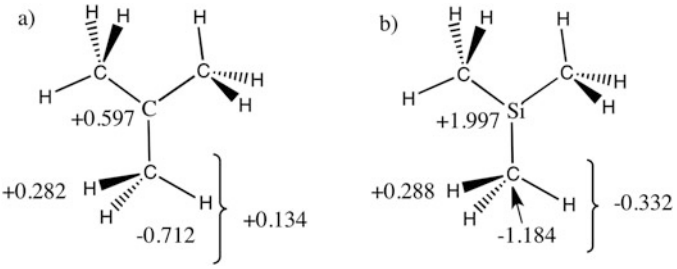

Fig. 11 NBO charge distribution on Me_3C^+ (**a**) and (**b**) Me_3Si^+ (calculated by NBO using B3LYP/cc-pVTZ level)

11 Transforming Covalent Bonds to CSBs by Substitution

We have discussed above the molecule [1.1.1]propellane and its curious inverted C–C bond, which was identified as a CSB, by contrast to the classical covalent wing C–C bonds [11, 58]. This is an interesting finding because it shows that bonds having the same atomic constituents can be either covalent or CSBs, depending on their molecular environment. Understanding the origins of CS bonding in the inverted C–C bond of [1.1.1]propellane is therefore important.

Figure 12 shows that the inverted bond in [1.1.1]propellane is embedded inside a cage of six wing C–C bonds, labeled as σ_w. If we make symmetry-adapted combinations of these six localized bonds, we find that two of the combinations possess the same symmetry as the inverted C–C bond and their electron densities are projected on the inverted bond. One of these is a cage orbital (σ_{cage}), which consists of three lobes pointing from the CH_2 moieties of the propellane to the center of the inverted bond, and the second one is the all-positive combination of the wing orbitals that projects on the axis (σ_{axis}). These two electron pairs repel the covalent structure of the inverted bond, making it repulsive much like in F–F (see above textbox) and eliciting thereby a large RE_{CS}, which makes the inverted bond a CS bond.

Understanding this principle, we can now set out to design a series of C–C bonds, which exhibit an excursion from classical covalent bonds to CS bonds [13]. The molecules are depicted in Scheme 5, and the target bond computed with VB theory is shown in a bold line.

For all these bonds, we computed by means of VB theory the bond energy and the RE_{CS} quantity. For propellanes, one cannot really calculate a bond dissociation energy (BDE), and therefore we calculated for all the molecules the in situ bond energy, $D_{in\text{-}situ}$, which gauges the bond energy of the molecule relative to a reference nonbonded structure, called the quasi-classical (QC) state [72]. The QC state has a single VB determinant where the spins are not allowed to exchange, and hence its energy does not include any bonding term due to spin pairing. To treat all the bonds in Scheme 5 on equal footing, all the bond energies, even for ethane, were calculated as $D_{in\text{-}situ}$. Scheme 6 shows the QC state and the various bond quantities that can be calculated by modern VB theory.

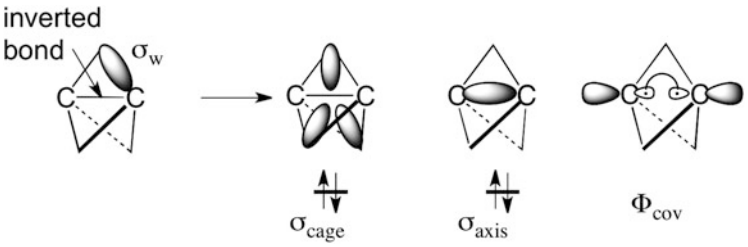

Fig. 12 Covalent bond-weakening repulsion exerted by the wing C–C bonds on the inverted central bond of [1.1.1]propellane [13]

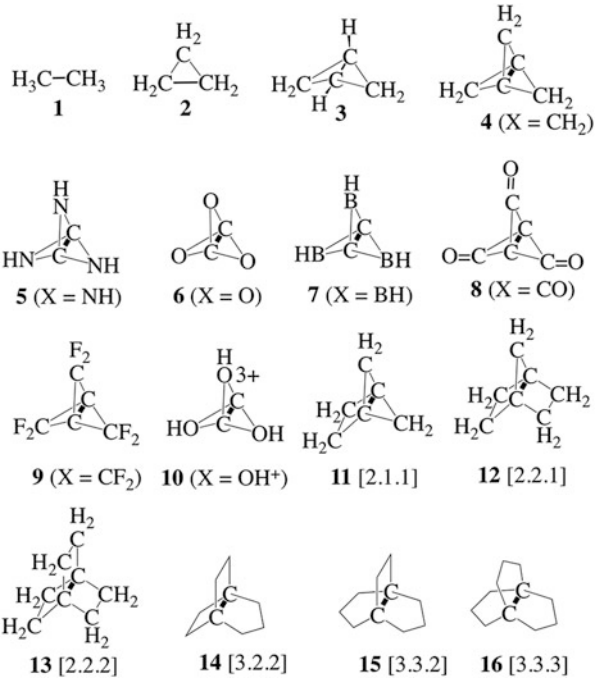

Scheme 5 Target C–C bonds highlighted in *bold* in a series of molecules. The molecules **4**–**10** are labeled by the wing fragment X. Adapted from [13] with permission of Wiley-VCH

Figure 13 shows a plot of the ratio of $RE_{CS}/D_{in\text{-}situ}$ vis-à-vis the Laplacian (L) at the bond critical point of the target bonds in Scheme 5. It is seen that the molecules fall into two families. At the lower left quadrant of the plot, we find the C–C bonds of ethane, propane, and the large [2.2.2]propellane. All these bonds have a low $RE_{CS}/D_{in\text{-}situ}$ ratio and negative L. Thus, in this family, most of the bond energy arises from the covalent spin pairing, and in accord with that, the Laplacian is negative as expected for classical covalent bonds. By contrast, in the upper right quadrant of Fig. 13, we find the inverted C–C bonds of the smaller propellanes and

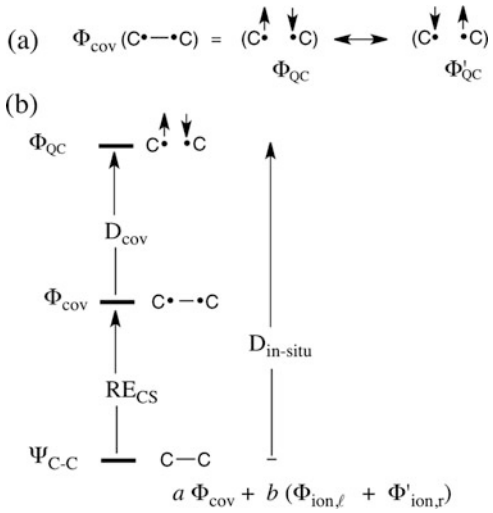

Scheme 6 VB calculations of $D_{\text{in-situ}}$ relative to the QC reference. (**a**) The constitution of the covalent structure. (**b**) The $D_{\text{in-situ}}$ value relative to the QC state. Adapted from [13] with permission of Wiley-VCH

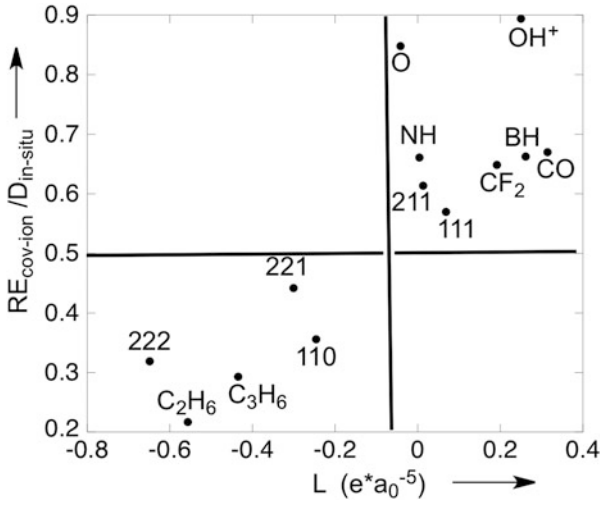

Fig. 13 A two-dimensional plot of $RE_{\text{cov-ion}}/D_{\text{in-situ}}$ (calculated by VB theory) vs. the Laplacian L (calculated by AIM, in atomic units) at the BCP for the target C–C bonds in **1–13** (Scheme 5), with *vertical lines* drawn to emphasize the separation into two families of C–C bonds. The substituted [1.1.1]-X_3-propellanes (**4–10** in Scheme 5) are specified by their wing fragment X (X=CH_2, NH, etc.). Reprinted from Fig. 5 in [13] with permission of Wiley-VCH

the wing substituted ones. All these bonds are typified by a low $RE_{CS}/D_{in\text{-}situ}$ ratio, which means that most of the bonding arises due to charge-shift resonance, and in accordance, the Laplacian is positive, indicating that these bonds suffer from Pauli repulsion pressure. It is conceivable that such two families of the same homopolar bond may exist for other atoms (fragments).

12 Experimental Manifestations of CS Bonding

Having shown the emergence of CS bonding and its promoting factors, here we follow with some evidence for the signature of this bond type in the chemical behavior.

12.1 Evidence for CSB from Electron Density Measurements

The existence of the CS bond family will eventually be consolidated by experimental means. One such technique involves the determination of the Laplacian of various bonds from experimental densities, as already done for propellane [58], N_2O_4 [73], $(Mg–Mg)^{2+}$ cores [74], etc. [56, 57]. Thus, as we already alluded to, for [1.1.1]propellane derivatives [58], the experimental Laplacian clearly shows the existence of a classical covalent C–C bond in the wing positions vis-à-vis a CS C–C bond in the inverted bond region. Such experimental characterization for other bonds will further show the importance of this new bond family.

In the meantime, the existence of two distinct families has already emerged from electron density difference maps (available experimentally), which plot the difference between the actual molecular density and the density of a reference state made from spherical atoms ($\Delta\rho = \rho_{Mol} - \rho_{Ref}$), placed at the same geometry as the molecule. These data [75–78] clearly show a group of bonds (e.g., Li–Li, C–C, Si–Si, C–H) with $\Delta\rho > 0$, which coincides with the classical covalent bond, and a second group (e.g., F–F, Cl–Cl, O–O, S–S, N–N, N–O, C–F, C–O, etc.) of *no-density bonds* with $\Delta\rho \leq 0$, which coincides with the CS bonding family outlined in this chapter. While the deformation density depends on the definition of the reference atomic state [79] (generally, a better reference state can be made from deformed rather than spherical atoms; see, [80]), the example of [1.1.1] propellanes [75–78] is virtually free of this limitation since the $\Delta\rho$ quantity is determined by comparing two different bonds in the same molecule and using the same ρ_{Ref}. The findings clearly show that the C–C bonds in the wings possess $\Delta\rho > 0$, while the "inverted" (C–C) has $\Delta\rho < 0$. Furthermore, these bond types were identified also by the experimental Laplacians, which revealed a fundamental difference between the wing and inverted C–C bonds [58].

12.2 Atom Transfer Reactivity as Means of Experimental Quantification of Charge-Shift Resonance Energies

We would expect to see manifestations of CSB on reactivity for cases that involve cleavage of CS bonds. Our studies [81] showed that one of these manifestations is the computational [82–86] and experimental [87] results that halogen transfer reactions (and especially of fluorine), Eq. (13a), have much larger barriers (by >20 kcal/mol for X=F) than the corresponding hydrogen transfer processes, Eq. (13b):

$$\mathrm{H}\bullet + \mathrm{X} - \mathrm{H}' \rightarrow \mathrm{H} - \mathrm{X} + \bullet\mathrm{H}', \tag{13a}$$

$$\mathrm{X}\bullet + \mathrm{H} - \mathrm{X}' \rightarrow \mathrm{X} - \mathrm{H} + \bullet\mathrm{X}'. \tag{13b}$$

Thus, as we demonstrated recently by means of VB calculations [81], the two processes have almost identical barriers for the covalent structures, but they differ in the status of the ionic VB structures near the transition state. In reaction (13a), the key combination of ionic structures, H• $\mathrm{X}:^-$ H^+ and H^+ $\mathrm{X}:^-$ •H, is destabilized by two repulsive 3-electron interactions [18, 69, 88] between H• and the X^- fragment (Scheme 7a). By contrast, the ionic combination $\mathrm{X}:^-$ H^+ •X and X• H^+ $\mathrm{X}:^-$, for (13b), is devoid of repulsive interactions (Scheme 7b vs. a). The destabilization of the ionic structures during X transfer results in a loss of RE_{CS} in the respective transition state. Since the H–X bonds, and especially so H–F, have large RE_{CS} to begin with, the loss is significant and the barrier is higher for the X transfer reaction. The largest destabilization occurs for X=F, since H–F has the largest RE_{CS} quantity among the hydrogen halides.

Interestingly, the barrier difference between the two series was found [81] to follow a very simple relationship, as ¼ of the RE_{CS} quantity of the H–X bond that undergoes cleavage during the two processes. Therefore, RE_{CS} is given as:

$$RE_{\mathrm{CS(H-X)}} \approx 4\left[\Delta E^{\ddagger}_{\mathrm{H/XH}} - \Delta E^{\ddagger}_{\mathrm{X/HX}}\right] \tag{14}$$

As such, measurement of the barrier difference for the two series enables to quantify the CS-resonance energy from experimental barriers.

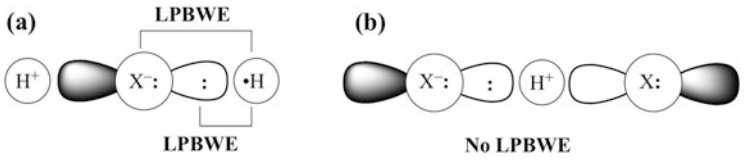

Scheme 7 Lone-pair bond-weakening effect (LPBWE) in the ionic structure for halogen (X) transfer reactions in (**a**) and the lack of LPBWE in the ionic structure of H transfer reactions in (**b**). Adapted from [9] with permission of Wiley-VCH

12.3 Mechanistic Impacts of CSB in the Ionic Chemistry of Silicon in Condensed Phases

A large CS-resonance energy typifies also bonds with a high static ionicity, like H–F, C–F, Si–F, Si–Cl, Ge–Cl, etc. (Table 1). This arises due to a combination of effects, one being the atomic shrinkage and LPBWE of the lone-pair-bearing heteroatom and the second being the strong covalent–ionic interaction due to the decreased energy gap between the two structures [6, 12]. As we mentioned above (Fig. 11), in the case of Si–X bonds, the ionic VB structure is highly stabilized because of the concentration of the positive charge on the silicon atom. This leads to some *unusual features of the ionic structure* as seen in Fig. 14, which compares the location of the energy minima for the ionic and covalent curves for H_3Si–Cl vs. H_3C–Cl [5, 6]. Thus, the concentration of the positive charge on Si shrinks the ionic radius of H_3Si^+ compared with H_3C^+ and causes thereby much stronger electrostatic interactions in the ionic structure $H_3Si^+Cl^-$ compared with $H_3C^+Cl^-$. *The result is that the minimum of the ionic curve becomes very deep for $H_3Si^+Cl^-$ and it coincides with the minimum of the covalent structure*, leading thereby to a strong covalent–ionic mixing and large RE_{CS} compared with the carbon analog (see Table 1). The same situation carries over to any R_3Si–Cl vs. R_3C–Cl, R=alkyl, etc. [6]. In a condensed phase, the ionic structure is stabilized by the environment, but since the Si^+Cl^- minimum is so tight, the further stabilization by the solvent will be only moderate, and hence, the ionic curve should remain close to the covalent curve, thereby retaining the large RE_{CS} interaction of the bond. Thus, in a condensed phase, the covalent–ionic mixing remains large giving rise to Si–X bonds that stay intact due to the large CS-resonance energy.

Indeed, as discussed above, our recent VB study showed [71] that the $Me_3Si^+Cl^-$ structure in aqueous solution retains the tight ion-pair minimum and thus mixes strongly with the covalent structure and acquires large RE_{CS}. This large RE_{CS} is the major reason why the bond will not undergo heterolysis in solution (but will prefer associative processes) and why in the solid state even Ph_3Si–$OClO_3$ is a covalent solid [46] by contrast to the carbon analog, which has an Na^+Cl^- type lattice with Ph_3C^+ and ClO_4^- ions [42], etc. [40–48].

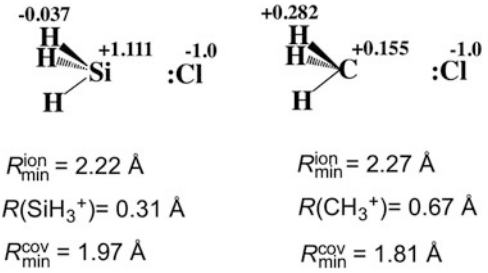

Fig. 14 Charge distribution and geometric parameters of the ionic structures $H_3C^+Cl^-$ and $H_3Si^+Cl^-$, calculated by VB theory. Reproduced from [9] with permission of Wiley-VCH

13 CSB and Electron-Rich Hypervalent Molecules

13.1 Hypervalency of Noble Gas and Isoelectronic Groups

Xenon and heavier noble gas, as well as sulfur, phosphorus, and chlorine atoms and elements residing below them in the periodic table, have a propensity to seemingly form more bonds than allowed by the traditional Lewis–Langmuir valence rules (e.g., XeF_2, $XeCl_2$, KrF_2, RnF_2, ClF_3, SF_4, PCl_5, and so on), a property referred to as hypervalency. By contrast, lighter elements of the family (e.g., ArF_2, NF_5, OF_4, FF_3) obey the octet rule, showing what has been called the "first-row anomaly." Hypervalency in such electron-rich complexes is generally understood in terms of the 3-center/4-electron (3c/4e) Rundle–Pimentel model [89, 90], which has replaced the old octet-expansion model of Pauling. However, the Rundle–Pimentel model is not always predictive; e.g., it cannot account for "the first-row anomaly" or the instability of H_3^- which contrasts with the stability of F_3^-, or of PH_5 vs. PCl_5, and so on.

Taking XeF_2 as a prototype for 3c/4e systems, Coulson has reexpressed the Rundle–Pimentel model in VB terms by projecting the simple MO wave function on a basis of VB structures [91], thus getting Eq. (15) below:

$$\begin{aligned}\Psi(XeF_2) = {} & F\bullet - \bullet Xe^+F^- - F^-Xe^+ \bullet - \bullet F + F^-Xe^{2+}F^- \\ & + \tfrac{1}{2}\left[F^-XeF^+ + F^+XeF^- + \sqrt{2}\bullet FXeF\bullet\right]\end{aligned} \tag{15}$$

Equation (15) is a good starting point for a VB treatment of hypervalency. Recently, two of us (BB and PCH) used VB computations and showed that the large atomization energy of XeF_2 (ca. 64 kcal/mol) cannot arise from the bonding energies of any of the individual VB structures of Eq. (15), which are all largely unbound relative to Xe+2F•. Instead, the stability of XeF_2 arises solely from the exceptionally large resonance energy due to the VB mixing of the structures [92], in accord with qualitative predictions that hypervalent compounds should be CSB bound [93].

Actually, the VB calculation [92] showed that a strong CSB character is already present in the normal-valent F–Xe^+ species, in which the RE_{CS} value, arising from the mixing of the F^+–Xe and F:$^-$ Xe^{2+} forms into the purely covalent F•–•Xe^+ form, is as large as 69.7 kcal mol^{-1}! In the XeF_2 complex itself, the stabilization due to the mixing of F•–•Xe^+ :F^- and F:$^-$ Xe^+•–•F is also very large, 82.9 kcal mol^{-1}, and another 70.1 kcal mol^{-1} is further gained by adding the remaining VB structures of Eq. (15), among which F:$^-$ Xe^{2+} :F^- is the most important one. Analogous results were found for other typical hypervalent molecules, SF_4, PF_5, and ClF_3, isoelectronic to XeF_2, in subsequent VB calculations [94]. As in the XeF_2 case, the VB structure in which the central atom is doubly ionized was found to be important in all cases. Thus, the model predicts that hypervalency manifests when the central atom (e.g., Xe) has a sufficiently low first ionization potential, as well as a low *second* ionization potential, and is bonded to electronegative ligands. Adherence or lack of it to these conditions accounts for the stabilities/instabilities of many 3c/4e systems.

Table 3 Ionization potentials of the central atom of some hypercoordinated species and their dissociation energies to normal-valent species +2 F. All energies in kcal mol^{-1}

Central atom A	1st IP of A[a]	2nd IP of A[a]	Dissociation energy (kcal mol^{-1})
P	10.5	19.7	$PF_5 \rightarrow PF_3 + 2F$ $\Delta E = 187.1$[a]
S	10.4	23.3	$SF_4 \rightarrow SF_2 + 2F$ $\Delta E = 150.7$[b]
Cl	13.0	23.8	$ClF_3 \rightarrow ClF + 2F$ $\Delta E = 60.2$[c]
Xe	12.1	21.2	$XeF_2 \rightarrow Xe + 2F$ $\Delta E = 64.1$[d]
Kr	14.0	24.4	$KrF_2 \rightarrow Kr + 2F$ $\Delta E = 23.1$[e]
Ar	15.8	27.6	ArF_2 unstable
N	14.5	29.6	NF_5 unstable
O	13.6	35.1	OF_4 unstable
F	17.4	35.0	F_4 unstable
Ne	21.6	41.0	NeF_2 unstable

[a]Woon and Dunning [95]
[b]Woon and Dunning [96]
[c]Chen et al. [97]
[d]Pepkin et al. [98]
[e]Bartlett and Sladky [99]

As an illustration of this point, Table 3 reports the first and second ionization potentials (IPs) for the central atom of some selected neutral hypercoordinated species of the type AF_n, together with the stability of these species with respect to dissociation of the hypervalent bonds. It can be seen that even if the first IP is an important parameter for the stability of AF_n, the second IP is at least as much important and indeed marks the limit between stable and unstable systems and in particular the first-row systems (NF_5, OF_4, F_4, NeF_2). The reason for the "first-row exception" is therefore quite clear within the present VB model.

Thus, the general model for hypervalency in electron-rich systems appears to be the VB version of the Rundle–Pimentel model, *coupled with the presence of* a *CSB feature*. This latter feature imposes the conditions for manifestation of hypervalency: (1) low first and second ionization potentials for the central atom and (2) ligands that are prone to CSB in their normal-valent states (i.e., being electronegative and bearing lone pairs like F, O, etc.). Lack of any of these features explains the many exceptions to the traditional MO-based Rundle–Pimentel model, like the instability of first-row 3c/4e systems, as well as that of ArF_2, H_3^-, and so on.

13.2 Pentacoordinated Silicon Compounds and Low-Barrier Hydrogen Bonds

Hypervalency is generally driven by CSB, and hence any species which maintains large covalent–ionic resonance energy, RE_{CS}, in a hypercoordinated geometry will exhibit hypervalency and give rise to a stable hypervalent species. Silicon is well known for its high propensity to form hypervalent compounds [100–102]; even SiH_5^- is a stable hypercoordinated species of D_{3h} symmetry [101, 102]. Similarly,

even hydrogen exhibits hypervalency in $(FHF)^-$, which belongs to the class known as "low-barrier hydrogen bonds" [103]. The root cause of the stability of these hypervalent species is the small size of the cationic state of the central atom, e.g., the silicenium cation, X_3Si^+ (see Fig. 14), and the proton, H^+. Owing to this small size, the triple-ion structure has a tight geometry with short distances, and it lies low in energy; hence, it mixes substantially with the corresponding covalent structures to create a charge-shift bonded hypervalent species. Thus, the triple ionic structure, $F^-\ H^+\ F^-$, mixes very strongly with the corresponding covalent structures, F•-•H : F^- and $F:^-$ H•-•F, and creates thereby a stable CSB $(FHF)^-$ species [103]. Similarly, the strong mixing of X^- (X_3Si^+) ^-X with the corresponding covalent structures creates a stable CSB $(SiX_5)^-$ species [103].

14 Scope and Territory of CS Bonding and Concluding Remarks

The territory of CSB for electron-pair bonding is in fact larger than we described above. In the area of electron-pair bonds, we should mention the recent VB study [104] by Galbraith who showed that coordinative (dative) bonding such as the one between tetravalent boron and amines, $R_3B–NR'_3$, is dominated by CS-resonance energy. Similarly, Coote et al. [105] found that the dependence of the relative bond strengths of R–X bonds (R=Me, Et, *iso*-Pr, *tert*-Bu; X=H, F, OH, OCH_3) follows the CS-resonance energy. Very recently, Ess et al. [15] have found that protonation of alcohols in water converts the C–O bond into a complete CSB, i.e., without RE_{CS} these bonds would immediately dissociate. A recent study of M–H bonds, where M is a first-row transition metal [106], showed that the CS-resonance energy is quite significant. In the same M–H series, RE_{CS} was found to increase from left to right in the period and to be affected by the presence of the $2s^22p^6$ core electron pairs, which behave as lone pairs on the transition metal. Based on the factors that contribute to the propensity of atoms (fragments) to generate CSB, we may expect bonds of first-row transition metals to be CSBs, especially when the bonding partner is an electronegative and/or lone-pair-rich atom. More such CSBs should be looked for among the bonds between the heavier elements of the periodic table.

We did not discuss in this manuscript odd-electron bonds [107]. In odd-electron bonds like in F_2^- or He_2^+, H_2^+, etc., the entire bonding arises from the charge-shift resonance energy due to the mixing of the odd-electron structures, as depicted in Scheme 8, for an archetypical odd-electron bond. Thus, for example, the 3-electron structures of F_2^- are by themselves repulsive partly because of the 3-electron repulsion between the two F moieties [108, 109] and in part because of the Pauli

$$F:^- \cdot F \longleftrightarrow F\cdot\ :F^- \qquad D_e = 30\ \text{kcal/mol}$$

Scheme 8 The resonance of the two 3-electron VB structures that constitute F_2^- and its bond dissociation energy (a CCSD(T)/aug-cc-pV5Z datum)

repulsion from the σ-lone pairs. Nevertheless, F_2^- is significantly bonded by ca. 30.0 kcal mol^{-1}, which arises due to a large RE_{CS} quantity that overcomes the repulsive interaction in the individual VB structures.

Future directions for articulating this bonding motif are many. A fruitful direction is hypercoordination (see above) and aggregation. Thus, for example, the small size of R_3Si^+ and heavier analogs mean that they will tend to form hypercoordinated compounds in solution, in the solid state [100], and even in the gas phase, where some unusual molecules have been reported [101, 110]. Silicon will also exhibit hypercoordination in bridged delocalized electron-pair systems, $(Si–X–Si)^+$, which participate in catalytic bond exchange reactions [111, 112]. Metal–metal bonds in some bimetallic complexes could well be CS bonds, as in M_2(formamidinate)$_4$ complexes (M=Nb, Mo, Tc, Ru, Rh, Pd) where large positive values of $\nabla^2\rho(\mathbf{r}_c)$ have been reported [113]. Other directions involve the generation of [1.1.1] propellane in which the CH_2 wings are substituted by heteroatoms that exert exchange repulsion pressure on the inverted C–C bond, e.g., HN, etc. [13]. The in-plane π-type bond in *ortho*-benzyne is another bond that suffers from exchange repulsion pressure. Protonation or methylation (by Me^+) of C–N bonds may convert them into CSBs[5], a fact that may concern DNA bases, and may have mechanistic effects, as in the protonated arginine in the mechanism of nitric oxide synthase [114]. Bonds under immense external pressure [115] are likely to be CSBs, and encapsulated highly positive ions may well be CS bound [116], etc. A growing territory lies ahead for exploration.

In conclusion, CSB originates from the equilibrium condition of the bond, defined by the virial ratio. It is promoted by two main factors:

(a) By Pauli repulsion that weakens the covalency of the bond and induces large covalent–ionic resonance energies (RE_{CS}). This excessive exchange repulsion is typical to electronegative and lone-pair-rich atoms or bonds weakened by exchange repulsion pressure, as the bridgehead C–C bond in [1,1,1]propellane and other small-ring propellanes.

(b) Fragments that form extremely small cations, which resemble a proton, with all the positive charge located at the central atom, like in silicenium cation, R_3Si^+ will promote CS bonding and hypercoordination, especially with electronegative and lone-pair-rich atoms.

With these promoters, CSB forms a distinct group of bonding that transcends consideration of static charge distribution and that possesses unique chemical signatures. Thus, CSB is not merely an academic abstraction. As new examples or experimental manifestations of CSB will start to accumulate and be recognized, the concept of CSB will gradually find more articulations [117] and ultimately be accepted by the chemical community.

Dedication The paper is dedicated to Walter Thiel, a mensch and a fellow scientist, for his 65th birthday.

[5] For a discussion of the N–CH_3 bond energy change due to methyl cation attachment to the nitrogen atom, see [93].

References

1. Shaik S (2007) J Comput Chem 28:51
2. Shaik S, Hiberty PC (2008) A chemist's guide to valence bond theory. Wiley, Hoboken, pp 1–25
3. Sini G, Maitre P, Hiberty PC, Shaik SS (1991) J Mol Struct (THEOCHEM) 229:163
4. Shaik S, Maitre P, Sini G, Hiberty PC (1992) J Am Chem Soc 114:7861
5. Lauvergnat DL, Hiberty PC, Danovich D, Shaik S (1996) J Phys Chem 100:5715
6. Shurki A, Hiberty PC, Shaik S (1999) J Am Chem Soc 121:822
7. Galbraith JM, Blank E, Shaik S, Hiberty PC (2000) Chem Eur J 6:2425
8. Lauvergnat D, Hiberty PC (1995) J Mol Struct (THEOCHEM) 338:283
9. Shaik S, Danovich D, Silvi B, Lauvergnat D, Hiberty PC (2005) Chem Eur J 11:6358
10. Zhang L, Ying F, Wu W, Hiberty PC, Shaik S (2009) Chem Eur J 15:2979
11. Wu W, Gu J, Song J, Shaik S, Hiberty PC (2009) Angew Chem Int Ed 48:1407
12. Shaik S, Danovich D, Wu W, Hiberty PC (2009) Nat Chem 1:443
13. Shaik S, Chen Z, Wu W, Stanger A, Danovich D, Hiberty PC (2009) ChemPhysChem 10:2658
14. Zhang H, Danovich D, Wu W, Braida B, Hiberty PC, Shaik S (2014) J Chem Theory Comput 10:2410
15. Anderson P, Petit A, Ho J, Mitoraj MP, Coote ML, Danovich D, Shaik S, Braïda B, Ess DH (2014) J Org Chem 79:9998
16. Silvi B, Savin A (1994) Nature 371:683
17. Bader RFW (1990) Atoms in molecules: a quantum theory. Oxford University Press, Oxford
18. Shaik S, Hiberty PC (2008) A chemist's guide to valence bond theory. Wiley, Hoboken, ch. 3, 9, 10
19. Wu W, Su P, Shaik S, Hiberty PC (2011) Chem Rev 111:7557
20. Lewis GN (1916) J Am Chem Soc 38:762
21. Langmuir I (1919) J Am Chem Soc 41:868
22. Jensen WB (1984) J Chem Educ 61:191
23. Heitler W, London F (1927) Z Phys 44: 455–472, English Translation Hettema H (2000) Quantum chemistry classic scientific paper. World Scientific, Singapore, pp 140–155
24. London F (1928) Z Phys 46:455
25. Pauling L (1939) The nature of the chemical bond. Cornell University Press, Ithaca (3rd Edition, 1960)
26. Slater JC (1965) J Chem Phys 43:S11
27. van Vleck JH, Sherman A (1935) Rev Mod Phys 7:167
28. Calvin M (1984) J Chem Educ 61:14
29. Saltzman MD (1996) Bull Hist Chem 19:25
30. Gavroglu K, Simoes A (1994) Stud Biol Phys Sci 25:47
31. Sanderson RT (1983) Polar covalence. Academic, New York
32. Edmiston C, Ruedenberg K (1963) Rev Mod Phys 35:457
33. Rutledge RM, Saturno AF (1965) J Chem Phys 43:597
34. Boys SF (1960) Rev Mod Phys 32:296
35. Foster JM, Boys SF (1960) Rev Mod Phys 32:300
36. Weinhold F, Landis CR (2005) Valency and bonding: a natural bond orbital donor-acceptor perspective. Cambridge Univeristy Press, Cambridge
37. Weinhold F, Landis CR (2012) Discovering chemistry with natural bond orbitals. Wiley, Hoboken
38. Bader RFW, Nguyen-Dang TT (1981) Adv Quantum Chem 14:63
39. Henn J, Ilge D, Leusser D, Stalke D, Engles D (2004) J Phys Chem A 108:9442
40. Apeloig Y (1989) In: Apeloig Y, Rappoport Z (eds) The chemistry of organic silicon compounds, vol 1. Wiley, Chichester, ch. 2
41. Laube T (1995) Acc Chem Res 28:399

42. Prakash GKS, Keyaniyan S, Aniszfeld SKR, Heiliger L, Olah GA, Stevens RC, Choi H-K, Bau R (1987) J Am Chem Soc 109:5123
43. Kato T, Reed A (2004) Angew Chem Int Ed 43:2908
44. Apeloig Y, Stanger A (1987) J Am Chem Soc 109:272
45. Lambert JB, Kania L, Zhang S (1995) Chem Rev 95:1191
46. Gomes de Mesquita AH, MacGillavry CH, Eriks K (1965) Acta Crystallogr 18:437
47. Lambert JB, Zhao Y (1997) Angew Chem Int Ed Engl 36:400
48. Kim K-C, Reed CA, Elliott DW, Mueller LJ, Tham F, Lin L, Lambert JB (2002) Science 297:825
49. Cremer D, Kraka E (1984) Angew Chem Int Ed Engl 23:627
50. Low AA, Hall MB (1990) In: Maksic ZB (ed) Theoretical models of chemical bonding. Springer, New York, pp 544–591, part 2
51. Schwarz WHE, Valtazanos P, Ruedenberg K (1985) Theor Chim Acta 68:471
52. Lusar R, Beltrán A, Andrés J, Noury S, Silvi B (1999) J Comput Chem 20:1517
53. Silvi B (2003) J Phys Chem A 107:3081
54. Rincon L, Almeida R (1998) J Phys Chem A 102:9244
55. Kraka E, Cremer D (1990) In: Maksic ZB (ed) Theoretical models of chemical bonding. Springer, New York, pp 457–543, part 2
56. Coppens P (2005) Angew Chem Int Ed 44:6810
57. Coppens P (1997) X-ray densities and chemical bonding. Oxford University Press, New York
58. Messershmidt M, Scheins S, Grubert L, Patzel M, Szeimies G, Paulmann C, Luger P (2005) Angew Chem Int Ed 44:3925
59. Polo V, Andres J, Silvi B (2007) J Comput Chem 28:857
60. Maynau D, Malrieu J-P (1998) J Chem Phys 88:3163
61. Hiberty PC, Ramozzi R, Song L, Wu W, Shaik S (2006) Faraday Discuss 135:261
62. Kutzelnigg W (1990) In: Maksic ZB (ed) Theoretical models of chemical bonding. Springer, New York, pp 1–44, part 2
63. Ruedenberg K (1962) Rev Mod Phys 34:326
64. Feinberg MJ, Ruedenberg K (1971) J Chem Phys 54:1495
65. Wilson CQ, Goddard WA III (1972) Theor Chim Acta 26:195
66. Rozendaal A, Baerends EJ (1985) Chem Phys 95:57
67. Ruedenberg K, Schmidt M (2007) J Comput Chem 28:391
68. Bickelhaupt FM, Baerends EJ (2000) Rev Comput Chem 15:1
69. Shaik SS (1989) In: Bertran J, Csizmadia GI (eds) New theoretical concepts for understanding organic reactions, vol C267, NATO ASI series. Kluwer, Dordrecht, pp 165–217
70. Ploshnik E, Danovich D, Hiberty PC, Shaik S (2001) J Chem Theory Comput 7:955
71. Su P, Song L, Wu W, Shaik S, Hiberty PC (2008) J Phys Chem A 112:2988
72. Hiberty PC, Danovich D, Shurki A, Shaik S (1995) J Am Chem Soc 117:7760
73. Messerschmidt M, Wagner A, Wong MW, Luger P (2002) J Am Chem Soc 124:732
74. Platts JA, Overgaard J, Jones C, Iversen BB, Stasch A (2011) J Phys Chem A 115:194
75. Dunitz JD, Seiler P (1983) J Am Chem Soc 105:7056
76. Dunitz JD, Schweizer WB, Seiler P (1983) Helv Chim Acta 66:123
77. Coppens P, Yang YW, Blessing RH, Cooper WF, Larsen FK (1977) J Am Chem Soc 99:760
78. Savariault J-M, Lehmann MS (1980) J Am Chem Soc 102:1298
79. Ruedenberg K, Schwarz WHE (1990) J Chem Phys 92:4956
80. Schwarz WHE, Ruedenberg K, Mensching L (1989) J Am Chem Soc 111:6926
81. Hiberty PC, Megret C, Song L, Wu W, Shaik S (2006) J Am Chem Soc 128:2836
82. O'Neal SV, Schaefer HF III, Bender CF (1974) Proc Natl Acad Sci U S A 71:104
83. Dunning TH Jr (1984) J Phys Chem 88:2469
84. Bender CF, Garrison BJ, Schaefer HF III (1975) J Chem Phys 62:1188
85. Voter AF, Goddard WA III (1981) J Chem Phys 75:3638
86. Dobbs KD, Dixon CA (1993) J Phys Chem 97:2085
87. Bartoszek FE, Manos DM, Polanyi JC (1978) J Chem Phys 69:933

88. Shaik S, Hiberty PC (2004) Rev Comput Chem 20:1
89. Hach RJ, Rundle RE (1951) J Am Chem Soc 73:4321
90. Pimentel GC (1951) J Chem Phys 19:446
91. Coulson CA (1964) J Chem Soc 1442
92. Braida B, Hiberty PC (2013) Nat Chem 5:417
93. Shaik SS (1991) In: Maksic ZB, Maksic ME (eds) An encomium to Linus Pauling. Molecules in natural science and medicine. Ellis Horwood, London
94. Braida B, Ribeyre T, Hiberty PC (2014) Chem Eur J 20:9643
95. Woon DE, Dunning TH Jr (2010) J Phys Chem A 114:8845
96. Woon DE, Dunning TH Jr (2009) J Phys Chem A 113:7915
97. Chen L, Woon DE, Dunning TH Jr (2009) J Phys Chem A 113:12645
98. Pepkin VI, Lebedev YA, Apin AY (1969) Zh Fiz Khim 43:869
99. Bartlett N, Sladky FO (1973) In: Blair JC, Emeleus HJ (eds) Comprehensive inorganic chemistry, vol 1. Pergamon, Oxford, Chapter 6
100. Kost D, Kalikhman I (2009) Acc Chem Res 42:303
101. Hajdasz DJ, Squires RR (1986) J Am Chem Soc 108:3139
102. Sini G, Ohanessian G, Hiberty PC, Shaik SS (1990) J Am Chem Soc 112:1407
103. Shaik S, Shurki A (1999) Angew Chem Int Ed 38:586
104. Fiorillo AA, Galbraith JM (2004) J Phys Chem A 108:5126
105. Coote ML, Pross A, Radom L (2003) Org Lett 5:4689
106. Galbraith JM, Shurki A, Shaik S (2000) J Phys Chem 104:1262
107. Hiberty PC, Humbel S, Danovich D, Shaik S (1995) J Am Chem Soc 117:9003
108. Hiberty PC, Humbel S, Archirel P (1994) J Phys Chem 98:11697
109. Wu W, Shaik S (1999) Chem Phys Lett 301:37
110. Dávalos JZ, Herrero R, Abboud J-LM, Mó O, Yáñez M (2007) Angew Chem Int Ed 46:381
111. Panisch R, Bolte M, Müller T (2006) J Am Chem Soc 128:9676
112. Lühmann N, Panisch R, Hirao H, Shaik S, Müller T (2011) Organometallics 30:4087
113. Llusar R, Beltran A, Andrés J, Fuster F, Silvi B (2001) J Phys Chem A 105:9460
114. Cho KB, Carvajal MA, Shaik S (2009) J Phys Chem B 113:336
115. Grochala W, Hoffmann R, Feng J, Ashcroft NW (2007) Angew Chem Int Ed 46:3620
116. Dognon J-P, Clavaguéra C, Pyykkö P (2009) J Am Chem Soc 131:238
117. Rupar P, Straoverov VN, Baines KM (2008) Science 322:1360

Struct Bond (2016) 170: 213–248
DOI: 10.1007/430_2015_185

Published online: 3 October 2015

The Relevance of the *ELF* Topological Approach to the Lewis, Kossel, and Langmuir Bond Model

Bernard Silvi

Abstract The electron localization function (*ELF*) approach to chemical bonding is revisited as a tool to check the falsifiability of the Lewis hypotheses. It is shown that the boundaries of the *ELF* basins correspond to zero-flux surfaces of the local integrated same spin pair probability enabling the determination of regions of the molecular space which maximizes the opposite spin pair density and therefore groups of electrons. The *ELF* yields a partition into core and valence basins which matches the Lewis model. The valence basins which correspond either to electron lone pairs or to bonds enable the definition of atomic valence shells in which bonding basins are shared by at least two atomic valence shells. The *ELF* basin populations take into account the mesomery which explains the deviations from ideal values. The organization of the basins around the atomic cores often complies with the VSEPR rules. The behavior of the *ELF* basins upon deformation of the nuclear frame sheds light onto the reactivity and reaction mechanisms, whereas the basin compressibilities provide chemical explanations of pressure-induced phase transitions.

Keywords Chemical bond • Electron localization function • Lewis theory • Reaction mechanisms • VSEPR

Contents

B. Silvi (✉)
Laboratoire de Chimie Théorique, Sorbonne Universités, UPMC, Univ Paris 06, UMR 7616, Case Courrier 137, 4 Place Jussieu, 75005 Paris, France
e-mail: silvi@lct.jussieu.fr

1 The Interpretation of Footprints Yields to Understand the Matter

We have known for more than a century that the matter is an assembly of interacting particles which cannot be described by classical physics. Each particle is a quantum object which "is intuitively given to an observer only by the actual isolated footprints it leaves in the perceptual world of the laboratory, the record of individual measurements" [1]. The description of the matter at the atomic scale and the understanding of its properties, which is one of the aims of chemistry, therefore require the identification of footprints and their interpretation. Cultural background is decisive to carry out this task successfully as it has been illustrated by a recent archaeological study in which a morpho-classificatory approach has been used to decipher human footprints from the Ice Age of 17,000 years ago preserved in painted caves of the south of France [2]. The footprints have been examined and interpreted by three indigeneous hunters/trackers from Kalahari who discovered marks unseen in previous archaeological investigations and who were able to determine the number of the prehistoric cave visitors, the sex of each individual, and an estimate of his age. Moreover, they proposed very plausible hypothesis on the activity at the origin of the footprints differing from former interpretations made by archaeologists in terms of "ritual dances" or ceremonial behavior. The footprints of the corpuscular structure of the matter have been found in the results of the early analytical chemistry which led to the formulation of the laws of conservation of mass, of definite proportions, and of multiple proportions. This latter involving integers or rational numbers is a strong support for the atomistic (discontinuous) theory which has been reformulated by John Dalton on this indirect experimental basis. Dalton explained the cohesion of the matter by the presence of caloric forces between bonded atoms [3]. It rapidly appeared to Berzélius that electric rather than caloric forces were accountable for the bonding [4]; this idea was further reformulated by Laming [5] in a fully atomistic fashion accounting for Faraday's electrochemical equivalent. Laming's hypotheses anticipate the atomic electronic shell structure introduced in the years preceding World War I by Charles G. Barkla and Henry G. J. Moseley and half a century before Joseph John Thomson's discovery of the electron:

> a mass of electrical matter, or electricity, may be regarded as composed of electrical atoms, just as a mass of ordinary matter contains ordinary atoms; and thus the sphere of electricity which surrounds an ordinary atom will consist of a number of electrical atoms arranged in concentric strata. The number of electrical atoms belonging to a given ordinary atom may be assumed to be such as to complete its external spherical stratum, or, on the contrary, it may be such as to leave that external spherical stratum more or less imperfect.

The atom of electricity was further called "electron" by G. J. Stoney who proposed an estimate of its charge (1.0×10^{-19} C.) on the basis of the electrolysis of water [6]. The footprints related to stoichiometry are at the origin of the concept of valence introduced by Frankland and Kolbe. This concept which rationalizes the coordination of atoms has been an important step ahead in the development of structural chemistry and an essential classification criterion for the elaboration of the periodic table.

A few years after Thomson's discovery of the electron, G. N. Lewis proposed in a memorandum dated March 28, 1902 [7], drawings representing a cubic atomic model in which the vertices are occupied or not by electrons according to the column of the element in the periodic table. In this way, he established a direct link between electrons and the valence concept. Lewis's early atomic model which has been conceived on the only basis of chemical arguments is closer to nowadays representations than Thomson's 1904 plum-pudding model [8]. After the discovery of the nucleus [9] and the introduction of the atomic number with Moseley's law, all the pieces of the puzzle but one, the spin of the electron, were available when Lewis published *The Atom and the Molecule* [7]. In this article, Lewis propose an atomic model based on six postulates which accounts for the formation of covalent bond. The stoichiometry of a large majority of molecules implies that the number of their valence electrons is even. This fact is one of the footprints of the electron spin which has been used by Lewis to introduce the concept of electron pair which is the cornerstone of his theory. The Lewis atom in molecule is composed of a kernel grouping the nucleus and the inner shell electrons and an outer shell, the valence shell. The atom tends to have an even number of electrons in its valence shell and especially eight electrons in order to fulfill Abegg's valence and countervalence law [10]. The shells of two bonded atoms mutually interpenetrate to form covalent bonds, and therefore electrons may belong to the valence shells of two bonded atoms. The same year Walther Kossel proposed an atomic model in order to explain the formation of ionic bonding [11], whereas Irving Langmuir presented a model close to Lewis's one based on 11 postulates in which he introduced energetic considerations [12] and emphasized the importance of the octet rule [13]. In spite of its simplicity, Lewis's approach is remarkably efficient and remains fundamental for basic chemical education.

Although Lewis's model explains the structure of a majority of molecular species, it fails, for example, to account for the hexagonal structure of benzene or for the paramagnetism of dioxygen. The attempts of Huggins to understand benzene by a single Lewis structure yielded chimerical representations [14], whereas the concept of mesomery, pioneered by Ingold [15, 16], which considers a weighted superposition of structures has been very successful with this respect and therefore

constitutes an important complement to Lewis's model. In order to be able to treat dioxygen, Linnett modified the original Lewis model by splitting the initial octet into two sets of four electrons, one having one spin quantum number and the other the opposite spin [17, 18].

The spatial extension of the bonding and nonbonding pairs has been accounted for by the model of Sidgwick and Powell [19] in which both shared and unshared groups have the same size which is uniquely determined by the type of considered spatial arrangement. Gillespie and Nyholm have substantially improved this model [20] explaining the arrangement of the pairs around of a given center as due to the exclusion principle. The repulsion depends on the type of pairs considered, for example, a lone pair is more repulsive than a bond, and on the electronegativity of the ligands. In the earliest version of the valence shell electron pair repulsion (VSEPR) model [21], the valence pairs are considered as points on a sphere in which the arrangement is found by maximizing the least distance between any pair of points. The points on a sphere were replaced in a first time by tangent spherical electronic domains attracted by the central positive core and further by ellipsoid, "pear"- and "egg"-shaped domains of different sizes [22]. Electron pair domains are defined as a charge cloud which occupies a given region of space and excludes other pairs from this region as a consequence of the Pauli exclusion principles. This electron pair domain version of VSEPR emphasizes the shape and size of the domains rather than the magnitude of their mutual repulsion. In addition to bond and lone pair domains, Gillespie considers single electron domains which are expected to be smaller than an electron pair domain [23]. The VSEPR model is very successful in predicting qualitatively the shape of molecules. It enables to understand many features of the molecular geometry in a qualitative fashion.

2 Electronic Domains in Quantum Mechanics

For almost a century, quantum mechanics has been the physical theory which describes the interaction between particles, such as electrons and nuclei in molecules, and therefore enables the quantitative exact predictions of observables. The reduction of chemistry to physics corresponds to the mechanistic working program of P. A. M. Dirac [24]:

> The underlying physical laws necessary for the mathematical theory of a large part of physics and the whole of chemistry are thus completely known, and the difficulty is only that the exact application of these laws leads to equations much too complicated to be soluble.

Although the predictive power of quantum mechanics is unquestionable, its ability to provide explanations has been questioned from an epistemological point of view by R. Thom [25]. As neither atoms in molecules nor bonding and nonbonding pairs are defined in terms of quantum mechanical observables, the bridges linking the intuitive chemical approach to quantum mechanics have been built

either by interpreting the approximate molecular wave functions or on the basis on the statistical interpretation of quantum mechanics.

The essential assumption of the Lewis model is that it is possible to identify groups of electrons spatially distributed in an atom or a molecule. Different techniques can be used in order to check the falsifiability of this hypothesis. Rather than electron positions, a first method considers the maxima of the distribution function $\Gamma^{(N)}(\xi_1, \xi_2, \ldots, \xi_N)$, defined in Appendix A (Eq. 15) and which provides the probability of finding the systems at the configuration given by the list of the arguments. A correspondence is then established between the electron coordinates of the maxima of $\Gamma^{(N)}$ and the arrangement of the N electrons in the models. The opposite spin pairs are identified on the basis of a distance criterion. It was initially proposed to consider the only absolute maximum of $\Gamma^{(N)}$ [26, 27], but the distribution function may have degenerated several maxima for symmetry reasons or maxima in a narrow window. The highest probability arrangements of the valence electrons in the water molecule have been investigated for both Hartree–Fock and correlated (VQMC) wave functions enabling the recovery of both Lewis's and Linnett's pictures [28]. A second group of methods aims to determine the regions of space which maximize the probability of finding a given number of electrons. In the loge theory [29–31], the space is divided in connected nonoverlapping volumes within which the probability P_n of finding n and only n electrons of given spins is evaluated. The difficulty of finding the loge boundaries has hampered the development of this method. The efficient recurrence formula derived by Cancès et al. [32] for single determinantal wave functions has been used to optimize the shape of maximum probability domains, not constrained to be nonoverlapping, and applied to linear molecules [33] and other simple systems [28]. Generally the method does not yield unique solutions, for example, in the FHF^- complex, two symmetry-related overlapping domains containing the proton correspond to the two F–H bonds. The overlap of these domains is interpreted as being due to the resonance of the [F–H + F^-] and [F^- + HF] structures. The partition of the space in adjacent nonoverlapping regions can be achieved by applying the dynamical system theory [34] to the *ELF* [35] gradient field [36, 37]. This yields basins of attractors which correspond to atomic cores, bonds, and lone pairs.

An alternative construction of electronic domains can be achieved by considering Gillespie's prescription for electron pair domains [22]:

> ...it is more realistic to consider an electron pair as a charge cloud that occupies a certain region of space and excludes other electrons from this space. That electrons behave in this way is a result of the operation of the Pauli exclusion principle, according to which electrons of the same spin have a high probability of being far apart and a low probability of being close together. As a consequence the electrons in the valence shell of an atom in a molecule tend to form pairs of opposite spin.

If we consider two pair domains Ω_A and Ω_B separated by a bounding surface S, the fulfillment of Gillespie's prescriptions implies that the same spin pair functions $\Pi_{\alpha\alpha}(\mathbf{r}, \mathbf{r}')$ and $\Pi_{\beta\beta}(\mathbf{r}, \mathbf{r}')$ (see Appendix A Eq. 18) approximately satisfy

$$\begin{gathered}\Pi_{\sigma\sigma}(\mathbf{r},\mathbf{r}') = 0.0 \text{ for } \mathbf{r},\mathbf{r}' \in \Omega_A \text{ or } \Omega_B \\ \Pi_{\sigma\sigma}(\mathbf{r},\mathbf{r}') \neq 0.0 \text{ for } \mathbf{r}, \in \Omega_A \text{ or } \Omega_B \text{ and } \mathbf{r}' \in \Omega_B \text{ or } \Omega_A , \\ \Pi_{\sigma\sigma'}(\mathbf{r}\mathbf{r}') \neq 0.0 \quad \forall \mathbf{r},\mathbf{r}'\end{gathered} \tag{1}$$

where σ, σ' stands for α or β with $\sigma \neq \sigma'$. The boundary can be located by sampling the space with a finite volume over which the pair functions are integrated. If the above hypotheses are verified, the integrated same spin pair functions should be nonzero when the sampling volume straddles the bounding surface. This technique is inspired by the Nansen bottles used to sample seawater at different depths, and here the sampling volume $V(\mathbf{r})$ is adjusted in order to contain a given amount of electron density; in other words

$$q = \int_{V(\mathbf{r})} \rho(\mathbf{r}) \; d\mathbf{r}, \tag{2}$$

with $q = 10^{-8}\, e^-$ and the sampling function is simply

$$\overline{N}_{\parallel}(\mathbf{r}) = \int_{V(\mathbf{r})} \Pi_{\alpha\alpha}(\mathbf{r}_1,\mathbf{r}_2)\, d\mathbf{r}_1\, d\mathbf{r}_2 + \int_{V(\mathbf{r})} \Pi_{\beta\beta}(\mathbf{r}_1,\mathbf{r}_2)\, d\mathbf{r}_1\, d\mathbf{r}_2. \tag{3}$$

A pair of helium atoms in the ground state at the internuclear distance found in the solid phase [38], 3.57 Å, is a suitable test system for which the midperpendicular plane of the internuclear axis is the bounding surface imposed by symmetry. Figure 1 displays $\overline{N}_{\parallel}(\mathbf{r})$ and $\rho(r)$ along the internuclear axis and along a parallel 1 bohr off this axis. $\overline{N}_{\parallel}(\mathbf{r})$ is very small in the regions far away from the internuclear midperpendicular plane, and the value at the maximum, in this plane, is almost the same on and off the internuclear axis. The ability of $\overline{N}_{\parallel}(\mathbf{r})$ to locate the boundaries of electronic domains is illustrated in Fig. 2. The maxima of the function correspond to the radii of the atomic shells. The radial electron distribution function $4\pi r^2\rho(r)$ which represents the probability of finding one electron on a sphere of radius r and of thickness dr is generally used to plot the electron distribution profiles of hydrogen-like atoms as well as of many electron atoms. The minima of the curve correspond to the nodes of the orbitals in hydrogen-like atoms, whereas in many electron atoms, they fairly reproduce the inner shell structure but often fail to locate the boundary of the valence and penultimate core shell as shown in Table 1. This table reports the radii and populations of the core shells of $^2S_{1/2}$ and $^1S_0$ ground state atoms found with $\overline{N}_{\parallel}(\mathbf{r})$ and $4\pi r^2\rho(r)$. Unlike the radial electron distribution function which samples the indirect effect of the Pauli principle on the one-electron density, $\overline{N}_{\parallel}(\mathbf{r})$ considers the variation of the same spin pair density which is directly related to the antisymmetry of the wave function. The sampling function yields satisfactory results for shell separation radii as testified by the values of the shell populations all close to the integers given by the electronic configurations. Such a sampling function is an electron localization function. In the examples previously considered, the electronic domains appear to be volumes bounded by

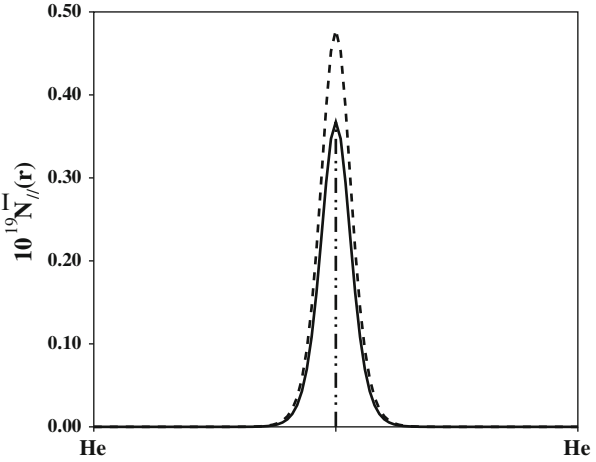

Fig. 1 Profiles of $\overline{N}_{\|}\rho(\mathbf{r})$ along the internuclear axis of He_2 (*full line*) and along a parallel to this axis at 1 bohr (*dashed line*); the location of the boundary is indicated by the *dot-dashed vertical line*

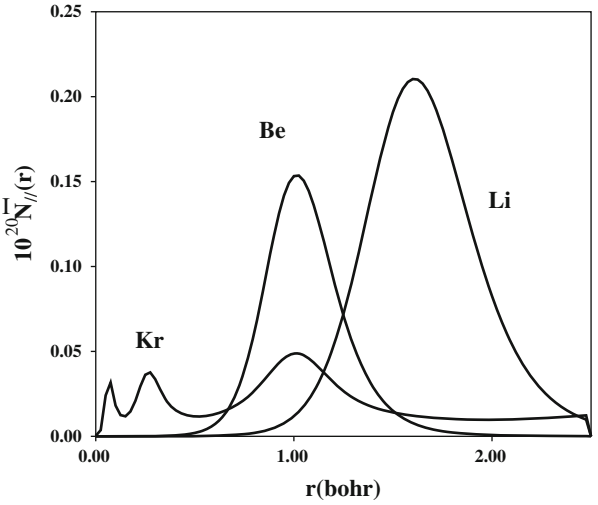

Fig. 2 Radial profiles of $\overline{N}_{\|}(\mathbf{r})$ for Li, Be, and Kr atoms

zero-flux surfaces of $\overline{N}_{\|}(\mathbf{r})$ allowed to extend to infinity. This corresponds to the definition of a *basin* of the gradient field of $-\overline{N}_{\|}(\mathbf{r})$ in the dynamical system theory [34, 39]; therefore an electronic domain can be defined as a basin of an electron localization function. This mathematical theory provides a partition of the space which is analogous to the more familiar partition made in hydrology in river basins delimited by watersheds. Another definition of the atomic domain should be a nonoverlapping volume which minimizes the variance of its population with respect to the variation of its boundaries. This definition applied to ground state atoms provides qualitatively the same answers as $\overline{N}_{\|}(\mathbf{r})$ as well as shell radii and population in excellent quantitative agreement [40]. In spite of its conceptual simplicity, $\overline{N}_{\|}(\mathbf{r})$

Table 1 Shell radii (a. u.) and shell populations e^- of $^2S_{1/2}$ and $^1S_0$ ground state atoms calculated from $\overline{N}_{\|}(\mathbf{r})$ and $4\pi r^2\rho(r)$

$\overline{N}_{\|}(\mathbf{r})$							$Q(r)$				
	K-shell		L-shell		M-shell						
	r_K	$\overline{N}_K$	r_L	$\overline{N}_L$	r_M	$\overline{N}_M$	K-shell		L-shell		M-shell
Li	1.608	2.019					1.784	2.054			
Be	1.014	2.017					1.098	2.060			
Ne	0.296	2.144					0.308	2.218			
Na	0.264	2.177	2.258	7.794			0.274	2.237			
Mg	0.236	2.179	1.662	7.853			0.244	2.239			
Ar	0.144	2.206	0.735	7.863			0.144	2.206	0.798	8.148	
K	0.135	2.211	0.669	7.851	3.207	8.020	0.136	2.227	0.724	8.146	
Ca	0.127	2.213	0.615	7.851	2.488	8.001	0.129	2.2478	0.663	8.107	
Zn	0.081	2.237	0.344	8.331	1.736	17.103	0.080	2.207	0.364	8.749	
Kr	0.066	2.235	0.267	8.520	1.012	17.089	0.066	2.235	0.282	8.968	

is not the only conceivable electron localization function. It has several drawbacks such as being defined for an arbitrary integrated density. The spin pair composition $c_\pi(\mathbf{r})$ [41] and the electron localization indicators for same spin pairs $\Upsilon_\omega^\sigma(\mathbf{r}_i)$ [42] and opposite pairs $\Upsilon_\omega^{\alpha\beta}(\mathbf{r}_i)$ [43] remove the arbitrariness contained in the definition of $N_\parallel(\mathbf{r})$ and they get rid of size dependence problems. These functions have been introduced by their authors in order to support the analysis of the electron localization function of Becke and Edgecombe [35], hereafter denoted by its acronym *ELF*, and to enable the generalization of this latter function to post Hartree–Fock approximate wave functions. *ELF* has been originally designed in order to identify "localized electronic groups in atomic and molecular systems." The *ELF* kernel, $\chi(\mathbf{r})$, is the ratio of the Laplacian of the Hartree–Fock conditional same spin pair probability to the homogeneous electron gas kinetic energy density:

$$\chi(\mathbf{r}) = \frac{D_\sigma(\mathbf{r})}{D_\sigma^0(\mathbf{r})}, \tag{4}$$

in which

$$D_\sigma(\mathbf{r}) = \tau_\sigma(\mathbf{r}) - \frac{1}{4}\frac{|\nabla\rho_\sigma(\mathbf{r})|^2}{\rho_\sigma(\mathbf{r})}, \tag{5}$$

where $\tau_\sigma(\mathbf{r})$ is the σ spin contribution to the positive definite kinetic energy density. For a closed shell singlet, $D_\sigma(\mathbf{r})$ is the difference between the total positive definite kinetic energy density $T_s(\mathbf{r})$ and the von Weizsäcker kinetic energy density functional $T_{vW}(\mathbf{r})$ [44],

$$D_\sigma(\mathbf{r}) = T_s(\mathbf{r}) - T_{vW}(\mathbf{r}), \tag{6}$$

whereas

$$D_\sigma^0(\mathbf{r}) = \frac{3}{5}\left(6\pi^2\right)^{2/3}\rho_\sigma^{5/3}(\mathbf{r}) \tag{7}$$

is the kinetic energy density of the homogeneous electron gas of density $\rho_\sigma(\mathbf{r})$. The *ELF* is confined in the [0,1] interval by a lorentzian cosmetic transformation:

$$ELF(\mathbf{r}) = \frac{1}{1+\chi(\mathbf{r})^2}. \tag{8}$$

Many interpretations of *ELF* have been proposed in order to get relationships with other theoretical tools. Savin et al. have demonstrated that the *ELF* formula

can be extended to DFT and Kohn–Sham orbitals; in this case the *ELF* kernel has the physical meaning of the ratio of the local excess kinetic energy density for the actual system and the same density jellium [45, 46]. Orbital-based interpretations are due to J. Burdett [47] and R. Nalewajski et al. [48] who considered the nonadditive interorbital Fisher information. Another route pioneered by Dobson [49] explicitly considers the pair functions.

3 The *ELF* Basins

The gradient field of *ELF* yields a partition of space into basins of attractors which correspond to cores, lone pairs, and bond regions [36, 37]. As noted by Gillespie and Robinson: "This function (ELF) exhibits maxima at the most probable positions of localized electron pairs and each maximum is surrounded by a basin in which there is an increased probability of finding an electron pair. These basins correspond to the qualitative electron pair domains of the VSEPR model and have the same geometry as the VSEPR domains" [50].

3.1 Nomenclature

The vocabulary of the mathematical tool used in the *ELF* analysis is given in the Appendix C.

The basins of the *ELF* gradient field faithfully account for the partition of the electron density expected in the Lewis picture. On the one hand the atomic kernel of the Lewis first postulate is recovered by the core basins labeled as C(A) where A is the atomic symbol of the element, which are usually gathered in a single super basin for atoms heavier than neon. Hydrogen and helium atoms are exceptions because their nuclei are encompassed by a valence rather than core basin. The core basins are surrounded by the valence basins which may belong to one or more atomic valence shells. The number of atomic valence shell to which a valence basin participates is called the synaptic order of the valence basins; there are accordingly monosynaptic basins, disynaptic basins, trisynaptic basins, and higher polysynaptic basins. Valence basins are labeled V(A,B,C,. . .) where A,B,C,. . . are the atomic symbols of the atomic shells to which they participate. Figure 3 displays the trace of the basins in the plane of the nuclei of the furan molecule. The *ELF* partition yields five core basins (four C(C) and one C(O)), four protonated disynaptic basins V(C, H), two V(C,O) on each side of the nuclear plane, and five V(C,C), one corresponding to the single bond and two groups of two accounting for the two double bonds. Each hydrogen valence shell contains one protonated disynaptic basin which is also involved in a carbon valence shell. The valence shells of the carbons in β position of the oxygen involve three V(C,C) basins and a V(C,H) basin,

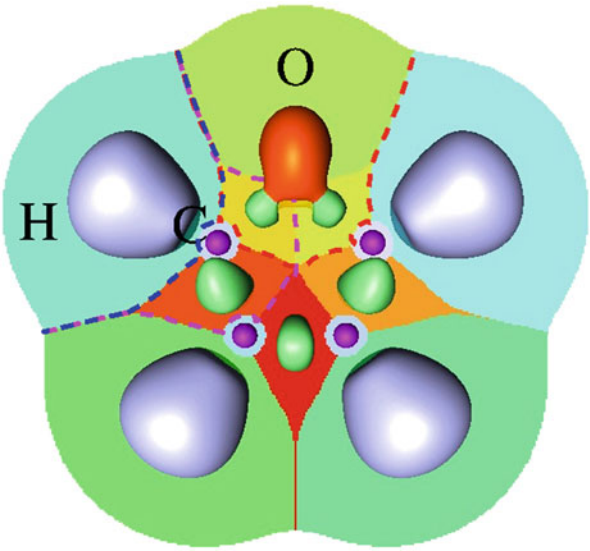

Fig. 3 Trace of the *ELF* basins and $ELF = 0.85$ isosurface of the furan molecule. The *red*, *magenta*, and *blue dotted lines* delineate the valence shells of oxygen atom, of a carbon linked to oxygen, and of the hydrogen linked to this carbon

whereas those of the carbons in α gather one V(C,O), two V(C,C), and a V(C,H), and finally two V(O) and two V(C,O) compose the oxygen valence shell.

3.2 Localization Domains

Localization domains are defined as regions of space bounded by a given isosurface of $ELF = f$ [51]. They are very useful for graphical representations of the bonding in molecules and crystals, and moreover their hierarchy with respect to the isosurface value can be exploited to discuss the bonding. A localization domain contains at least one attractor of the dynamical system; in this case it is said irreducible. If it contains more than one attractor, it is said reducible. Except for atoms and linear molecules, the irreducible localization domains are filled volumes with a ball topology, whereas reducible domains may be hollowed volumes or donuts. Starting from a low value of *ELF* defining a single-parent reducible domain, the increase of the isovalue splits this latter into several composite child domains each containing less attractors than the parent domain. This process called reduction of localization occurs at turning points which are critical points of index 1 located on the separatrix of two basins involved in the parent domain. These critical points are called basin interconnection points often abbreviated by *bips* [52]. Tree diagrams ordering these turning points are built in order to discuss the bonding in terms of the hierarchy of the basins [53]. Figure 4 displays the diagrams obtained for a molecule, CH_2ClCCH, and a weak hydrogen-bonded complex $FH\cdots N_2$. In the molecular case, the first separations occur at c. a. $ELF \sim 0.15$ between the molecular valence shell domain which is topologically a hollow ball with four cavities and the core

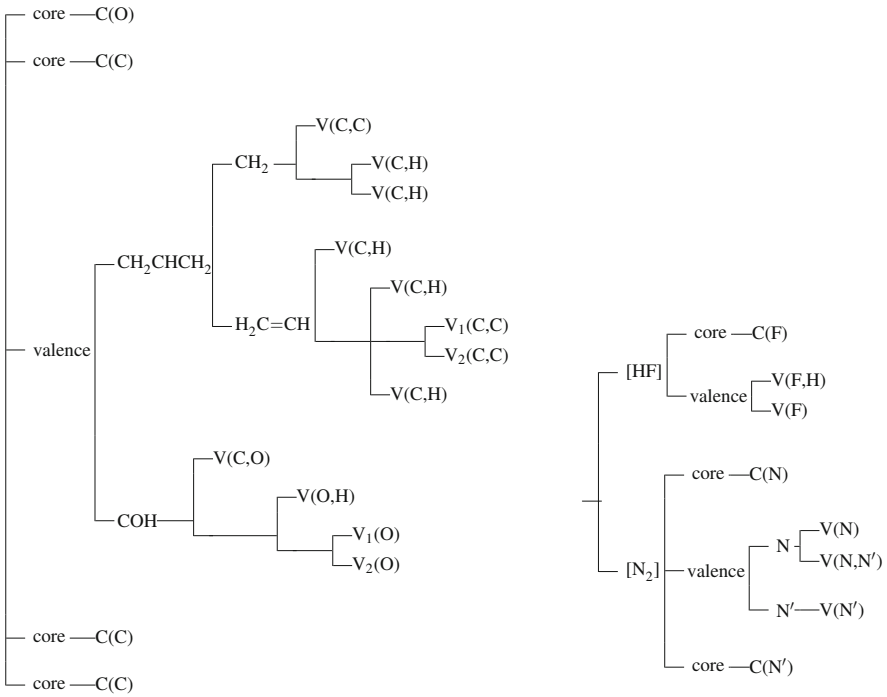

Fig. 4 Reduction of localization diagram of allyl alcohol (*left*) and FH···N_2 (*right*)

domains. The valence domain afterward splits into group domains and then in irreducible domains. The OH group which corresponds to the highest electronegativity of the central atom is the first domain group to be separated from the remaining valence domain as the *ELF* isovalue is increased. The parent domain of the weak hydrogen-bonded complex is separated into reducible domains corresponding to each moiety at a very low *ELF* value, the appearance of the core domains occurring at higher values. The core valence bifurcation (CVB) index has been introduced as an *ELF*-based criterion of the hydrogen bond strength [54]; it is defined as

$$\mathrm{CVB} = ELF(\mathbf{r}_{\mathrm{cv}}) - ELF(\mathbf{r}_{\mathrm{vv}}), \tag{9}$$

where $ELF(\mathbf{r}_{\mathrm{cv}})$ and $ELF(\mathbf{r}_{\mathrm{vv}})$ are, respectively, the largest *ELF* value at the *bips* between core and valence basins and the smallest *ELF* value for the *bips* between valence basins. A negative CVB is the signature of a single chemical species, whereas a positive CVB indicates the presence of several species. The CVB index indicates if an interaction is chemical or not; it is useful to classify hydrogen bonds [54–56] and to characterize the adsorption on a catalyst [57]. For hydrogen-bonded systems, AH···B an almost linear correlation can be observed between the CVB index and the experimental frequency shift of the proton donor stretching

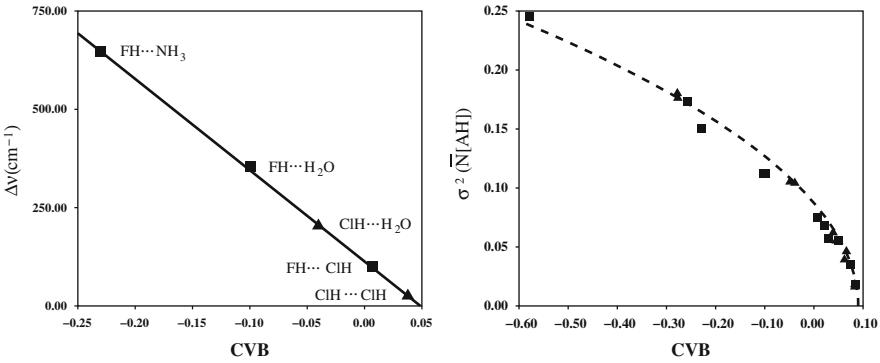

Fig. 5 *Left* $\Delta\nu$ vs. CVB, right $\sigma^2\left(\overline{N}[\mathrm{AH}]\right)$ vs. CVB.$(-)\sigma^2 \approx 0.291\sqrt{0.09 - \mathrm{CVB}}$.. *Filled triangle*: AH = FH. *Filled square*: AH = ClH

mode, $\Delta\nu = \nu_{\mathrm{free}}(\mathrm{AH}) - \nu_{\mathrm{AH\cdots B}}$ as shown in the left part of Fig. 5; the same kind of correlation also holds for complexation energies [54, 56]. In the selected complexes, $\mathrm{FH}\cdots\mathrm{NH_3}$ and $\mathrm{FH}\cdots\mathrm{H_2O}$ are representative of the medium hydrogen bond, the remaining complexes being considered as weakly bonded since their complexation energies are less than 20 kJ mol^{-1}. The right part of Fig. 5 shows that the CVB index provides a measure of the intermolecular electron delocalization which is generally interpreted in terms of hydrogen bonding covalence [58, 59].

The graphical representations of bounding isosurfaces of the localization domain with colors corresponding to the type of basin provide attractive and informative pictures and convenient representation of the bonding. The choice of the isosurface value depends on the nature of the investigated system. It is made in order to provide a clear display of the important features of the ELF output. The example of Fig. 6 shows the allyl alcohol and 3-chloroprop-1-yne localization domains corresponding to the $ELF = 0.8$ isovalue. The C=C double bond of $\mathrm{CH_2CHCH_2OH}$ gives rise to two irreducible localization domains for a higher *ELF* value, whereas a toroidal domain due to the local axial symmetry accounts for the $\mathrm{CHCCH_2Cl}$ triple bond. The same local symmetry also yields a torus for the chlorine lone pair. The bonding domains represented in green are always smaller than the lone pair domains in redbrick in agreement with the VSEPR assumptions. However, the V(C,H) domain extension is in apparent contradiction with this model; however the *ELF* picture delivers the message that as the hydrogen atom has no core, the V(A,H) basins spatially behave as a V(A) lone pair encompassing a proton [60].

Another interest of the domain isosurface representation is the clear evidence of multicenter bonds such as in the examples of $\mathrm{B_4Cl_4}$ and diborane (cf. Fig. 7). In boron tetrachloride, the V(B,B,B) trisynaptic basins have their attractors in front of the boron tetrahedron giving rise to the green reducible localization at $ELF = 0.85$ which splits into four irreducible domains for $ELF = 0.875$. In diborane, the two V(B,H,B) trisynaptic basins in which a proton is embedded support the protonated double bond picture of Pitzer [61].

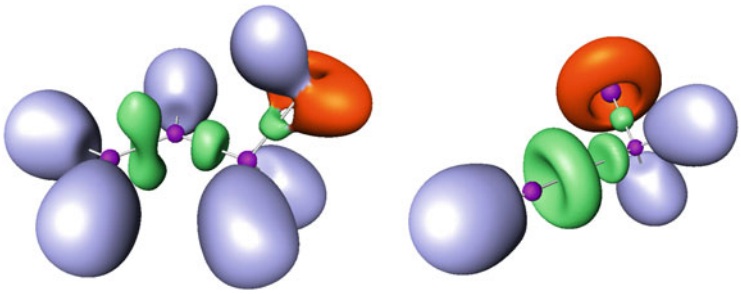

Fig. 6 *ELF* = 0.80 isosurfaces of the CH_2=$CHCH_2OH$ and CH≡CCH_2Cl molecules. Color code, *magenta* = core, *redbrick* = valence monosynaptic, *green* = valence disynaptic, and *light blue* = valence protonated disynaptic

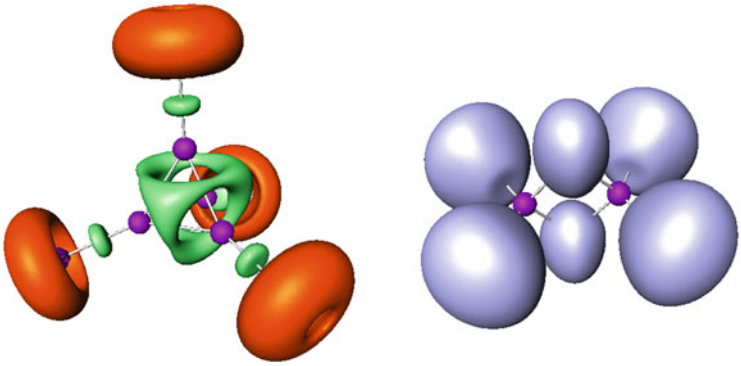

Fig. 7 *ELF* = 0.85 isosurfaces of the B_4Cl_4 and B_2H_6 molecules. Same color code as Fig. 6

4 The Properties of the *ELF* Basins

Although the graphical representations of the *ELF* domains provide a very useful informative picture of the bonding, it is necessary to consider other qualitative and quantitative pieces of information in order to characterize the bonding and to get a chemically explanatory description of the molecules and of their reactivity.

4.1 The ELF *Population Analysis*

The *ELF* population analysis relies on the methodology described in Appendix B; its output consists in one-electron populations $\overline{N}_\sigma(\Omega)$, pair populations $\overline{N}_{\sigma\sigma'}\left(\Omega, \Omega^{'}\right)$ where σ, σ' stand for the α or β spin components, the covariance matrices, and the electron probability distribution which gives the probability of finding exactly n electrons in a given basin, the remaining $N - n$ being anywhere. In most

applications, the total basin populations $\overline{N}(\Omega) = \overline{N}_{\alpha}(\Omega) + \overline{N}_{\beta}(\Omega)$ are considered instead of their spin components. With respect to QTAIM [62], the *ELF* core and monosynaptic basins are subsets of atomic basins, whereas polysynaptic basins have a nonempty intersection with several atomic basins. Combining the *ELF* and AIM approaches, Raub and Jansen [63] have introduced a bond polarity index defined as

$$P_{XY} = \frac{\overline{N}\left[V(X,Y)\middle|X\right] - \overline{N}\left[V(X,Y)\middle|Y\right]}{\overline{N}\left[V(X,Y)\middle|X\right] + \overline{N}\left[V(X,Y)\middle|Y\right]}, \tag{10}$$

where $\overline{N}\left[V(X,Y)\middle|X\right]$ denotes the contribution of the X atom to the population of the V(X,Y) basin.

The *ELF* population analysis often yields basin populations close to the integer values expected from the Lewis model; however the deviations from even integers have been interpreted by some authors as a deficiency of the partition scheme [64, 65]. Figure 8 displays $\overline{N}[V(A,H)]$ and p_{AH} for the second and third period hydrides as a function of the Pauling electronegativity of A, $\chi(A)$. For the elements of the left side of the periodic table, i.e., Li–C and Na–Si, there are no lone pair basins in the valence shell of A and therefore $\overline{N}[V(A,H)] \sim 2.0$, whereas it consistently decreases as $\chi(A)$ increases. The polarity index p_{AH} almost linearly increases with the electronegativity of A: for $\chi(A) < \chi(H)$, one expects the ionic contribution $A^+ + H^-$ to be important, and therefore p_{AH} should be negative and $\overline{N}[V(A,H)] \sim 2.0$, whereas for $\chi(A) > \chi(H)$, the ionic contribution is due to $A^- + H^+$ which implies $p_{AH} > 0.0$ and $\overline{N}[V(A,H)] < 2.0$. Instead of a drawback of the partition scheme, the difference from ideal integer values is the consequence of the account for the other mesomeric structures explaining the chemical properties of these different hydrides. Analogous considerations explain why the population of the V(*N*,*N*) basin of N_2 is not 6 but 3.54 e^-.

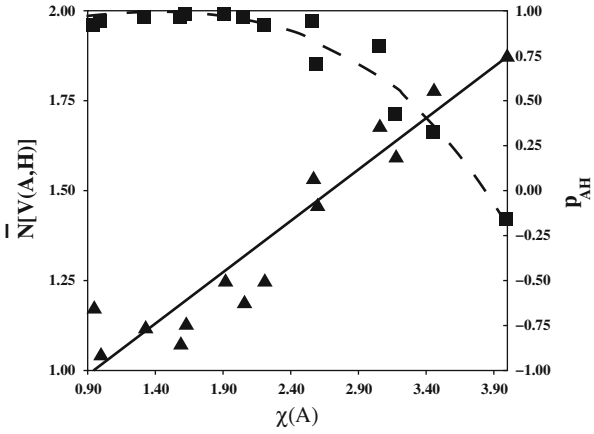

Fig. 8 $\overline{N}[V(A,H)]$ (*filled square*) and p_{AH} (*filled triangle* of the second and third period hydrides vs. Pauling electronegativity $\chi(A)$

Table 2 Basin populations $\overline{N}(\Omega)$, covariance matrix elements $\langle\widehat{\mathrm{cov}}(\Omega,\Omega')\rangle$, and electron number probabilities $P_n(\Omega)$ of N_2

$\langle\widehat{\mathrm{cov}}(\Omega,\Omega')\rangle$									
Basin	$\overline{N}(\Omega)$	V(N)	V(N,N')	V(N')	$P_2(\Omega)$	$P_3(\Omega)$	$P_4(\Omega)$	$P_5(\Omega)$	$P_6(\Omega)$
V(N)	3.11	1.11	−0.62	−0.31	0.26	0.37	0224	0.08	0.01
V(N,N')	3.54	−0.62	1.49	−0.62	0.16	0.30	0.29	0.16	0.05
V(N')	3.11	−0.31	−0.62	1.11	0.26	0.37	0.24	0.08	0.01

In the mesomery model, the charge distribution is represented by a superposition of weighted structures, the *ELF* populations and population covariances enable therefore to estimate the weights of the considered structures [66, 67]; moreover the electron number probabilities provide additional pieces of information about the electron delocalization. In the N_2 case, first consider the QTAIM partition in which each atom occupies a half space bonded by the midperpendicular plane of the internuclear axis. The symmetry of the molecule requires the population of each atom to be exactly 7 e^-; however the calculated variance amounts to 1.52 because the probabilities of finding 5, 6, 7, 8, and 9 electrons in the atomic basin are, respectively, 10%, 23%, 31%, 23%, and 10%. The *ELF* populations and covariance are reported in Table 2. The analysis of the covariance matrix clearly indicates important delocalization not only between basins sharing a common boundary, i.e., V(N,N') and V(N) or V(N'), but also "through the space" between V(N) and V(N'). It is interesting to note that the probability of the nitrogen triple bond, P_6(V(N,N') = 6, is very small. The *ELF* analysis suggests the superposition of three major structures:

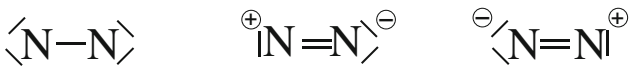

This result questions the fulfillment of the octet rule since the population of the nitrogen valence shell is calculated to be 6.65 e^- instead of 8 being expected. This problem was addressed by Gillespie and Silvi [68] who examined the valence shell populations of the central atom of a series of hypervalent molecules involving ligands both more and less electronegative than the central atom. It was found that the central atom population varies dramatically with the electronegativity of the ligand: it is less than 8 for the more electronegative ligands and greater than eight for the less electronegative ligands. Molecules involving polar bonds imply that the bonding electron pairs do not contribute equally and fully to the valence shells of both bonded atoms but contribute more to the valence shells of the ligands than to the valence shell of the central atom contrary to the assumption made by Lewis in formulating the octet rule. Indeed, no molecule with polar bonds can have exactly eight electrons in the valence shell of the central atom except by chance. The molecules with less electronegative ligands have more than eight electrons in their valence shell, for example, the valence shell population of PMe_5 is calculated to be close to 10 e^-.

5 The *ELF* Basins and the Molecular Geometry

The close relationship of *ELF* basins with molecular geometry has been exploited to understand and explain, by chemical arguments, the geometry of molecules and crystals as, for example, the origin of the short vanadyl bond in V_2O_5 [69, 70]. The *ELF* patterns even help to improve the determination of crystalline structure such as hydrogen positions in hydrides which cannot be found by X-ray diffraction as explained by Savin et al. for CaH_2 [46].

5.1 Arrangement of the Basins and VSEPR Rules

The VSEPR model is usually understood as a way to explain molecular geometries as determined by the arrangement of bonding and lone pair electronic domains themselves provided by Lewis's structures. The distribution of the valence electrons among the electronic domains does not consider the mesomery and assumes that a perfect pairing and octet or extended octet rules are satisfied. The *ELF* population analysis does not support these two assumptions: lone pair populations often exceed 2 e^- and electronegative ligands tend to increase their own lone pair basin populations at the expense of the central atom valence shell. However, the VSEPR model works remarkably well for many molecules. Instead of looking for experimentally available structural data from a hypothetical electron distribution, one may consider that the number and the arrangement of the electronic domains are driven by the positions of the nuclei. The geometric parameters and the populations of the lone pair *ELF* basins have been investigated by D. B. Chesnut [71] who reported the angles made by lone pair and bond directions in second and third period hydrides and in the $HP(CH)_n$ and $HN(CH)_n$ series. He found that the angles between bonds are smaller than the angles between bonds and lone pairs except for CH_3^-, H_3O^+, and H_3F^{2+}. The hydrides are not the best series of molecules for such a discussion because, as already noted in a previous paragraph, the sizes of the V(A,H) and V(A) basins are often similar. Calculations carried out with a larger basis set including polarization functions on hydrogen atoms and a post-Hartree–Fock treatment of the electronic correlation (CCSD/cc-pVTZ) yield larger values of the total lone pair populations and put the CH_3^- in agreement with the VSEPR assumptions but confirm the findings of D. B. Chesnut's B3LYP/6-31 + G(d) calculations on H_3O^+ and H_3F^{2+}. In H_3O^+ the volumes of the V(O) basin are calculated smaller than that of V(O,H). The H_3F^{2+} dication illustrates the specific behavior of the V(A,H) basins: with two V(F) and three V(F,H) basins, one could expect a T-shape geometry corresponding to the AX_3E_2 VSEPR structure rather than an equilateral triangular or triangular bipyramidal geometry (provided the V(F) basins are taken into account) consistent with AX_2E_3. The calculated populations of V(F,H) and V(F) are, respectively, 1.42 and 1.81 e^-; the polarity index of V(F,H), $p_{FH} = 0.92$, is very large; and the V(F,H) basin volume is 1.75

Table 3 Lone pair basin population $\overline{N}[\mathrm{V(A)}]$ (e^-), covariance of the V(A) basin populations $\langle \widehat{\mathrm{cov}}(\overline{N}[\mathrm{V_1(A)}], \overline{N}[\mathrm{V_2(A)}r)\rangle$, volumes of the V(A) and V(A,X) basins v(A), v(A,X) (bohr^3), angles between the lone pair and bond direction in the AX_2 and AX_3E_2 series. For SeF_2 there is no V(Se,F) basin

AX_2	$\overline{N}[\mathrm{V(A)}]$	Covariance	v(A)	v(A,X)	$\angle lpAlp$	$\angle lpAX$	$\angle XAX$
H_2O	2.28	−0.38	110.4	115.8	117.1	108.6	104.4
H_2S	2.12	−0.33	262.3	181.8	123.6	107.4	92.8
SF_2	2.23	−0.27	221.8	4.0	141.1	103.6	98.7
SeF_2	2.41	−0.25	269.7		148.6	97.7	
SCl_2	2.33	−0.29	198.5	14.1	140.3	103.1	104.0
$SeCl_2$	2.46	−0.26	241.4	15.5	145.4	101.7	102.1
AX_3E_2							
ClF_3	2.55	−0.27	128.6	3.0	152.6	103.7	
BrF_3	2.57	−0.23	168.8	4.1	155.3	102.3	

times larger than that of V(F) which explains the interchange of the lone pairs and bonds in the VSPER structure.

In the AX_2E_2 and AX_3E_2 VSEPR structures, the location of the *ELF* attractors of the V(A) basins enables to estimate the angle between the lone pair directions. Table 3 reports the data calculated for a selection of molecules. In all systems the angle of the lone pair basin direction is much more larger than the tetrahedral value, and except for hydrogen ligands, the V(A) volumes are more than ten times the V(A,X) ones. The V(A) population is always larger than 2.0 and there is an important electron delocalization among the central atom valence shell indicated by the absolute value of the covariance of the V(A) populations.

The exceptions to the VSEPR rules are mostly found for central atoms heavier than potassium. The d^0 molecules of the period 4 metals were investigated with *ELF* by R. J. Gillespie and coworker [72] who evidenced a structuring of the M-shell into several well-separated basins yielding important distortions with respect to the VSEPR expectation. The *M*-shell basins are characterized by their positions with respect to the ligands. The different types are ligand opposed (LO), ligand not opposed (NLO), and ligand directed (LD). In MX_2 and MX_3 molecules, in addition to the two or three LO basins, two additional NLO basins are formed, completing a disphenoidal or trigonal-bipyramidal arrangement of core basins as a consequence of Pauli repulsion between the M-shell electrons. The ability of the external core (or subvalence) shell of fourth period elements to split in several domains provides chemical explanations not only to purely structural data but also to more complex phenomena. For instance, it was shown that the cation selectivity in enzymes involved in blood coagulation is driven by the subvalence distortions: the calcium cations are clearly able to form specific interactions between the subvalence basins of the metal ion and the carboxylate oxygen lone pairs, whereas magnesium does not have such ability [73].

Other non-VSEPR structures are provided by strained molecules, such as borane cages. The first *ELF* study of closo boron cluster was carried out on B_4X_4, $B_6X_6^{2-}$

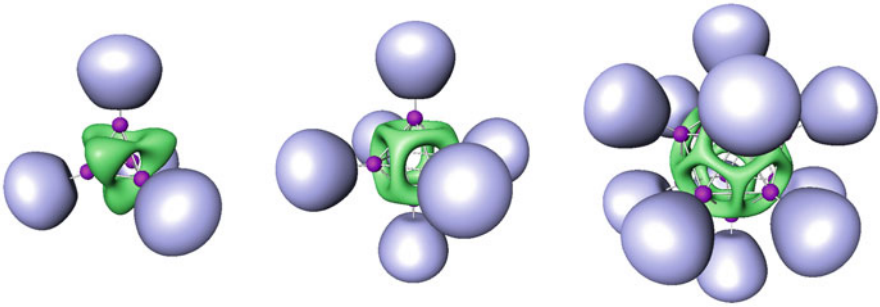

Fig. 9 *ELF* = 0.8 isosurface of B_4H_4, $B_6H_6^{2-}$, and $B_{12}H_{12}^{2-}$. Color code as in Fig. 6

(X = H, Cl, Br, I), and $B_{12}H_{12}^{2-}$ [74]. It revealed that high *ELF* regions formed polyhedral networks which are the duals of the boron skeleton as displayed in Fig. 9. In all systems the *ELF* = 0.8 isovalue delineates the boron core domains, the B–H bond domains, and a single reducible valence domain corresponding to the bonding between boron atoms. The *ELF* values at the attractors and at the basin interconnection points are in a narrow window, and therefore a rather important electron delocalization can be expected. A quantitative analysis yields the following indications. In B_4H_4, eight valence electrons are available for the bonding of the cage giving rise to four trisynaptic V(B,B,B) basins located in front of the faces of the B_4 tetrahedron. The calculated V(B,B,B) population amounts to 1.87 e^- and its variance is 1.06. In $B_6H_6^{2-}$, the number of available valence electrons is 14, and there are 12 attractors located on the B–B edge bisector defining 12 V(B,B) basins each connected to three other V(B,B) basins. Their populations are 1.07 e^- with a variance of 0.78. Finally in $B_{12}H_{12}^{2-}$, where the number of cage valence electron is 26, 50 attractors are found: 20 are located in front of the faces of the boron icosahedron and 30 on the edge bisectors. The populations of the V(B,B,B) basins in front of the faces are 0.24 e^- against 0.66 e^- for the V(B,B) ones. The variances of these basin populations are, respectively, 0.23 and 0.53.

The metallic bond has not been considered by Lewis and is another example for which the VSEPR rules do not apply. The simplest model of a metal is constituted by a periodic array of positively charged ions embedded in a uniform homogeneous electron gas. This model implies that the value of the *ELF* should be almost constant and equal to 0.5, the jellium value, in the off-core region. The analysis of the gradient fields of the electron charge density and of the *ELF* of metals is consistent with the expectations which can be made from the homogeneous electron gas model [75]. Moreover the *ELF* analysis provides a complementary picture of the metallic bond which is a generalization of that of Pauling [76]. The metallic bond is basically a partial covalent bond. Here partial does not refer to any possible ionic contribution but rather to the fact that the basin populations are always very low (typically less than 1 e^-). Figure 10 displays the *ELF* localization domains of Li and Na for couples of isosurfaces close to the other. In lithium, there are two valence electrons and twelve attractors by cell and therefore the population of each

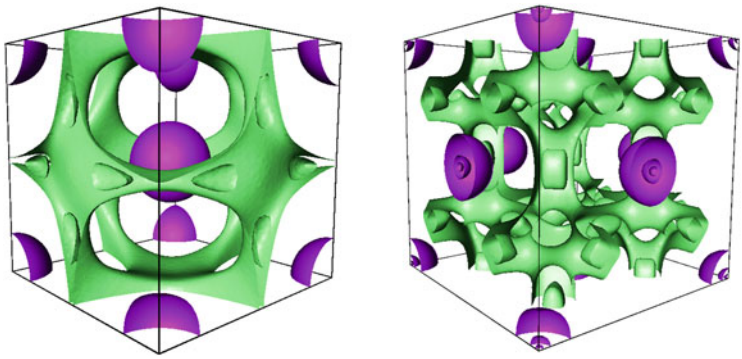

Fig. 10 *Left*: $ELF = 0.66$ and $ELF = 0.68$ isosurfaces of Li bcc crystal. *Right*: $ELF = 0.56$ and $ELF = 0.60$ isosurfaces of Al fcc crystal. Color code as in Fig. 6

valence basin is c.a. 0.16 e^-, whereas in aluminum the twelve valence electrons are shared by 20 basins.

5.2 *Molecular Deformations: Reactivity and Reaction Mechanisms*

There is a formal analogy between the VSEPR model and the first theorem of Hohenberg and Kohn [77]. This theorem establishes that the external potential, i.e., the nucleus–nucleus and electron–nuclei coulombic potential, of a *N*-electron system in the ground state is a unique functional of the one-electron density conversely. As the external potential fixes the Hamiltonian, it determines the *N*-electron wave function and, therefore, the pair densities. This means that for a given ground state electron density, there is one and only one set of nuclear coordinates and alternatively for a given set of nuclear coordinates, there is one and only one ground state electron density. In the VSEPR model the equilibrium molecular geometry, in other words the external potential, is determined by the arrangement of the electronic domains of the central atom valence shells which is a property of the electron density. Alternatively, one can adopt a reciprocal formulation in which the location of the nuclei determines the arrangements of the electronic domains for a given population of the central atom valence shell. The compliance with the "reciprocal VSEPR" rules is not mandatory for nonequilibrium geometries. The electronic arrangements can be determined with the *ELF*, and compared with the "reciprocal VSEPR" expectations providing insights on the reactivity and reaction mechanisms, there are therefore VSEPR compliant and VSEPR defective arrangements.

The halides of groups II and XIII have formally two and three electron pairs in the valence shell of the central atom. Upon a bending deformation, it is not possible

to comply with the reciprocal VSEPR AX_2E or AX_3E configurations which require at least the availability of one electron more. The bent structures are VSEPR defective and are expected to be more reactive than the linear or planar geometry with respect to the approach of a Lewis base. The increase of the electrophilicity indicator [78] ω upon the bending provides a quantitative piece of information. The minimum of the ground state of the Born–Oppenheimer energy surface of $BeCl_2$ corresponds to a linear geometry, and the vibrationally averaged structure is bent with $\angle ClBeCl = 163°$ [79]. There are formally two electron pairs in the Be valence shell and consequently the bent structure arrangement of the electronic domains is VSEPR defective. The addition of a Lewis base such as NH_3 is spontaneous (the reaction is calculated exothermic by about 120 kJ mol^{-1}). The frequency of the π_u bending mode responsible for the bent structure is low, 252 cm^{-1} [79], which explains the absence of barrier. The electrophilicity of the vibrationally averaged bent structure is larger than that of the linear one by about 0.2 eV. For a bent angle of 120°, the increase of ω reaches 1.4 eV. The same description holds for the boron trifluoride for which the active bending vibrational mode, v_2, is observed at 691 cm^{-1} [80]. The addition of NH_3 is also spontaneous and exothermic by 129 kJ mol^{-1} [81]. The increase of the electrophilicity upon pyramidalization is calculated to be as large as 1.9 eV for $\angle FBF = 109.47°$.

The process of creation–annihilation of electronic domains has been formalized in the bonding evolution theory (BET) of Krokidis et al. [82] in which the gradient vector field of *ELF* is used to build the mathematical model. In the BET, the nuclear coordinate set defines the control space which is the union of a series of structural stability domains characterized by different landscapes of the vector field along the reaction pathway. Thom's catastrophe theory [83] provides a description and a nomenclature of the bifurcations at the turning points between structural stability domains. This method has been widely applied to investigate organic reaction mechanisms [84–90]. The method is illustrated here by the 1,3-butadiene cyclization reaction. The so-called "*cis*" butadiene is in fact conformer of C_4H_6 which is not planar and has a C_2 symmetry, as shown by Chattaraj et al. [91]. The energy profile along the rotation coordinate shows a barrier of about 30 kJ mol^{-1}. The reaction pathway linking *trans*-butadiene through "*cis*"-butadiene to cyclobutene preserves the C_2 symmetry. This implies that the reaction mechanism must be consistent with the C_2 symmetry and therefore conrotatory which is observed. Figure 11 displays the energy profile along the reaction coordinate and the evolution of the basin populations. The system visits successively five structural stability domains (SSD I–V), two of which are located before the transition state. The localization domains of SSD-I, SSD-II, and SSD-V are represented in Fig. 12. At first turning point between SSD-I and SSD-II, a dual fold catastrophe merges the attractors of the double bonds making easier the free rotation around these bonds; just before the transition state, the system evolves to SSD-III with the appearance through a fold catastrophe of two monosynaptic basins, V(1) and V(C4), on the terminal carbons through a dual fold catastrophe. At this step the out of plane bending of the $=CH_2$ groups yields VSEPR compliant AX_2E structures. The next catastrophe is of the cusp type; it splits the attractor of the inner C–C bond yielding

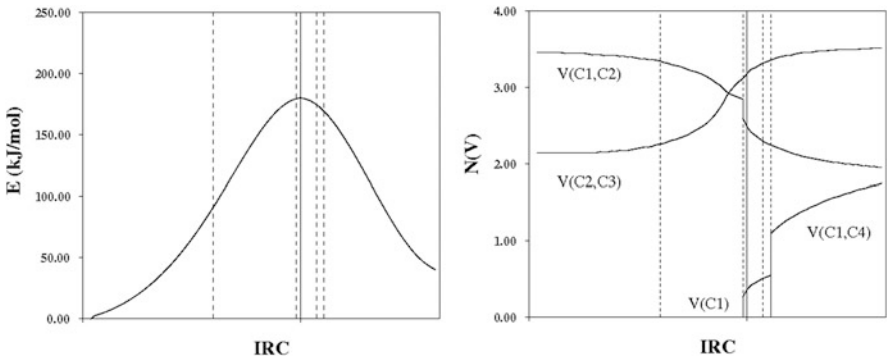

Fig. 11 IRC profile (*left*) and basin populations along the IRC path (*right*)

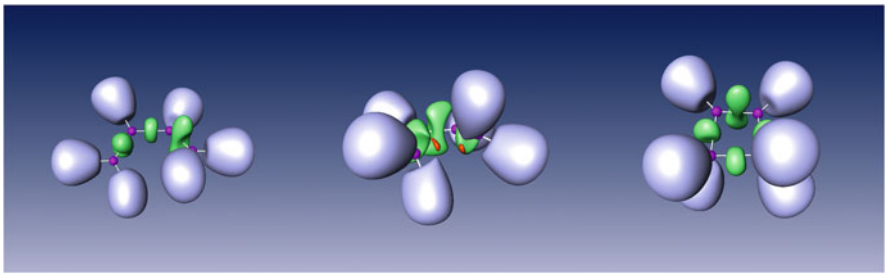

Fig. 12 Localization domains along the reaction path $ELF = 0.8, 0.72, 0.8$

a double bond. The closure of the cycle is achieved when V(C1) and V(C4) merge into a disynaptic basin by a cusp catastrophe. The evolution of the basin population can be further used to discuss the density transfers implied by the nuclear displacements.

The study of phase transitions at high pressure is another field of investigation in which the displacements of the nuclei might provide chemical explanations. The compressibility of a solid, k, can be expressed in terms of a sum of electronic domain contributions in the sense of the VSEPR model:

$$k = -\frac{1}{V}\left(\frac{\partial V}{\partial P}\right) = \sum_i \frac{V_i}{V} k_i, \tag{11}$$

with

$$k_i = -\frac{1}{V_i}\left(\frac{\partial V_i}{\partial P}\right), \tag{12}$$

where P denotes the pressure, V the cell volume, and V_i the volume of the electronic domain labeled by i. The electron–electron electrostatic repulsion, and therefore the averaged electron density, $\overline{\rho}_i = N_i/V_i$, is the determining factor of the domain compressibilities. In the case of pair domains, the compressibility varies with the

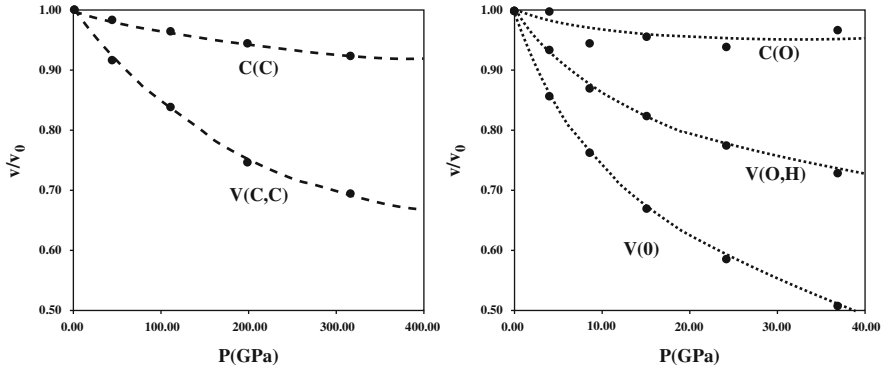

Fig. 13 Reduced basin volumes, $v/v_{0,}$ vs. pressure in GPa. *Left* diamond, *right* ice VIII

domain volumes. Moreover, the weight of a domain compressibility to the total contribution is proportional to the domain volume. On this basis, it can be expected that the contributions are in the following order: core < bonds < lone pairs. This behavior is illustrated in Fig. 13 which represents the reduced basin volumes, i.e., the volume ratio for a given pressure and zero pressure, as a function of the pressure in the cases of a covalent crystal, diamond, and of a hydrogen-bonded molecular crystal, ice VIII. The compressibility of the *ELF* basins has been studied by J. Contreras-García et al. [92–95] in order to understand the pressure-induced phase transitions. It was found that monosynaptic basins are more compressible than disynaptic and other polysynaptic ones which are themselves usually more compressible than core basins. The core compressibility decreases as the core size decreases, or in other words as the atomic number increases in a period and as it decreases in a group. In a phase transition induced by pressure, the system tends to reduce its volume at the least energetic cost. This can be achieved by increasing the contribution of bonding basins at the expense of lone pair basins. The rare gas insulator–metal transition observed for xenon [96] can be explained by this process; the *ELF* calculations provide a clear indication of the splitting of the spherical valence shell at high pressure. In the case of molecular crystals, the formation of pseudo polymeric phases is mostly due to rearrangements of the mono- and disynaptic basins [93].

6 Characterization of the Bonding

The title of the article introducing the topological analysis of *ELF*, "Classification of chemical bonds based on topological analysis of electron localization functions [36]," unambiguously indicated the goal to reach. It considered the electron-shared and electron-unshared interaction classes proposed before by Bader and Essén [97] based on the sign of the Laplacian of the charge density at the bond critical point but

with another criterion, the presence of at least one bond attractor between the cores of the interacting atoms. Covalent, dative, and metallic bonds are subclasses of the shared-electron interaction, whereas ionic, hydrogen, and electrostatic bonds belong to the other class. The subclasses of each interaction are determined with the help of the following criteria:

1. The core valence bifurcation index indicates if an interaction is chemical or not. This index is useful to classify hydrogen bonds [54–56, 98, 99] and to characterize the adsorption on a catalyst [57].
2. The topological behavior of the *ELF* gradient field along the dissociative pathway is characterized by the variation of the number of basins, $\Delta\mu$, and if $\Delta\mu = 0$ by the variation of the synaptic order of the valence basin involved in the interaction ($\Delta\sigma$) [82]. For example, breaking a covalent bond increases the number of basins by one as the disynaptic basin V(A,B) at equilibrium geometry splits into a V(A) and V(B) in the reaction products, whereas in a donor–acceptor bond, it becomes monosynaptic, the number of basins remaining unchanged. The bonding situation where two monosynaptic basins are present at the equilibrium distance and which merge into a disynaptic one at a shorter distance is said protocovalent [100]; in this case, the V(A)–V(B) bip *ELF* value is close to that of the V(A) and V(B) attractors [100].
3. The multiplicity of the disynaptic basin V(A,B) is not automatically correlated to an equal multiplicity of the A–B bond. On the one hand, the location of the attractors should be consistent with the point symmetry and therefore the disynaptic basins multiplicity can be explained by symmetry considerations rather than by chemical arguments. On the other hand, conventional multiple bonds are often limit resonance structures which are not always the dominant ones. The bond multiplicity QTAIM and *ELF* criteria were discussed by Chesnut [101] who concluded that the measures are dependent on the nature of the AB pair.
4. Multicenter bonds imply the presence of polysynaptic basins.
5. When the bonding can be represented by a dominant mesomeric structure, the V(A,B) basin population should be approximately twice the expected bond order.
6. The covariance matrix elements $\left\langle \widehat{\mathrm{cov}}\left(\overline{N}[\mathrm{V}_t(\mathrm{A})], \overline{N}[\mathrm{V}_t(\mathrm{B})]\right)\right\rangle$ where V_t is the union of the basins of the valence shell of A except V(A,B) or the V(A) and V(B) components of a protocovalent bond and $\left\langle \widehat{\mathrm{cov}}\left(\overline{N}[\mathrm{C}(\mathrm{A})], \overline{N}[\mathrm{C}(\mathrm{B})]\right)\right\rangle$ quantify the delocalization on the one hand in three-electron [102, 103] and charge-shift bonds [104] and on the other hand in metal–metal bonds in polynuclear transition metal complexes [105–108].
7. The bond polarity index enables to discuss polar bonds.

Table 4 summarizes the properties of the different subclasses of bonds with respect to the *ELF* criteria. Charge-shift and metal–metal bonds are on the borderline of the electron-shared and electron-unshared interactions because their

Table 4 Classification of bonding interaction according to *ELF* criteria: core valence bifurcation index ϑ; bond dissociation variations of the number of basins, $\Delta\mu$, and of the basin synaptic orders $\Delta\sigma$; disynaptic basin population $\overline{N}[\mathrm{V(A,B)}]$; polarity index p_{AB}; and covariance matrix elements. In the case of the charge-shift bonding, V(A,B) may be replaced by a protocovalent pair of basin or absent; in metal–metal bond it may be absent

Bond type	ϑ	$\Delta\mu$	$\Delta\sigma$	$\overline{N}[\mathrm{V(A,B)}]$	p_{AB}	Covariance	
						V_t(A)–V_t(B)	C(A)–C(B)
Electron-unshared interactions							
Van der Waals	>0	0	0			~0.0	0.0
Weak H bond	>0	0	0			~0.0	0.0
Medium-strong H bond	<0	0	0			~0.0	0.0
$3e$ bonds	<0					~ -0.3	0.0
Intermediate bonds							
Charge-shift bond	<0	$\neq 0$		<1.0		~ -0.2	0.0
Metal–metal	<0			$\ll 2 \times$ BO		$\sim -0.5 \times$ BO	<0.0
Electron-shared interactions							
Donor–acceptor	<0	0	$\neq 0$	$\sim 2 \times$ BO		~0.0	0.0
Covalent	<0	$\neq 0$	0	$\sim 2 \times$ BO	~0.0	~0.0	0.0
Polar covalent	<0	$\neq 0$	0	$<2 \times$ BO	$\neq 0.0$	~0.0	0.0

disynaptic basin may be absent or replaced by a protocovalent pair of monosynaptic basins. The possibility of protocovalent pairs of monosynaptic basins at the equilibrium geometry [100] has been the first evidence of the charge-shift bonding [109, 110] without recourse to valence bond calculations. The *ELF* criteria of the charge-shift bonding were later examined in details [104] and a specific covariance index accounting for through the space delocalization

$$\langle \mathrm{cov(A,B)} \rangle = \left\langle \widehat{\mathrm{cov}}\left(\overline{N}[\mathrm{V(A)}], \overline{N}[\mathrm{V(B)}]\right)\right\rangle + \sum_{\mathrm{X}\neq \mathrm{B}} \sum_{\mathrm{Y}\neq \mathrm{A}} \left\langle \widehat{\mathrm{cov}}\left(\overline{N}[\mathrm{V(A,X)}], \overline{N}[\mathrm{V(B,Y)}]\right)\right\rangle, \tag{13}$$

which is usually of the order of -0.5 against c.a. -0.2 for a standard covalent bond. The bridging carbon–carbon interaction in the [1.1.1]propellane is an interesting example of charge-shift bonding [111]. Figure 14 displays the $ELF = 0.85$ localization domains of this molecule. The "wing" C–C bonds which give rise to disynaptic basins with a population of 1.73 e^- and a covariance index of -0.06 are clearly covalent. The bridging carbon–carbon interaction is characterized by the large magnitude of the covariance index, -0.77, and the presence of monosynaptic basins outside of the cage on each axial carbon with populations of 1.27 e^- and of a small disynaptic basin at the center of the cage which is not represented because of its size and of the *ELF* value at its attractor below the isosurface value. The population of this basin is moreover very small, 0.13 e^-. The main difference with QTAIM-based classification is that donor–acceptor bonds belong to the electron-shared interaction.

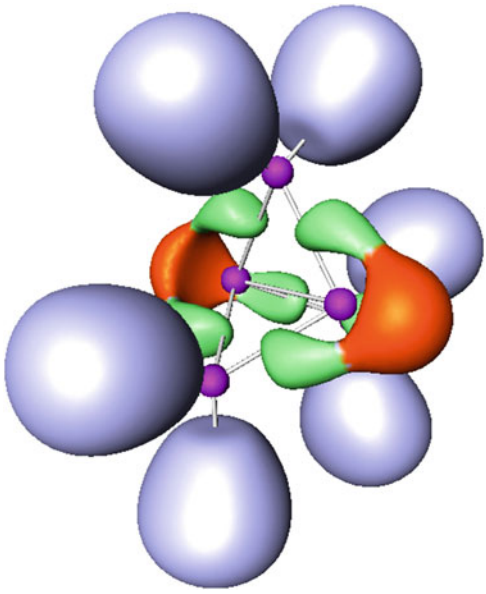

Fig. 14 $ELF = 0.85$ localization domains of [1.1.1]propellane. Color code as in Fig. 6

In addition to delocalization criteria, scales based on "partial *ELF*" have been proposed as aromaticity indicators. "Partial *ELF*s" are functions constructed with the *ELF* formula restricted to a subset of molecular orbitals. The ELF_σ and ELF_π scales [112] are based on the value of such "partial *ELF*s" at their *bips* between their valence basins assumed to contribute to the aromaticity. Although there is no clear theoretical support behind these scales, the analysis clearly distinguishes aromatic and antiaromatic systems. The aromaticity of polycyclic aromatic hydrocarbons is correctly taken into account; moreover this indicator provides a good basis to discuss σ and π aromaticity.

7 A Useful Tool to Explain Chemistry

One of the goals of the *ELF* approach is to provide an interpretative tool of quantum chemical calculations in terms of purely chemical concepts without the recourse to the nature of the approximate wave functions. The *ELF* recovers many features of the simple chemical models based on a spatial distribution of the valence electron, namely, the valence theory of G. N. Lewis, the mesomery concept of C. K. Ingold, and the VSEPR model of R. J. Gillespie and R. S. Nyholm. The partition of the electron density based on a statistical criterion provides a quantum mechanical support to the hypotheses which are explicitly or implicitly assumed in these models. Indeed, this statistical approach provides at least formally a mathematical bridge between quantum mechanics and chemistry which enables to critically think about the content and the definition of many chemical concepts related to the

bonding. The improvement of these latter can be achieved in order to remove any assumption in contradiction with the laws of quantum mechanics and take into account important features which had been neglected, for example, the possibility of multicenter bonds in Lewis's theory. The substitution of a classical statement by its statistical formulation is often sufficient to make it consistent.

By considering the response of the basin properties to a perturbation of the external potential, the *ELF* approach goes beyond the bonding models and it sheds light onto reactivity and reaction mechanisms. The study of reactions with *ELF* has inspired the idea that the hypotheses underlying the VSEPR model can be used to predict and explain the density transfers occurring along a reaction pathway, extending to reaction mechanisms the field of applications of the VSEPR model. For all the reactions studied in the BET framework, it is possible to give a reciprocal VSEPR description.

The integration of the electron density over the *ELF* basins provides distributed multipoles which ensure a good convergence of the molecular electrostatic potential and serve as basis to build molecular force fields [113–115] extending the applications of the *ELF* to molecular mechanics modelizations.

Appendix A: Density of Probability Functions

Assuming the Born–Oppenheimer separation, the electronic wave function is a function of 4N variables: each electron, labeled by i, is described by the three components of its position vectors $\mathbf{r}_i$ and by its spin coordinates $\boldsymbol{\sigma}_i$. In order to simplify, the notations $\mathbf{r}_i$ and $\boldsymbol{\sigma}_i$ are gathered in a four-component (space + spin) vector $\boldsymbol{\xi}_i$. According to the statistical interpretation of quantum mechanics, the product

$$P_N(\boldsymbol{\xi}_1, \boldsymbol{\xi}_2, \ldots, \boldsymbol{\xi}_N) = \Psi(\boldsymbol{\xi}, \boldsymbol{\xi}_2, \ldots, \boldsymbol{\xi}_N)\Psi^*(\boldsymbol{\xi}, \boldsymbol{\xi}_2, \ldots, \boldsymbol{\xi}_N), \tag{14}$$

represents the probability of finding the electrons labeled 1,2,...,N in the volume elements $d\,d\boldsymbol{\tau}_1, d\boldsymbol{\tau}_2, \ldots, d\boldsymbol{\tau}_N$ located at points $\mathbf{r}_1$,$\mathbf{r}_2$,...,$\mathbf{r}_N$ with the spin coordinates $\boldsymbol{\sigma}_1$,$\boldsymbol{\sigma}_2$,...,$\boldsymbol{\sigma}_N$. The indiscernability of the electrons implies that the probability of finding any N electrons at these positions is

$$\Gamma^{(N)}(\boldsymbol{\xi}_1, \boldsymbol{\xi}_2, \ldots, \boldsymbol{\xi}_N) = N! P_N(\boldsymbol{\xi}_1, \boldsymbol{\xi}_2, \ldots, \boldsymbol{\xi}_N). \tag{15}$$

The probability of finding k electrons with the ordered space and spin coordinates specified by the list of variables $\boldsymbol{\xi}_1$,$\boldsymbol{\xi}_2$,...,$\boldsymbol{\xi}_k$), the remaining $N - k$ being anywhere, is given by

$$\Gamma^{(k)}(\boldsymbol{\xi}_1,\boldsymbol{\xi}_2,\ldots,\boldsymbol{\xi}_k)=\frac{N!}{(N-K)!}\int d\tau_{k+1}\int d\tau_{k+2}\cdots\int d\tau_N P_N\left(\boldsymbol{\xi}_1,\boldsymbol{\xi}_2,\ldots,\boldsymbol{\xi}_k,\boldsymbol{\xi}_{k+1},\ldots,\boldsymbol{\xi}_N\right). \tag{16}$$

Particularly important are the first- and second-order distribution functions $\Gamma^{(1)}(\boldsymbol{\xi})$ and $\Gamma^{(2)}(\boldsymbol{\xi},\boldsymbol{\xi}')$. Integration of $\Gamma^{(1)}(\boldsymbol{\xi})$ over the spin coordinate $\boldsymbol{\sigma}$ yields the electron density $\rho(\mathbf{r})$, since the spin coordinate is discrete; this integration is actually the sum of two contributions $\rho_\alpha(\mathbf{r})$ and $\rho_\beta(\mathbf{r})$ which correspond to the two values $\pm\frac{1}{2}$ of $\boldsymbol{\sigma}$:

$$\rho(\mathbf{r})=\rho_\alpha(\mathbf{r})+\rho_\beta(\mathbf{r}), \tag{17}$$

The procedure described above to get the electron density and its spin components is applied to $\Gamma^{(2)}(\xi,\xi')$ in order to obtain the pair function and its four spin components:

$$\begin{aligned}\Pi(\mathbf{r},\mathbf{r}')&=\int\int\Gamma^{(2)}(\xi,\xi')d\sigma d\sigma'\\&=\Pi_{\alpha\alpha}(\mathbf{r},\mathbf{r}')+\Pi_{\alpha\beta}(\mathbf{r},\mathbf{r}')+\Pi_{\beta\alpha}(\mathbf{r},\mathbf{r}')+\Pi_{\beta\beta}(\mathbf{r},\mathbf{r}')\end{aligned}. \tag{18}$$

Though the pair function appears to be the suitable quantity enabling the discussion of the pairing, it is a six-dimensional function and therefore it should be helpful to grasp its properties in a three-dimensional mathematical object. It is convenient to define the conditional probability as

$$\frac{\Pi_{\sigma\sigma'}(\mathbf{r},\mathbf{r}')}{\rho_{\sigma'}(\mathbf{r}')}=\rho_\sigma(\mathbf{r}')[1+f_{\sigma\sigma'}(\mathbf{r},\mathbf{r}')], \tag{19}$$

where $\boldsymbol{\sigma}$ and $\boldsymbol{\sigma}'$ stand for the spin labels. The function $f_{\sigma\sigma'}(\mathbf{r},\mathbf{r}')$ is the correlation factor and the product $\rho_\sigma(\mathbf{r})f_{\sigma\sigma'}(\mathbf{r},\mathbf{r}')$ describes the correlation hole around the reference electron. According to the values of $\boldsymbol{\sigma}$ and $\boldsymbol{\sigma}'$, there are two kinds of correlation holes: the Coulomb hole ($\boldsymbol{\sigma}\neq\boldsymbol{\sigma}'$) accounts for the Coulombic interaction, whereas the antisymmetry of the wave function is responsible for the Fermi hole ($\boldsymbol{\sigma}=\boldsymbol{\sigma}'$).

Appendix B: Statistical Population Analysis for Nonoverlapping Partition

The space partitioning into nonoverlapping regions makes the evaluation of the properties of these regions much more straightforward than in interpenetrating (fuzzy atoms) schemes. If the density of property is well defined, the basin property is just the integral of the density of property over the basin volume. The case of the

electron count is particularly interesting because the sum of the basin populations should recover the total number of electrons. The population $\overline{N}[\Omega_A]$ of the basin denoted by Ω_A is given by

$$\overline{N}[\Omega_A] = \int_{\Omega_A} \rho(\mathbf{r})\, d\mathbf{r}. \tag{20}$$

Alternatively, $\overline{N}[\Omega_A]$ can be calculated as the expectation value of the basin population operator introduced by Diner and Claverie [116]:

$$\overline{N}[\Omega_A] = \sum_i^N \hat{y}(\mathbf{r}_i) \text{ with } \hat{y}(\mathbf{r}_i) \begin{cases} \hat{y}(\mathbf{r}_i) = 1\ \mathbf{r}_i \in \Omega_A \\ \hat{y}(\mathbf{r}_i) = 0\ \mathbf{r}_i \notin \Omega_A \end{cases}, \tag{21}$$

where N denotes the total number of electrons. The population operator of the union of two basins Ω_A and Ω_B is given by

$$\hat{N}[\Omega_A \cup \Omega_B] = \sum_i^N \hat{y}(\mathbf{r}_i) \text{ with } \hat{y}(\mathbf{r}_i) \begin{cases} \hat{y}(\mathbf{r}_i) = 1\ \mathbf{r}_i \in \Omega_A \cup \Omega_B \\ \hat{y}(\mathbf{r}_i) = 0\ \mathbf{r}_i \notin \Omega_A \cup \Omega_B \end{cases}, \tag{22}$$

which is not the sum $\hat{N}[\Omega_A] + \hat{N}[\Omega_B]$. Considering the whole space, i.e., $\bigcup_A \Omega_A$ one gets the sum rule

$$\hat{N}\left[\bigcup_A \Omega_A\right] = N. \tag{23}$$

The eigenvalues, $N[\Omega_A]$, of $\hat{N}[\Omega_A]$ belong to the series of integer 0,...,N and represent all the accessible numbers of electrons within Ω_A. As a consequence of 23, the eigenvalues of the population operators of different basins are correlated since they also obey the closure relation

$$\sum_A N[\Omega_A] = N. \tag{24}$$

The expectation values of the population operators

$$\overline{N}[\Omega_A] = \langle \Psi | \hat{N}[\Omega_A] | \Psi \rangle = \int_{\Omega_A} \rho(\mathbf{r})\, d\mathbf{r} \tag{25}$$

can be expressed in terms of the volume integral of the one-electron probability distribution over the basins:

$$\overline{N}[\Omega_A] = \sum_{v=1}^{N} v\, p_v(\Omega_A), \tag{26}$$

where $p_v(\Omega_A)$ is the probability of having v electrons in a spatial region Ω_A. They are real numbers and can be understood as the average of the measurements of the electron numbers $N[\Omega_A]$. They also fulfill a closure relation, i.e.,

$$\sum_{A} \overline{N}[\Omega_A] = N. \tag{27}$$

In fact, these eigenvalues and expectation values are determined simultaneously.

The closure relation of the basin population operators enables to carry out a statistical analysis of the basin populations through the definition of a covariance matrix [67]. The covariance operator is a matrix operator in which elements are deduced from the classical expression of the covariance:

$$\widehat{\mathrm{cov}}(\Omega_A, \Omega_B) = \hat{N}\,[\Omega_A]\hat{N}\,[\Omega_B] - \overline{N}[\Omega_A]\overline{N}[\Omega_B]. \tag{28}$$

The covariance matrix element expectation value is the difference between the actual pair populations $\overline{\Pi}(\Omega_A, \Omega_B)$ and their "classical" analogs $\overline{N}[\Omega_A]\overline{N}[\Omega_B]$ and $\overline{N}[\Omega_A]\big(\overline{N}[\Omega_A] - 1\big)$ in the case of the diagonal elements:

$$\langle\widehat{\mathrm{cov}}(\Omega_A, \Omega_A)\rangle = \overline{\Pi}(\Omega_A, \Omega_A) - \overline{N}[\Omega_A]\big(\overline{N}[\Omega_A] - 1\big), \tag{29}$$

$$\langle\widehat{\mathrm{cov}}(\Omega_A, \Omega_B)\rangle = \overline{\Pi}(\Omega_A, \Omega_B) - \overline{N}[\Omega_A]\overline{N}[\Omega_B]. \tag{30}$$

The diagonal elements of the covariance matrix (the variances) are often noted $\sigma^2\big(\overline{N}\big)$ as they classically represent the square of the standard deviation $\boldsymbol{\sigma}$.

The probability of finding exactly n electron within a given volume Ω_I, the remaining $N - n$ being anywhere outside Ω_I [117], is given by

$$P_n(\Omega_I) = \binom{N}{n} \int_{\Omega_I} d\xi_1 \ldots d\xi_n \int_{\mathbb{R}^3 - \Omega_I} \Psi^* \Psi d\xi_{n+1} \ldots d\xi_N. \tag{31}$$

It can be efficiently evaluated with the algorithm of Cancès et al. [32].

Appendix C: Mathematical Glossary

This appendix provides the mathematical definitions used in the topological analysis of the *ELF*.

Dynamical System

A *dynamical system* is a vector field $\mathbf{X}(\mathbf{m})$ bound on a manifold M. It has no discontinuities. To each and every point of M at position **m,** a formal analogy with a velocity field, $d\mathbf{m}/dt = \mathbf{X}(\mathbf{m})$ where t is a fictitious time, enables the determination of an unique trajectory $h(\mathbf{m})$ by integrating the evolution equation with respect to the time variable. The limit sets of $h(\mathbf{m})$ for $t \leftrightarrow \pm\infty$ are called the α and ω limit sets. Although the analogy with a velocity field is purely formal, this method is widely used to model the time evolution of many phenomena.

A *gradient dynamical system* is the gradient vector field $\nabla V(\mathbf{m})$ of a function, called *potential function*, the first and second derivatives of which are defined at any point of M.

Critical Points

Two types of points are defined according to the value of $\mathbf{X}(\mathbf{m})$; on the one hand are the *wandering points* for $\mathbf{X}(\mathbf{m}) \neq 0$ and on the other hand the *critical points* for $\mathbf{X}(\mathbf{m}_c) = 0$. A critical point is either an α or an ω limit of a trajectory. The *stable manifold* of m_c is the set of points of the trajectories for which m_c is an ω limit, whereas the *unstable manifold* of m_c the set of trajectories for which it is an α limit. The dimension of the *unstable manifold* is called *index* of the *critical point*. The set of the *critical points* satisfies the Poincaré–Hopf formula:

$$\sum_{\mathrm{P}} (-1)^{I_{\mathrm{P}}} = \chi(M), \tag{32}$$

where I_P is the index of the *critical point* P and $\chi(M)$ the Euler characteristic of the manifold.

A *basin* is the stable manifold of a critical point of index $I_P = 0$, called *attractor*. The stable manifold of a critical point of index $I_P > 0$ is called *separatrix* and is the border of two or more basins.

The *index* of a *critical point* m_c of a *gradient dynamical system* is the number of positive eigenvalues of the matrix of the second derivatives of the *potential function* at m_c. In this case, a *critical point* is said to be *hyperbolic* if none of the eigenvalues are zero. In the case of a *gradient dynamical system*, the index of a critical point is the number of positive eigenvalues of the matrix of the second derivatives of its *potential function* at m_C. A *critical point* is said *hyperbolic* if none of the eigenvalues are zero.

Domain

A *domain* is a subset M_A of M such that any two points **a** and **b** belonging to the M_A can be connected by a path totally contained in *MA*.

Computational Details

Molecular wave function calculations have been carried out with the Gaussian-09 software [118] at the B3LYP [119–122] hybrid Hartree–Fock density functional level with the cc-pVTZ basis set [123, 124]. Calculations of crystalline solids have been performed with the CRYSTAL98 program [125]. The *ELF* analysis was performed by means of TopMod [126] and Topond98 [127] packages. The graphical representations of the *ELF* isosurfaces have been done with the Amira software [128].

References

1. Heelan PA (2003) Ann N Y Acad Sci 988(1):114
2. Pastoors A, Lenssen-Erz T, Ciqae T, Kxunta U, Thao T, Bégouën R, Biesele M, Clottes J (2015) Camb Archaeol J 25:551
3. Dalton J (1808) New system of chemical philosophy. R. Bickerstaff, London
4. Berzélius JJ (1819) Essai sur la théorie des proportions chimiques et sur l'influence chimique de l'électricité, par J. J. Berzélius,. . . Traduit du suédois sous les yeux de l'auteur et publié par lui-même. Méquignon-Marvis, Paris
5. Laming R (1845) Philos Mag 27:420
6. Stoney GJ (1881) Philos Mag 11:381
7. Lewis GN (1916) J Am Chem Soc 38:762
8. Thomson JJ (1904) Philos Mag 7:237
9. Rutherford E (1911) Philos Mag Ser 6 21:669
10. Abegg A (1904) Z Anorg Chem 39:330
11. Kossel W (1916) Ann Phys 354(3):229
12. Langmuir I (1919) J Am Chem Soc 41:868
13. Langmuir I (1920) J Am Chem Soc 42:274
14. Huggins ML (1922) Science 55:679
15. Ingold CK (1922) J Chem Soc 121:1133
16. Ingold CK (1933) J Chem Soc 143:1120
17. Linnett JW (1961) J Am Chem Soc 83:2643
18. Linnett JW (1964) The electronic structure of molecules. A new approach. Methuen, London
19. Sidgwick NV, Powell HM (1940) Proc R Soc A 176:153
20. Gillespie RJ, Nyholm RS (1957) Quart Rev Chem Soc 11:339
21. Gillespie RJ (1963) J Chem Educ 40:295
22. Gillespie RJ (1991) Chem Soc Rev 21:59
23. Gillespie RJ, Robinson EA (1996) Angew Chem Int Ed Engl 35:495
24. Dirac PAM (1929) Proc R Soc A 123:714
25. Thom R (1993) Prédire n'est pas expliquer. Flammarion, Paris

26. Artmann K (1946) Z Naturforsch 1:426
27. Howard J, Zimmerman K, Rysselberghe PV (1949) J Chem Phys 17(7):598
28. Scemama A, Caffarel M, Savin A (2007) J Comput Chem 28:442
29. Daudel R (1953) C R Acad Sci 237(12):601
30. Daudel R, Odiot S, Brion H (1954) J Chim Phys 51(2):74
31. Daudel R, Brion H, Odiot S (1955) J Chem Phys 23(11):2080
32. Cancès E, Keriven R, Lodier F, Savin A (2004) Theor Chem Acc 111:373
33. Gallegos A, Carbó-Dorca R, Lodier F, Cancès E, Savin A (2005) J Comput Chem 26:455
34. Abraham RH, Marsden JE (1994) Foundations of mechanics. Addison Wesley, Redwood City
35. Becke AD, Edgecombe KE (1990) J Chem Phys 92:5397
36. Silvi B, Savin A (1994) Nature 371:683
37. Häussermann U, Wengert S, Nesper R (1994) Angew Chem Int Ed Engl 33:2069
38. Keesom W, Taconis K (1938) Physica 5:161
39. Abraham RH, Shaw CD (1992) Dynamics: the geometry of behavior. Addison Wesley, Redwood City
40. Silvi B, Fourré I, Alikhani E (2005) Monatsh Chem 136:855
41. Silvi B (2003) J Phys Chem A 107:3081
42. Kohout M, Pernal K, Wagner FR, Grin Y (2004) Theor Chem Acc 112:453
43. Kohout M, Pernal K, Wagner FR, Grin Y (2005) Theor Chem Acc 113:287
44. von Weizsäcker CF (1935) Z Phys 96:431
45. Savin A, Becke AD, Flad J, Nesper R, Preuss H, von Schnering HG (1991) Angew Chem Int Ed Engl 30:409
46. Savin A, Nesper R, Wengert S, Fässler TF (1997) Angew Chem Int Ed Engl 36:1809
47. Burdett JK, McCormick TA (1998) J Phys Chem A 102:6366
48. Nalewajski RF, Koster AM, Escalante S (2005) J Phys Chem A 109(44):10038
49. Dobson JF (1991) J Chem Phys 94:4328
50. Gillespie RJ, Robinson EA (2007) J Comput Chem 28:87
51. Savin A, Silvi B, Colonna F (1996) Can J Chem 74:1088
52. Kohout M, Wagner FR, Grin Y (2002) Theor Chem Acc 108:150
53. Calatayud M, Andrés J, Beltrán A, Silvi B (2001) Theor Chem Acc 105:299
54. Fuster F, Silvi B (2000) Theor Chem Acc 104:13
55. Alikhani ME, Fuster F, Silvi B (2005) Struct Chem 16:203
56. Gutierrez-Oliva S, Joubert L, Adamo C, Bulat F, Zagal J, Toro-Labbe A (2006) J Phys Chem A 110:5102
57. Krebs E, Silvi B, Raybaud P (2009) J Chem Theory Comput 5(3):580
58. Weinhold F, Klein RA (2012) Mol Phys 110(9–10):565
59. Weinhold F, Klein RA (2014) Chem Educ Res Pract 15:276
60. Silvi B, Gillespie R (2007) In: Matta CF, Boyd RJ (eds) The quantum theory of atoms in molecules: from solid state to DNA and drug design. Wiley, New York, pp 141–161
61. Pitzer KS (1946) J Am Chem Soc 67:1126
62. Bader RFW (1990) Atoms in molecules: a quantum theory. Oxford University Press, Oxford
63. Raub S, Jansen G (2001) Theor Chem Acc 106:223
64. Ponec R, Chaves J (2007) J Comput Chem 28:109
65. Gonthier JF, Steinmann SN, Wodrich MD, Corminboeuf C (2012) Chem Soc Rev 41:4671
66. Lepetit C, Silvi B, Chauvin R (2003) J Phys Chem A 107:464
67. Silvi B (2004) Phys Chem Chem Phys 6:256
68. Gillespie RJ, Silvi B (2002) Coord Chem Rev 233–234:53
69. Silvi B, Savin A, Kempf J, von Schnering H (1994) Bull Pol Acad Sci 42:413
70. Silvi B, Pilmé J, Fuster F, Alikhani EM (2003) In: Russo N, Witko M (eds) Metal-ligand interactions in molecular, nano, micro, and macro-systems in complex environments, NATO-ASI series. Kluwer, Dordrecht, pp 241–284

71. Chesnut DB (2000) J Phys Chem A 104:11644
72. Gillespie RJ, Noury S, Pilmé J, Silvi B (2004) Inorg Chem 43:3248
73. de Courcy B, Pedersen LG, Parisel O, Gresh N, Silvi B, Pilmé J, Piquemal JP (2010) J Chem Theory Comput 6(4):1048
74. Burkhardt A, Wedig U, von Schnering HG, Savin A (1993) Z Anorg Allg Chem 619:437
75. Silvi B, Gatti C (2000) J Phys Chem A 104:947
76. Pauling L (1948) The nature of the chemical bond. Cornell University Press, Ithaca
77. Hohenberg P, Kohn W (1964) Phys Rev 136:B864
78. Parr RG, Szentpály LV, Liu S (1999) J Am Chem Soc 121:1922
79. Girichev AG, Giricheva NI, Vogt N, Girichev GV, Vogt J (1996) J Mol Struct 384(2–3):175
80. Herzberg G (1945) Molecular spectra and molecular structure. II. Infrared and Raman spectra of polyatomic molecules. Van Nostrand, Princeton
81. Wagman D, Evans W, Parker V, Schumm R, Halow I, Bailey S, Churney K, Nuttall R (1982) J Phys Chem Ref Data 11(Suppl 2):1
82. Krokidis X, Noury S, Silvi B (1997) J Phys Chem A 101:7277
83. Thom R (1972) Stabilité Structurelle et Morphogénèse. Intereditions, Paris
84. Berski S, Andrés J, Silvi B, Domingo L (2003) J Phys Chem A 107:6014
85. Polo V, Andres J, Castillo R, Berski S, Silvi B (2004) Chem Eur J 10:5165
86. Santos JC, Andrés J, Aizman A, Fuentealba P, Polo V (2005) J Phys Chem A 109(16):3687
87. Berski S, Andrés J, Silvi B, Domingo LR (2006) J Phys Chem A 110:13939
88. Andrés J, Berski S, Domingo LR, Polo V, Silvi B (2011) Curr Org Chem 15:3566
89. Andrés J, Berski S, Domingo LR, González-Navarrete P (2012) J Comput Chem 33:748
90. González-Navarrete P, Domingo LR, Andrés J, Berski S, Silvi B (2012) J Comput Chem 33:2400
91. Chattaraj PK, Fuentealba P, Gómez B, Contreras R (2000) J Am Chem Soc 122:348
92. Contreras-García J, Martín Pendás A, Silvi B, Recio JM (2008) J Phys Chem Solids 69:2204
93. Contreras-García J, Silvi B, Martín Pendás A, Recio JM (2009) J Phys Chem B 113:1068
94. Contreras-Garcia J, Martín Pendás A, Recio JM, Silvi B (2009) J Chem Theory Comput 5 (1):164. doi:10.1021/ct800420n
95. Contreras-Garcia J, Mori-Sanchez P, Silvi B, Recio JM (2009) J Chem Theory Comput 5 (8):2108
96. Reichlin R, Brister KE, McMahan AK, Ross M, Martin S, Vohra YK, Ruoff AL (1989) Phys Rev Lett 62:669
97. Bader RFW, Essén H (1984) J Chem Phys 80:1943
98. Fuster F, Grabowski SJ (2011) J Phys Chem A 115(35):10078
99. Grabowski SJ (2011) Chem Rev 111(4):2597
100. Llusar R, Beltrán A, Andrés J, Noury S, Silvi B (1999) J Comput Chem 20:1517
101. Chesnut DB (2001) Chem Phys 271:9
102. Fourré I, Silvi B, Sevin A, Chevreau H (2002) J Phys Chem A 106:2561
103. Fourré I, Silvi B (2007) Heteroat Chem 18:135
104. Shaik SS, Danovich D, Silvi B, Lauvergnat D, Hiberty P (2005) Chem Eur J 21:6358
105. Llusar R, Beltrán A, Andrés J, Fuster F, Silvi B (2001) J Phys Chem A 105:9460
106. Feliz M, Llusar R, Andrés J, Berski S, Silvi B (2002) New J Chem 26:844
107. Andrés J, Berski S, Feliz M, Llusar R, Sensato F, Silvi B (2005) C R Chim 8:1400
108. Andrés J, Feliz M, Fraxedas J, Hernandez V, Lopez-Navarrete JT, Llusar R, Sauthier G, Sensato FR, Silvi B, Bo C, Campanera JM (2007) Inorg Chem 46:2159
109. Shaik SS, Maitre P, Sini G, Hiberty PC (1992) J Am Chem Soc 114:7861
110. Shaik SS, Danovich D, Wu W, Hiberty P (2009) Nat Chem 1:443
111. Polo V, Andrés J, Silvi B (2007) J Comput Chem 28:857
112. Santos JC, Tiznado W, Contreras R, Fuentealba P (2004) J Chem Phys 120(4):1670
113. Pilme J, Piquemal JP (2008) J Comput Chem 29:1440
114. Chaudret R, De Courcy B, Marjolin A, van Severen MC, Ren PY, Wu JC, Parisel O, Piquemal JP (2012). In: Simos T, Maroulis G (eds) International conference of computational

methods in sciences and engineering 2009 (ICCMSE 2009), AIP conference proceedings, vol 1504, pp. 699–702
115. Robin C, Nohad G, Andrés CG, Anthony S, Jean-Philip P (2013) Can J Chem 91:804
116. Diner S, Claverie P (1976) In: Chalvet O, Daudel R, Diner S, Malrieu JP (eds) Localization and delocalization in quantum chemistry, vol II. Reidel, Dordrecht, pp 395–448
117. Bader RFW, Stephens ME (1974) Chem Phys Lett 26:445
118. Frisch MJ, Trucks GW, Schlegel HB, Scuseria GE, Robb MA, Cheeseman JR, Scalmani G, Barone V, Mennucci B, Petersson GA, Nakatsuji H, Caricato M, Li X, Hratchian HP, Izmaylov AF, Bloino J, Zheng G, Sonnenberg JL, Hada M, Ehara M, Toyota K, Fukuda R, Hasegawa J, Ishida M, Nakajima T, Honda Y, Kitao O, Nakai H, Vreven T, Montgomery JA Jr, Peralta JE, Ogliaro F, Bearpark M, Heyd JJ, Brothers E, Kudin KN, Staroverov VN, Kobayashi R, Normand J, Raghavachari K, Rendell A, Burant JC, Iyengar SS, Tomasi J, Cossi M, Rega N, Millam JM, Klene M, Knox JE, Cross JB, Bakken V, Adamo C, Jaramillo J, Gomperts R, Stratmann RE, Yazyev O, Austin AJ, Cammi R, Pomelli C, Ochterski JW, Martin RL, Morokuma K, Zakrzewski VG, Voth GA, Salvador P, Dannenberg JJ, Dapprich S, Daniels AD, Farkas A, Foresman JB, Ortiz JV, Cioslowski J, Fox DJ (2009) Gaussian 09 revision D.01. Gaussian Inc., Wallingford
119. Becke AD (1993) J Chem Phys 98:5648
120. Becke AD (1988) Phys Rev A 38:3098
121. Lee C, Yang Y, Parr RG (1988) Phys Rev B37:785
122. Miehlich B, Savin A, Stoll H, Preuss H (1989) Chem Phys Lett 157:200
123. Dunning TH Jr (1989) J Chem Phys 90:1007
124. Kendall RA, Dunning TH Jr, Harrison RJ (1992) J Chem Phys 96:6796
125. Saunders VR, Dovesi R, Roetti C, Causà M, Harrison NM, Orlando R, Zicovitch-Wilson CM (1998) CRYSTAL98, User's manual. Torino, Italy
126. Noury S, Krokidis X, Fuster F, Silvi B (1999) Comput Chem 23:597
127. Gatti C (1998) Topond98 manual. CNR-CSRSRC, Milano
128. Amira 3.0 (2002) TGS, Template Graphics Software Inc., San Diego

Struct Bond (2016) 170: 249–264
DOI: 10.1007/430_2015_191

Published online: 7 November 2015

Comparison of the Cr–Cr Quadruple and Quintuple Bonding Mechanisms

Andrés Falceto and Santiago Alvarez

Abstract A molecular orbital analysis of model unbridged complexes with Cr–Cr formal bond orders four and five is presented, based on density functional calculations. The orbital and symmetry analysis discloses a special type of δ bonding in the case of the $[Cr_2L_4]^{2+}$ complexes that induces a significant bond shortening going from quadruple Cr^{II}–Cr^{II} to quintuple Cr^{I}–Cr^{I} bonds.

Keywords DFT calculations · Metal–metal quintuple bonds · Molecular orbitals · Pyramidality effect

Contents

A. Falceto and S. Alvarez (✉)
Departament de Química Inorgànica and Institut de Química Teòrica i Computacional, Universitat de Barcelona, Martí i Franquès 1-11, 08028 Barcelona, Spain
e-mail: santiago@qi.ub.es

1 Introduction

The existence of quadruple bonds between two metal atoms has been one of the most appealing developments in bonding theory of the last century. Its discovery in the 1960s triggered a vast amount of research that led to the synthesis and characterization of a wide variety of quadruply bonded complexes [1]. A few decades elapsed, though, before the first quintuple Cr–Cr bond was reported by Power and coworkers [2], followed soon by a variety of systems with quintuple Cr–Cr [3] or Mo–Mo bonds [4]. Here we are concerned with the structural and electronic effects associated with multiple metal–metal bonding [5] and with the analogies and differences between quadruple and quintuple Cr–Cr bonds.

2 The History of Multiple Bonding

In his landmark paper [6], Gilbert N. Lewis described the valence electron shell of an atom as a cube, so each of its vertices could be occupied by one of the eight electrons required by the octet rule. For atoms with incomplete shells, the octet rule could be achieved by sharing an electron pair with a neighboring atom, represented in his model as two cubes sharing an edge or a face (Fig. 1).

Lewis was aware of the limitations of his cubical atom model, since it could neither explain "the phenomenon of the mobility about a single bond" nor represent the triple bond. He then placed the electrons paired on four edges of the cube, in such a way as to represent the tetrahedral orientation of the four bonds of an atom. "As usual," he said, "two tetrahedra, attached by one, two or three corners of each represent respectively the single, the double and the triple bond." As a more practical means, he represented the triple bond in acetylene by drawing three colons between the symbols of the two carbon atoms: **H:C:::C:H**. He did not go further, since he was considering only main group elements, and to him, "The triple bond represents the highest possible degree of union between two atoms."

According to Mulliken [7], "it was Hund [8] who first referred to σ and π bonds: a single bond is a σ bond, a double bond is a σ plus one π bond, a triple bond is a σ

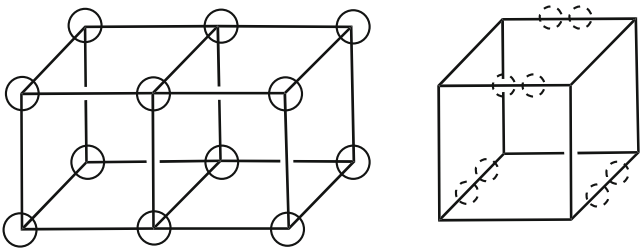

Fig. 1 Lewis cubical atom model of a double bond (*left*) and placement of the electron pairs on edges of the cube to account for the tetrahedral arrangement of the four bonds of an atom (*right*)

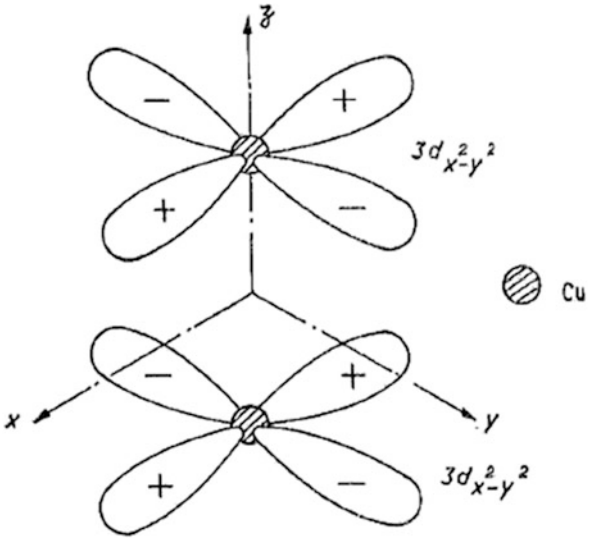

Fig. 2 Depiction by Figgis and Martin of the δ-type overlap between the x^2-y^2 orbitals of two Cu atoms in copper(II) acetate

plus two π bonds, and each bond corresponds to a pair of electrons in a bond MO localized around the two atoms of the bond."

A new bond type, the δ bond, was introduced in 1956 by Figgis and Martin [9] in their analysis of bonding in the dinuclear molecule of copper(II) acetate (Fig. 2). According to those authors, it was:

> the first case in which a δ-bond is the sole direct link between two atoms. However, the bond is so weak that the configuration of the binuclear molecule can only be maintained by the four bridging acetate groups.

They went on to analyze the diamagnetism of chromium(II) acetate, whose structure had recently been solved by Niekerk and Schoening [10, 11], and explicitly proposed the existence of σ, π, and δ metal–metal bonding components, which they supposed to be weak, but "sufficient effectively to pair the spins of the eight electrons occupying 3d levels in each chromous acetate molecule and to account for the observed diamagnetism." They did not verbalize, however, that they were describing for the first time a quadruple bond.

A few years later, in 1963, Cotton and coworkers determined the structure of "$CsReCl_4$," which was seen to correspond to a triangular cluster (Fig. 3) [12]. They noted "very short" Re–Re distances (2.47 Å) and carried out a molecular orbital symmetry analysis and concluded that "There are just six bonding orbitals which are filled by the 12 electrons, thus accounting for the experimentally observed diamagnetism." If only implicitly, they were stating that there were Re–Re double bonds in the anionic cluster.

At about the same time, Kuznetsov and Koz'min reported the structure of a salt of what they formulated as the $[Re_2Cl_8]^{4-}$anion [13] and noticed a short (2.22 Å) Re–Re distance. Cotton and coworkers then redetermined the structure [14], verified that the correct formula was $[Re_2Cl_8]^{2-}$, and offered a convincing theoretical

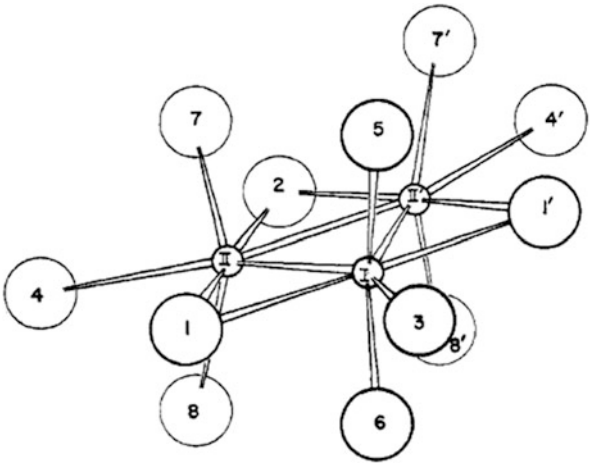

Fig. 3 The structure of $Cs_3[Re_3Cl_{12}]$ determined by Cotton and coworkers in 1963

explanation of the metal–metal bonding that could account for both the diamagnetism and the eclipsed conformation and concluded "This would appear to be the first quadruple bond to be discovered." The story is told in more detail in a book [1] and in a recent review [15], which summarizes also the synthesis in 2005 by Power and coworkers of the first quintuple Cr–Cr bond and further developments in subsequent years [2].

3 Variability of the Cr–Cr Distances and Pyramidality Effect

To illustrate the structural variability that the quadruple and quintuple bonds have incorporated into present-day chemistry, we show in Fig. 4 the distribution of bond distances as a function of bond order for the Cr–Cr bonds, compared with those for C–C and Mo–Mo bonds, as found in a Cambridge Structural Database (CSD) search [16]. It can be seen that the metal–metal multiple bonds have not only expanded the bond orders that can be achieved, but also that there is a much wider variation in bond distances. Also, the variation of Cr–Cr bond distances with the same bond order is much larger than in the case of the Mo–Mo and C–C bonds. Thus, while the C–C bonds vary in a wide sample of structures analyzed by us between 1.54 and 1.16 Å (but a C–C bond as long as 1.70 Å has been described [17]), the Cr–Cr distances vary between 2.97 and 1.71 Å [18].

In the case of the Cr–Cr quadruple bonds, the wide range of bond distances found (Fig. 4) led the Cotton group to classify some of them as "super-short" [1]. We found [19, 20] that the bond distances and bond angles (α in Fig. 6) are nicely correlated, regardless of the existence of one or two axially coordinated ligands, thus providing some rationale for the wide range of lengths of the Cr–Cr

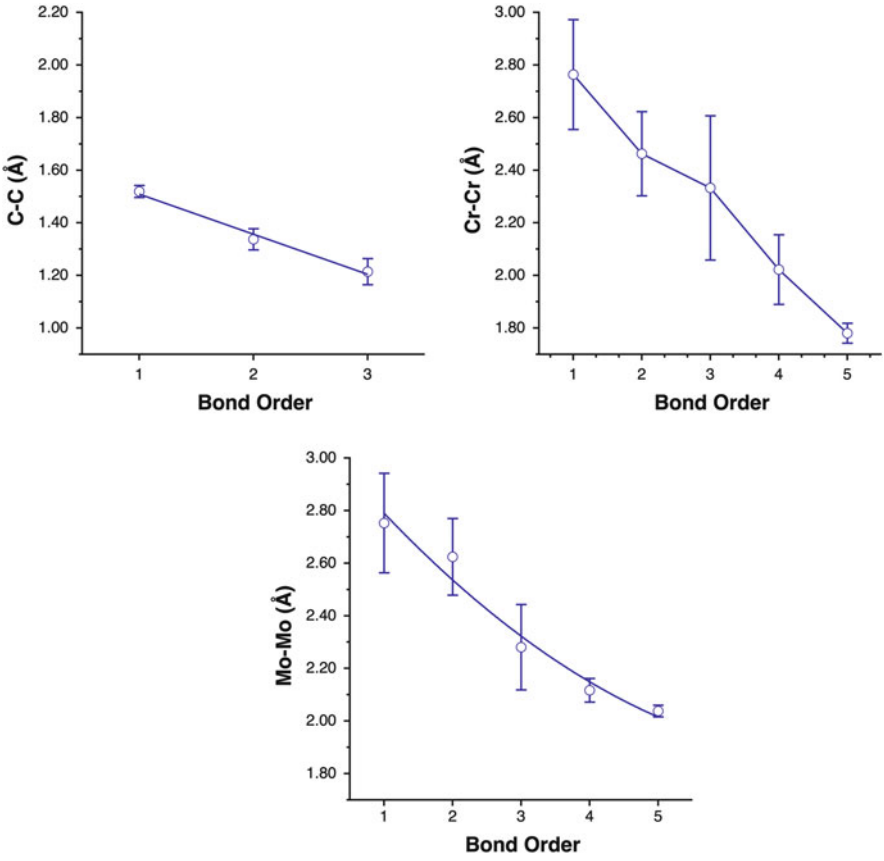

Fig. 4 Distribution of the bond lengths found in the CSD as a function of the bond order for (from *top* to *bottom*) C–C, Cr–Cr, and Mo–Mo bonds

quadruple bonds. Such a correlation still holds 20 years later, after incorporation of a number of new structures (Fig. 5). A similar correlation was seen to be present also in quadruple bonds involving Mo, W, Re, or Os and including the unbridged Re–halide complexes [20].

A molecular orbital explanation was then provided for the strengthening of the metal–metal bond at larger bond angles, based on extended Hückel calculations and confirmed by CASSCF calculations on Os(III) and Os(IV) compounds [20]. We argued that, beyond the geometrical constraints imposed by bridging ligands that join two Cr^{II} ions, the pyramidalization of the coordination sphere around them favors a hybridization of both σ and π components of the quadruple bond (Fig. 6), thus strengthening the Cr–Cr bond as the bond angle increases. Detailed studies on hybridization at metal centers in transition metal complexes were published by Mingos and Zhenyang [21, 22].

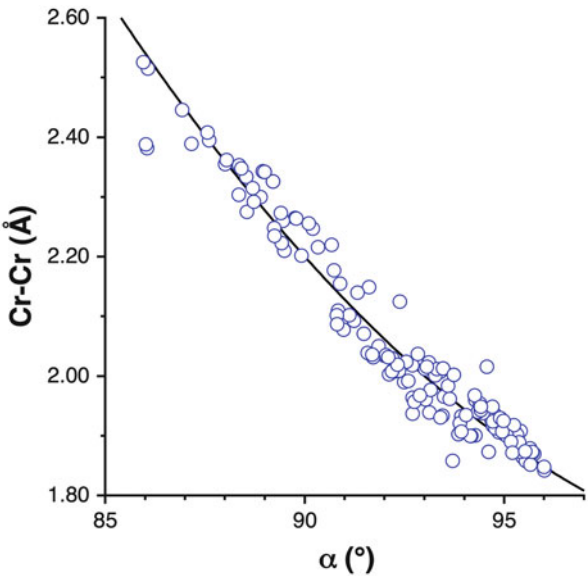

Fig. 5 Correlation between the Cr–Cr bond distance and the average Cr–Cr–L bond angle in quadruply bonded Cr(II) complexes with N or O donor atoms for 184 structural data sets found in the CSD

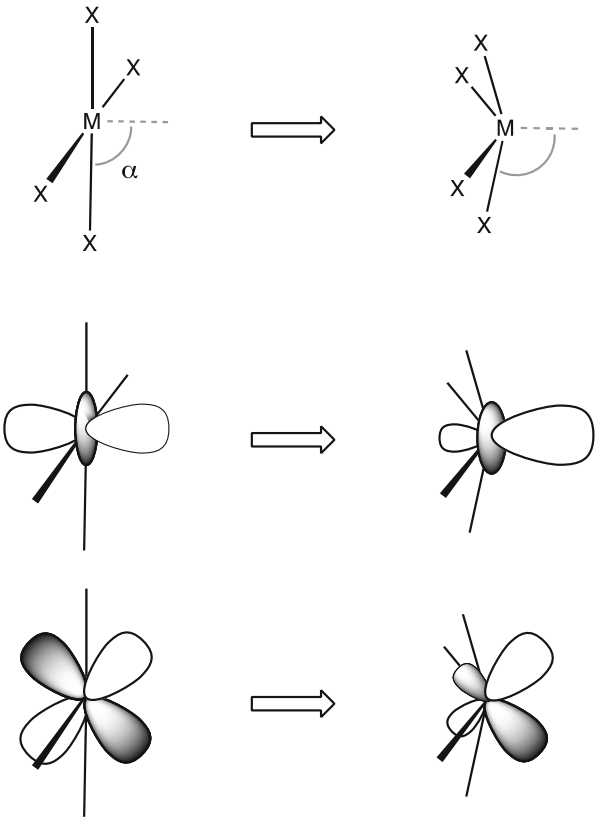

Fig. 6 Hybridization of the s and p metal d orbitals upon pyramidalization of the MX_4 fragments in a multiply bonded M_2X_8 complex

4 Representative MO Diagrams for Cr–Cr Multiple Bonds

The simple MO scheme devised by Cotton when first reporting a quadruple bond can be represented by the Kohn–Sham orbitals of the model Cr(II) complex to be discussed later in this work, $[Cr_2(NH_3)_8]^{4+}$. The energy ordering of the d-based MOs responsible for the metal–metal bond (Fig. 7) is $\sigma \leq \pi < \delta < \delta^* < \pi^* \leq \sigma^*$, although the relative energies of the σ and π orbitals may vary depending on the Cr–Cr–N bond angle, without actually affecting the general bonding description. Notice that there is only one δ bonding orbital (b_{2g}), since the x^2-y^2 metal orbital (b_{1g}) is involved in metal–ligand bonding and it is unoccupied due to its strong antibonding metal–ligand character.

In the case of a quintuply bonded model $[Cr_2(NH_3)_4]^{2+}$, a similar orbital pattern emerges (Fig. 8), but with some significant differences. First, due to the lesser coordination number, the x^2-y^2 orbital $a_{1g}(\delta)$ is effectively metal–metal δ bonding. As a result, there are now five metal–metal bonding MOs to accommodate the 10 valence electrons of the two Cr(I) ions and account for the formal quintuple bond, as initially proposed by Power and coworkers [2]. Another relevant aspect is that the π-bonding b_{2u} orbital is now devoid of the metal–ligand antibonding character found in the $e_u(\pi)$ orbitals of the quadruple bonds (Fig. 7) and is therefore significantly more stable.

Computationally, the multiple metal–metal bonds have long posed a problem, since the small gap between the δ and δ* orbitals results in significant multiconfigurational character of the wave function [23]. Naturally, since that orbital gap increases for shorter metal–metal distances, it has been found that the single configuration description of the electronic structure becomes a better approximation at short bond lengths [20]. For quintuply bonded system with bridging ligands and a short Cr–Cr bond distance, the expected $\sigma^2\pi^4\delta^4$ configuration may make up 70% of the multiconfigurational CASSCF wave function [18]. However, for an unsupported paramagnetic Cr(I) compound with a long (2.65 Å) Cr–Cr distance, a highly multiconfigurational wave function is found for the singlet state, which is nearly degenerate with triplet and quintet states [18]. In general, however, DFT calculations that take into account some of the electron correlation provide rather accurate results in terms of bond distances and angles [24]. The multiconfigurational character becomes critical in the absence of ligands, as in the neutral Cr_2, Mo_2, and W_2 diatoms, for which a sextuple metal–metal bond is proposed [25, 26], but which are out of the scope of this paper and will not be discussed further.

Recently [24], we have carried out a theoretical and computational study of quintuply bonded Cr^I complexes, in which both the pyramidality effect and the influence of the bridging ligand topology were explored in depth. In summary, we concluded that besides the pyramidality effect, there is a dependence on the bite distance of the ligand, such that ligands with larger bites give longer Cr–Cr distances for the same pyramidality angle in order to optimize metal–ligand bonding. Moreover, the variation of Cr–Cr distances for ligands with the same bite

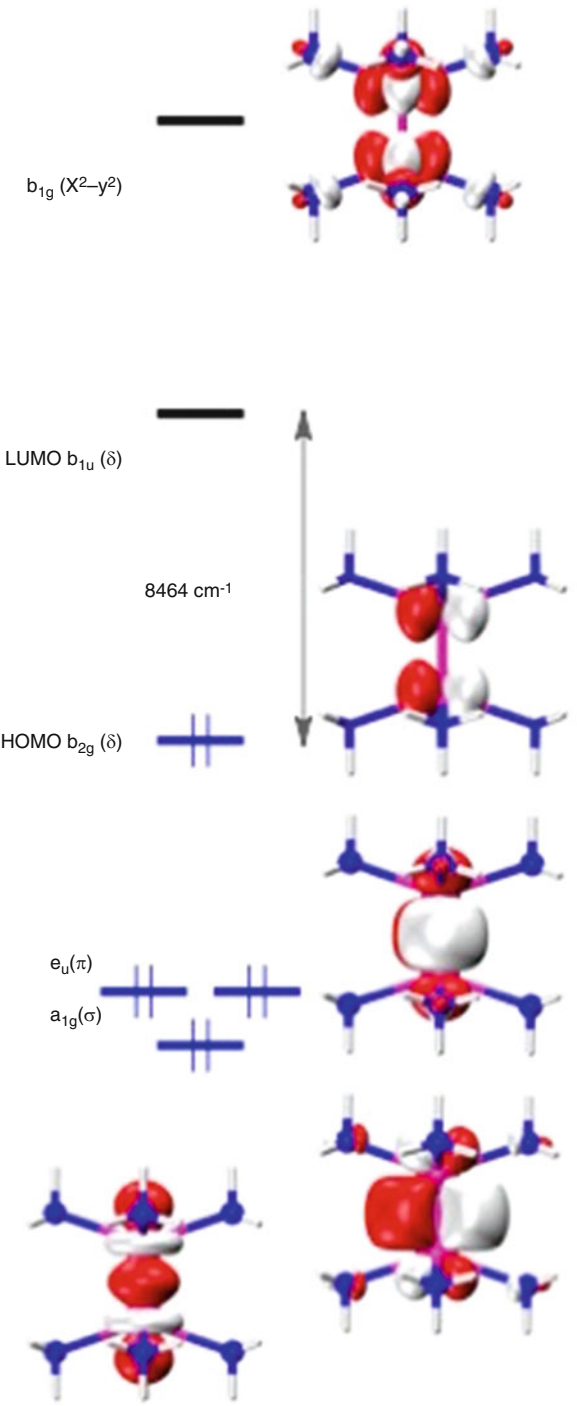

Fig. 7 Molecular orbitals of the d-block for the $[Cr_2(NH_3)_8]^{4+}$ cation with a quadruple Cr–Cr bond

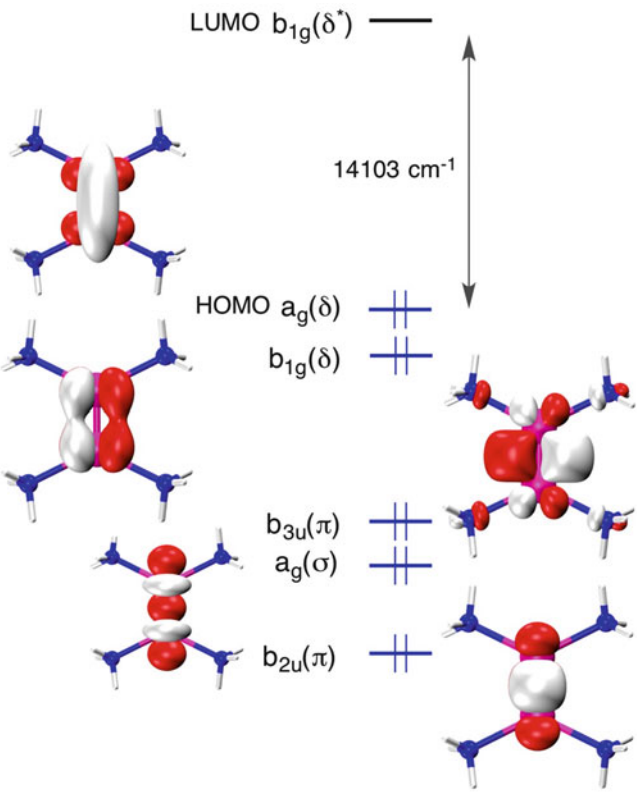

Fig. 8 Molecular orbitals of the d-block for the $[Cr_2(NH_3)_4]^{2+}$ cation with a quintuple Cr–Cr bond

depends on the orientation of the ligand's lone pair orbitals. In brief, the optimal Cr–Cr bond distance is estimated at around 1.6 Å, and the longer distances experimentally found are the result of adjusting the size of the Cr_2 unit to maximize the metal–ligand bonding interactions.

5 Quadruple vs. Quintuple Cr–Cr Bonds

In this section we discuss the results of calculations on model Cr^{II} and Cr^{I} complexes with monodentate ligands. In this way, we can analyze the pyramidality effect without the geometric constraints imposed by the bridging ligand. As a ligand, we have chosen the ammonia molecule, to keep a comparable donor set as in the experimentally known amidinato complexes, and we explore the behavior of complexes with different number of ligands, $[Cr_2(NH_3)_{2n}]^{2+/4+}$, where $n = 2$, 3, and 4. The calculated Cr–Cr distances are presented in Fig. 9 as a function of the

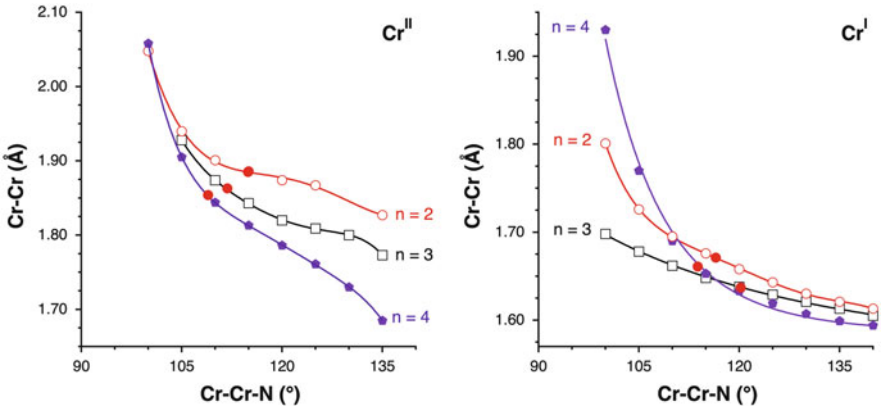

Fig. 9 Calculated Cr–Cr bond distance as a function of the Cr–Cr–L bond angle in model complexes $[Cr_2(NH_3)_{2n}]^{4+}$ (*left*) and $[Cr_2(NH_3)_{2n}]^{2+}$ (*right*). The *filled circles* correspond to the optimized structures

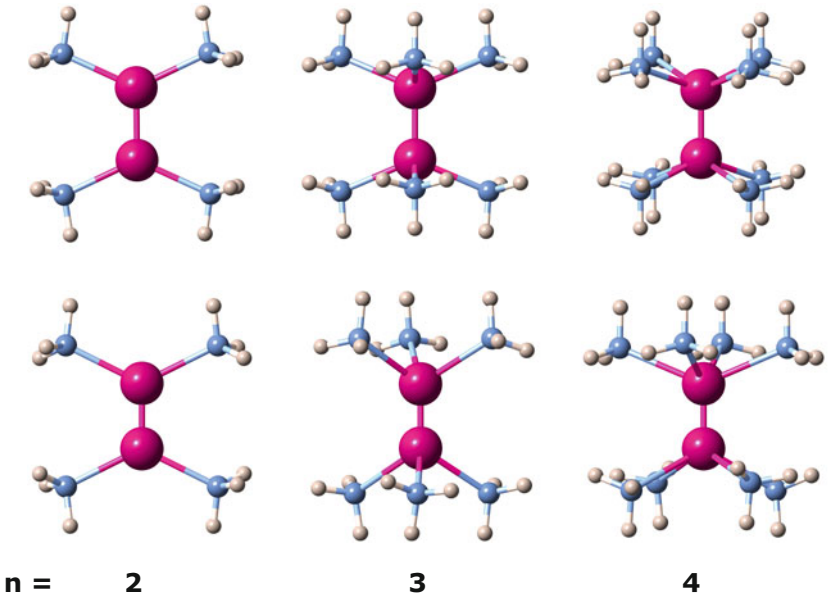

Fig. 10 Optimized geometries of the $[Cr_2(NH_3)_{2n}]^{n+}$ complexes with quadruple ($n = 4$, *upper row*) and quintuple ($n = 2$, *lower row*) Cr–Cr bonds

bond angle, while the optimized geometries are shown in Fig. 10 and numerical data are given in Table 1.

In Fig. 9 we can see a similar pyramidality behavior of the Cr^{II} and Cr^{I} complexes, with a strong dependence of the bond distance on the bond angle at small angles, but only a moderate dependence at larger angles. It can also be seen

Table 1 DFT calculated Cr–Cr and Cr–N bond distances and Cr–Cr–L bond angles in $[Cr_2(NH_3)_{2n}]$ model complexes of Cr^{II} and Cr^{I}

Compound	Conformation	Cr–Cr	Cr–N	α (°)
Cr^{II}				
$[Cr_2(NH_3)_4]^{4+}$	Eclipsed D_{2h}	1.885	2.105	114.9
$[Cr_2(NH_3)_6]^{4+}$	Eclipsed C_{2v}	1.863	2.135	111.9
$[Cr_2(NH_3)_8]^{4+}$	Eclipsed D_{4h}	1.854	2.191	109.0
Cr^{I}				
$[Cr_2(NH_3)_4]^{2+}$	Eclipsed D_{2h}	1.671	2.170	116.5
$[Cr_2(NH_3)_6]^{2+}$	Staggered D_{3d}	1.637	2.291	120.2
$[Cr_2(NH_3)_8]^{2+}$	Staggered D_{4d}	1.661	2.396	113.8

that the number of ligands has little influence in the case of Cr^{I} but for Cr^{II} a higher number of ligands results in shorter bond distances for the same bond angle. The Cr–N bond distances, in contrast, increase with the number of ligands, in agreement with the general trend that bond distances increase with the coordination number of the metal. The Cr^{I}–N bond distances are also found to be longer than the Cr^{II}–N ones in complexes with the same number of ligands, a fact that is associated to the greater covalent character of the metal–ligand bonds for the higher oxidation state [27].

The optimized geometries (Fig. 10 and Table 1) differ for the Cr^{II} and Cr^{I} versions of the $Cr_2(NH_3)_8$ and $Cr_2(NH_3)_6$ complexes. While the quadruply bonded complexes appear in an eclipsed conformation, the quintuply bonded analogues present staggered conformations. The $Cr_2(NH_3)_4$ systems with only two ligands per metal atom, however, present an eclipsed conformation for both bond orders.

As expected, at a given bond angle, the quintuple bonds are shorter than the quadruple ones. Moreover, Table 1 shows that all the optimized quintuple bonds are significantly shorter (1.63−1.67 Å) than the shortest quadruple bond (1.85 Å), a remarkable difference if we take into account that the additional bond is of the supposedly weak δ type. Interestingly, the optimized structures for the quintuply bonded complexes have also larger bond angles than the analogous quadruply bonded ones, in agreement with our finding that the two sets of complexes with *N*-donor sets follow the same bond angle dependence of the bond distance [24].

It must also be noted that the present Cr^{I} model complexes with monodentate ligands yield larger bond angles and shorter distances than complexes with bridging ligands in experimental structures and in calculations reported in a previous work [24]. This behavior has some similarities and some differences with that previously found for Cr^{II} systems [20], as seen in Fig. 11. There we can see that for both Cr^{II} and Cr^{I} the unbridged complexes are expected to present longer Cr–Cr bond distances than bridged ones at the same bond angle. However, the unbridged complexes can adopt the electronically preferred geometries with larger bond angles, resulting in short distances, specially in the case of the Cr^{I} model complexes, which yield quite short Cr–Cr bond lengths.

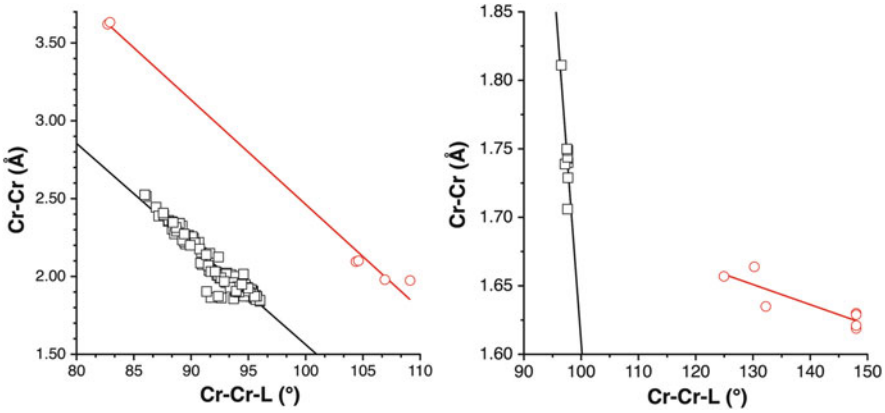

Fig. 11 Cr–Cr bond distances as a function of the Cr–Cr–L bond angle for $Cr_2^{II}L_8$ (*left*) and $Cr_2^{I}L_4$ (*right*) complexes. *Squares* correspond to bridged and *circles* to unbridged complexes; the unbridged Cr^I data comes from calculated structures

6 A Close-Up on the Molecular Orbitals

We have analyzed the bond angle dependence of the composition of the d-block molecular orbitals of the six model complexes with ammonia ligands and will briefly discuss here the most significant differences between the two most relevant cases, those that have the largest number of experimental analogues: the quadruply bonded $[Cr_2(NH_3)_8]^{4+}$ and the quintuply bonded $[Cr_2(NH_3)_4]^{2+}$.

The π orbitals show an increasing p + d hybridization with increasing bond angle in the two cases, accounting for some electronic pyramidality effect. Moreover, the π orbitals are strongly involved in the Cr–Cr vs. Cr–N bonding competition, losing Cr–Cr bonding character and enhancing its participation in Cr–L bonding as the bond angle increases, as can be seen in Fig. 12.

The δ orbital whose nodal planes contain the ligands is practically a pure d metal orbital in both $[Cr_2(NH_3)_8]^{4+}$ and $[Cr_2(NH_3)_4]^{2+}$, unhybridized as dictated by symmetry and practically insensitive to changes in the bond angle. The second δ orbital, in contrast, behaves quite differently in the quadruply bonded $[Cr_2(NH_3)_8]^{4+}$ than in the quintuply bonded $[Cr_2(NH_3)_4]^{2+}$. In the former case, it is strongly involved in metal–ligand bonding, as could be expected for an approximately square planar coordination, and its ligand contribution increases significantly at bond angles greater than 120° (Fig. 13, left). In the quintuply bonded complex, there is little ligand participation, and a strong s + d hybridization appears at small bond angles that decreases dramatically as the bond angle increases (Fig. 13, right).

The interesting symmetry-allowed orbital mixing present in the $Cr^I{}_2L_4$ complexes (Fig. 13, right) incorporates σ character into one of the δ bonding molecular orbitals (see **1** and the MO plot on top of Fig. 13, right), mostly from the chromium 4s atomic orbital. There is also some mixing of the z^2 orbital, which is maximum at around 115°, close to the energy minimum. These results mean that the second δ

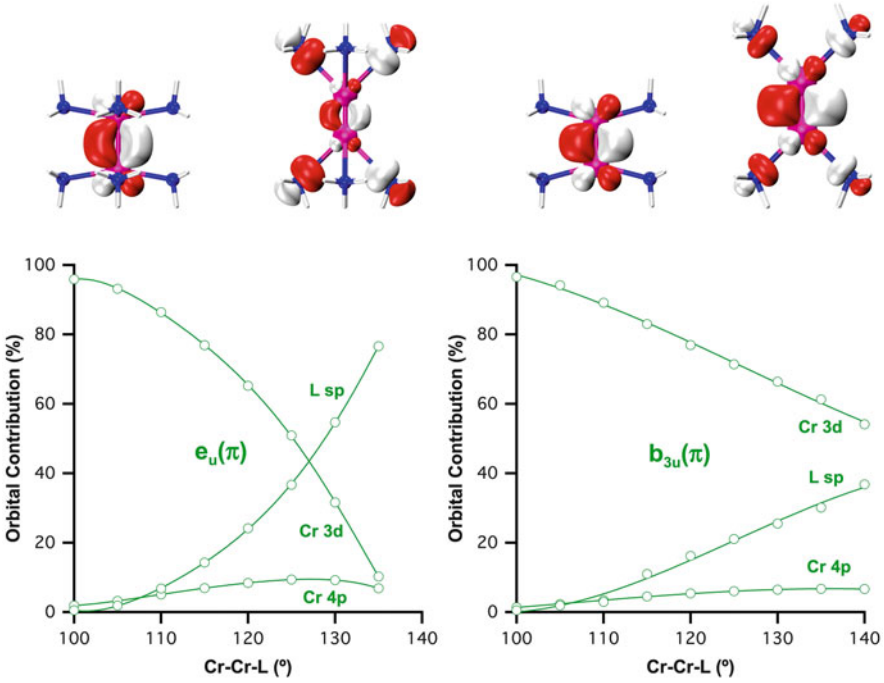

Fig. 12 Contributions to the Cr–Cr π bonding orbital as a function of the Cr–Cr–L bond angle in $[Cr_2(NH_3)_8]^{4+}$ (*left*) and $[Cr_2(NH_3)_4]^{2+}$ (*right*). Plots of the MOs shown on *top* correspond to isocontours of 0.05 at 115 and 135°

component in the quintuple Cr–Cr bonds is stronger than the one present in the quadruple bonds and accounts for the significant bond shortening on going from Cr^{II} to Cr^{I} compounds, which is stronger than one would expect for a pure δ bond. Moreover, the δ component is seen to present an inverted pyramidality effect than the σ and π components that can account for a less pronounced dependence of the bond distance on the bond angle. Notice that the metal p_z orbital is allowed by symmetry to hybridize with this d orbital, but it is not topologically suited and mixes strongly with the z^2 orbital (Fig. 6), and there is practically no $p_z + x^2 - y^2$ mixing in our calculations (Fig. 13, right).

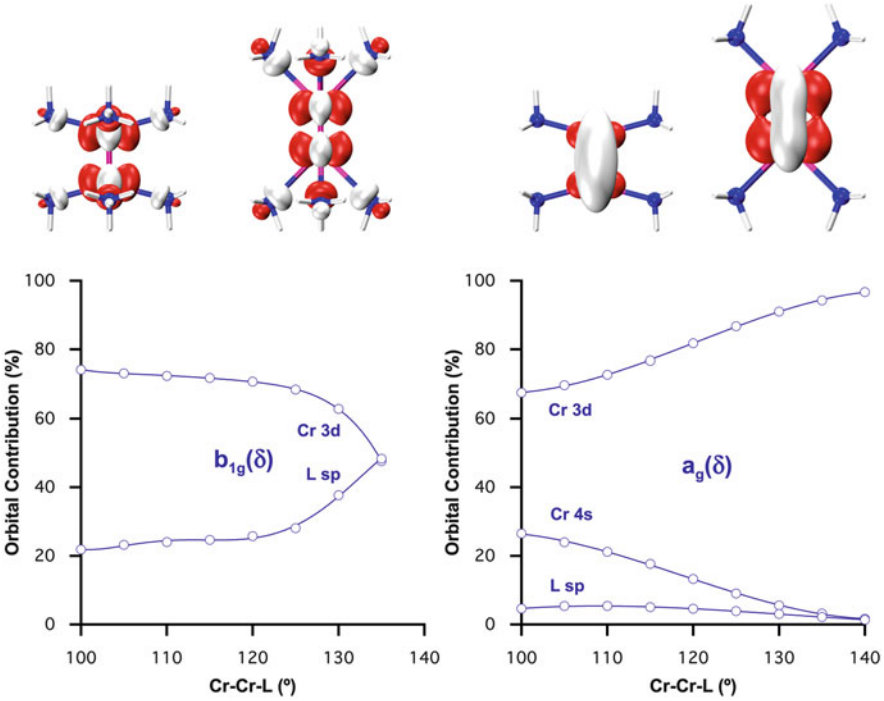

Fig. 13 Contributions to one of the Cr–Cr δ molecular orbitals as a function of the Cr–Cr–L bond angle in $[Cr_2(NH_3)_8]^{4+}$ (*left*) and $[Cr_2(NH_3)_4]^{2+}$ (*right*). Plots of the MOs shown on top correspond to isocontours of 0.05 at 115 and 136°

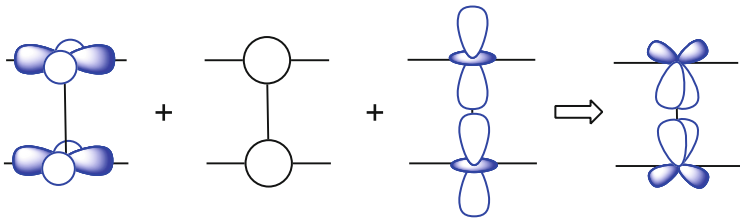

A symmetry analysis indicates that the σ + δ hybridization is only possible in D_{2h} and D_{2d} point groups for $[Cr_2(NH_3)_4]^{x+}$, but neither in D_{3h} or D_{3d} groups of $[Cr_2(NH_3)_6]^{x+}$ nor ih the D_{4h} or D_{4d} groups of $[Cr_2(NH_3)_8]^{x+}$ is it allowed by symmetry. Such hybridization is therefore specific of the M_2L_2 stoichiometry.

7 Conclusions

The second δ bond in quintuply bonded $[Cr_2L_4]^{2+}$ complexes is stronger than the one present in quadruply bonded analogues, as a result of a symmetry-dictated s + d hybridization that introduces significant σ character into the formally δ bonding a_{1g} MO. The strength of the fifth bond is reflected in bond distances some 0.2 Å shorter for Cr^{I} than for Cr^{II} complexes. Moreover, the inverted pyramidality effect on this orbital results in a smaller variability of the Cr–Cr quintuple bond distances as compared to the wide range of bond distances found for the quadruple bonds.

8 Computational Details

The optimizations have been done at the density functional theory (DFT) level with the Gaussian 09 program [28] using the hybrid B3LYP functional. The triple-ζ all-electron Gaussian basis set with polarization functions by Ahlrichs and co-workers has been used for all atoms [29]. A subsequent vibrational analysis has been carried out within the harmonic approximation. For the study of the pyramidality effect, the model complexes $[Cr_2(NH_3)_{2n}]^{2+/4+}$ with $n = 2$, 3, and 4 have been partially optimized at each fixed Cr–Cr–L bond angle. All orbital contributions given have been calculated through a Mulliken population analysis.

Acknowledgments This work was supported by the Spanish Ministerio de Economía y Competitividad (MINECO, project CTQ2011-23862-C02-01). A. F. thanks MINECO for a Ph.D. grant.

References

1. Cotton FA, Murillo CA, Walton RA (2005) Multiple bonds between metal atoms, 3rd edn. Clarendon, Oxford
2. Nguyen T, Sutton AD, Brynda M, Fettinger JC, Long GJ, Power PP (2005) Synthesis of a stable compound with fivefold bonding between two chromium(I) centers. Science 310:844–847
3. Noor A, Kempe R (2015) M5M – Key compounds of the research field metal–metal quintuple bonding. Inorg Chim Acta 424:75–82
4. Nair AK, Harisomahajula NVS, Tsai Y-C (2015) The lengths of the metal-to-metal quintuple bonds and reactivity thereof. Inorg Chim Acta 424:51–62
5. McGrady JE (2013) Metal–metal bonding. In: Reedijk J, Poeppelmeier K (eds) Comprehensive inorganic chemistry II, vol 9. Elsevier, Amsterdam, pp 321–340
6. Lewis GN (1916) The atom and the molecule. J Am Chem Soc 38:762–785
7. Mulliken R (1972) Spectroscopy, molecular orbitals, and chemical bonding. In: Nobel lectures, chemistry 1963–1970. Elsevier, Amsterdam, pp 131–160
8. Hund F (1931) Zur Frage der chemischen Bindung. Z Phys 73:1–30

9. Figgis BN, Martin RL (1956) Magnetic studies with copper(II) salts. Part I. Anomalous paramagnetism and δ-bonding in anhydrous and hydrated copper(II) acetates. J Chem Soc 3837–3846
10. Niekerk JNV, Schoening FRL, Wet JFD (1953) The structure of crystalline chromous acetate revealing paired chromium atoms. Acta Crystallogr 6:501–504
11. Niekerk JNV, Schoening FRL (1953) X-Ray evidence for metal-to-metal bonds in cupric and chromous acetate. Nature 171:36–37
12. Bertrand JA, Cotton FA, Dollase WA (1963) The metal–metal bonded polynuclear complex anion in $CsReCl_4$. J Am Chem Soc 85:1349–1350
13. Kuznetsov VG, Koz'min PA (1963) A study of the structure of $(PyH)HReCl_4$. Zh Strukt Khim (Russ J Struct Chem) 4:49–55
14. Cotton FA, Curtis NF, Harris CB, Johnson BFG, Lippard SJ, Mague JT, Robinson WR, Wood JS (1964) Mononuclear and polynuclear chemistry of rhenium(III): its pronounced homophilicity. Science 145:1305–1307
15. Falvello LR, Foxman BM, Murillo CA (2014) Fitting the pieces of the puzzle: the delta bond. Inorg Chem 53:9441–9456
16. Allen FH (2002) The Cambridge structural database: a quarter of a million crystal structures and rising. Acta Crystallogr B 58:380–388
17. Schreiner PR, Chernish LV, Gunchenko PA, Tikhonchuk EY, Hausmann H, Serafin M, Schlecht S, Dahl JEP, Carlson RMK, Fokin AA (2011) Overcoming lability of extremely long alkane carbon-carbon bonds through dispersion forces. Nature 477:308–311
18. Noor A, Bauer T, Todorova TK, Weber B, Gagliardi L, Kempe R (2013) The ligand-based quintuple bond-shortening concept and some of its limitations. Chem Eur J 19:9825–9832
19. Losada J, Alvarez S, Novoa JJ, Mota F, Hoffmann R, Silvestre J (1990) The large range of Cr-Cr quadruple bond distances: structural and theoretical analysis. J Am Chem Soc 112: 8998–9000
20. Mota F, Novoa JJ, Losada J, Alvarez S, Hoffmann R, Silvestre J (1993) Pyramidality and metal–metal multiple bonding: structural correlations and theoretical study. J Am Chem Soc 115:6216–6229
21. Mingos DMP, Zhenyang L (1989) Non-bonding orbitals in co-ordination, hydrocarbon and cluster compounds. Struct Bond 71:1–56
22. Mingos DMP, Zhenyang L (1990) Hybridization schemes for co-ordination and organometallic compounds. Struct Bond 72:73–111
23. Hall MB (1987) Problems in the theoretical description of metal–metal multiple bonds or how I learned to hate the electron correlation problem. Polyhedron 6:679–684
24. Falceto A, Theopold KH, Alvarez S (2015) Cr–Cr quintuple bonds: ligand topology and interplay between metal–metal and metal–ligand bonding. Inorg Chem, in press, doi: 10.1021/acs.inorgchem.5b02059
25. Brynda M, Gagliardi L, Roos BD (2009) Analysing the chromium–chromium multiple bonds using multiconfigurational quantum chemistry. Chem Phys Lett 471:1–10
26. Roos BD, Borin AC, Gagliardi L (2007) Reaching the maximum multiplicity of the covalent chemical bond. Angew Chem Int Ed 46:1469–1472
27. Aullón G, Alvarez S (2009) Oxidation states, atomic charges and orbital populations in transition metal complexes. Theor Chem Acc 123:67–73
28. Klene M, Li X, Knox JE, Hratchian HP, Cross JB, Bakken V, Adamo C, Jaramillo J, Gomperts R, Stratmann RE, Yazyev O, Austin AJ, Cammi R, Pomelli C, Ochterski JW, Ayala PY, Morokuma K, Voth GA, Salvador P, Dannenberg JJ, Zakrzewski VG, Dapprich S, Daniels AD, Strain MC, Farkas O, Malick DK, Rabuck AD, Raghavachari K, Foresman JB, Ortiz JV, Cui Q, Baboul AG, Clifford S, Cioslowski J, Stefanov BB, Liu G, Liashenko A, Piskorz P, Komaromi I, Martin RL, Fox DJ, Keith T, Al-Laham MA, Peng CY, Nanayakkara A, Challacombe M, Gill PMW, Johnson B, Chen W, Wong MW, Gonzalez C, Pople JA (2010) Gaussian09, B.1st edn. Gaussian, Wallingford
29. Schaefer A, Huber C, Ahlrichs R (1994) Fully optimized contracted Gaussian basis sets of triple zeta valence quality for atoms Li to Kr. J Chem Phys 100:5829–5835

Index